Exploring the Unimolecular Chemistry of Representative Terpenes Under Protonated and Pyrolysis Conditions

Edgar White Buenger

Thesis submitted to the University of Ottawa
in partial Fulfillment of the requirements for the
Doctorate in Philosophy – Science (Chemistry)

Department of Chemistry and Biomolecular Sciences
Faculty of Science
University of Ottawa

Dedicated to my family and closest friends for following me along all the twists, turns, hops, skips, and jumps that my academic journey has taken me on.

“I believe that you could be exemplified by a quote from George Eliot.

"Adventure is not outside man; it is within."

i.e., adventure can stem from a person's inner spirit of curiosity and willingness to step beyond their comfort zone, rather than from external experiences or physical journeys alone.”

- Prof. Gavin E. Reid, G.Dip.Adv. Supervisor

Abstract

The art of combining experiment and theory together allows for the painting of a complete chemical picture. In this work, the two concepts were married to investigate the unimolecular gas-phase decomposition of representative terpene molecules under protonated and extreme thermal conditions. Protonation studies were carried out experimentally using tandem mass spectrometry with collision-induced dissociation. Protonated isoprene was dominated by the neutral loss of C_2H_4, while its derivative prenol had competition between the neutral losses of C_3H_6, CH_2O, CH_3OH, and H_2O. The dissociation of the monoterpenes showed abundant neutral losses of C_3H_6 and C_4H_8, with minor appearance of C_2H_4 and C_3H_8 in some examples. The monoterpenoid derivatives showed similar dissociation products but introduced the neutral losses of oxygenated compounds. Density functional theory calculations were used to unravel the minimum energy reaction pathways that describe the mechanisms by which each given protonated terpene was converted to the observed product ions in the experiment. In nearly all cases, the initial site of protonation was a key driver for the observed dissociation chemistry of the protonated terpenes.

The decomposition of terpenes under extreme thermal conditions was investigated using flash pyrolysis at the Swiss Light Source synchrotron using the iPEPICO beamline. This experiment enabled the identification of novel isomeric products that have not been previously described in the literature when experiments were performed with isoprene. Density functional theory calculations revealed a new mechanism that could feasibly produce the newly observed cyclopentene intermediate on the pathway towards cyclopentadiene, a previously described pyrolysis product. These calculations were also used to help confirm product identities with Franck-Condon simulations and were used to reveal the mechanisms by which these products were formed. Similar experimental and theoretical methodology was applied for representative

monoterpenes. Here, there was a clear differentiation in the product distribution that was observed for α-pinene, dominated by sequential losses of methyl radicals to yield substituted benzenes, a process not observed in β-pinene or limonene, which were shown to have some degree of overlap between their decomposition chemistries. Unique to the former was the appearance of abundant propargyl radicals, while the latter was shown to be dominated by intermolecular cleavage to yield two molecules of isoprene. In the end, when experiment and theory are combined to provide the same picture, we can have more confidence that the individual images were captured correctly.

Acknowledgements

First are foremost, I must provide the deepest of thanks to all of my family. In particular I must mention my parents Usha and Keith, as without their financial, and domestic support, I would not have managed to make it to this point. For these reasons and more, I am eternally grateful for their continuous presence. As our paths have crossed over the last five years of study, all of my various grandparents, aunts, uncles, and cousins have voiced their support for my academic journey, and their encouragement has not gone unnoticed.

Next, I would like to acknowledge and thank the various chemistry teachers, mentors and guides that have led me on the academic journey that brought me here. Going back all the way to high school, Mr. Lama imparted the foundation of my knowledge in chemistry, and inspired me to study biochemistry at Carleton, as he had done, setting off the beginning of my academic voyage. At Carleton, Dr. Jeff Manthorpe began my research journey by taking me on for my Honour's project due to my (at the time, somehow) synthetic organic chemistry skills. This project led to collaboration with Dr. Jeff Smith who sparked my appreciation and enamour for analytical mass spectrometry, setting me off on the trajectory for graduate studies in that field. This guidance led me to the University of Melbourne, where under the supervision of Dr. Gavin Reid I believe that I was able to truly cement myself as a researcher contributing towards knowledge and discoveries in bioanalytical mass spectrometry. If it wasn't for the influence of these four individuals, I doubt that I would have landed up in the position I find myself today.

I have the utmost appreciation for my Doctoral thesis supervisor Dr. Paul Mayer. He was patient as I completely transitioned gears from my bioanalytical background towards fundamental gas-phase ion chemistry, arguably complete opposite ends of the research space. His excellence in teaching and continuous guidance was instrumental in ensuring that I could understand the necessary physical chemical background knowledge required to complete our projects, and to further develop myself as a competent independent researcher. I must also shout out Dr. Sharon Barden, the facility manager here at the small molecule division of the mass spectrometry facility, for all the instrumentation, wet lab assistance and eventual sanity checks when ensuring the instruments were performing as we needed them to.

Over the years I have been part of multiple research groups and have come to the realization that the people in the mass spectrometry community are simply awesome. A quirky balance of an easygoing nature, combined with intelligence, ambition, and playfulness appear to be a common trend. This has been exemplified greatly over the past five years of my presence in the Mayer group. I cannot begin to name all of you as I'm afraid I'd forget someone, but the adventures we've been on, the games and pranks we've played, and even the mundane day-to-day grind of student life, I couldn't think of a better group to share these times with. You know who you are, and I hope we stay in touch long after our time here.

Finally, I have saved the best, and most important to me, for last. Most of all I must acknowledge and express my deepest thanks to Nathalie, my newlywed wife, who has been by my side throughout my entire academic journey, starting all the way back to Mr. Lama's high school chemistry class. She has always been there for me, gracefully accepting whatever challenges came our way, including travel to the other side of the planet and back so that I could pursue my academics. She has been my rock when times get turbulent, my cheerleader during the highs, and my partner in crime for everything in between. I could never imagine having gone through this journey without my soulmate hand-in-hand. I did it honey, my PhD thesis is complete now!

Table of Contents

List of Figures

List of Tables

List of Abbreviations

Abbreviation	Description	Abbreviation	Description
APCI	Atmospheric pressure chemical ionization	MERP	Minimum energy reaction pathway
B88	Becke 88	MS	Mass spectrometry
B3LYP	Becke's three-parameter hybrid, LYP correlation	MS/MS	Tandem mass spectrometry
BVOC	Biogenic volatile organic compound	ms-TPES	Mass selected threshold photoelectron spectrum
CEM	Chain ejection model	m/z	Mass-to-charge ratio
CID	Collision induced dissociation	NMF	Non-negative matrix factorization
CSS	Closed shell singlet	NMVOC	Non-methane volatile organic compound
CRM	Charge residue model	OSS	Open shell singlet
CGTO	Contracted Gaussian type orbital	P	Heating power
CTST	Canonical transition state theory	PAH	Polycyclic aromatic hydrocarbon
d	Distance	PEPICO	Photoion photoelectron coincidence spectrcoscopy
DC	Direct current	PES	Photoelectron spectroscopy
DFT	Density functional theory	PTR-MS	Proton transfer mass spectrometry
E	Internal energy	QqQ	Triple quadrupole mass spectrometer
E_{CoM}	Center-of-mass frame of reference collision energy	RF	Radio frequency
E_{Lab}	Laboratory frame collision energy	ROKS	Open-shell Kohn-Sham

E_k	Kinetic energy	RRK	Rice-Ramsperger-Kassel
E_p	Potential energy	RRKM	Rice-Ramsperger-Kassel-Marcus
ESI	Electrospray ionization	sccm	Standard cubic centimetres per minute
eV	Electronvolt	STQN	Synchronous Transit-Guided Quasi-Newton
FC	Franck-Condon	S-VWN	Slater exchange, Vosko-Wilk-Nusair correlation
GC-MS	Gas chromatography mass spectrometry	t	Time
GC-FID	Gas chromatography flame ionization detector	T	Temperature
GGA	Generalized gradient approximations	TPEPICO	Theshold photoion photoelectron coincidence spectrcoscopy
IE	Ionization energy	U	Electrical potential
IEM	Ion evaporation model	UV	Ultraviolet radiation
iPEPICO	Imaging photoion photoelectron coincidence spectroscopy	VOC	Volatile organic compounds
LDA	Local density approximation	VUV	Vacuum ultraviolet
LYP	Lee-Yang-Parr	XUV	Extreme ultraviolet radiation
m	Mass	z	Charge

Chapter 1 – Introduction

1.1 – The Atmosphere

The collection of gases that surrounds the Earth represents the atmosphere that is responsible for harbouring the conditions that enable life as we know it in its current form. The atmosphere is generally accepted to be partitioned into different layers, each with unique physical characteristics, as summarized in Figure 1.1.[1] There is an additional layer that is sometimes considered part of the atmosphere known as the exosphere, that lies beyond the thermosphere, and is characterized by a fleetingly small density of gaseous molecules which marks the transition from the Earth's atmosphere to the interstellar environment.[2]

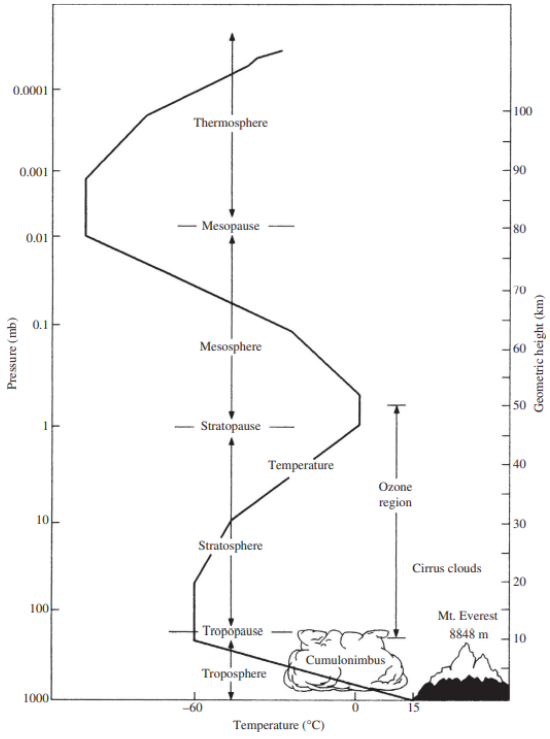

Figure 1.1: Diagram containing the different zones present in the Earth's atmosphere. Reproduced from ref. 1 with permission.

The thermosphere extends from approximately 80 km to upwards of 500 km above the surface of the Earth and represents the outermost layer that is universally considered part of the Earth's atmosphere. The unique properties of this layer include the extremely high molecular temperatures (potential excess of 2000 ºC), brought upon by the excessive absorption of UV and XUV photons, primarily by molecular nitrogen and oxygen, leading to their photodissociation and subsequent excitation of the atomic substituents.[3]

Below the thermosphere lies the mesopause, approximately 80 km above the Earth's surface and represents a boundary region that signifies the change in environment between the thermosphere and mesosphere layers, primarily driven by a drastic change in temperature. The mesosphere layer sits approximately 50-80 km above the surface of the Earth (Figure 1.1), and like the thermosphere chemistry in this layer is primarily driven by the absorption of higher-energy solar radiation, however in the mesosphere molecular temperatures are much lower, leading to the coldest portion of the Earth's atmosphere with mean temperatures in the range of -100 ºC.[4]

Similar to the thermosphere, the stratosphere is a region of the atmosphere that is characterized by a relative increase in environmental temperature, with the peak temperature at the highest point at the stratopause. Here, there is an increased presence of molecular gasses, denoted by the relatively higher pressure compared with the higher layers (Figure 1.1). The temperature increase is associated with the absorption of lower energy UV radiation by the high concentration of ozone gas contained within the stratosphere, a key process for protecting life contained in the troposphere.[5] Historically there have been environmental concerns about the human dependent depletion of ozone in the stratosphere and the consequences this may have for life, however global policy changes have ameliorated this issue.[6]

The lowest layer of the atmosphere that extends directly from the Earth's surface until approximately 10 km of altitude is known as the troposphere and contains the vast majority of the gaseous density of the atmosphere, as evidenced by the high pressure values compared with the other layers (Figure 1.1). Significant quantities of water vapour are present in the troposphere and represent the bulk of molecular content in this layer.[7] Other compounds present in the troposphere include smaller quantities of environmental oxidants, including inorganic compounds like NO_x, SO_2, $OH^\cdot$, HNO_3, and H_2S, contributing towards the overall reactivity and relative acidity present in this layer.[7] In addition to these inorganic gases, there are considerable volatile organic compounds (VOC) present in the troposphere due to their ability to readily reach the gas phase, with methane being the most abundant and generally considered separately.[7,8] The presence of VOC is an important feature of the troposphere, leading to a variety of oxidation chemistries, as well as the formation of aerosols that are present near the Earth's surface.[8] Understanding the flux of VOC in the troposphere is an active field of research. One important class of VOCs is the terpene family of molecules.

1.2 – Terpenes

Terpenes are a broad category of hydrocarbons that are produced in a wide variety of plant species. A common structural theme that has been postulated for terpenes is the isoprene rule, whereby different groups of terpenes are categorized depending upon the number of isoprene units contained within the overall molecule.[9] Isoprene is considered to be the simplest terpene and lies in a category of its own. When two isoprene units are joined together, the resulting terpene falls under the monoterpene category; three joined isoprene units lead to sesquiterpenes, four to diterpenes, and so on.[9] Biologically, these terpenes are largely produced through the methylerythitol phosphate or mevalonate pathways that ultimately lead to the formation of dimethylallyl phosphate, a key precursor to the formation of isoprene and larger terpenes.[10] Due to the presence of multiple positions of unsaturation within these molecular species, there is a significant degree of molecular complexity, including the possibility for functionalization, leading to a subcategory of compounds known as terpenoids (Figure 1.2).

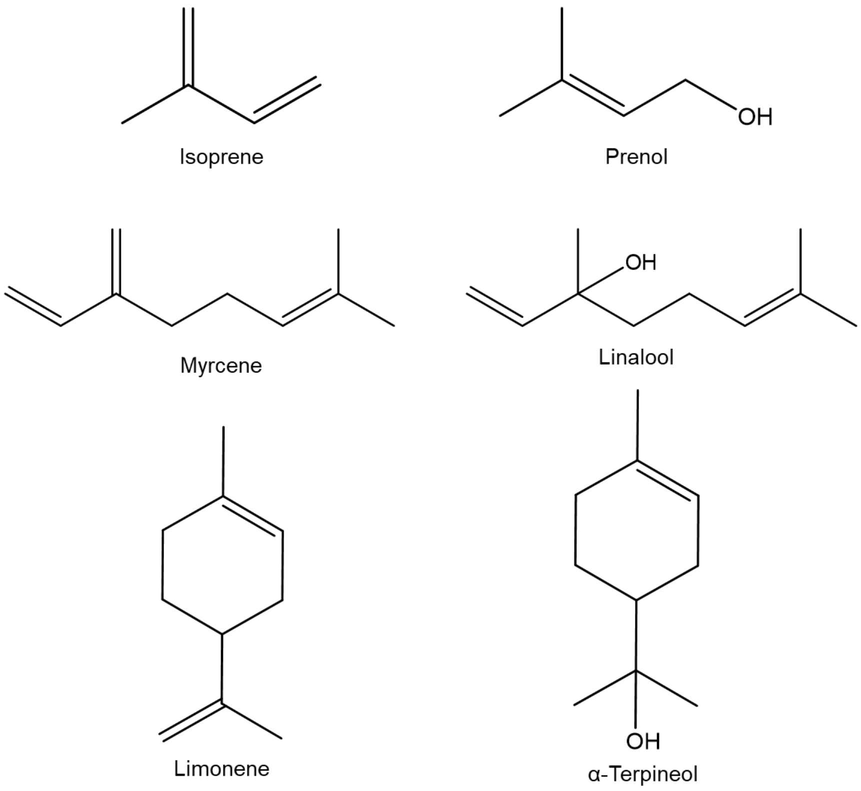

Figure 1.2: Representative terpene and terpenoid structures, highlighting their structural diversity**.**

Resulting from the relatively high vapour pressure of terpenes with lower molecular weight (isoprene, monoterpenes and sesquiterpenes primarily), these compounds are volatile enough to be emitted from plant material into the troposphere and represent a significant portion of the global annual VOC emissions.[11–13] In addition to the natural emission of terpenes from plants, these are valuable compounds for a variety of human industries including fuel, fragrance and flavour, and pharmaceuticals,[14–17] ultimately leading to additional quantities of these compounds being emitted into the atmosphere. These emissions are important because the unsaturation of terpenes means that they are relatively reactive, and they participate in atmospheric chemistry processes, primarily oxidation reactions.

The main source of isoprene oxidation in the troposphere results from the reaction with hydroxyl radicals, produced by the photodegradation of ozone.[18,19] The primary products from this reaction include hydroxylated isoprene structures, which themselves are highly reactive and continue to react with atmospheric oxygen to produce isoprene peroxy radicals.[19] Other tropospheric reactions include isoprene, or its peroxy radical derivative, reacting with NO_x species to introduce nitrosylated groups, or with atmospheric Cl.[19] Similarly, monoterpenes are primarily reactive towards environmental $OH^{\cdot}$ and yield monoterpene derivatives that contain hydroxyl and carboxylic acid functional groups,[20] and minor pathways are also observed with other environmental oxidants like O_3 and NO_x.[21,22] These oxidized terpenes are important atmospheric contaminants as they contribute towards secondary organic aerosol formation, which can lead to the condensation of fine particulate matter and can have impacts on air quality and even the health and safety of humans.[23,24] Suffice to say, understanding the chemical consequences of terpene emissions and their ultimate fate in our environment is a significant research concern.

1.3 – Protonation and Ion Chemistry

The bulk of literature that focuses on gas-phase terpene chemistry in the atmosphere is concerned with oxidation reactions, as described in the previous section. A lesser appreciated mechanism for the consumption of atmospheric terpenes is protonation and subsequent polymerization. This process of gas-phase protonation was first described in the literature by Liggio *et al.*, where they were interested in, and successfully demonstrated polymerization reactions of isoprene and pinene on the surface of acidic aerosols.[25] This initial discovery spurned the work of Enami and colleagues to observe the effects of acidic water droplets and how they may interact with gas-phase terpenes. Their work showed that under certain pH conditions of water droplets, typically below 5, gas-phase terpenes would interact with the acidic droplets and become protonated on the surface.[26–30] These protonated terpenes were then shown to continue to react through oligomerization and polymerization reactions, contributing towards secondary organic aerosol formation.[26–30] An aspect of this protonated terpenes chemistry that has been overlooked is the energetic breakdown of protonated terpenes, and what sort of products may be expected to be obtained from these processes, presenting an avenue for further research in this space.

1.4 – Thermal Decomposition

Aside from the oxidation reactions that occur naturally in the atmosphere, described in previous sections, there are also mechanisms by which terpenes can be decomposed under high temperature conditions. With trends in shifting climates, there has been a predicted increase in wildfire abundance and intensity, ultimately leading to the emission and thermal decomposition of volatile terpenes.[31–33] Furthermore, due to their potential use as combustion-based fuel sources for anthropogenic applications,[14,34,35] there are additional mechanisms involved in the thermal degradation of terpenes that must be considered.

There have been numerous reports in the literature that are concerned with the thermal degradation of terpenes. Egloff *et al.* published a review of the thermal degradation products of numerous terpenes including isoprene, monoterpenes, and larger terpenes, at a range of temperatures from 100-800 ºC, and showed a broad range of decomposition, polymerization and bimolecular reaction products, dependent upon the temperature.[31] More recent studies on isoprene pyrolysis have shown similar decomposition products, including attempts to develop a broader kinetic model that can describe the multitude of possible pathways.[36–38] Additionally, studies have focused on the thermal degradation of monoterpenes and showed a variety of products depending upon the starting structure, including the formation of isoprene, small molecule radicals, and aromatic compounds.[39–41] Despite these works in the literature, there has been little focus on very high temperature, short reaction timescales, providing an opportunity for further research.

1.5 – Objective

The overarching goal of this thesis-based research project was to investigate the unimolecular decomposition of a variety of representative terpene compounds, primarily constituting the monoterpene subcategory, when subject to extreme environmental conditions, including protonation and thermal degradation. The compounds contained within the monoterpene regime are structurally diverse compounds with many different isomeric structures due to their multiple degrees of unsaturation. Moreover, these are VOC that may readily be emitted into the atmosphere, necessitating the understanding of their gas-phase chemistry, particularly under niche and extreme conditions. Both protonated and neutral gas-phase terpene chemistries are relevant in atmospheric activity. Protonated species will be interrogated using collision-induced dissociation tandem mass spectrometry, including isoprene, myrcene, limonene, their hydroxylated derivatives, and pinene. The thermal degradation of neutral terpenes will be carried out using a pyrolysis reactor with imaging photoion photoelectron coincidence spectroscopy to accurately identify the products obtained. Computational chemistry using density functional theory will be applied to calculate minimum energy reaction pathways that describe the mechanistic transformations along the reaction coordinate from reactant to final observed products. These mechanisms ultimately describe the unimolecular chemistry that occurs in the reactions of these gas-phase terpenes under specific atmospheric conditions.

1.6 – Chapter 1 References

(1) Schlesinger, W. H.; Bernhardt, E. S. The Atmosphere. In *Biogeochemistry*; Elsevier, 2020; pp 51–97. https://doi.org/10.1016/B978-0-12-814608-8.00003-7.

(2) Fahr, H. J.; Shizgal, B. Modern Exospheric Theories and Their Observational Relevance. *Rev. Geophys.* **1983**, *21* (1), 75–124. https://doi.org/10.1029/RG021i001p00075.

(3) Roble, R. G. Dynamics of the Earth's Thermosphere. *Rev. Geophys.* **1983**, *21* (2), 217–233. https://doi.org/10.1029/RG021i002p00217.

(4) Thomas, L. The Composition of the Mesosphere and Lower Thermosphere. *Philos. Trans. R. Soc. Lond. Ser. Math. Phys. Sci.* **1980**, *296* (1418), 243–260. https://doi.org/10.1098/rsta.1980.0167.

(5) Thrush, B. A. The Chemistry of the Stratosphere. *Rep. Prog. Phys.* **1988**, *51* (10), 1341–1371. https://doi.org/10.1088/0034-4885/51/10/002.

(6) Manzer, L. E. The CFC-Ozone Issue: Progress on the Development of Alternatives to CFCs. *Science* **1990**, *249* (4964), 31–35. https://doi.org/10.1126/science.249.4964.31.

(7) Ayers, G. P.; Gillett, R. W. Tropospheric Chemical Composition: Overview of Experimental Methods in Measurement. *Rev. Geophys.* **1990**, *28* (3), 297–314. https://doi.org/10.1029/RG028i003p00297.

(8) Sahu, L. K. Volatile Organic Compounds and Their Measurements in the Troposphere. *Curr. Sci.* **2012**, *102* (12).

(9) Ruzicka, L. The Isoprene Rule and the Biogenesis of Terpenic Compounds. *Experientia* **1953**, *9* (10), 357–367. https://doi.org/10.1007/BF02167631.

(10) Pichersky, E.; Raguso, R. A. Why Do Plants Produce so Many Terpenoid Compounds? *New Phytol.* **2018**, *220* (3), 692–702. https://doi.org/10.1111/nph.14178.

(11) Graedel, T. E. Terpenoids in the Atmosphere. *Rev. Geophys.* **1979**, *17* (5), 937. https://doi.org/10.1029/RG017i005p00937.

(12) Acosta Navarro, J. C.; Smolander, S.; Struthers, H.; Zorita, E.; Ekman, A. M. L.; Kaplan, J. O.; Guenther, A.; Arneth, A.; Riipinen, I. Global Emissions of Terpenoid

VOCs from Terrestrial Vegetation in the Last Millennium. *J. Geophys. Res. Atmospheres* **2014**, *119* (11), 6867–6885. https://doi.org/10.1002/2013JD021238.

(13) Guenther, A. B.; Jiang, X.; Heald, C. L.; Sakulyanontvittaya, T.; Duhl, T.; Emmons, L. K.; Wang, X. The Model of Emissions of Gases and Aerosols from Nature Version 2.1 (MEGAN2.1): An Extended and Updated Framework for Modeling Biogenic Emissions. *Geosci. Model Dev.* **2012**, *5* (6), 1471–1492. https://doi.org/10.5194/gmd-5-1471-2012.

(14) Mewalal, R.; Rai, D. K.; Kainer, D.; Chen, F.; Külheim, C.; Peter, G. F.; Tuskan, G. A. Plant-Derived Terpenes: A Feedstock for Specialty Biofuels. *Trends Biotechnol.* **2017**, *35* (3), 227–240. https://doi.org/10.1016/j.tibtech.2016.08.003.

(15) Bicas, J. L.; Dionísio, A. P.; Pastore, G. M. Bio-Oxidation of Terpenes: An Approach for the Flavor Industry. *Chem. Rev.* **2009**, *109* (9), 4518–4531. https://doi.org/10.1021/cr800190y.

(16) Weston-Green, K.; Clunas, H.; Jimenez Naranjo, C. A Review of the Potential Use of Pinene and Linalool as Terpene-Based Medicines for Brain Health: Discovering Novel Therapeutics in the Flavours and Fragrances of Cannabis. *Front. Psychiatry* **2021**, *12*, 583211. https://doi.org/10.3389/fpsyt.2021.583211.

(17) Paduch, R.; Kandefer-Szerszeń, M.; Trytek, M.; Fiedurek, J. Terpenes: Substances Useful in Human Healthcare. *Arch. Immunol. Ther. Exp. (Warsz.)* **2007**, *55* (5), 315–327. https://doi.org/10.1007/s00005-007-0039-1.

(18) Hewitt, C. N.; Harrison, R. M. Tropospheric Concentrations of the Hydroxyl Radical—a Review. *Atmospheric Environ. 1967* **1985**, *19* (4), 545–554. https://doi.org/10.1016/0004-6981(85)90033-2.

(19) Wennberg, P. O.; Bates, K. H.; Crounse, J. D.; Dodson, L. G.; McVay, R. C.; Mertens, L. A.; Nguyen, T. B.; Praske, E.; Schwantes, R. H.; Smarte, M. D.; St Clair, J. M.; Teng, A. P.; Zhang, X.; Seinfeld, J. H. Gas-Phase Reactions of Isoprene and Its Major Oxidation Products. *Chem. Rev.* **2018**, *118* (7), 3337–3390. https://doi.org/10.1021/acs.chemrev.7b00439.

(20) Larsen, Bo. R.; Di Bella, D.; Glasius, M.; Winterhalter, R.; Jensen, N. R.; Hjorth, J. Gas-Phase OH Oxidation of Monoterpenes: Gaseous and Particulate Products. *J. Atmospheric Chem.* **2001**, *38* (3), 231–276. https://doi.org/10.1023/A:1006487530903.

(21) Grosjean, D.; Williams, E. L.; Grosjean, E.; Andino, J. M.; Seinfeld, J. H. Atmospheric Oxidation of Biogenic Hydrocarbons: Reaction of Ozone with .Beta.-Pinene, D-Limonene and Trans-Caryophyllene. *Environ. Sci. Technol.* **1993**, *27* (13), 2754–2758. https://doi.org/10.1021/es00049a014.

(22) Hallquist, M.; Wängberg, I.; Ljungström, E.; Barnes, I.; Becker, K.-H. Aerosol and Product Yields from NO_3 Radical-Initiated Oxidation of Selected Monoterpenes. *Environ. Sci. Technol.* **1999**, *33* (4), 553–559. https://doi.org/10.1021/es980292s.

(23) Iinuma, Y.; Böge, O.; Miao, Y.; Sierau, B.; Gnauk, T.; Herrmann, H. Laboratory Studies on Secondary Organic Aerosol Formation from Terpenes. *Faraday Discuss.* **2005**, *130*, 279. https://doi.org/10.1039/b502160j.

(24) Rohr, A. C. The Health Significance of Gas- and Particle-Phase Terpene Oxidation Products: A Review. *Environ. Int.* **2013**, *60*, 145–162. https://doi.org/10.1016/j.envint.2013.08.002.

(25) Liggio, J.; Li, S.; Brook, J. R.; Mihele, C. Direct Polymerization of Isoprene and *α* -pinene on Acidic Aerosols. *Geophys. Res. Lett.* **2007**, *34* (5), 2006GL028468. https://doi.org/10.1029/2006GL028468.

(26) Enami, S.; Hoffmann, M. R.; Colussi, A. J. Dry Deposition of Biogenic Terpenes via Cationic Oligomerization on Environmental Aqueous Surfaces. *J. Phys. Chem. Lett.* **2012**, *3* (21), 3102–3108. https://doi.org/10.1021/jz301294q.

(27) Matsuoka, K.; Sakamoto, Y.; Hama, T.; Kajii, Y.; Enami, S. Reactive Uptake of Gaseous Sesquiterpenes on Aqueous Surfaces. *J. Phys. Chem. A* **2017**, *121* (4), 810–818. https://doi.org/10.1021/acs.jpca.6b11821.

(28) Ishizuka, S.; Fujii, T.; Matsugi, A.; Sakamoto, Y.; Hama, T.; Enami, S. Controlling Factors of Oligomerization at the Water Surface: Why Is Isoprene Such a Unique VOC? *Phys. Chem. Chem. Phys.* **2018**, *20* (22), 15400–15410. https://doi.org/10.1039/C8CP01551A.

(29) Qiu, J.; Ishizuka, S.; Tonokura, K.; Sato, K.; Inomata, S.; Enami, S. Effects of pH on Interfacial Ozonolysis of α-Terpineol. *J. Phys. Chem. A* **2019**, *123* (32), 7148–7155. https://doi.org/10.1021/acs.jpca.9b05434.

(30) Colussi, A. J.; Enami, S.; Ishizuka, S. Hydronium Ion Acidity Above and Below the Interface of Aqueous Microdroplets. *ACS Earth Space Chem.* **2021**, *5* (9), 2341–2346. https://doi.org/10.1021/acsearthspacechem.1c00067.

(31) Egloff, Gustav.; Herrman, Margaret.; Levinson, B. L.; Dull, M. F. Thermal Reactions of Terpene Hydrocarbons. *Chem. Rev.* **1934**, *14* (3), 287–383. https://doi.org/10.1021/cr60049a001.

(32) Wotton, B. M.; Flannigan, M. D.; Marshall, G. A. Potential Climate Change Impacts on Fire Intensity and Key Wildfire Suppression Thresholds in Canada. *Environ. Res. Lett.* **2017**, *12* (9), 095003. https://doi.org/10.1088/1748-9326/aa7e6e.

(33) Hatch, L. E.; Jen, C. N.; Kreisberg, N. M.; Selimovic, V.; Yokelson, R. J.; Stamatis, C.; York, R. A.; Foster, D.; Stephens, S. L.; Goldstein, A. H.; Barsanti, K. C. Highly Speciated Measurements of Terpenoids Emitted from Laboratory and Mixed-Conifer Forest Prescribed Fires. *Environ. Sci. Technol.* **2019**, *53* (16), 9418–9428. https://doi.org/10.1021/acs.est.9b02612.

(34) Wang, S.; Wang, Z.; Wang, Y.; Nie, Q.; Yi, X.; Ge, W.; Yang, J.; Xian, M. Production of Isoprene, One of the High-Density Fuel Precursors, from Peanut Hull Using the High-Efficient Lignin-Removal Pretreatment Method. *Biotechnol. Biofuels* **2017**, *10* (1), 297. https://doi.org/10.1186/s13068-017-0988-5.

(35) Kumar, M.; Tung Chong, C.; Karmakar, S. Comparative Assessment of Combustion Characteristics of Limonene, Jet A-1 and Blends in a Swirl-Stabilized Combustor under the Influence of Pre-Heated Swirling Air. *Fuel* **2022**, *316*, 123350. https://doi.org/10.1016/j.fuel.2022.123350.

(36) Weber, K. H.; Zhang, J. Mechanistic Study of Thermal Decomposition of Isoprene (2-Methyl-1,3-Butadiene) Using Flash Pyrolysis Supersonic Jet VUV Photoionization Mass Spectrometry. *J. Phys. Chem. A* **2007**, *111* (45), 11487–11492. https://doi.org/10.1021/jp075689+.

(37) Grajales-González, E.; Kukkadapu, G.; Nagaraja, S. S.; Shao, C.; Monge-Palacios, M.; Chavarrio, J. E.; Wagnon, S. W.; Curran, H. J.; Pitz, W. J.; Mani Sarathy, S. An Experimental and Kinetic Modeling Study of the Pyrolysis of Isoprene, a Significant Biogenic Hydrocarbon in Naturally Occurring Vegetation Fires. *Combust. Flame* **2022**, *242*, 112206. https://doi.org/10.1016/j.combustflame.2022.112206.

(38) Chen, G.; Ding, W.; Cheng, Z.; Wang, J.; Xing, L.; Li, W.; He, Y.; Lin, F.; Yang, J.; Zhao, L.; Yan, B. Experimental and Kinetic Modeling Studies of Isoprene Pyrolysis at Low and Atmospheric Pressures. *Combust. Flame* **2022**, *246*, 112445. https://doi.org/10.1016/j.combustflame.2022.112445.

(39) McGraw, G. W.; Hemingway, R. W.; Ingram, L. L.; Canady, C. S.; McGraw, W. B. Thermal Degradation of Terpenes: Camphene, Δ^3 -Carene, Limonene, and α-Terpinene. *Environ. Sci. Technol.* **1999**, *33* (22), 4029–4033. https://doi.org/10.1021/es9810641.

(40) Coudour, B.; Chetehouna, K.; Lemée, L.; Bertin, P.; Garo, J.-P. Thermal Degradation of α-Pinene Using a Py–GC/MS. *J. Therm. Anal. Calorim.* **2019**, *137* (4), 1315–1328. https://doi.org/10.1007/s10973-019-08028-8.

(41) Kolicheski, M. B.; Cocco, L. C.; Mitchell, D. A.; Kaminski, M. Synthesis of Myrcene by Pyrolysis of β-Pinene: Analysis of Decomposition Reactions. *J. Anal. Appl. Pyrolysis* **2007**, *80* (1), 92–100. https://doi.org/10.1016/j.jaap.2007.01.005.

Chapter 2 – Techniques

2.1 – Mass Spectrometry

The experimental technique of mass spectrometry is a simple, yet sophisticated form of chemical analysis. The concept of analyzing the mass-to-charge ratio of charged particles dates to J.J. Thomson's cathode ray tube experiments, wherein he identified the elementary particle that we now know as the electron.[1] These elementary experiments paved the way for the development of what we know modernly as mass spectrometry (MS), a powerful and versatile tool in the chemists' arsenal that has found wide-ranging chemical applications, from bioanalytics to kinetics. The technique revolves around the formation of ionized molecules from a sample of interest and then manipulating those intact ions in such a way that they can be detected, using electric or magnetic fields to direct their motion. Fundamentally, a complete mass spectrometer instrument consists of an ionization source, a mass analyzer, and a detector (Figure 2.1). This text will focus on specific examples of these features that will find themselves directly applied in this work.

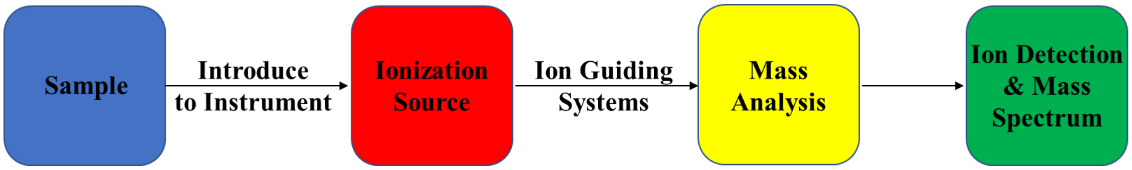

Figure 2.1: A simple flowchart representing the key features of a mass spectrometry experiment.

2.1.1 – Electrospray Ionization

The electrospray ionization (ESI) technique was developed in the later half of the 20th century and is widely used today. ESI is useful for compounds that contain polar, ionizable functional groups. Furthermore, ESI is considered a 'soft' ionization technique, meaning that little to no in source fragmentation of the molecular ion is expected to occur. To simply describe ESI, a solution containing a sample of interest is passed through a small capillary, across which a high voltage is applied. This process enables the direct formation of gaseous sample ions that can be identified through the mass spectrometer. A visual representation of ESI is presented in Figure 2.2.[2]

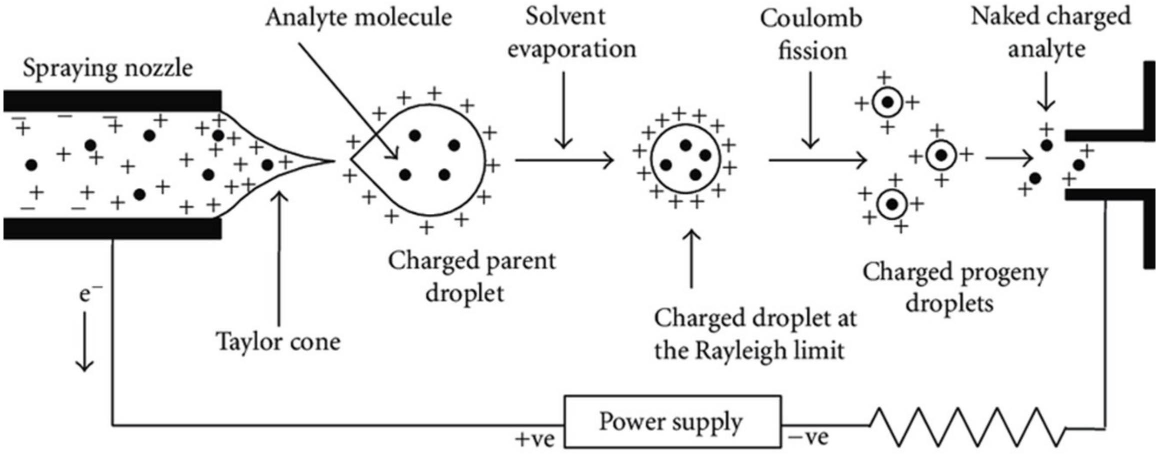

Figure 2.2: Diagram illustrating the processes involved in the electrospray ionization technique. (Reproduced from ref. 2, licensed under CC BY 3.0 https://creativecommons.org/licenses/by/3.0/)

Two theoretical principles are being combined in ESI: the Taylor Cone, and the Rayleigh limit. A Taylor Cone is formed as an electrically conductive liquid (i.e., water) travels through a strong electric field. For instance, imagine that a jet of water is travelling through a capillary which has a high voltage applied across the exit. As the jet of water exits the capillary and enters the electric field, the strength of the field can overcome the surface tension of the water, leading the jet to spray out many little liquid droplets that form the shape of a cone with a given angle, the Taylor Cone.[3] The sample of interest is now contained within these liquid droplets and charged (ionized). As the droplets continue travelling in space, the liquid solvent can evaporate, bringing the ionized sample molecules closer and closer together. When the droplets become smaller, they become subjected to the Rayleigh limit, a principle which states that the Coulomb repulsive forces between the charged particles can overcome the surface tension of the liquid droplet, leading to the explosive formation of two smaller droplets that can accept the charge contained within them.[4] The smaller droplets continue to be subjected to solvent evaporation, once again reaching the Rayleigh limit, and repeating the process described.

The ultimate release of the sample ions into the gas-phase proceeds through three primarily accepted models: the ion evaporation model (IEM), the charge residue model (CRM), and the chain ejection model (CEM), summarized visually in Figure 2.3.

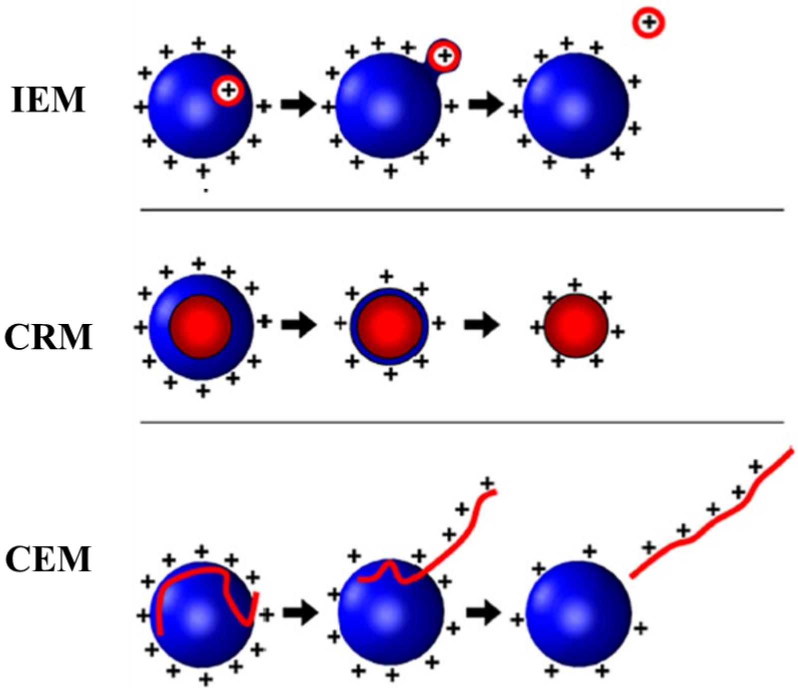

Figure 2.3: Proposed models of ion ejection from solvent droplets. IEM: ion evaporation model, CRM: charge residue model, CEM: chain ejection model. (Adapted with permission from ref. 5, Copyright 2013)

Each of these models are relevant in certain situations, depending upon the nature of the ion being ejected into the gas-phase. In the IEM, the Rayleigh droplets contain numerous small, charged particles. As the charged droplets become smaller, there comes a point where they are small enough that the electric field emitted from the charged droplet is large enough to induce the ejection of partially solvated sample ion clusters.[5] As these clusters travel in space and towards the mass spectrometer, the solvent dissociates and leaves behind gas-phase sample ions that can be manipulated by the instrument.[5] In the CRM, a single large molecule (i.e. a globular protein) is contained within the charged Rayleigh droplets. As the droplet travels in space towards the mass spectrometer, the solvent evaporates away and the charge contained in the droplet is transferred to the molecule and subsequently analyzed by the instrument.[5] Finally, the CEM combines aspects of the other two models. It is like CRM in that a single large molecule is involved, except in this case the large molecule is not globular but rather a large open chain polymer, such as an unfolded protein. The ejection of the polymer out of the Rayleigh-droplet and into the gas-phase follows a process like the IEM.[5] The polymer migrates towards the edge of the droplet and the charge transfers from the droplet to the polymer as it travels past the solvent-air interface, eventually leading to free gas-phase charged polymer.

2.1.2 – Atmospheric Pressure Chemical Ionization

Atmospheric pressure chemical ionization (APCI) is an alternative ionization method to ESI. The method is well suited towards thermally stable compounds, while readily ionizing less polar compounds than ESI can. Much like ESI, APCI is a ‘soft’ ionization technique, leading to minimal fragmentation of the molecular ion in the source, although some fragmentation may be observed. However, unlike ESI, APCI is primarily applicable towards small molecules and is typically not well amenable towards large proteins or polymers.

An APCI source fundamentally features the following components: a capillary containing solvent-sample mixture of interest, a heating element, a corona discharge needle, and a low-vacuum pinhole entrance into the mass spectrometer (Figure 2.4).[6]

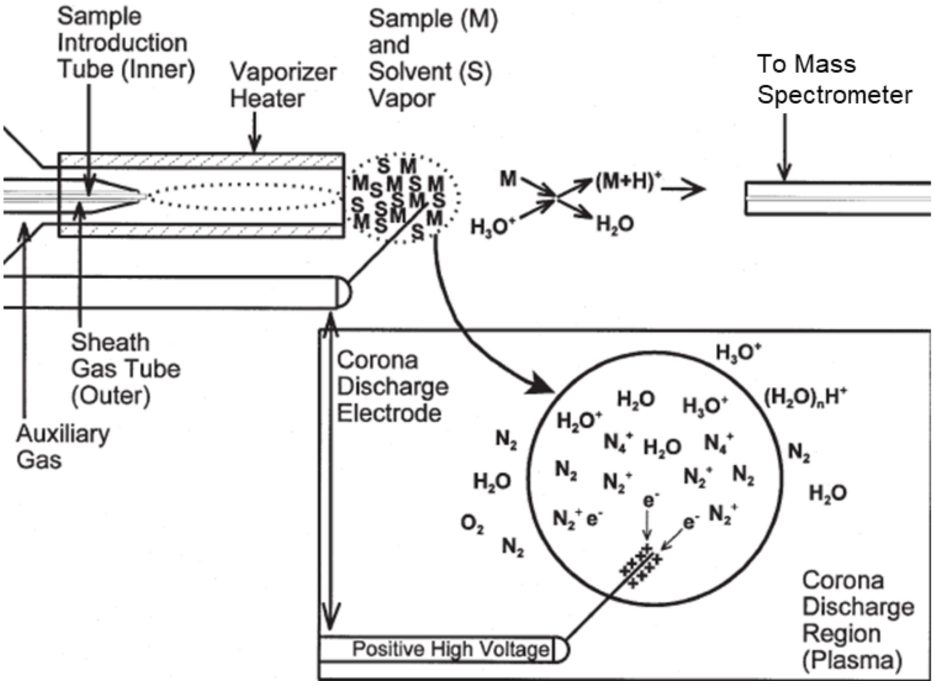

Figure 2.4: Visualization of the key features of an APCI source. (Reproduced with permission from ref. 6, Copyright 2001)

The role of the capillary is to ensure that the solvent-containing sample of interest is directed towards the heating element through the assistance of gas flows. Once the sample passes through the capillary it enters the heating element, which is maintained at a relatively high temperature (150 ºC or greater) to ensure volatilization of the solvent, leaving behind a neutral solvent-sample vapor mixture. Following volatilization, the vapor mixture is directed towards the corona discharge needle, where a high voltage is applied. This high voltage initiates the chemical ionization process within the corona discharge region, leading to free gaseous sample ions. Finally, the sample ions are directed towards the vacuum pinhole entrance with the assistance of the gas flow, which helps to facilitate complete evaporation of remaining solvent for ion clusters that are still associated to the solvent, ensuring the introduction of unencumbered sample ions into the mass spectrometer. Once passed through the vacuum inlet, the ions can be manipulated through electric and magnetic fields to proceed through the instrument.

The ionization mechanism in APCI is dependent upon atmospheric conditions for two factors: first, to ensure that sufficient collisions occur in the corona discharge region to facilitate the ionization process and second, to ensure that the correct molecular species are present for the ionization to occur, specifically nitrogen gas and water vapor. The mechanism proceeds because of the following seven chemical reactions:[6]

$$(1)\ N_2 + e \rightarrow\ N_2^{+} + 2\ e$$

$$(2)\ N_2^{+} + 2\ N_2 \rightarrow\ N_4^{+} + N_2$$

$$(3)\ N_4^{+} + H_2O \rightarrow\ H_2O^{+} + 2\ N_2$$

$$(4)\ H_2O^{+} +\ H_2O \rightarrow\ H_3O^{+} + OH^{\cdot}$$

$$(5)\ H_3O^{+} + H_2O\ + N_2 \rightarrow\ H^{+}(H_2O)_2 +\ N_2$$

$$(6)\ H^{+}(H_2O)_{n-1} + H_2O\ + N_2 \rightarrow\ H^{+}(H_2O)_n + N_2$$

$$(7)\ H^{+}(H_2O)_n + M \rightarrow MH^{+} +\ (H_2O)_n$$

The ionization process begins due to the corona discharge voltage, which causes nitrogen gas to become ionized (1). The ionized nitrogen gas is then capable of undergoing collisions with the plentiful, neutral nitrogen gas, the result of which leads to an activated N_4^{+} species (2). The activated N_4^{+} species can interact with water vapor, leading to the production of activated, ionized water molecules (3). The ionized water molecules can react with neutral water, leading to a hydronium ion (4). Following the production of the hydronium ion, neutral water molecules are attracted to the charged particle, which leads to the formation of clusters (5,6). These charged water clusters can react with the neutral sample molecule of interest (M), and through a proton-transfer reaction, the charge is shifted from the water cluster to M, finally producing the gas-phase molecular ion that was desired (7).

2.1.3 – Quadrupole Mass Analyzer

Following the ionization source, it is now the responsibility of the mass analyzer to filter and separate all the ions that were produced in the source, to enable accurate detection of what was contained within the sample. The most frequently used mass analyzer is the quadrupole, due to its cost-effective performance capabilities. The primary drawbacks of the quadrupole mass analyzer are its inability to separate very large mass-to-charge ratio ions (m/z, labeled as m/e in Figure 2.5)[7], and its somewhat poor resolution compared to more sophisticated mass analyzers.

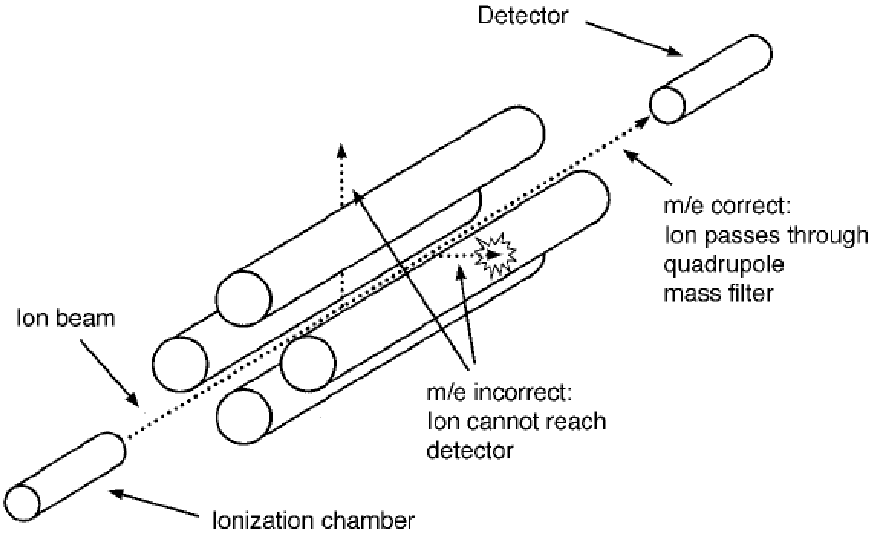

Figure 2.5: Cartoon schematic presenting the physical layout of the quadrupole mass analyzer (Reproduced with permission from ref. 7, Copyright 2003).

The quadrupole mass analyzer is physically made up of four identical cylindrical metal rods that are oriented parallel to one another, with a 90º angle separating each rod from one another along the central axis. Opposing rods, i.e., those directly across from each other in space are electrically connected to one another. The operation of the quadrupole proceeds by applying a radio frequency (RF) voltage followed by an offset direct current (DC) voltage to one pair of the connected rods. At the same time, an equal RF/DC potential, but the opposite polarity, is applied to the other pair of connected rods. Over the timeframe of the analysis, the polarity of the opposing rod pairs is rapidly alternated back and forth. This alternating RF/DC potential produces an oscillating electric field that dictates ion motion through the quadrupole. At a given RF and DC potential, ions with a certain m/z can travel through the quadrupole's oscillating electric field. Ions with a different m/z do not have a stable trajectory and strike one of the quadrupole rods during their path, causing them to be lost from the analysis.

Motion through the quadrupole is complicated but has been previously simulated.[8] Steel & Henchman presented simulated models that plot the stable trajectory of ions through the quadrupole as a plot of DC voltage against the RF amplitude, and these plots are called stability diagrams.

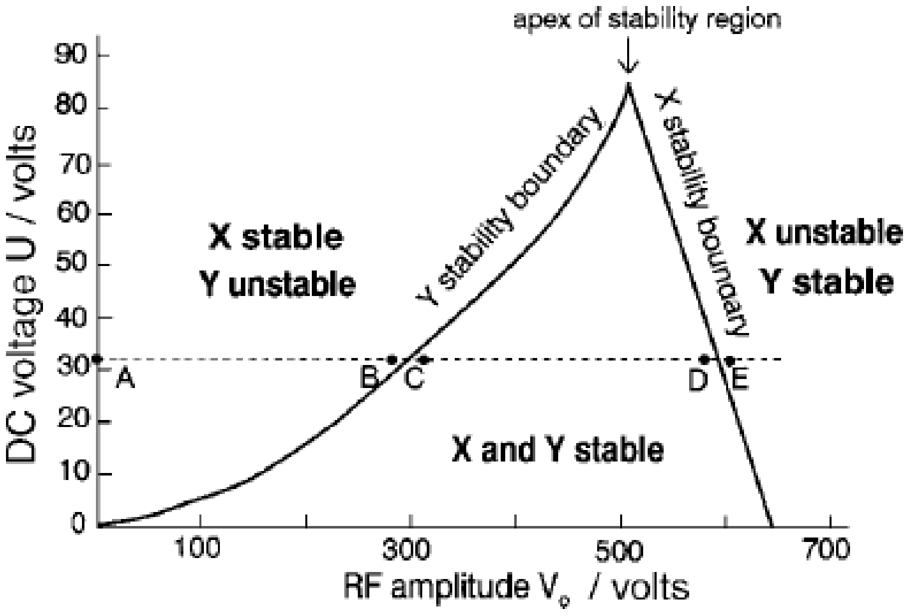

Figure 2.6: Stability diagram describing stable motion through the quadrupole mass analyzer. (Reproduced with permission from ref. 8, Copyright 1998)

Ions that fall under the curve of the stability diagram are stably transmitted through the quadrupole (Figure 2.6 C, D), while those outside of the curve are lost (Figure 2.6 A, B, E). The stability diagram can be generalized to all ions by incorporating the ion mass into the plot, and this treatment describes how a range of ion masses can be scanned using the quadrupole.[8]

2.1.4 – Triple Quadrupole Mass Spectrometer

In the previous section, a general overview of a quadrupole as a standalone mass analyzer was presented. In many applications, three quadrupoles are aligned in tandem and such an orientation gives rise to tandem mass spectrometry (MS/MS) experiments. In this arrangement, the first quadrupole (Q1) is used to mass select the ion of interest, as previously described. The second quadrupole (q2) acts as a collision cell in conjunction with the introduction of an inert gas and an excitation potential, facilitating molecular ion fragmentation through collision induced dissociation (CID). Furthermore, q2 is operated in RF only mode (no DC potential), allowing for all fragment ions that are produced to pass through. The final quadrupole (Q3) acts as a mass analyzer to filter the ions produced in q2. This Q1q2Q3 arrangement allows for several experiments to be performed: product ion scans, precursor ion scans, neutral loss scans and selected reaction monitoring.[9,10]

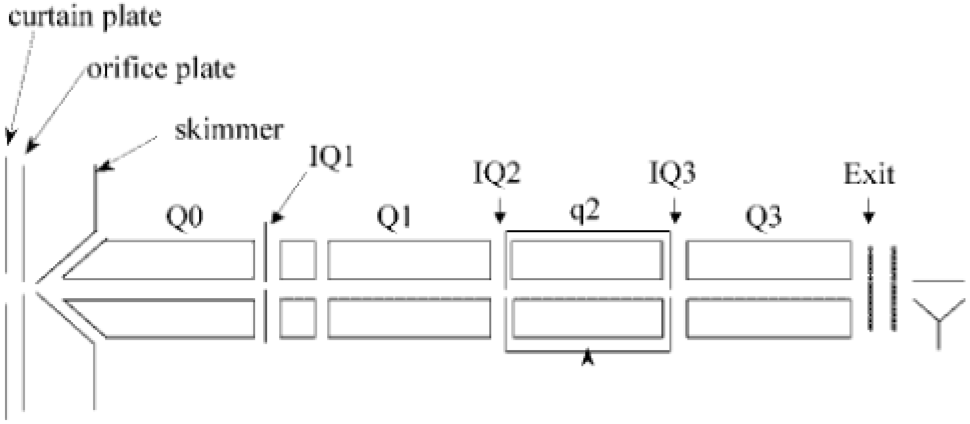

Figure 2.7: Cartoon schematic of the triple quadrupole mass analyzer set up. (Reproduced with permission from ref. 10, Copyright 2003)

A general representation of the triple quadrupole experimental layout is presented in Figure 2.7, using a product ion scan as an example. In a product ion scan, Q1 is set to operate such that only the selected ion of defined m/z is passed through it and guided towards q2 for CID, and all product ions that were produced through CID are scanned in Q3. This experiment is useful for structure determination of an unknown since the resulting product ions are fragments and pieces of the molecular ion. The fragments can be pieced together to determine the structure of the molecular ion. In a precursor ion scan, Q1 is set to scan across all m/z, which are then fragmented via CID in q2 and Q3 is set to a predetermined m/z. This arrangement is useful for determining which initial molecular ions contained a particular functional group that can be selected for in Q3. During a neutral loss scan Q1 and Q3 are both set to scan across all m/z, except the scan in Q3 is affected by a predetermined mass difference, representing the loss of a neutral species from the molecular ion. For instance, if the molecular ion lost a water molecule, a mass offset of 18 m/z would be applied between Q1 & Q3. Finally, in selected reaction monitoring both Q1 and Q3 are each set to a predetermined m/z: a certain molecular ion of interest is selected for in Q1 and specific product ion that is obtained from this molecular ion selected for in Q3. This experiment can potentially be used for analyte quantification and offers increased sensitivity, when required.

2.1.5 – Time-of-Flight Mass Analyzer

While Thomson's experiments certainly construed a time-of-flight (TOF) measurement, this term did not gain prominence in the literature until the concept was refined through the late 1940s and early 1950s.[11] This development led to the commercialization of the technique. The principle of operation is relatively straightforward and is shown diagrammatically in Figure 2.8.[12]

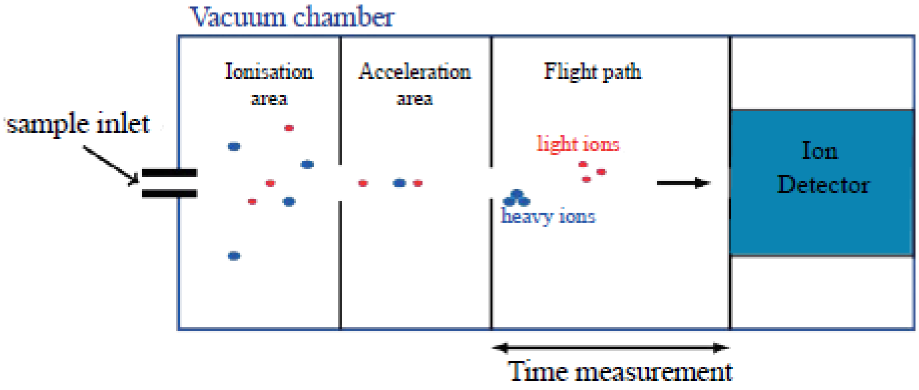

Figure 2.8: Simplified diagram illustrating the operation of the time-of-flight mass analyzer. (Reproduced from ref. 12, licensed under CC BY 4.0 https://creativecommons.org/licenses/by/4.0/))

Once an ion is produced in the ion source, it proceeds into an electric field which imparts an electrical potential energy (E_p) equal to its charge (z) times the electrical potential (U) applied on the TOF.

$$E_p = zeU$$

Furthermore, this electrical potential accelerates the ion through the TOF into the flight tube, converting the electrical potential energy into kinetic energy, where E_k is the kinetic energy, m is the mass of the ion and v is the velocity of the ion.

$$E_p = E_k$$

$$zeU = ½\, mv^2$$

If there is no electrical field or potential applied in the flight tube, the ion will proceed through it with a constant velocity (v) following the acceleration. Since the distance of the flight tube is known (d), and the time it takes the ion to travel through the flight tube can be measured (t), these values can be substituted for v, recalling that v = d/t.

$$qU = ½\, m\left(\frac{d}{t}\right)^2$$

Solving for the flight time leads to:

$$t = \frac{d}{\sqrt{2U}}\sqrt{\frac{m}{z}}$$

Since d and U are known parameters, it is therefore demonstrated that the flight time of an ion is dependent upon the square root of its mass to charge ratio. This analyzer is relatively popular, although somewhat eclipsed by the quadrupole in robustness, but they are often employed together. Its primary advantages over the quadrupole are an increase in mass resolving power and the ability to analyze exceptionally large m/z ions.

2.2 – Threshold Photoelectron Photoion Coincidence Spectroscopy (TPEPICO)

Threshold photoelectron spectroscopy (TPES) is a method that was designed to provide improved results when compared to traditional photoelectron spectroscopy (PES). When performing a PES experiment, the aim is to determine the abundance of molecules that become ionized following exposure to high-energy radiation (i.e., UV, X-ray). These experiments provide sensitive information regarding electronic structure and precise energy measurements. However, traditional PES methods rely on radiation sources that are outputting at a fixed wavelength of light. This drawback leads to poor Franck-Condon overlap of the neutral molecule structure and its corresponding ionic ground state structure, leading to a loss of ionization at certain energies. The result of this poor overlap is a gap in the resulting spectrum, which leads to the loss of electronic structural information within that range. To overcome this issue, threshold PES techniques were developed and the features of the TPEPICO approach used in this work will be described in the subsequent sections.

2.2.1 – Pyrolysis

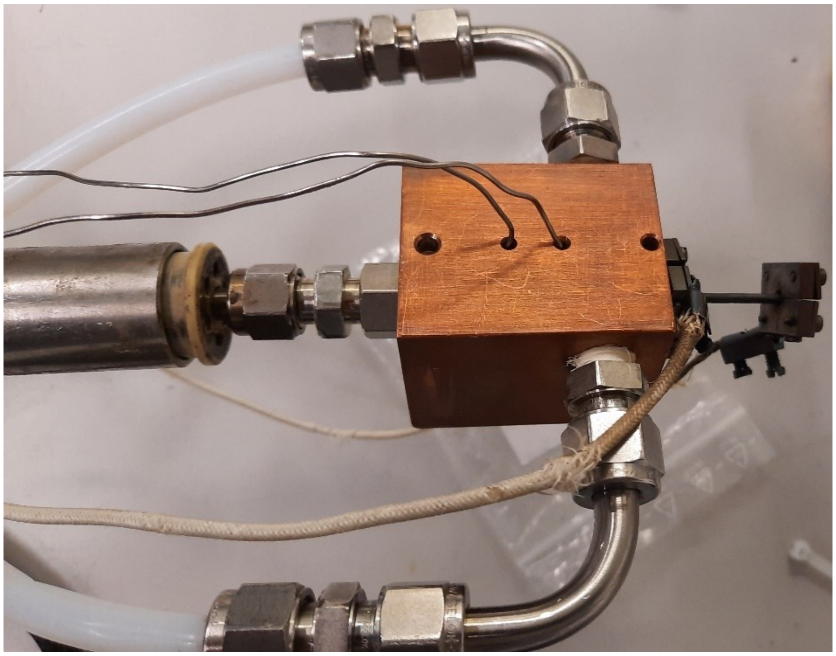

Figure 2.9: Image showing the components of the pyrolysis apparatus that is part of the TPEPICO beamline. Gaseous compounds are sampled through the water-cooled copper jacket and led towards SiC heating chamber.

Pyrolysis experiments were performed by passing argon, at a pressure of 1 bar and a flow rate of 1 standard cubic centimetres per minute (sccm), over a vial containing the targeted samples at room temperature. This mixture was then diluted with 20 sccm of argon to produce a beam with approximately 2.5% sample, which expanded through a 200 μm pinhole into the 3 cm long, 1 mm internal diameter, resistively heated SiC pyrolysis microreactor (Figure 2.9). Reactor surface temperatures have been derived based on a previously observed power dependence measured in an identical pyrolysis setup by a type C thermocouple, defined by the equation below:

$$T/^{\circ}\mathrm{C} = P/\mathrm{W} \times 14.27 + 303$$

Where *T* is the reactor temperature and *P* is the heating power. The reactor temperature is considered to represent the gas temperature inside the reactor to within 100 ºC.[13] The pressure and residence time in the reactor has been estimated to be 10–40 mbar and up to 100 μs, respectively.[13,14] The reactor is placed in the source vacuum chamber, where the pressure was ~ 5×10^{-5} mbar during measurements. The molecular beam exiting the pyrolysis reactor is passed through a 2 mm diameter skimmer into the detection chamber, kept at a pressure of 10^{-6} mbar during measurements. The reactor can be heated to temperatures between 200 and 2000 °C to explore the distribution of pyrolysis products as a function of temperature by recording their ms-TPES.

2.2.2 – Photoionization

Following pyrolysis of the target molecules, the first component of a TPEPICO experiment is the photoionization process. Unlike PES, which uses a fixed-wavelength light source, TPEPICO experiments are performed at synchrotron light sources. These sources of light are highly precise, laser-like in intensity, and most importantly tuneable across a variety of wavelengths. The tunability of the radiation source is the key component of what defines a TPEPICO experiment. The energy of the photons produced by the synchrotron is described by the expression $E = h\nu$. During the photoionization process, part of the photon's energy is consumed to produce the radical cation and free electron pair, representing the ionization energy of the molecule. The remaining photon energy is distributed into the internal energy content of the radical cation, and to kinetic energy of the electron released from the photoionization event.

2.2.3 – Energy Selection

The tunability of the synchrotron enables the production of radical cations with a well-defined internal energy distribution. The complimentary electron produced as part of the ionization process is released with an associated kinetic energy component. These electrons are ejected from the ionization event with a range of kinetic energies, depending upon the photon energy and the internal energy of the ion. A small portion of these electrons will be ejected with zero (or functionally zero) kinetic energy, and these electrons are termed threshold electrons. The threshold electrons are selected for by the electron detector through the placement of a small slit; those electrons with sufficient kinetic energy to veer off the slit axis will be lost to the detector. The radical cation produced through the photoionization process can be analyzed using TOF, as previously described in section 2.1.5. These two detections are designed to occur simultaneously, defining the coincidence component of the experiment. The result is the detection of radical cations with precisely defined m/z and internal energy.

2.2.4 – Imaging Detector

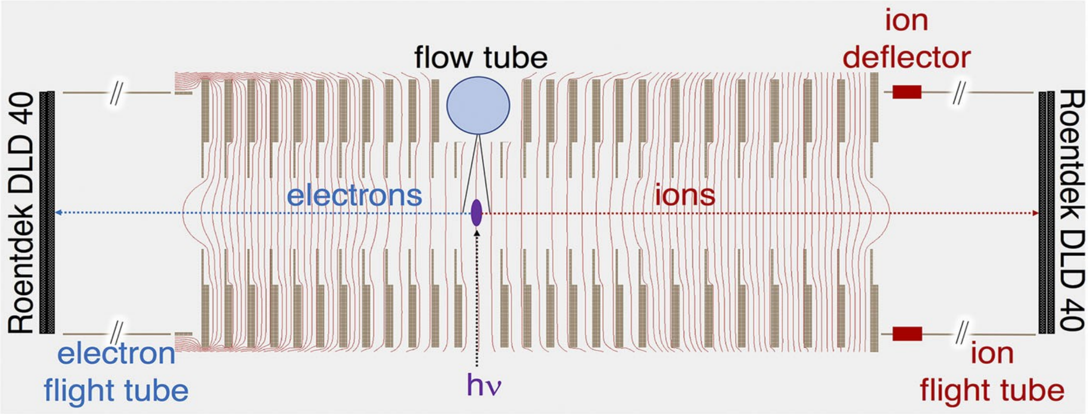

Figure 2.10: Schematic representing the key components of the PEPICO apparatus (reproduced with permission from ref. 14, Copyright 2017)

In the previous section, the detection of threshold electrons was described for a general TPEPICO experiment. Recently, PEPICO experiments have been modified, such that the threshold electrons can be detected using an imaging system, like the Roentdek DLD 40 presented in Figure 2.10.

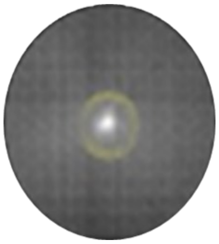

Figure 2.11: An electron image obtained from an iPEPICO experiment, with vibrant center spot representing zero-kinetic energy electrons striking the detector.

The detector is set up such that the threshold electrons are concentrated along the central axis in a vibrant centre-spot, and energetic electron spots are scattered across the entire image, as shown in the example presented in Figure 2.11. However, there is a small probability that an energetic electron travels down the same axis as a threshold electron. This occurrence is accounted for by subtracting the signal obtained from electrons just outside the center circle from those obtained in the ring itself (faintly visible in Figure 2.11). It is assumed that the energetic electrons just outside of the ring contain the same experimental data as the energetic electrons in the ring, thus cancelling them out of the intensity.

2.3 – Density Functional Theory

Density functional theory (DFT) is a computational chemistry method used across a variety of disciplines that attempts to solve the electronic structure of many-body systems. The primary advantage over other methods is its relatively low computational cost, facilitating the completion of calculations within a reasonable timeframe, when compared to other available methods such as ab initio (from first principles). This section will aim to briefly describe the theoretical underpinnings of DFT.

2.3.1 – Quantum Mechanical Background

As with all quantum mechanical approaches, the development of DFT begins at the Schrödinger equation and attempts to solve it to obtain the energy levels contained within a particle. While the Schrödinger equation can be solved for a simple system where there is a single particle (the hydrogen atom),[15] as the systems become larger, the equation becomes impossible to solve and approximations must be made. The first approximation that has gained universal acceptance, and predates DFT, is the Born-Oppenheimer approximation.[16] Shortly following the publication of the Schrödinger equation, Born & Oppenheimer presented a set of simplifying assumptions, which postulated that since nuclear and electronic mass & motion are substantially different, the nuclear and electronic wavefunctions in the Schrödinger equation can be treated separately.[16] This treatment simplifies the Schrödinger equation into a nuclear component and an electronic component that can be computed more readily. However, even with these assumptions, the calculations are daunting and further assumptions must be made.

2.3.2 – Hohenberg-Kohn Theorems

The primary assumptions that paved the way for DFT were presented as two theorems by Hohenberg and Kohn in 1964.[17] They are applicable to any system which contains electrons that are in motion under the control of an external potential. The first theorem states that the ground state properties of a given many-electron system can be defined as a unique functional of the electron density.[17] This assumption massively simplifies the many-electron computation into a more manageable three-dimensional problem, consisting of the spatial coordinates in which the electron density is contained. The second theorem posits that the ground state energy can be obtained through variational approaches, and that the correct electron density is that which minimizes the total energy of the system. Thus, it is the electrons and their density in space that can ultimately define all properties available in the ground state. Unfortunately, these theorems do not offer a practical solution for actively calculating this ground state electron density, since there are numerous unknown values contained within the energy functional. Further improvements were necessitated to achieve practical outcomes.

2.3.3 – Kohn-Sham Approach

To improve upon the Hohenberg-Kohn theorems and make them amenable towards practical applications, Kohn and Sham developed an approach which allows for an exact treatment of the kinetic energy term. This treatment begins by assuming that there is an imaginary, non-interacting system of electrons created that is described by the exact same electron density as the real, interacting system of electrons.[18] Through this assumption, the kinetic energy term of the non-interacting system can be calculated by summing the total kinetic energy of each individual electron contained within the system.[18] This treatment solves the kinetic energy component of the electron density functional, and leaves one remaining unknown component: the exchange-correlation term.

2.3.4 – Exchange-Correlation

The exchange-correlation term of the density functional contains correction factors for the pieces of unknown information. For instance, the kinetic energy treatment is not exact but an approximation using the sum of individual electrons. Additionally, the Coulombic term assumes an average charge distribution across the electron density and does not account for the possibility of sudden electron-electron repulsion within the electron density. This possibility is accounted for in the exchange-correlation term. Together, these modifications constitute unknown parameters that must be approximated to fully solve the density functional: the exchange term, and the correlation term. There are numerous approximations that have been developed and generally increase in accuracy and computational demand.

2.3.5 – Representative Exchange-Correlation Functionals

As the only unknown component in DFT, the development of the technique has centered around improving the accuracy of these exchange-correlation functionals. In the local density approximation (LDA), the electron density is treated as a uniform electron gas where the electrons are smoothly distributed within the gas. With this model employed, the exchange term can be expressed with Slater's simplification of the Hartree-Fock approach.[19] The correlation term was treated with quantum Monte Carlo simulations and parametrized with a two-point Padé approximant interpolation formula by Vosko, Wilk and Nusair, yielding to improved accuracy.[20] Combining these two terms leads to the functional known in the literature as S-VWN, for Slater exchange + Vosko, Wilk and Nusair correlation. While the S-VWN functional improved accuracy compared to previous approaches, it still tended to overestimate certain parameters and improved functionals continued to develop.

It was eventually realized that the uniform electron gas model was not the most accurate representation of the electron density surrounding the nucleus. Due to charge interactions, there should theoretically be a greater abundance of electrons closer to the nucleus, which decreases as the distance from the nucleus increases. By accounting for this fact, it was realized that the exchange-correlation functional should be dependent on both the electron density and the gradient of the electron density, to represent the expected abundance disparity within the density. This led to the development of functionals now termed generalized gradient approximations (GGA). One of the most popular approaches for handling the exchange term was developed by Becke in 1988 and has been termed B88.[21] In this approach, an additional term was developed to incorporate the derivative of the electron density, to represent the gradient nature of the model. This value is then subtracted from the value computed through LDA exchange. With regards to the correlation term, one of the most popular methods was developed by Lee, Yang and Parr and this treatment is now known as LYP in their honour.[22] In this approach, the correlation term is expressed in terms of both the electron density and the gradient of local kinetic energy density. To improve accuracy meta-GGA approaches were later developed, in which one can use the Laplacian of the kinetic energy density, at the cost of increased computing time.[23] While both GGA and meta-GGA's were useful functionals that improved upon LDA, the introduction of hybrid functionals are what really propelled DFT into a practical tool beyond theoretical chemistry.

Hybrid functionals were first presented by Becke in 1993, which combines many of the previous approaches into a single functional.[24] The most popular hybrid functional was developed shortly after by Stephens *et al*, which expands on Becke's three-parameter hybrid.[25] In this approach, the exchange-correlation functional features components from LDA, Hartree-Fock, B88 and GGA, where the GGA component used LYP correlation. The results of using the functional of this form offered unprecedently improved accuracy, and the method has become named B3LYP (Becke's three-parameter hybrid, LYP correlation). One can also opt to use meta-GGAs in the place of the GGA term, and a popular set of functionals that use this approach are the Minnesota functionals.[26] As we proceed from the LDA model towards the hybrid functionals, the accuracy of the calculation increases, however, computational complexity increases, and thus the time for calculations to complete.

2.3.6 – Basis Sets

Basis sets are a set of functions that mathematically describe the orbital structure present in a quantum mechanical system. There are many options available and each suits the respective system being modeled. One of the most popular and efficient basis sets applied in DFT are those developed by Pople.[27] In the simplest form, the minimal basis set, each atomic orbital is made up of three Gaussian functions, which aims to appear like a Slater-type orbital. Increasing in complexity is the split-valence double-zeta basis set, which contains separate functions describing core and valence orbitals. The core is treated as a single contracted Gaussian type orbital (CGTO) consisting of six Gaussian functions, while the valence is treated with a combination of two CGTO's, one made up of three Gaussian functions and a second one made up of a single Gaussian function. This split-valence double-zeta basis set as described by Pople is abbreviated to 6-31G. Triple-zeta basis sets are also used, which add an additional CGTO made up of one Gaussian function to describe the valence orbitals (6-311G). Polarization functions can be included, which include additional functions to minimize electron-electron repulsion, by accounting for the possibility of the electrons occupying orbitals with increased angular momentum. For instance, d-orbital polarization functions can be added to describe orbitals of carbon (6-311G(d)), and furthermore p-orbital functions can be further added to describe polarization in hydrogen (6-311G(d,p)). Finally, diffuse sp functions can be included to describe and improve the accuracy of calculations involving electron-electron repulsion in more extreme situations than polarization, such as anionic species. The addition of diffuse functions can be applied to both non-hydrogen atoms (6-311G+(d,p) and hydrogen atoms alike (6-311G++(d,p)). As the number of functions contained within the basis set increases, so does the computational time, so there is a trade-off between accuracy and calculation time to be considered when choosing a basis set for each system.

2.4 – Unimolecular Reaction Modelling

The first two sections of this paper covered experimental techniques that could be used to obtain physical evidence of the unimolecular reactions of the target molecules. The experimental data can be supplemented by DFT calculations, as described in the third section. These calculations enable the determination of optimized structural geometries, vibrational frequencies, and rotational constants of the chemical species involved throughout the unimolecular reaction. There is one component that has not been considered yet, and that is the rate of the reaction. This issue will be addressed by using Rice-Ramsperger-Kassel-Marcus (RRKM) theory.

2.4.1 – Rice-Ramsperger-Kassel-Marcus Theory

RRKM theory of chemical reactivity has its roots in the work first presented by Rice-Ramsperger-Kassel (RRK) in the late 1920s.[28,29] In this model, the chemical system is treated as a collection of identical harmonic oscillators, and there is one critical oscillator which enables the conversion of reactants to products. This treatment is statistical and only considers the probability that available energy is distributed into the critical oscillator. RRK theory is limited by assuming identical harmonic oscillators. This is not a realistic picture of a chemical system, since the oscillations (vibrational modes) would not be identical, but rather dependent upon the individual atoms and their arrangement. The RRK model was improved by Marcus into the RRKM model by incorporating the ideas of conventional transition state theory (CTST). In CTST the rate constant of a reaction (speed at which the reaction proceeds) is derived as a function of the systems internal temperature, and the critical oscillator responsible for the reaction to proceed is called the transition state.[30,31] Marcus adjusted the RRK model by suggesting that each vibrational mode in the molecule be treated individually, as opposed to a collection of identical oscillators.[32] Furthermore, the model expresses the rate constant as a function of the systems internal energy, as opposed to temperature.[32] This is advantageous since the internal energy of a system is a more fundamental value, the temperature can be derived through knowing the internal energy, but not vice-versa. Thus, this refined RRKM model is a practical model for describing unimolecular reactions and can be described by the equation below:

$$k(E) = \frac{\sigma N^{\ddagger}(E - E_0)}{h\rho(E)}$$

In this expression, the k(E) term represents the rate constant of a reaction at a given internal energy. In the denominator, the h is Planck's constant and ρ(E) refers to the density of the rotational-vibrational states of the reactants at a given internal energy level E. In the numerator, the σ term corresponds to the degeneracy of the reaction (the number of different ways that a reaction may proceed along a pathway towards the same product), while the $N^{\ddagger}(E-E_0)$ term corresponds to the sum of the rotational-vibrational states of the transition state of given internal energy level E, incorporating the difference of the 0 K activation energy E_0.

2.5 – Chapter 2 References

(1) Thomson, J. J. XL. Cathode Rays. *Lond. Edinb. Dublin Philos. Mag. J. Sci.* **1897**, *44* (269), 293–316. https://doi.org/10.1080/14786449708621070.

(2) Banerjee, S.; Mazumdar, S. Electrospray Ionization Mass Spectrometry: A Technique to Access the Information beyond the Molecular Weight of the Analyte. *Int. J. Anal. Chem.* **2012**, *2012*, 1–40. https://doi.org/10.1155/2012/282574.

(3) Taylor, Geoffrey Ingram. Disintegration of Water Drops in an Electric Field. *Proc. R. Soc. Lond. Ser. Math. Phys. Sci.* **1964**, *280* (1382), 383–397.

(4) Rayleigh, Lord. XX. On the Equilibrium of Liquid Conducting Masses Charged with Electricity. *Lond. Edinb. Dublin Philos. Mag. J. Sci.* **1882**, *14* (87), 184–186. https://doi.org/10.1080/14786448208628425.

(5) Konermann, L.; Ahadi, E.; Rodriguez, A. D.; Vahidi, S. Unraveling the Mechanism of Electrospray Ionization. *Anal. Chem.* **2013**, *85* (1), 2–9. https://doi.org/10.1021/ac302789c.

(6) Byrdwell, W. C. Atmospheric Pressure Chemical Ionization Mass Spectrometry for Analysis of Lipids. *Lipids* **2001**, *36* (4), 327–346. https://doi.org/10.1007/s11745-001-0725-5.

(7) Honour, J. W. Benchtop Mass Spectrometry in Clinical Biochemistry. *Ann. Clin. Biochem. Int. J. Lab. Med.* **2003**, *40* (6), 628–638. https://doi.org/10.1258/000456303770367216.

(8) Henchman, M.; Steel, C. Understanding the Quadrupole Mass Filter through Computer Simulation. *J. Chem. Educ.* **1998**, *75* (8), 1049. https://doi.org/10.1021/ed075p1049.

(9) de Hoffmann, E. Tandem Mass Spectrometry: A Primer. *J. Mass Spectrom.* **1996**, *31* (2), 129–137. https://doi.org/10.1002/(SICI)1096-9888(199602)31:2%253C129::AID-JMS305%253E3.0.CO;2-T.

(10) Hager, J. W.; Yves Le Blanc, J. C. Product Ion Scanning Using a Q-q-$Q_{\text{linear ion trap}}$ (Q TRAP$^{\text{TM}}$) Mass Spectrometer. *Rapid Commun. Mass Spectrom.* **2003**, *17* (10), 1056–1064. https://doi.org/10.1002/rcm.1020.

(11) Price, D. Time-of-Flight Mass Spectrometry: The Early Years as Chronicled by the European Time-of-Flight Symposia. *Am. Chem. Soc. ACS Symp. Ser.* **1994**, 1–15.

(12) Plocoste, T.; Jacoby Koaly, S. Impact of a New Legislation on Volatile Organic Compounds Emissions in an Open Landfill in Tropical Insular Climate. *Int. J. Waste Resour.* **2016**, *6* (3). https://doi.org/10.4172/2252-5211.1000236.

(13) Guan, Q.; Urness, K. N.; Ormond, T. K.; David, D. E.; Barney Ellison, G.; Daily, J. W. The Properties of a Micro-Reactor for the Study of the Unimolecular Decomposition of Large Molecules. *Int. Rev. Phys. Chem.* **2014**, *33* (4), 447–487. https://doi.org/10.1080/0144235X.2014.967951.

(14) Sztáray, B.; Voronova, K.; Torma, K. G.; Covert, K. J.; Bodi, A.; Hemberger, P.; Gerber, T.; Osborn, D. L. CRF-PEPICO: Double Velocity Map Imaging Photoelectron Photoion Coincidence Spectroscopy for Reaction Kinetics Studies. *J. Chem. Phys.* **2017**, *147* (1), 013944. https://doi.org/10.1063/1.4984304.

(15) Haines, L. K.; Roberts, D. H. One-Dimensional Hydrogen Atom. *Am. J. Phys.* **1969**, *37* (11), 1145–1154.

(16) Born, M.; Oppenheimer, R. Zur Quantentheorie der Molekeln. *Ann. Phys.* **1927**, *389* (20), 457–484. https://doi.org/10.1002/andp.19273892002.

(17) Hohenberg, P.; Kohn, W. Inhomogeneous Electron Gas. *Phys. Rev.* **1964**, *136* (3B), B864–B871. https://doi.org/10.1103/PhysRev.136.B864.

(18) Kohn, W.; Sham, L. J. Self-Consistent Equations Including Exchange and Correlation Effects. *Phys. Rev.* **1965**, *140* (4A), A1133–A1138. https://doi.org/10.1103/PhysRev.140.A1133.

(19) Slater, J. C. A Simplification of the Hartree-Fock Method. *Phys. Rev.* **1951**, *81* (3), 385–390. https://doi.org/10.1103/PhysRev.81.385.

(20) Vosko, S. H.; Wilk, L.; Nusair, M. Accurate Spin-Dependent Electron Liquid Correlation Energies for Local Spin Density Calculations: A Critical Analysis. *Can. J. Phys.* **1980**, *58* (8), 1200–1211. https://doi.org/10.1139/p80-159.

(21) Becke, A. D. Density-Functional Exchange-Energy Approximation with Correct Asymptotic Behavior. *Phys. Rev. A* **1988**, *38* (6), 3098–3100. https://doi.org/10.1103/PhysRevA.38.3098.

(22) Lee, C.; Yang, W.; Parr, R. G. Development of the Colle-Salvetti Correlation-Energy Formula into a Functional of the Electron Density. *Phys. Rev. B* **1988**, *37* (2), 785–789. https://doi.org/10.1103/PhysRevB.37.785.

(23) Becke, A. D. A New Inhomogeneity Parameter in Density-Functional Theory. *J. Chem. Phys.* **1998**, *109* (6), 2092–2098. https://doi.org/10.1063/1.476722.

(24) Becke, A. D. Density-functional Thermochemistry. III. The Role of Exact Exchange. *J. Chem. Phys.* **1993**, *98* (7), 5648–5652. https://doi.org/10.1063/1.464913.

(25) Stephens, P. J.; Devlin, F. J.; Chabalowski, C. F.; Frisch, M. J. Ab Initio Calculation of Vibrational Absorption and Circular Dichroism Spectra Using Density Functional Force Fields. *J. Phys. Chem.* **1994**, *98* (45), 11623–11627. https://doi.org/10.1021/j100096a001.

(26) Zhao, Y.; Truhlar, D. G. The M06 Suite of Density Functionals for Main Group Thermochemistry, Thermochemical Kinetics, Noncovalent Interactions, Excited States, and Transition Elements: Two New Functionals and Systematic Testing of Four M06-Class Functionals and 12 Other Functionals. *Theor. Chem. Acc.* **2008**, *120* (1–3), 215–241. https://doi.org/10.1007/s00214-007-0310-x.

(27) Ditchfield, R.; Hehre, W. J.; Pople, J. A. Self-Consistent Molecular-Orbital Methods. IX. An Extended Gaussian-Type Basis for Molecular-Orbital Studies of Organic Molecules. *J. Chem. Phys.* **1971**, *54* (2), 724–728. https://doi.org/10.1063/1.1674902.

(28) Kassel, L. S. Studies in Homogeneous Gas Reactions. I. *J. Phys. Chem.* **1928**, *32* (2), 225–242. https://doi.org/10.1021/j150284a007.

(29) Rice, O. K.; Ramsperger, H. C. THEORIES OF UNIMOLECULAR GAS REACTIONS AT LOW PRESSURES. *J. Am. Chem. Soc.* **1927**, *49* (7), 1617–1629. https://doi.org/10.1021/ja01406a001.

(30) Eyring, H. The Activated Complex in Chemical Reactions. *J. Chem. Phys.* **1935**, *3* (2), 107–115. https://doi.org/10.1063/1.1749604.

(31) Evans, M. G.; Polanyi, M. Some Applications of the Transition State Method to the Calculation of Reaction Velocities, Especially in Solution. *Trans. Faraday Soc.* **1935**, *31*, 875. https://doi.org/10.1039/tf9353100875.

(32) Marcus, R. A. Unimolecular Dissociations and Free Radical Recombination Reactions. *J. Chem. Phys.* **1952**, *20* (3), 359–364. https://doi.org/10.1063/1.1700424.

Chapter 3 – Protonated Isoprene and Prenol

Based on the publication White Buenger, E.; Mayer, P. M. Unraveling the Unimolecular Ion Chemistry of Protonated Isoprene and Prenol. *J. Am. Soc. Mass Spectrom.* **2024**, *35* (1), 31–39. https://doi.org/10.1021/jasms.3c00297.

Contribution Statement

E. White Buenger carried out the experiments, computational studies, prepared and revised the manuscript for submission. P. M. Mayer conceptualized the idea, supervised the work and revised the manuscript.

3.1 – Introduction

Volatile organic compounds (VOCs) have been described as organic compounds that feature a high vapour pressure and are insoluble in water, eventually leading to their emission into the atmosphere as gases. Methane is an important VOC due to its environmental and atmospheric impact,[1] and is generally treated separately from other VOCs, termed "non-methane" (NMVOC). NMVOCs can be emitted from biogenic and anthropogenic sources and have been studied extensively on a global scale.[2–5] The most abundant NMVOC is isoprene (Figure 3.1a), which is primarily emitted into the atmosphere from biogenic sources.[6] Models have been developed that attempt to describe the rate of isoprene emission from leaves.[7] Furthermore, isoprene can be emitted from anthropogenic sources, including motor vehicle exhaust gases,[8] and even human breath.[9] Together, these findings demonstrate that there is a significant amount of isoprene present in the environment, and its impacts on atmospheric chemistry is an active field of research.

Isoprene is more reactive than saturated alkanes owing to it being a conjugated diene. Because of its high reactivity, the atmospheric lifetime of isoprene is on the order of hours to a couple of days, depending on the reactant.[10] The majority of isoprene oxidation has been predicted to result from reaction with hydroxyl radicals, leading to the formation of isoprene peroxy radicals.[11] Although addition of the hydroxyl radical can occur at any of the four unsaturated carbons, two structures are typically observed, corresponding to addition at the primary carbons.[12] Although the majority of isoprene is consumed through the hydroxyl radical pathway described above, a sizeable minority of isoprene participates in ozonolysis.[13] Addition of ozone can occur across either one of the double bonds present in isoprene, with a slight preference for the unsubstituted position.[14] The direct products obtained from the ozonolysis include methyl vinyl ketone, methacrolein, formaldehyde, and a variety of Criegee intermediates (some of which are stable, most are not).[14] The stable Criegee intermediates can react further leading a complex web of products.[15] Finally, the reaction with NO_3 to form isoprene-derived nitrates is a relatively minor sink of atmospheric isoprene.[16] The primary reaction consists of the addition of $NO_3^\bullet$ across either one of the carbon-carbon double bonds, with a strong preference for the substituted position, followed by the addition of O_2, leading to the isoprene nitrooxy peroxy radical.[17] It should be noted that the background presented above is an incredibly simplified and brief overview of the atmospheric chemistry of isoprene, a highly intricate and complex topic. For those interested in more depth regarding the kinetics, mechanisms, and information concerning the fate of isoprene oxidations products themselves, the reader is encouraged towards the review article contained in ref. 15.

It can be readily observed that the focus of isoprene chemistry in the literature is heavily centered around the neutral molecule. There has been little interest looking into the chemistry of protonated isoprene, although this may be an underappreciated area of research. Enami's research group has published a number of papers arguing that NMVOCs, including isoprene, can become protonated in the gas-phase via interactions with acidic water microdroplets.[18–20] It was initially observed that gaseous NMVOCs could undergo collisions with the acidic water microdroplets, leading to the weakly bound H_3O^+ ions at the surface of the microdroplet undergoing a proton transfer reaction, driven by the relatively higher proton affinity of the NMVOC when compared with the bulk of the water contained within the microdroplet.[18] Further studies revealed the highly reactive nature of the protonated isoprene that was formed, where significantly increased rates of polymerization were observed when compared with other relatively small unsaturated hydrocarbon NMVOC compounds.[19] Most recently, their work concerned itself with unequivocally determining the mechanism through which the NMVOCs were becoming protonated. When a relatively small concentration (in the range of μM) of gaseous isoprene was interacted with acidic water droplets, evidence of protonated isoprene could be observed in their mass spectrometry apparatus.[20] By contrast, when a relatively high concentration (in the range of mM) of isoprene was prepared by dissolving it into low pH water microdroplets, there was no protonated isoprene observed in the mass spectrum.[20] It is important to note that in both cases gaseous isoprene will be produced as a consequence of the mass spectrometer set up, implying that the protonation of isoprene must have occurred through collisions between gas-phase isoprene and the acidic water droplets and not through ejection from the acidic water droplets themselves.[20] Since it is possible for acidic water droplets to form in the troposphere, there is an opportunity for protonated isoprene to be present at this point in the atmosphere.[21]

In this work, we will aim to specifically address the unimolecular reactions of protonated isoprene by modelling them with collision-induced dissociation tandem mass spectrometry. These experiments are unlike the previous studies which focused on bimolecular reactions that lead to polymerization. The experimental data will be supported with computational chemistry, to uncover the mechanisms involved in the unimolecular breakdown of protonated isoprene. We also include an oxidized version of isoprene, prenol (3-methyl-2-buten-1-ol, Figure 3.1b), as a representative molecule to assess the impact of hydroxy functionalization on the unimolecular chemistry of protonated isoprene. Like isoprene, prenol can be emitted into the atmosphere from both biogenic and anthropogenic sources.[22,23] Recently, prenol and its isomers have been identified as suitable candidates as a next-generation biofuel additive, particularly due to its increased energy density when compared with ethanol, among other beneficial features.[23,24] Although the proton affinity of prenol is not readily available, it is reasonable to assume that it is greater than water and would become protonated in a similar manner to isoprene as described in the previous paragraph.

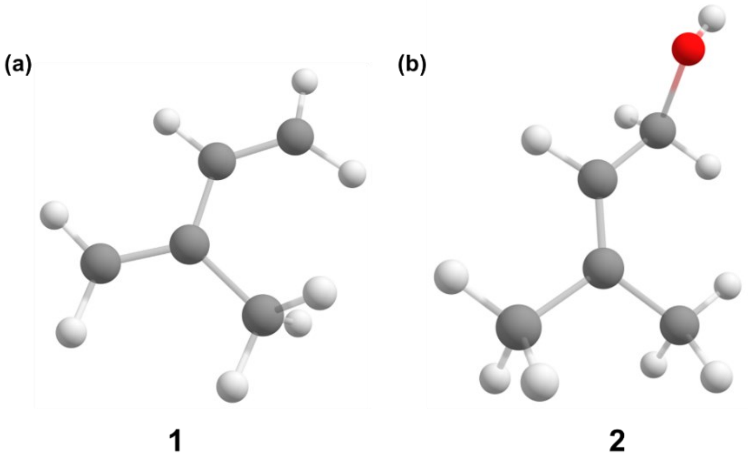

Figure 3.1: Optimized minimum energy structures determined for: a) neutral isoprene (**1**) and b) neutral prenol (**2**), calculated at the B3LYP/6-311+G(d,p) level of theory.

3.2 – Methods

Isoprene was purchased from Sigma-Aldrich (99%, Sigma-Aldrich, Oakville, Ontario, CA), and prenol was purchased from TCI America (3-methyl-2-buten-1-ol, 98%, TCI America, Portland, OR, USA). Both compounds were used as received, without further modification or purification.

3.2.1 – Tandem Mass Spectrometry

Isoprene and prenol solutions were prepared with methanol as the solvent to a concentration of 100 μg/mL (isoprene: 1.5 mM; prenol: 1.2 mM) prior to being introduced to the Micromass Ultima triple-quadrupole mass spectrometer. Solutions were delivered by means of a syringe pump, operating at a flow rate of 30 μL/min. The isoprene solution was ionized using atmospheric pressure chemical ionization (APCI), with the probe set to 200°C, the source set to 100°C, and the corona discharge needle operating at 10 μA. Desolvation gas (N_2) was set to a flow rate of 36 L/hour. The prenol solution was ionized using APCI in the same manner as described for isoprene, as well electrospray ionization (ESI), where the source and heater temperatures were both set to 100°C, and the capillary voltage was set to 3.0 kV. Desolvation gas (N_2) was set to a flow rate of 25 L/hour. No cone gas was used in either experiment. The cone voltage was set to 100 V in both experiments. Both APCI and ESI experiments were carried out in the positive ion mode. Protonated isoprene and prenol were identified by their m/z and subsequently mass-selected using the first quadrupole. Collision-induced dissociation (CID) experiments were conducted in the collision cell with argon collision gas at a pressure that resulted in a 50% reduction in the main molecular ion beam intensity. The product ions obtained from the

CID process were then analyzed in the final quadrupole. The CID-MS/MS data was then processed into breakdown diagrams, which plot the relative abundance of ions as a function of collision energy. The collision energy term is obtained by converting the lab-frame (instrument software controlled) collision energy (E_{Lab}) to the center-of-mass collision energy (E_{CoM}) according to the following equation:

$$E_{CoM} = E_{Lab}\left(\frac{m_{Ar}}{m_{Ar} + m_I}\right)$$

where m_{Ar} is the mass of an argon atom (the collision gas) and m_I is the mass of the ion undergoing CID.

3.2.2 – Computational Methods

All calculations (optimizations, vibrational frequency, and intrinsic reaction coordinate) were performed with the GAUSSIAN 16 suite of programs at the B3LYP level of theory using the 6-311+G(d,p) basis set.[25–27] Single-point energy calculations were performed using the CBS-QB3 composite method on the B3LYP output files, to refine the energy obtained from the B3LYP calculations.[28,29] Intrinsic reaction coordinate calculations were used to confirm transition state structures featuring a single negative vibrational mode. All relative energies are reported at 0 K, and all processes are described in terms of energy (eV).

Rice-Ramsperger-Kassel-Marcus (RRKM) theory was applied to calculate *k(E)* according to the following equation:[30,31]

$$k(E) = \frac{\sigma N^{\ddagger}(E - E_0)}{h\rho(E)}$$

where σ represents the reaction degeneracy, h is Planck's constant, $N^{\ddagger}(E - E_0)$ is the number of internal states for the transition state at internal energy $(E - E_0)$ and $\rho(E)$ is the density of states for the reactant ion at internal energy (E) as calculated via the Beyer and Swinehart direct count algorithm.[32]

3.3 – Results and Discussion – Tandem Mass Spectrometry

Representative CID-MS/MS spectra obtained from compounds **1** and **2** are presented in Figure 3.2, and breakdown diagrams are presented in Figure 3.3. In the case of **1**, two prevalent product ions were observed over the course of CID, the neutral losses of molecular hydrogen, and ethylene (Figure 3.2a). It is apparent from the breakdown diagram that the loss of ethylene from **1** is heavily favoured over the loss of molecular hydrogen (Figure 3.3a).

Both APCI and ESI were used to protonate prenol, leading to two distinct breakdown diagrams, one obtained from each source (Figure 3.3b,c). Four reactions were observed following the CID of **2** (Figure 3.2b), resulting from the neutral losses of water, formaldehyde, methanol, and propene. When ESI was used, at relatively low collision energies (approximately 0-1.5 eV), there is a degree of competition between all four pathways (Figure 3.3b). As the collision energy increases, there becomes a distinct separation between 'major' pathways (loss of methanol and propene), and 'minor' pathways (loss of water and formaldehyde). A similar pattern was observed when protonated prenol was formed using APCI, however the water loss and formaldehyde loss channels were more abundant throughout the collision energy range, and the propene loss channel did not start to significantly increase until higher collision energies (E_{CoM} > 4.0 eV).

It must be emphasized here that due to a lack of knowledge about the post-collision internal energy distribution in these experiments, only a qualitative comparison between the dissociation channels is possible.

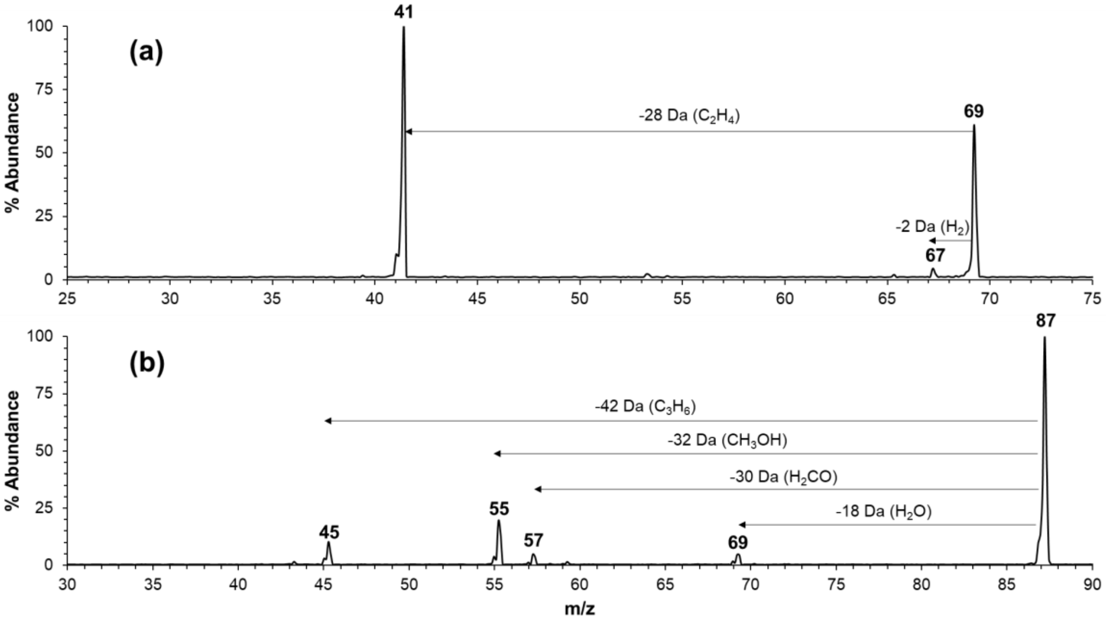

Figure 3.2: Representative CID mass spectra obtained from protonated isoprene and prenol at specified collision energies (E_{Lab}): a) protonated isoprene, m/z = 69, E_{Lab} = 10 eV. b) protonated prenol, m/z = 87, E_{Lab} = 7 eV, generated by ESI. The small shoulders to low mass on the peaks in the spectra are due to the collisional broadening of the precursor ion in the collision cell that skews the molecular ion peak also to low mass.

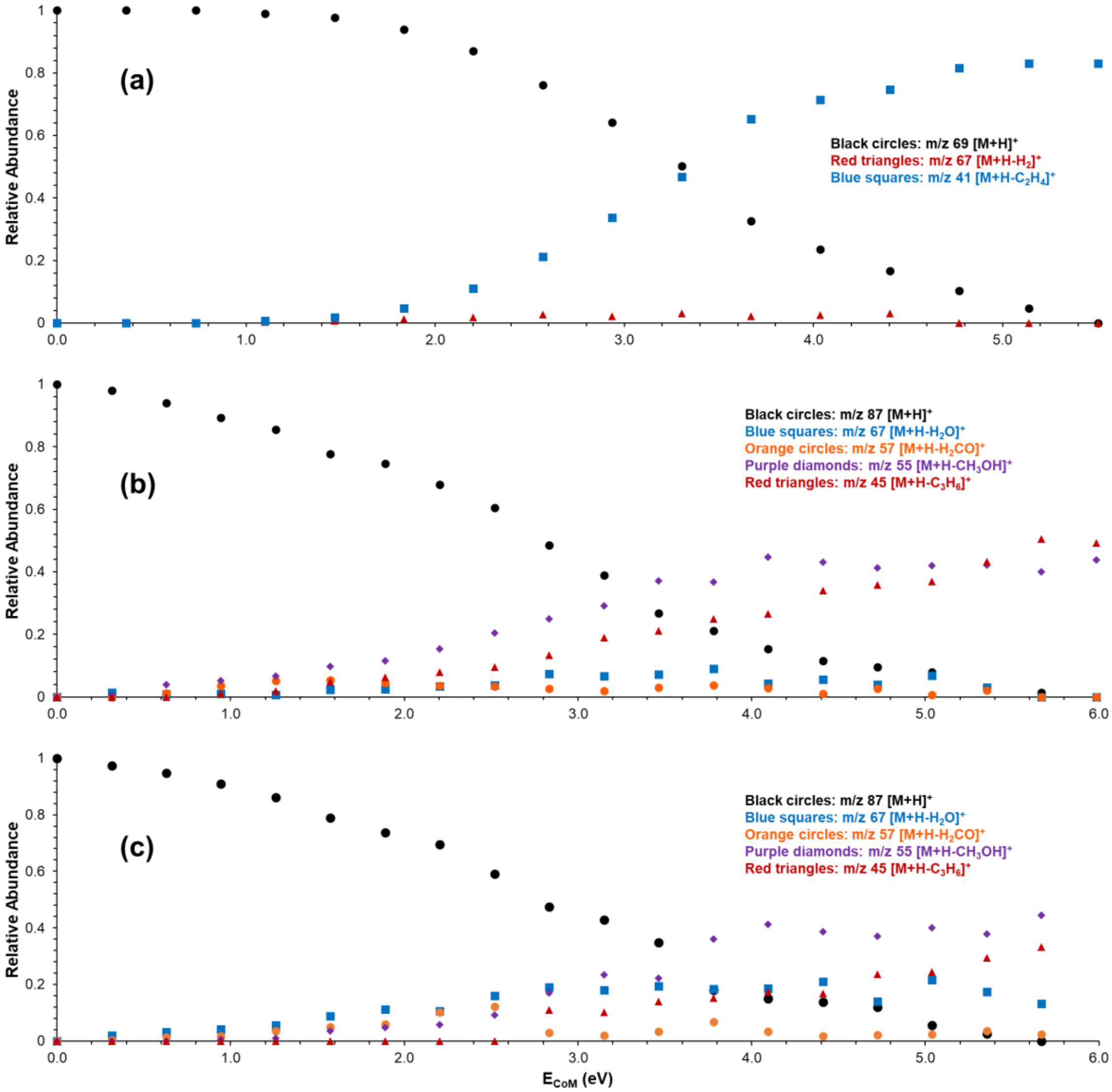

Figure 3.3: CID breakdown curves obtained from a) protonated isoprene (**1**), b) protonated prenol (**2**) generated by ESI, and c) protonated prenol (**2**) generated by APCI. The data was found to be consistent across two separate measurement days.

3.4 – Results and Discussion – Calculated Reaction Mechanisms

3.4.1 – Protonated Isoprene

The minimum energy reaction pathways that were calculated for the dissociation of protonated isoprene are presented in Figure 3.4. The reaction leading to the loss of molecular hydrogen from **1** is relatively straightforward, beginning with hydrogen abstraction. This motion has an energy barrier of 2.57 eV and brings the abstracted hydrogen near one of the hydrogens on the opposing methyl carbon (**TS1-1a**), facilitating the loss of H_2 and leading to the observed product ion at m/z 67 (**1a**). An alternate pathway, leading to $HC{\equiv}CC(CH_3)_2^+$ + H_2 was found to have a barrier of 2.86 eV.

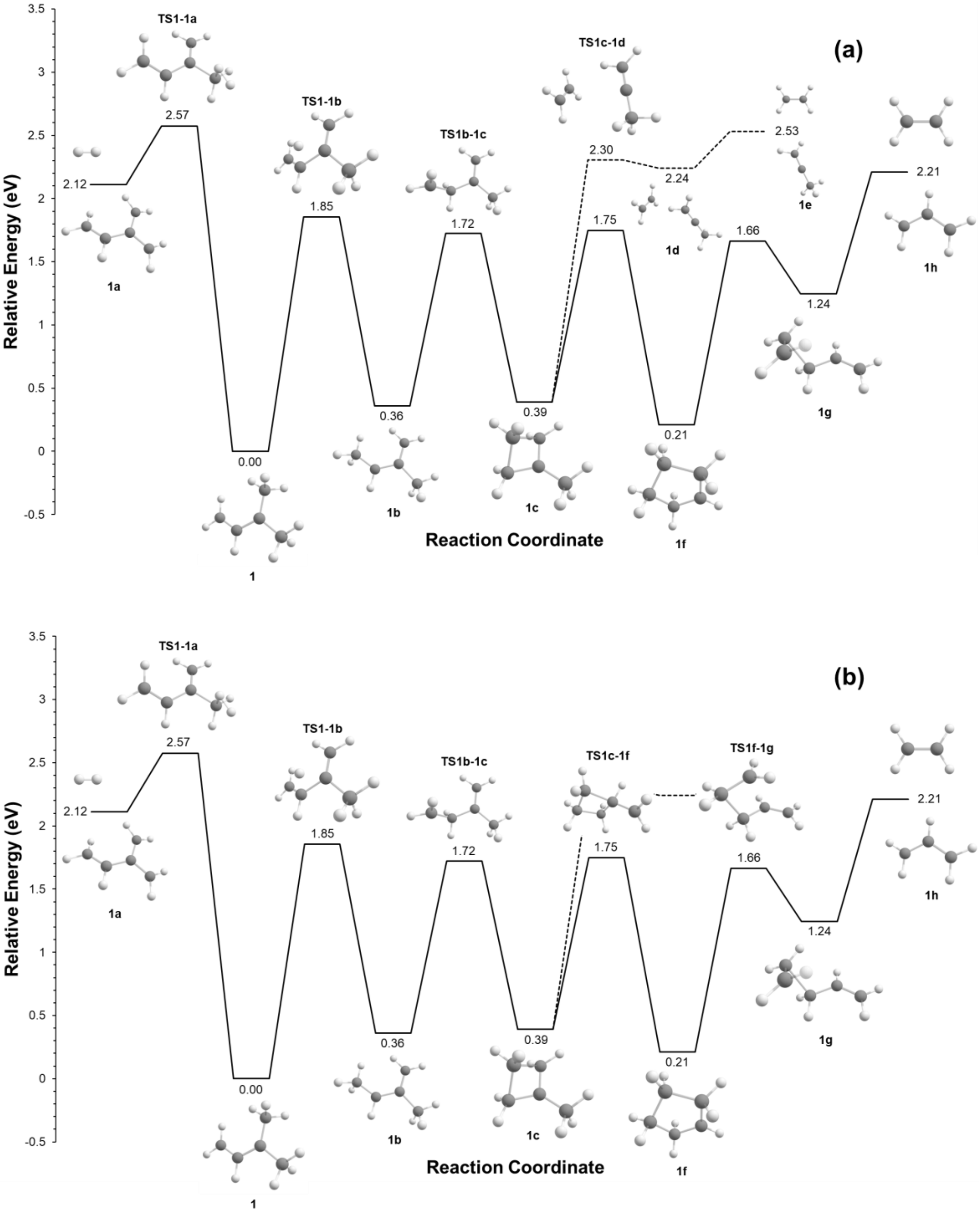

Figure 3.4: Minimum energy reaction pathways calculated for protonated isoprene (**1**), leading to H_2 loss (left pathway towards **1a**), and C_2H_4 loss (right pathways towards **1e** & **1h**). Indicated energy values (CBS-QB3) are set relative to the optimized structure of **1**. Panels a) and b) highlight the different structures involved in two pathways leading to the neutral loss of C_2H_4.

The reaction leading to the loss of ethylene is relatively more complex with two pathways calculated and shown in Figure 3.4. Both involve a 1,4-H shift, transferring a hydrogen atom from the proximate methyl carbon to the methylene carbon (**TS1-1b**), with an energy requirement of 1.85 eV, leading to the first intermediate with a relative internal energy of 0.36 eV (**1b**). The reaction proceeds from **1b** via a 1,2 H-shift (**TS1b-1c**), leading to the formation of an intermediate featuring a 4-membered ring (**1c**) over a 1.72 eV barrier. At this point the two paths diverge. The path leading to **1e** proceeds through a transition state in which the C-C bonds that are holding the C_2H_4 moiety in the ring break (**TS1c-1d**), leading to an ion-molecule complex in which the C_2H_4 is bound to the $C_3H_5^+$ (m/z 41, **1d**) which can then lose C_2H_4. A lower energy path leading to **1h** goes through the cyclopentyl cation **1f** before ring-opening to **1g** and losing ethene (Figure 3.4b).

3.4.2 – Protonated Prenol – Global Reaction Pathways

The global MERP that was calculated for the dissociation of protonated prenol is shown in Figure 3.5. This Figure serves as a visual representation of all the dissociation pathways and how they compare to one another energetically. The panels in Figure 3.6 highlight the individual rearrangements and transformations involved in each of the individual reaction pathways of protonated prenol.

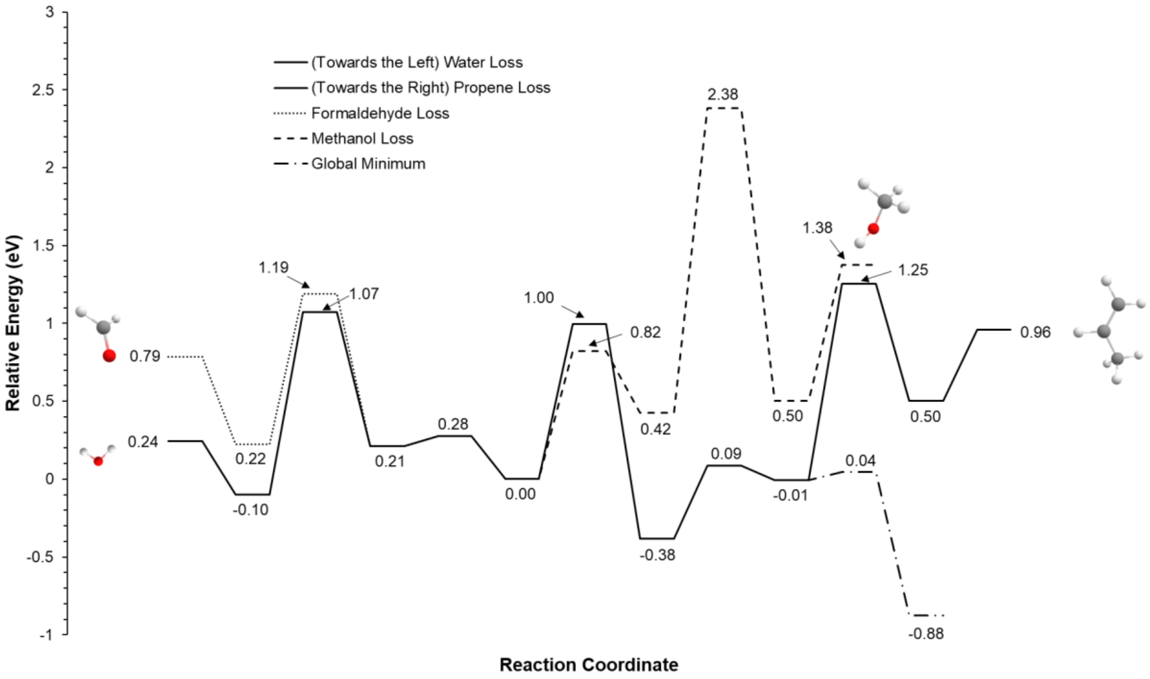

Figure 3.5: Summarized minimum energy reaction pathways calculated for protonated prenol (**2**), presenting all the different pathways in one plot and how they are related to one another. Structures at the end of each path represent the final neutral loss product obtained from that pathway.

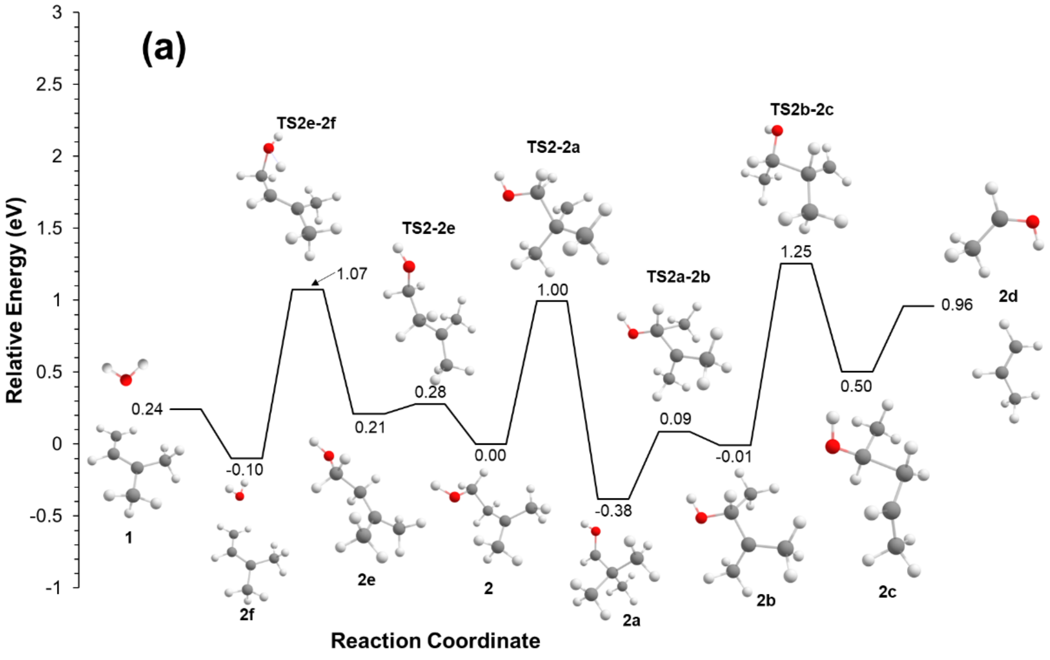

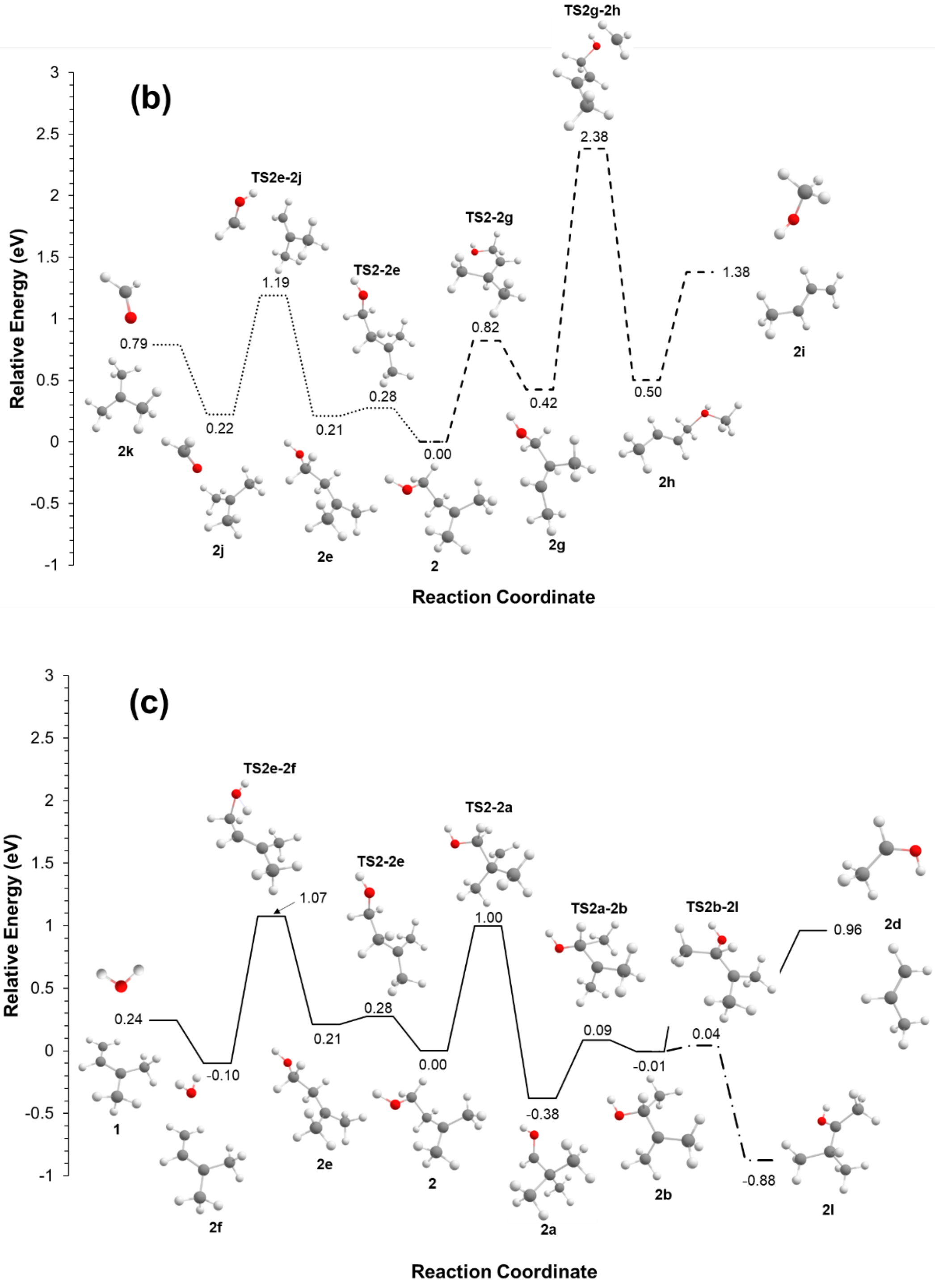

Figure 3.6: Detailed minimum energy reaction pathways involved in the breakdown of protonated prenol. Panel **a**) highlights the structures involved in the neutral losses of water (towards the left) and propene (towards the right). Panel **b**) highlights the structures involved in the neutral losses of formaldehyde (dotted line, left) and methanol (dashed line, right). Panel **c**) shows a side reaction that leads to the global minimum of the surface (starting from **2b** and going to **2l**).

3.4.3 – Protonated Prenol – Water Loss

The pathway that leads to the neutral loss of water has been presented in Figure 3.6a. The most obvious route to water loss is the initial protonation on the hydroxy group to form **2f**. However, the dissociation barrier for this ion is so low, that it will not survive the transit from the ion source to the first quadrupole. Starting from the relative zero energy structure **2**, the reaction proceeds towards the left through the transition state **TS2-2e** with a barrier of 0.28 eV, where the C-O bond is rotated breaking the hydrogen bond in **2** leading to rotamer **2e**. From this intermediate the reaction can proceed through **TS2e-2f** where one of the hydrogens in the CH_2 attached to the carbocation undergoes a 1,3-H shift to transfer over to the oxygen atom, leading to the ion-molecule complex **2f** which sits at a relative -0.10 eV. The reaction completes when the products dissociate from one another, leading to the neutral loss of water and protonated isoprene (**1**).

3.4.4 – Protonated Prenol – Propene Loss

The pathway that leads to the neutral loss of C_3H_6 has also been presented in Figure 3.6a. This reaction begins from the starting point **2** towards the right through transition state **TS2-2a** where one of the CH_2 hydrogens of the CH_2OH moiety undergoes a 1,2-H shift to transfer over to the adjacent CH_2 group. This motion is accompanied by a rearrangement leading to the trimethyl intermediate **2a** which sits at -0.38 eV. The reaction proceeds with a rearrangement through **TS2a-2b** where one of the methyl groups is transferred from the carbocation center to the CH carbon bearing the OH, leading to intermediate **2b**. The reaction continues through **TS2b-2c** where one of the hydrogens on the methyl groups undergoes a 1,2-H shift transferring over to the carbocation, leading to the ion-molecule complex **2c** which dissociates to the neutral loss product C_3H_6 and the observed ion **2d** at m/z 45.

3.4.5 – Protonated Prenol – Global Minimum

Along the reaction pathway towards the neutral loss of C_3H_6 and **2d** there is a competing pathway that leads towards the global minimum **2l** from the intermediate **2b**, highlighted in Figure 3.6c. The global minimum **2l** sits at a relative -0.88 eV and can be reached through **TS2b-2l** where the CH hydrogen undergoes a 1,2-H shift to transfer over to the bare carbon atom. **2l** does not proceed further but may continue back to **2b**.

3.4.6 – Protonated Prenol – Formaldehyde Loss

The pathway that leads to the neutral loss of formaldehyde is presented in Figure 3.6b, towards the left side. The reaction begins from **2** towards **2e** as previously described in the water loss section. From intermediate **2e** the reaction can proceed towards formaldehyde through the transition state **TS2e-2k** where the C-C bond holding the CH_2OH moiety is elongated, and the hydrogen attached to the oxygen transfers over towards the remaining hydrocarbon system. This rearrangement leads to the ion-molecule complex **2k** (0.22 eV), before dissociating to products of neutral formaldehyde and the $C_4H_9^+$ ion **2k**, observed at m/z 57 in the experiment.

3.4.7 – Protonated Prenol – Methanol Loss

The pathway that leads to the loss of methanol is presented in Figure 3.6b, towards the right. The reaction begins from **2** through the transition state **TS2-2g** with a relative energy barrier of 0.82 eV, where one of the hydrogens on the CH_2 carbon adjacent to the carbocation carbon undergoes a 1,2-H shift to yield a HC-CH system. This motion is accompanied by a rearrangement of one of the CH_3 groups, which transfers from one CH to the other CH, ultimately leading to the intermediate **2g**, which sits at a relative 0.42 eV. The reaction proceeds towards methanol loss through the transition state **TS2g-2h**, which has a high relative energy barrier of 2.38 eV, where the CH_3 group transferred to the CH from the previous step undergoes another rearrangement to associate with the OH group, leading to the ion-molecule complex **2h** at a relative 0.50 eV. The two products can dissociate from one another to provide the neutral loss of methanol and the observed ion **2i** at m/z 55, which collectively have a relative internal energy value of 1.38 eV.

3.5 – Relating Calculated Reaction Pathways to Breakdown Diagrams

3.5.1 – Protonated Isoprene

Isoprene can initially become protonated at four different positions in the ion source, each of the unsaturated carbons being a viable protonation site (refer to Figure 3.1a for the structure of neutral isoprene). Ultimately, three optimized structures of protonated isoprene were obtained, the C=C system distal to the -CH_3 group led to identical structures following optimization. The optimized structure of protonated isoprene presented in Figure 3.4, where the proton was added to the CH_2 group attached to the fully unsaturated C atom, was the only relevant structure for the observed reaction pathways and set as the relative zero energy value for this surface (structure **1**, Figure 3.4). The optimized structures of protonated isoprene that were obtained through this work are generally in agreement with those previously obtained with a different level of theory by Ishizuka *et al.*[19]

The breakdown diagrams obtained experimentally via CID-MS/MS are generally in agreement with the theoretical calculations in the case of **1**. There is little fragmentation observed until E_{CoM} is approximately 1.8 eV, at which point there is a brief period of competition between the two channels between (H_2 loss versus C_2H_4 loss), before the C_2H_4 loss dominates the other channel (Figure 3.3a). These results are consistent with the calculated pathways, which have first step barriers of 1.85 and 2.57 eV for the formation of C_2H_4 and H_2, respectively (Figure 3.4). Despite more steps required to achieve the more abundant product (C_2H_4 loss), it has relatively lower activation barriers along the reaction coordinate, at which point it is easier to dissociate towards products than go backwards along the reaction coordinate all the way towards the minor product (H_2 loss).

3.5.2 – Protonated Prenol

There are three viable points along the structure of neutral prenol that can be reasonably protonated, the oxygen and the unsaturated C and CH carbons (Figure 3.1b). If the proton were to be added to the oxygen, the resulting structure would ultimately result as an ion-molecule complex between the newly formed water and the remaining hydrocarbon moiety, which would resemble protonated isoprene. However, this ion-molecule complex is unlikely to be stable enough to travel through the mass spectrometer to become mass selected by the quadrupoles. It is most likely the neutral water will dissociate, and the remaining protonated isoprene analogue would not be selected by the mass spectrometer. The remaining two sites of protonation ultimately lead to two different stable prenol cations. At the current level of theory used in this work, attempting to protonate the unsaturated C carbon leads to rearrangement to transfer the proton over towards the unsaturated CH carbon. Two stable protonated prenol structures were determined, which depended upon the position at which the protonation occurred, represented by structures **2** and **2e** (Figure 3.6a,b,c). The proton can be bound to the neutral prenol in an open chain fashion, leading to structure **2e**, or the proton can be bound to the neutral prenol in such a way that it hydrogen bonds with one of the hydrogens on the methyl group, leading to a tighter, more ring-like configuration, represented by structure **2**. These structures represent the starting point for the reaction, as these are the structures that are stable enough to be mass selected by the quadrupole of the mass spectrometer and able to enter the collision cell for the CID experiment.

The most interesting observation regarding the calculations and how they relate to the experimental data, is that the most abundant product ion corresponding to the neutral loss of methanol had the highest relative reaction barrier along its MERP at 2.43 eV, which is counterintuitive. This observation can be rationalized only if **2h** can be generated in the ion source under atmospheric pressure collision conditions.

3.6 – Conclusion

In this work the reaction dynamics of protonated isoprene and prenol were investigated experimentally by using CID-MS/MS and supported mechanistically using DFT with supplemented with CBS-QB3 single-point calculations. Experimental breakdown of protonated isoprene revealed two fragmentation pathways, a major pathway that led to the neutral loss of C_2H_4 and a minor pathway that led to the neutral loss of H_2. Calculations were consistent with the experimental data, showing that there were significantly lower energetic barriers along the reaction coordinate leading towards C_2H_4 loss when compared to the high barrier leading to H_2 loss. In the case of protonated prenol, the experimental breakdown diagram revealed two major and two minor fragmentation pathways, the neutral losses of methanol and propene, and the neutral losses of water and formaldehyde, respectively. The calculated minimum energy reaction pathways were, at initial glance, not consistent with the experimental results. However, when considering the experimental design, particularly the energetic input of in-source collisional excitation following the initial protonation in the ion source, certain reaction barriers could be overcome, leading to key intermediates reaching the collision cell for the CID portion of the experiment. Thus, in this view, the experimental results and theoretical calculations can be considered consistent with one another. Ultimately, the relatively low energetic barriers present in the reaction pathway for isoprene and prenol presents the opportunity for these protonated species to undergo this chemistry within the atmosphere.

3.7 – Chapter 3 References

(1) Wuebbles, D. Atmospheric Methane and Global Change. *Earth-Sci. Rev.* **2002**, *57* (3–4), 177–210. https://doi.org/10.1016/S0012-8252(01)00062-9.

(2) Piccot, S. D.; Watson, J. J.; Jones, J. W. A Global Inventory of Volatile Organic Compound Emissions from Anthropogenic Sources. *J. Geophys. Res. Atmospheres* **1992**, *97* (D9), 9897–9912. https://doi.org/10.1029/92JD00682.

(3) Guenther, A.; Hewitt, C. N.; Erickson, D.; Fall, R.; Geron, C.; Graedel, T.; Harley, P.; Klinger, L.; Lerdau, M.; Mckay, W. A.; Pierce, T.; Scholes, B.; Steinbrecher, R.; Tallamraju, R.; Taylor, J.; Zimmerman, P. A Global Model of Natural Volatile Organic Compound Emissions. *J. Geophys. Res.* **1995**, *100* (D5), 8873. https://doi.org/10.1029/94JD02950.

(4) Sindelarova, K.; Granier, C.; Bouarar, I.; Guenther, A.; Tilmes, S.; Stavrakou, T.; Müller, J.-F.; Kuhn, U.; Stefani, P.; Knorr, W. Global Data Set of Biogenic VOC Emissions Calculated by the MEGAN Model over the Last 30 Years. *Atmospheric Chem. Phys.* **2014**, *14* (17), 9317–9341. https://doi.org/10.5194/acp-14-9317-2014.

(5) Li, B.; Ho, S. S. H.; Li, X.; Guo, L.; Chen, A.; Hu, L.; Yang, Y.; Chen, D.; Lin, A.; Fang, X. A Comprehensive Review on Anthropogenic Volatile Organic Compounds (VOCs) Emission Estimates in China: Comparison and Outlook. *Environ. Int.* **2021**, *156*, 106710. https://doi.org/10.1016/j.envint.2021.106710.

(6) Sharkey, T. D.; Wiberley, A. E.; Donohue, A. R. Isoprene Emission from Plants: Why and How. *Ann. Bot.* **2007**, *101* (1), 5–18. https://doi.org/10.1093/aob/mcm240.

(7) Monson, R. K.; Grote, R.; Niinemets, Ü.; Schnitzler, J. Modeling the Isoprene Emission Rate from Leaves. *New Phytol.* **2012**, *195* (3), 541–559. https://doi.org/10.1111/j.1469-8137.2012.04204.x.

(8) Borbon, A.; Fontaine, H.; Veillerot, M.; Locoge, N.; Galloo, J. C.; Guillermo, R. An Investigation into the Traffic-Related Fraction of Isoprene at an Urban Location. *Atmos. Environ.* **2001**, *35* (22), 3749–3760. https://doi.org/10.1016/S1352-2310(01)00170-4.

(9) Salerno-Kennedy, R.; Cashman, K. D. Potential Applications of Breath Isoprene as a Biomarker in Modern Medicine: A Concise Overview. *Wien. Klin. Wochenschr.* **2005**, *117* (5–6), 180–186. https://doi.org/10.1007/s00508-005-0336-9.

(10) Atkinson, R.; Arey, J. Gas-Phase Tropospheric Chemistry of Biogenic Volatile Organic Compounds: A Review. *Atmos. Environ.* **2003**, *37*, 197–219. https://doi.org/10.1016/S1352-2310(03)00391-1.

(11) Paulot, F.; Henze, D. K.; Wennberg, P. O. Impact of the Isoprene Photochemical Cascade on Tropical Ozone. *Atmospheric Chem. Phys.* **2012**, *12* (3), 1307–1325. https://doi.org/10.5194/acp-12-1307-2012.

(12) Teng, A. P.; Crounse, J. D.; Wennberg, P. O. Isoprene Peroxy Radical Dynamics. *J. Am. Chem. Soc.* **2017**, *139* (15), 5367–5377. https://doi.org/10.1021/jacs.6b12838.

(13) Kamens, R. M.; Gery, M. W.; Jeffries, H. E.; Jackson, M.; Cole, E. I. Ozone-Isoprene Reactions: Product Formation and Aerosol Potential. *Int. J. Chem. Kinet.* **1982**, *14* (9), 955–975. https://doi.org/10.1002/kin.550140902.

(14) Aschmann, S. M.; Atkinson, Roger. Formation Yields of Methyl Vinyl Ketone and Methacrolein from the Gas-Phase Reaction of O3 with Isoprene. *Environ. Sci. Technol.* **1994**, *28* (8), 1539–1542. https://doi.org/10.1021/es00057a025.

(15) Wennberg, P. O.; Bates, K. H.; Crounse, J. D.; Dodson, L. G.; McVay, R. C.; Mertens, L. A.; Nguyen, T. B.; Praske, E.; Schwantes, R. H.; Smarte, M. D.; St Clair, J. M.; Teng, A. P.; Zhang, X.; Seinfeld, J. H. Gas-Phase Reactions of Isoprene and Its Major Oxidation Products. *Chem. Rev.* **2018**, *118* (7), 3337–3390. https://doi.org/10.1021/acs.chemrev.7b00439.

(16) Horowitz, L. W.; Fiore, A. M.; Milly, G. P.; Cohen, R. C.; Perring, A.; Wooldridge, P. J.; Hess, P. G.; Emmons, L. K.; Lamarque, J.-F. Observational Constraints on the Chemistry of Isoprene Nitrates over the Eastern United States. *J. Geophys. Res.* **2007**, *112* (D12), D12S08. https://doi.org/10.1029/2006JD007747.

(17) Skov, H.; Hjorth, J.; Lohse, C.; Jensen, N. R.; Restelli, G. Products and Mechanisms of the Reactions of the Nitrate Radical (NO3) with Isoprene, 1,3-Butadiene and 2,3-Dimethyl-1,3-Butadiene in Air. *Atmospheric Environ. Part Gen. Top.* **1992**, *26* (15), 2771–2783. https://doi.org/10.1016/0960-1686(92)90015-D.

(18) Enami, S.; Hoffmann, M. R.; Colussi, A. J. Dry Deposition of Biogenic Terpenes via Cationic Oligomerization on Environmental Aqueous Surfaces. *J. Phys. Chem. Lett.* **2012**, *3* (21), 3102–3108. https://doi.org/10.1021/jz301294q.

(19) Ishizuka, S.; Fujii, T.; Matsugi, A.; Sakamoto, Y.; Hama, T.; Enami, S. Controlling Factors of Oligomerization at the Water Surface: Why Is Isoprene Such a Unique VOC? *Phys. Chem. Chem. Phys.* **2018**, *20* (22), 15400–15410. https://doi.org/10.1039/C8CP01551A.

(20) Colussi, A. J.; Enami, S.; Ishizuka, S. Hydronium Ion Acidity Above and Below the Interface of Aqueous Microdroplets. *ACS Earth Space Chem.* **2021**, *5* (9), 2341–2346. https://doi.org/10.1021/acsearthspacechem.1c00067.

(21) Pye, H. O. T.; Nenes, A.; Alexander, B.; Ault, A. P.; Barth, M. C.; Clegg, S. L.; Collett Jr., J. L.; Fahey, K. M.; Hennigan, C. J.; Herrmann, H.; Kanakidou, M.; Kelly, J. T.; Ku, I.-T.; McNeill, V. F.; Riemer, N.; Schaefer, T.; Shi, G.; Tilgner, A.; Walker, J. T.; Wang, T.; Weber, R.; Xing, J.; Zaveri, R. A.; Zuend, A. The Acidity of Atmospheric Particles and Clouds. *Atmospheric Chem. Phys.* **2020**, *20* (8), 4809–4888. https://doi.org/10.5194/acp-20-4809-2020.

(22) König, G.; Brunda, M.; Puxbaum, H.; Hewitt, C. N.; Duckham, C. Relative Contribution of Oxygenated Hydrocarbons to the Total Biogenic VOC Emissions of Selected Mid-European Agricultural and Natural Plant Species. *Atmos. Environ.* **1995**, *29* (8), 861–874. https://doi.org/10.1016/1352-2310(95)00026-U.

(23) Monroe, E.; Gladden, J.; Albrecht, K. O.; Bays, J. T.; McCormick, R.; Davis, R. W.; George, A. Discovery of Novel Octane Hyperboosting Phenomenon in Prenol Biofuel/Gasoline Blends. *Fuel* **2019**, *239*, 1143–1148. https://doi.org/10.1016/j.fuel.2018.11.046.

(24) Ramirez-Corredores, M. M.; Vega-Montoto, L.; Davis, R. W.; Monroe, E. The Intrinsic Value of Bioblendstocks: Prenol as a Case Study. *Fuel* **2022**, *311*, 122617. https://doi.org/10.1016/j.fuel.2021.122617.

(25) Frisch, M. J.; Trucks, G. W.; Schlegel, H. B.; Scuseria, G. E.; Robb, M. A.; Cheeseman, J. R.; Scalmani, G.; Barone, V.; Petersson, G. A.; Nakatsuji, H.; Li, X.; Caricato, M.; Marenich, A. V.; Bloino, J.; Janesko, B. G.; Gomperts, R.; Mennucci, B.; Hratchian, H. P.; Ortiz, J. V.; Izmaylov, A. F.; Sonnenberg, J. L.; Williams; Ding, F.; Lipparini, F.; Egidi, F.; Goings, J.; Peng, B.; Petrone, A.; Henderson, T.; Ranasinghe, D.; Zakrzewski, V. G.; Gao, J.; Rega, N.; Zheng, G.; Liang, W.; Hada, M.; Ehara, M.; Toyota, K.; Fukuda, R.; Hasegawa, J.; Ishida, M.; Nakajima, T.; Honda, Y.; Kitao, O.;

Nakai, H.; Vreven, T.; Throssell, K.; Montgomery Jr., J. A.; Peralta, J. E.; Ogliaro, F.; Bearpark, M. J.; Heyd, J. J.; Brothers, E. N.; Kudin, K. N.; Staroverov, V. N.; Keith, T. A.; Kobayashi, R.; Normand, J.; Raghavachari, K.; Rendell, A. P.; Burant, J. C.; Iyengar, S. S.; Tomasi, J.; Cossi, M.; Millam, J. M.; Klene, M.; Adamo, C.; Cammi, R.; Ochterski, J. W.; Martin, R. L.; Morokuma, K.; Farkas, O.; Foresman, J. B.; Fox, D. J. Gaussian 16 Rev. C.01, 2016.

(26) Becke, A. D. Density-functional Thermochemistry. III. The Role of Exact Exchange. *J. Chem. Phys.* **1993**, *98* (7), 5648–5652. https://doi.org/10.1063/1.464913.

(27) Lee, C.; Yang, W.; Parr, R. G. Development of the Colle-Salvetti Correlation-Energy Formula into a Functional of the Electron Density. *Phys. Rev. B* **1988**, *37* (2), 785–789. https://doi.org/10.1103/PhysRevB.37.785.

(28) Ochterski, J. W.; Petersson, G. A.; Montgomery, J. A. A Complete Basis Set Model Chemistry. V. Extensions to Six or More Heavy Atoms. *J. Chem. Phys.* **1996**, *104* (7), 2598–2619. https://doi.org/10.1063/1.470985.

(29) Montgomery, J. A.; Frisch, M. J.; Ochterski, J. W.; Petersson, G. A. A Complete Basis Set Model Chemistry. VI. Use of Density Functional Geometries and Frequencies. *J. Chem. Phys.* **1999**, *110* (6), 2822–2827. https://doi.org/10.1063/1.477924.

(30) Baer, T.; Mayer, P. M. Statistical Rice-Ramsperger-Kassel-Marcus Quasiequilibrium Theory Calculations in Mass Spectrometry. *J. Am. Soc. Mass Spectrom.* **1997**, *8* (2), 103–115. https://doi.org/10.1016/S1044-0305(96)00212-7.

(31) Baer, T.; Hase, W. L. *Unimolecular Reaction Dynamics: Theory and Experiments*; Oxford University Press on Demand, 1996; Vol. 31.

(32) Beyer, T.; Swinehart, D. F. Algorithm 448: Number of Multiply-Restricted Partitions. *Commun. ACM*, 1973, *16*, 379.

Chapter 4 – Protonated Limonene and α-Terpineol

Based on the publication White Buenger, E.; Mansour, K.; Mayer, P. M. Exploring the Unimolecular Chemistry of Protonated Limonene and α-Terpineol. *International Journal of Mass Spectrometry* **2024**, *498*, 117204. https://doi.org/10.1016/j.ijms.2024.117204.

Contribution Statement

K. Mansour performed initial exploratory experiments and computational studies. E. White Buenger further developed and completed the experimental work, computational studies, and prepared and revised the manuscript for submission. P. M. Mayer conceptualized the idea, supervised the work and revised the manuscript.

4.1 – Introduction

Terpenes are an incredibly diverse category of biogenic volatile organic compounds that are predominantly produced through metabolic processes carried out in plants.[1] Additionally, terpenes are used in numerous anthropogenic applications, such as the food, flavor, and perfume industries, in the production of novel elastomers,[2] and as a potential avenue for biofuel development.[3] As a result of their growing importance, understanding the fundamental chemistry of these terpenes and the consequences thereof, has become an active area of research. Due to their intrinsic volatility, a significant amount of terpene molecules can be emitted into the atmosphere on a global scale. Previous studies have demonstrated that a majority of global biogenic emissions can be attributed to isoprene and monoterpenes.[4,5]

It has been previously demonstrated that gaseous terpenes can interact with acidic water droplets to become protonated on the surface of that water droplet.[6] It has also been shown that these protonated gaseous terpenes, including protonated limonene, can undergo oligomerization reactions producing larger hydrocarbon oligomers.[7] The mechanism of protonation has been postulated to produce these protonated terpenes in the gas-phase, as opposed to the solution-phase, making protonation feasible under atmospheric conditions.[8]

A few studies have been published in the literature that focus specifically on the chemistry of protonated terpenes including limonene. Fernandez *et al.* reported on the proton affinity and gas-phase basicity of protonated limonene using density functional theory calculations, and discussed the site of protonation.[9] Several proton transfer mass spectrometry (PTRMS) experiments were reported which fragmented a variety of protonated monoterpenes, including limonene. Across multiple studies it was observed that the dominant product ion observed in the PTRMS of limonene was m/z 81.[10,11] Additional product ions that were observed include m/z 95, 79, 77, and 67.[10,11] However, these studies did not discuss mechanistic details of how these reactions occurred.

In this work, we will aim to address this shortcoming in the literature, by employing a combination of collision-induced dissociation (CID) tandem mass spectrometry and theory. CID identifies the unimolecular dissociation channels as a function of collision energy to separate parallel and sequential dissociations. The experimental data are supplemented using DFT calculations to model the individual transformations that occur throughout the unimolecular dissociations. We will also investigate a terpenoid that is closely related to limonene, α-terpineol, using the same methodology. It is structurally identical to limonene except a water molecule has been added across the double bond in the exocyclic propyl moiety. The goal of incorporating this molecule into the study is to observe what effect the hydroxyl moiety imparts on the unimolecular chemistry of protonated limonene.

4.2 – Methods

4.2.1 – Sample Preparation

DL-Limonene was purchased from Sigma-Aldrich (>97%, Oakville, Ontario, CA). α-terpineol was purchased from TCI America (>95%, Portland, Oregon, USA). Both compounds were used as purchased, without further purification. Both species were prepared as individual solutions in methanol and diluted to 100 μg/mL prior to injection into the mass spectrometer. Optimized structures of limonene and α-terpineol in their neutral form are shown in Figure 4.1.

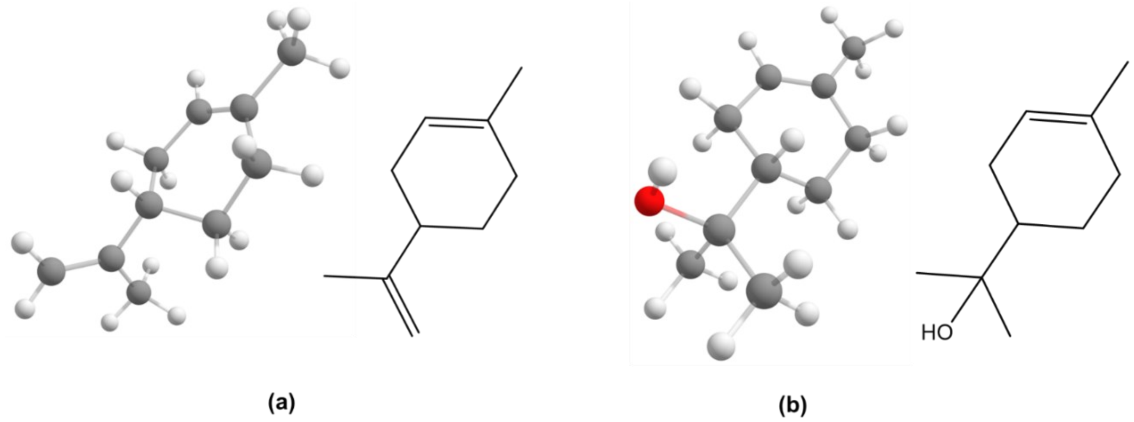

Figure 4.1: Optimized minimum energy structures obtained for (a) neutral limonene and (b) neutral α-terpineol calculated at the B3LYP/6-311+G(d,p) level of theory.

4.2.2 – Tandem Mass Spectrometry

Solutions were introduced into the triple quadrupole mass spectrometer (Waters Micromass Ultima, Manchester, UK) using a syringe pump operating at a flow rate of 50 μL/min. An atmospheric pressure chemical ionization (APCI) source was used to generate protonated limonene, with the probe set to a temperature of 200 °C, the source operating at 100 °C and the corona discharge needle set to 10 μA. Desolvation gas (N_2) was set to a flow rate of 36 L/hour. An electrospray ionization (ESI) source was used to form protonated α-terpineol, where the source and heater temperatures were both set to 100 °C, and the capillary voltage was set to 3.0 kV. Desolvation gas (N_2) was set to a flow rate of 25 L/hour. The cone voltage was set to 100 V in both experiments. No cone gas was used in either experiment. Both APCI and ESI were operated in the positive ionization mode to yield the protonated molecular ions of the target compounds. The ions were mass selected according to their m/z ratio with the first quadrupole, underwent collisions with argon gas in the collision cell, and the product ions were filtered in the final quadrupole. The amount of argon gas in the collision cell resulted in a 50% reduction in the initial main molecular ion beam intensity. The CID experiments were performed using 0-20 eV of collision energy (laboratory frame, E_{Lab}), at intervals of 1 eV.

4.2.3 – Breakdown Diagrams

The collection of CID data was compiled into breakdown diagrams, where the relative abundance of the ions observed in the CID mass spectra are plotted as a function of increasing collision energy. To compare the breakdown behaviour of different ions more accurately, the collision energy applied by the instrument (E_{Lab}) is first converted to the centre-of-mass frame of reference (E_{CoM}). This conversion accounts for differences in the efficiency of energy transfer during the collisional activation, according to the equation below:

$$E_{COM} = E_{Lab}\left(\frac{m_{Ar}}{m_{Ar} + m_I}\right)$$

where m_{Ar} is the mass of argon, and m_I is the mass of the ion undergoing CID.

4.2.4 – Computational Methods

All calculations (geometry optimizations and vibrational frequency calculations and intrinsic reaction coordinate) were performed with the GAUSSIAN 16 suite of programs at the B3LYP/6-311+G(d,p) level of theory.[12–14] The B3LYP output files were used for single-point energy calculations using the CBS-QB3 composite method, to provide more accurate energy values.[15,16] Transition state structures featuring a single negative vibrational mode were verified using intrinsic reaction coordinate calculations. The optimized geometries and relative energies obtained through these sets of calculations were used to produce minimum energy reaction pathways (MERP). All relative energies are reported at 0 K in eV. Rice-Ramsperger-Kassel-Marcus (RRKM) theory was applied to calculate *k(E)* according to the following equation:[17,18]

$$k(E) = \frac{\sigma N^{\ddagger}(E - E_0)}{h\rho(E)}$$

where σ represents the reaction degeneracy, h is Planck's constant, $N^{\ddagger}(E - E_0)$ is the number of internal vibrational states for the transition state at internal energy $(E - E_0)$ and $\rho(E)$ is the density of vibrational states for the reactant ion at internal energy (E) as calculated via the Beyer and Swinehart direct count algorithm.[19] Due to the qualitative nature of the kinetic modeling, we employed harmonic vibrational frequencies in the RRKM calculations.

4.3 – Results and Discussion – Mass Spectrometry

Representative CID mass spectra along with breakdown diagrams are presented in Figure 4.2. In the case of protonated limonene, there are four significant product ion signals. The neutral loss of 56 Da from the molecular ion (m/z 137), predicted to be C_4H_8, leads to the most prominent product ion observed at m/z 81. Another relatively abundant product ion was observed at m/z 95, which would correspond with the neutral loss of C_3H_6 (42 Da). These two product ions can be considered the major products resulting from the breakdown of protonated limonene. Two additional minor product ions can be observed in the mass spectrum, at m/z 109 and m/z 93, corresponding to the neutral losses of C_2H_4 (28 Da) and C_3H_8 (44 Da), respectively. The same trend is observed when the collection of CID data was compiled into the breakdown diagram for protonated limonene (Figure 4.2b). At low E_{CoM} the initial pathway leading towards m/z 81 dominates over the other fragmentation channels, while the remaining three are in competition with one another. As the collision energy increases, the pathway leading towards the product ion at m/z 95 begins to outcompete the other channels. The observation of both major product ion channels have been previously reported by Hewitt *et al.* and Müller *et al.*,[10,11] however our observation of the minor product ion channels m/z 109 and m/z 93 have not been previously reported.

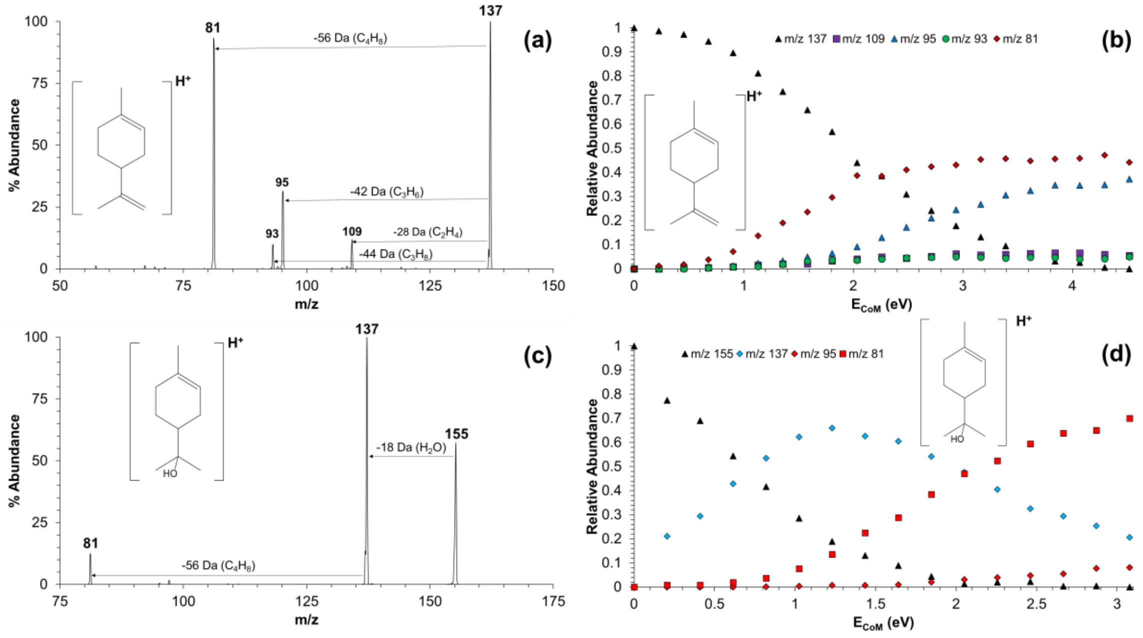

Figure 4.2: Representative CID-MS/MS spectra and breakdown diagrams obtained for protonated limonene (panels **a**,**b**, m/z 137, $E_{Lab} = 10$ eV) and protonated α-terpineol (panels **c**,**d**, m/z 155, $E_{Lab} = 5$ eV). The data was consistent across two separate measurement days.

In the case of protonated α-terpineol, there are two prominent product ions observed, one at m/z 137 and another at m/z 81 (Figure 4.2c,d). The product ion at m/z 137 most likely corresponds to the neutral loss of water from protonated α-terpineol, leading to a structure that is either protonated limonene or an isomer thereof. Water loss is so facile that it was always present in the CID mass spectrum, even at nominally zero collision energy. Evident from the breakdown data is that the product ions observed at m/z 81 and 95 are most likely the result of sequential dissociation arising from the m/z 137 product ion, and thus come from protonated limonene (or isomer thereof). This data trend (with the channel leading to m/z 81 being kinetically more favorable that that leading to m/z 95) is similar to the product ion distribution observed in the breakdown diagram of protonated limonene (1-3 eV region of Figure 4.2b vs Figure 4.2d). Thus, the data suggests that protonated α-terpineol undergoes sequential dissociation of water and then of the formed protonated limonene (or isomer).

4.4 – Results and Discussion – Calculated Reaction Pathways

4.4.1 – Protonated Limonene (Major Product Ions)

The calculated minimum energy rection pathways (MERPs) for the major product ions observed in the breakdown of protonated limonene (m/z 95 and m/z 81) are presented in Figure 4.3. In this context, major refers to those product ion channels that are at relatively higher abundance. The lowest energy optimized structure of protonated limonene has been represented as structure **1** in the MERP, where the proton has been added to the CH_2 moiety of the exocyclic double bond, leading to a formal positive charge on the central carbon atom of the propyl group (Figure 4.1). This structure is labeled as 0.00 eV as it is the relative baseline to which every other energy value associated with the structures along the reaction coordinate have been compared.

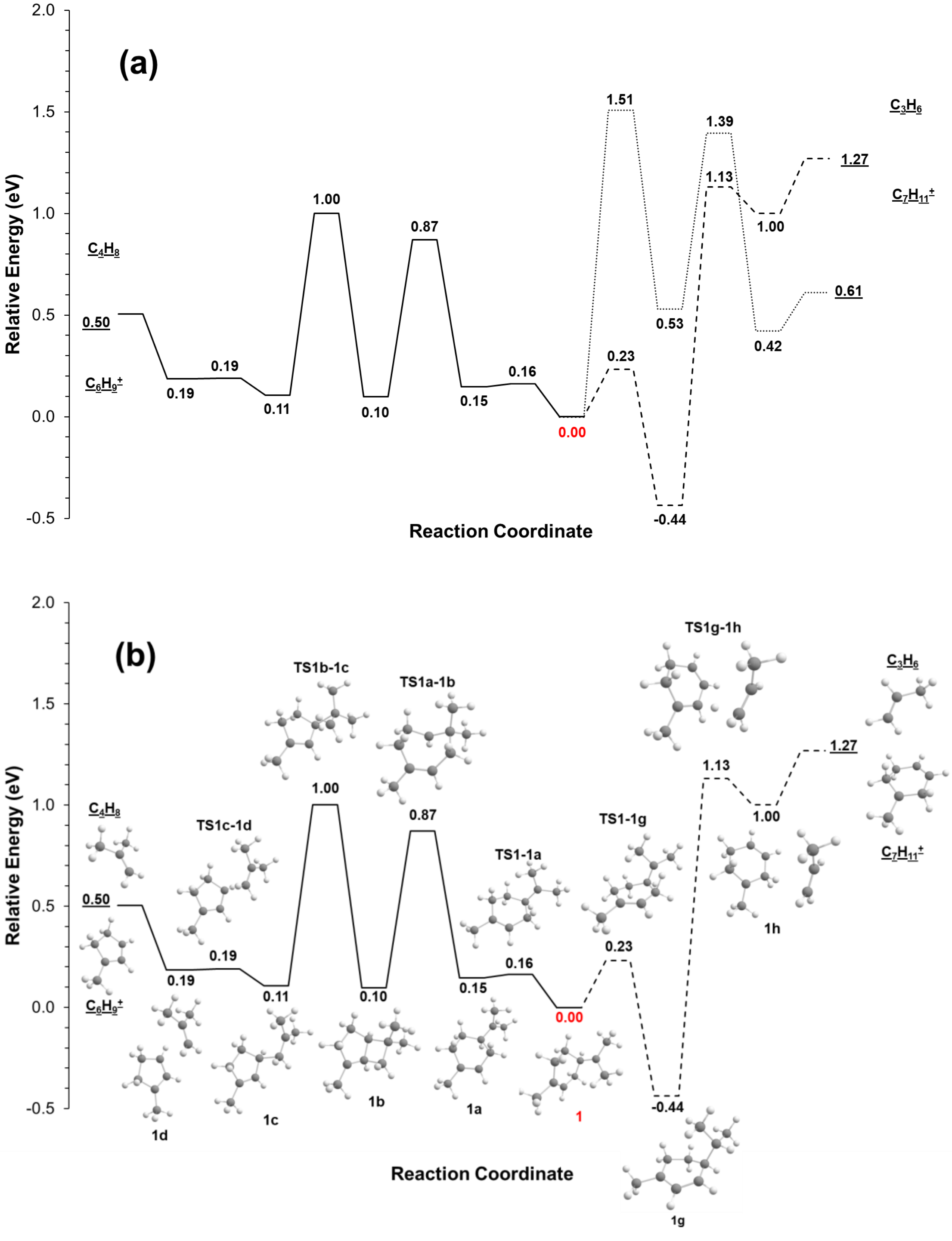
(a)
2.0
1.5
1.0
0.5
0.0
-0.5
Relative Energy (eV)
Reaction Coordinate
C_4H_8
0.50
$C_6H_9^+$
0.19
0.19
0.11
1.00
0.10
0.87
0.15
0.16
0.00
1.51
0.23
0.53
-0.44
1.39
1.13
1.00
0.42
C_3H_6
1.27
$C_7H_{11}^+$
0.61
(b)
2.0
1.5
1.0
0.5
0.0
-0.5
Relative Energy (eV)
Reaction Coordinate
TS1b-1c
TS1a-1b
TS1g-1h
C_3H_6
C_4H_8
TS1c-1d
1.00
0.87
TS1-1a
TS1-1g
1.13
1.27
1.00
$C_7H_{11}^+$
0.50
0.19
0.19
0.11
0.10
0.15
0.16
0.00
0.23
-0.44
1h
$C_6H_9^+$
1d
1c
1b
1a
1
1g

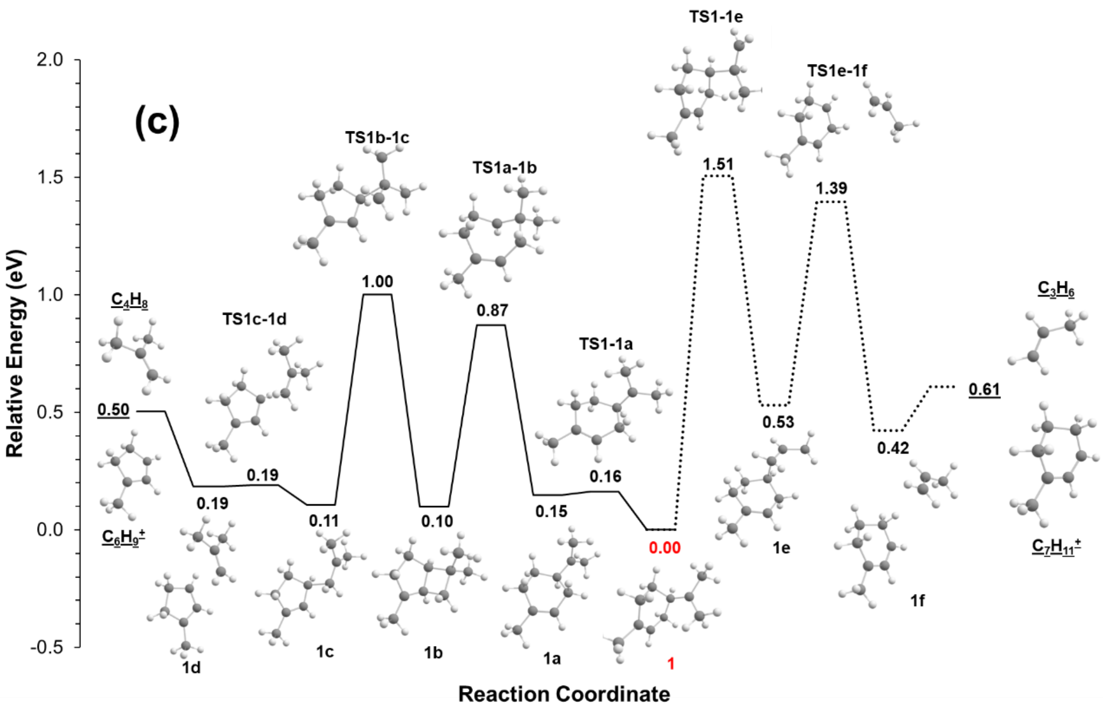

Figure 4.3: CBS-QB3(sp)//B3LYP/6-311+G(d,p) calculated minimum energy reaction pathways for the major product ions observed in the breakdown of protonated limonene (**1**). Panel **a**) serves as a visual comparison between the energetics of the different pathways. Panel **b**) shows greater structural detail involved in the neutral loss of C_4H_8 (solid black line, left) and a pathway towards the neutral loss of C_3H_6 (dashed line, right). Panel **c**) highlights an alternative pathway towards the neutral loss of C_3H_6 that leads to more energetically stable products through a higher initial barrier (dotted line, right). The indicated energy terms associated with each structure are set relative to the optimized structure of **1**, labeled in red.

The dissociation channel that leads towards the product ion observed at m/z 81 ($C_6H_9^+$) begins from **1** through transition state **TS1-1a** with a relatively low energy barrier of 0.16 eV, where the CH carbon attached to the propyl group slightly elongates one of its HC−CH_2 bonds to allow for a rotation in the propyl system, leading to intermediate **1a** that sits at a relative energy of 0.15 eV (Figure 4.3b & 4.3c, left pathway, solid black line). This intermediate is an isomer of the initial protonated limonene structure **1**, that has the propyl group in a more sterically favourable position for the following step along the reaction coordinate. This step proceeds through transition state **TS1a-1b** with a relative energy barrier of 0.87 eV where the CH groups in the ring system associate with one another, leading to the [4+5]-bicyclic intermediate **1b**. From intermediate **1b**, the reaction proceeds through transition state **TS1b-1c** (relative 1.00 eV), where the 4-membered ring system is broken, leading to intermediate **1c**. In this intermediate, the tertiary carbon that was bonded to the 5-membered ring system in intermediate **1b** has been replaced by the CH_2 carbon that was part of the 4-membered ring system. From intermediate **1c**, the reaction continues along the coordinate through transition state **TS1c-1d** where the newly formed bond in the last step is elongated, leading towards the ion-molecule complex **1d**. The bound neutral C_4H_8 and the $C_6H_9^+$ ion dissociate from one another to become independent products which collectively have a relative energy value of 0.50 eV, representing the barrier to separate the ion-molecule complex.

The other two dissociation channels presented in Figures 4.3b and 4.3c towards the right side, lead to the other major product ion that was observed in the experiment, m/z 95 ($C_7H_{11}^+$). The first of these channels, presented in Figure 4.3b with the black dashed line, proceeds through **TS1-1g** with a relative energy barrier of 0.23 eV, where a hydrogen from the ring undergoes a 1,3-H shift to become associated with the central carbon of the propyl group, leading to intermediate **1g**, sitting at a relative energy of -0.44 eV. From **1g** the reaction continues through **TS1g-1h** (1.13 eV), where one of the methyl hydrogens undergoes a 1,4-H shift to transfer onto the CH carbon of the ring system, leading to the ion-molecule complex **1h**, before dissociating towards the final products which sit at 1.27 eV.

The other pathway that leads towards the loss of C_3H_6 begins from **1** through the transition state **TS1-1e** (1.51 eV), where the bond holding the CH moiety of the propyl group onto the cyclic structure elongates to accommodate the CH_2 group taking its place (Figure 4.3c, dotted black line). This motion leads to the intermediate **1e**, sitting at 0.53 eV. From intermediate **1e** the reaction proceeds further through transition state **TS1e-1f** (1.39 eV) and corresponds to the motion where the CH_2 group bonded to the ring stretches, leading to intermediate **1f**, the ion-molecule complex where neutral C_3H_6 is weakly bound to the ion $C_7H_{11}^+$. A small energy input is required to dissociate towards the final separated products.

4.4.2 – Protonated Limonene (Minor Product Ions)

The minor product ions observed in the breakdown of protonated limonene are presented in Figure 4.4, where both MERPs are in the same Figure, serving to compare the energetic differences between the two pathways, blue leading towards the neutral loss of C_2H_4 and orange leading to the neutral loss of C_3H_8. A common intermediate **1g** (-0.30 eV) is shared between both pathways, which can be accessed from **1** through the transition state **TS1-1g** where the hydrogen atom that is bonded to the endocyclic tertiary carbon bearing the propyl group undergoes a 1,2 H-shift, leading to intermediate **1g** where the hydrogen atom is now bonded to the exocyclic carbon that is part of the propyl moiety. Figure 4.4 below shows the summarized MERPs with annotated relative energy values for each pathway. More detailed structural information involved in each of the individual transformations can be seen in Figures 4.5 and 4.6.

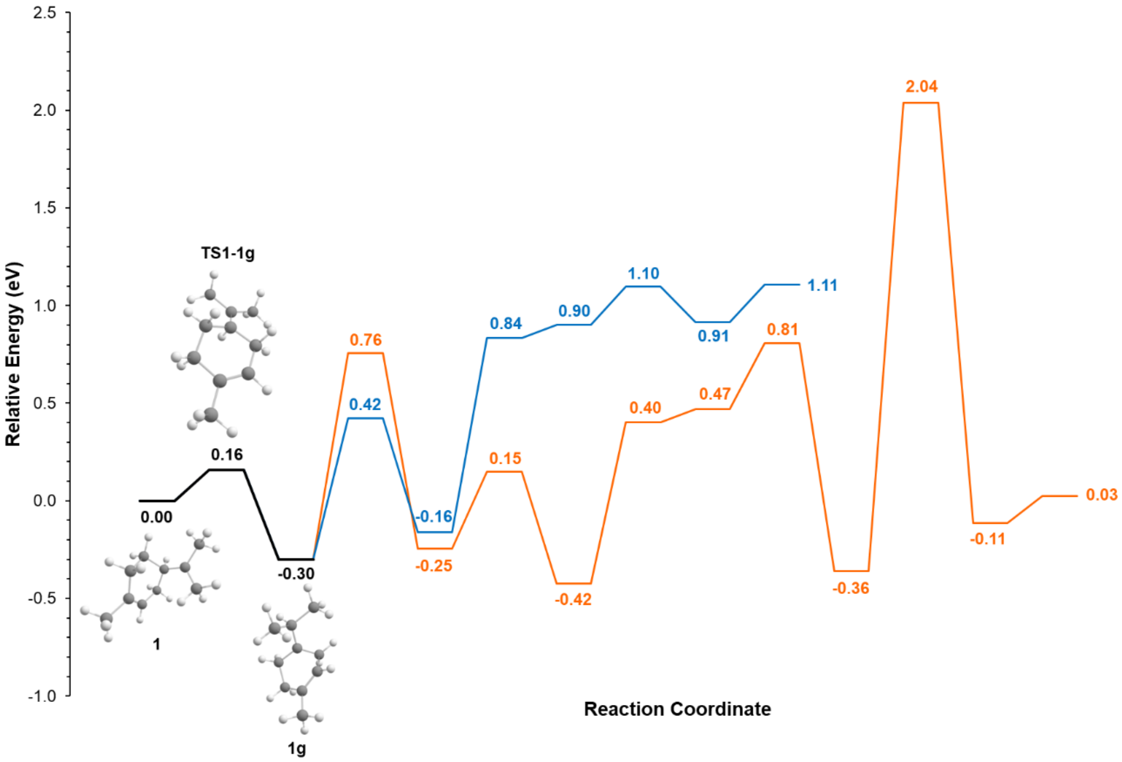

Figure 4.4: CBS-QB3(sp)//B3LYP/6-311+G(d,p) calculated minimum energy reaction pathways for the minor product ions observed in the breakdown of protonated limonene (**1**), highlighting both pathways starting from a shared intermediate and diverging into separate blue and orange pathways (C_2H_4 loss and C_3H_8 loss, respectively). The indicated energy terms associated with each structure are set relative to the optimized structure of **1**.

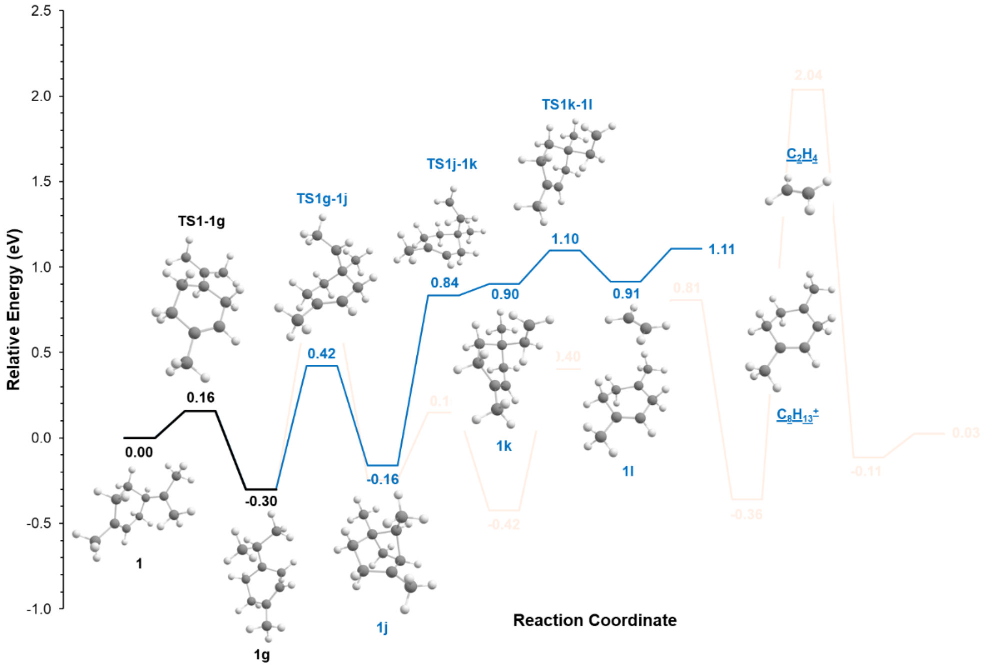

Figure 4.5: Structurally detailed minimum energy reaction pathway for the dissociation of **1** towards the neutral loss of C_2H_4.

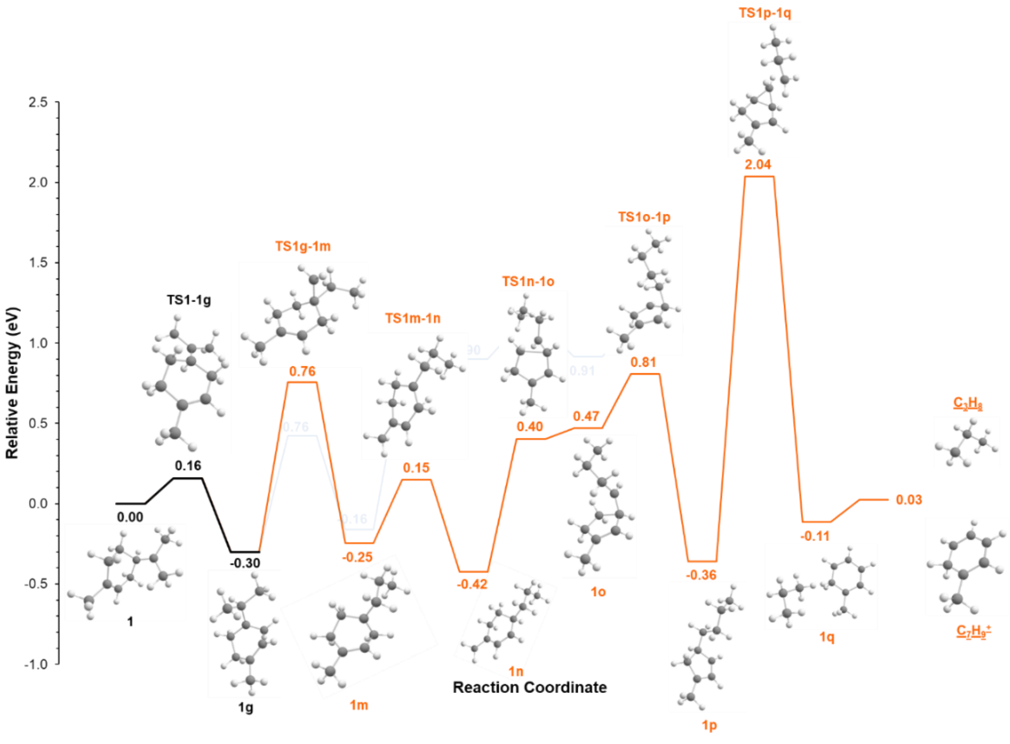

Figure 4.6: Structurally detailed minimum energy reaction pathway for the dissociation of **1** towards the neutral loss of C_3H_8.

The blue pathway that leads to the neutral loss of C_2H_4 proceeds forward from intermediate **1g** through transition state **TS1g-1j** (0.42 eV), where one of the methyl groups that is part of the exocyclic propyl system undergoes a 1,2 shift to become directly attached to the ring system, leading to intermediate **1j** (Figure 4.5). The reaction continues from this point through transition state **TS1j-1k** where one of the hydrogen atoms bonded to the methyl carbon of the H_3CCH system transfers over to the CH carbon, leading to intermediate **1i**. From this point the reaction proceeds through transition state **TS1k-1l** where the carbon atom that holds the newly formed C_2H_4 to the ring system undergoes a stretching motion, which leads to the ion-molecule complex **1l**. The ion-molecule complex dissociates into the neutral loss product C_2H_4 and the observed product ion $C_8H_{13}^+$ (m/z 109).

The orange MERP presented in Figure 4.6 highlights the individual chemical transformations involved in the neutral loss of C_3H_8 from protonated limonene. This pathway begins from intermediate **1g** through the transition state **TS1g-1m** where one of the hydrogen atoms bonded to one of the methyl groups in the propyl system transfers over to the CH carbon of the propyl system. This motion is accompanied by the remaining methyl group of the propyl system undergoing a 1,2 shift to become bonded to the newly formed central CH_2 carbon, leading to the intermediate **1m**. The reaction proceeds forward from **1m** through the transition state **TS1m-1n** in which one of the hydrogen atoms bonded to the CH_2 carbons adjacent to the tertiary carbon of the ring system undergoes a 1,2 H-shift, leading to intermediate **1n** where that hydrogen has now become bonded to the tertiary carbon. The reaction continues along the coordinate through the transition state **TS1n-1o** where a ring pinching reaction occurs, transforming the 6-membered ring into a

5-membered ring system, transferring the HC-CH_2 bond from one CH to the other CH in the system, leading to intermediate **1o**. From this intermediate, the reaction proceeds through the transition state **TS1o-1p** where a 1,2 H-shift occurs taking one of the hydrogens bonded to the CH_2 adjacent to the CH carbon and transfers that hydrogen over to the CH carbon, which yields the intermediate **1p**. The final transition state in this MERP is **TS1p-1q**, where the CH_2 group that is attached to the 5-membered ring briefly associates with the opposing CH moiety to form a cyclopropyl feature, such that one of the hydrogen atoms can be in a position to interact with the $H_3C(CH_2)_2$ system. Following this transition state leads to the ion-molecule complex **1q** which involves the C_3H_8 moiety weakly bound to the ion observed in the breakdown diagram $C_7H_9^+$ (m/z 93). The ion-molecule complex can dissociate towards the final products, the neutral loss of C_3H_8 and $C_7H_9^+$.

4.4.3 – Protonated α-Terpineol

There are three positions which are liable for protonation: the oxygen and both the unsaturated carbons in the ring, which ultimately lead to two protonated α-terpineol structures. An ion-molecule complex between neutral water and a structure that resembles protonated limonene arises from protonation at the oxygen, while protonating at the unsaturated carbons leads to a tertiary carbocation. Both structures are comparable in relative energy, with 0.008 eV separating the two following CBS-QB3 single-point calculations. The relevant structure for the reaction that was observed in the MS experiment is the ion-molecule complex resulting from protonation at the oxygen. This ion-molecule complex can dissociate into the two products, neutral water and the ion observed at m/z 137 ($C_{10}H_{17}^+$) with a 0.96 eV barrier, as seen in Figure 4.7. In fact, the neutral loss of water appears to happen so quickly, the produced m/z 137 ion seems to dissociate further, as there is evidence of protonated limonene breakdown products in the breakdown diagram of protonated α-terpineol (m/z 81 in particular). Other pathways were explored, including the loss of water from the other protonated α-terpineol structure, and the possibility of the neutral loss of $C_4H_{10}O$ which may lead to the ion observed at m/z 81 directly from protonated α-terpineol, however both these pathways had initial energy barriers in excess of 2.5 eV relative energy.

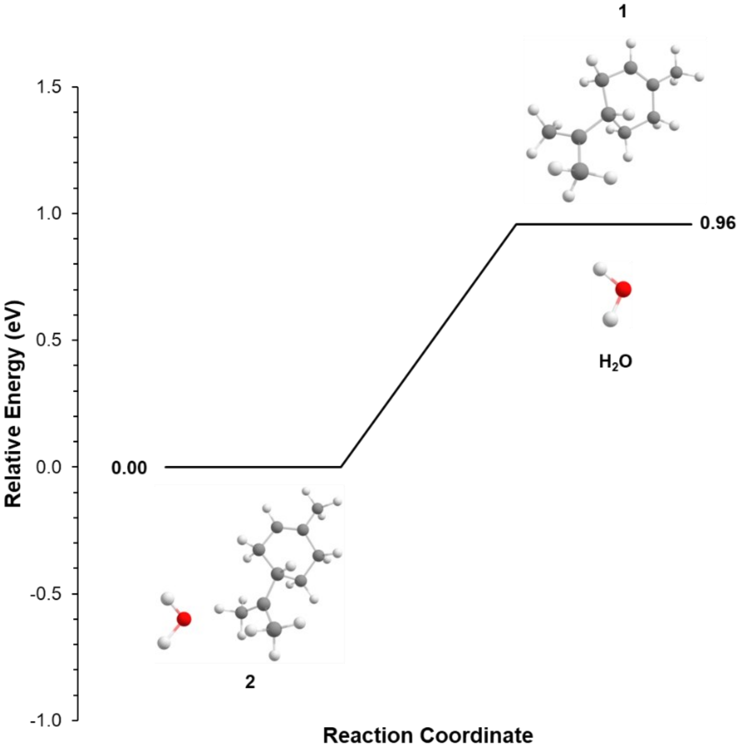

Figure 4.7: Calculated minimum energy reaction pathway for the formation of protonated α-terpineol (**2**), and subsequent dissociation of neutral water from the formed ion-molecule complex.

4.5 – Relating Breakdown Diagrams to Calculated Mechanisms

4.5.1 – Protonated Limonene

Neutral limonene may potentially become protonated at three different carbon atoms: the central propyl carbon, and the two unsaturated carbons in the ring system. These options ultimately lead to two isomers of protonated limonene, the structure corresponding to **1** in Figure 4.3 is one of them, and the other one is the result of protonation across the double bond, leading to a tertiary carbocation. This structure was not included in any of the MERPs as it did not contribute significantly towards the observed chemistry.

The most abundant product ion observed in the breakdown diagram at m/z 81, corresponding to the neutral loss of C_4H_8, can be readily rationalized by the calculated MERP. From the starting point of **1** on the reaction coordinate, proceeding towards the left is energetically favoured compared to the other possible options. Furthermore, the energy barriers to overcome as you proceed further along the reaction coordinate are relatively lower when compared with other channels.

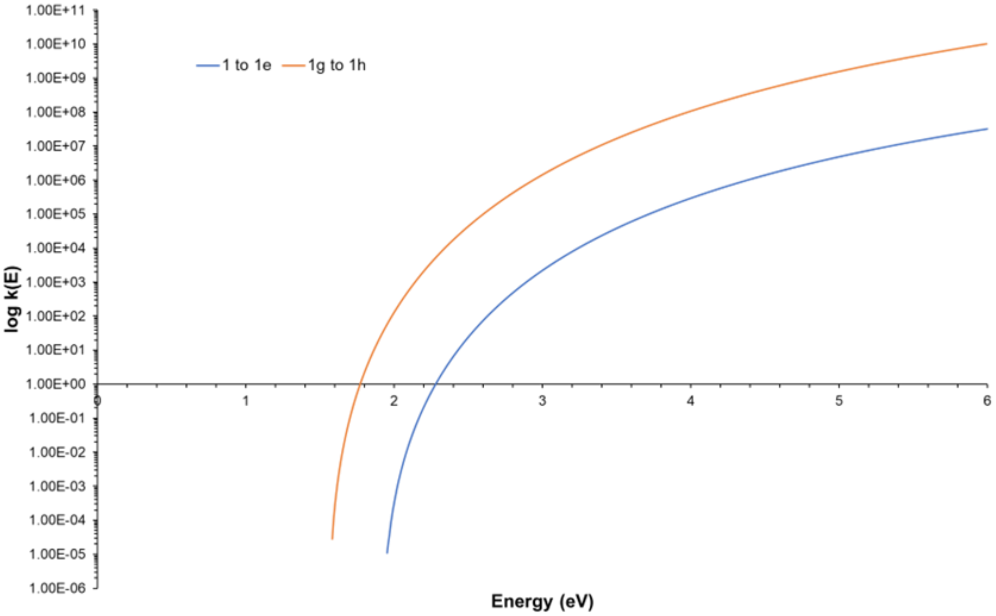

Figure 4.8: RRKM-derived log k(E) vs E curves comparing the relative rate of reaction between overcoming the barrier from **1** to **1e** (blue curve) and overcoming the barrier from **1g** to **1h** (orange curve), towards the different mechanisms leading to the neutral loss of C_3H_6.

The other major product ion that was observed in the breakdown diagram, but at relatively lower abundance, was m/z 95, corresponding to the neutral loss of C_3H_6. Two different pathways were presented in the MERP to reach those products from the starting point **1**. One pathway proceeds through a relatively higher energy barrier from the starting point and ultimately leads to more energetically stable products. The other pathway begins with a relatively low energy barrier that leads to a relatively stable intermediate, that then proceeds through a lower energy barrier to reach the final products, however the products are significantly less energetically stable when compared with the other pathway. RRKM calculations revealed that the rate constant for the latter reaction, involving lower initial barrier and higher energy products, was significantly higher when compared with the former (Figure 4.8). Thus, on the timescale of the experiment performed, MS/MS on a conventional triple quadrupole instrument, it is most likely that the reaction highlighted in Figure 4.3b towards the right, leads to the observed product ion at m/z 95.

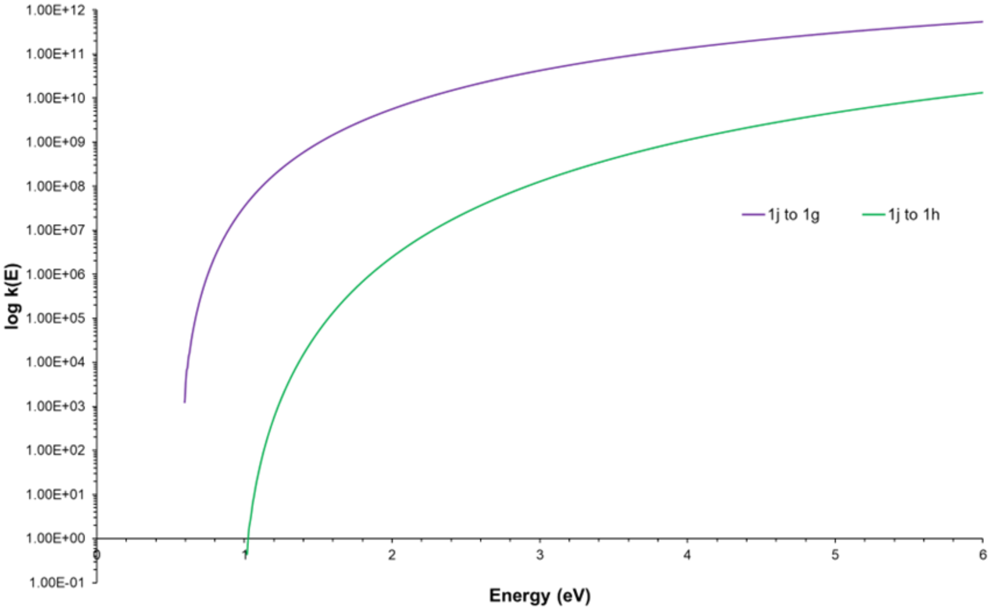

Figure 4.9: RRKM-derived log k(E) vs E curves comparing the relative rate of reaction between overcoming the barrier from **1j** to **1g** (purple curve, going back towards other reactions), compared to overcoming the barrier from **1j** to **1h** (green curve, going towards the C_2H_4 loss products).

When considering the minor fragmentation channels of protonated limonene, the experimental and theoretical results for the pathway that leads to the neutral loss of C_3H_8 are consistent with one another. The relatively high final barrier of 2.04 eV acts as the rate limiting step for this reaction, explaining why the abundance of this product ion channel does not exceed approximately 5% in the breakdown diagram. The other minor fragmentation channel, leading to the neutral loss of C_2H_4 is somewhat more difficult to rationalize. At first glance, the MERP for this pathway is energetically comparable with the pathways leading to the major product ions and should compete with those, however like the pathway leading to the neutral loss of C_3H_8, the C_2H_4 loss pathway does not exceed approximately 5% in relative abundance. This discrepancy can be resolved using RRKM calculations, by comparing the k(E) curves for travelling out of the well from structure **1j** at -0.16 eV (Figure 4.5) towards the left and towards the right, presented in Figure 4.9. This plot shows that the rate of proceeding back towards the left of the MERP and feeding back into other reactions is orders of magnitude greater than proceeding forward towards the right and onwards to products. Thus, this step acts as a kinetic bottleneck for the C_2H_4 loss pathway, reducing the overall rate of product formation, and ultimately explaining why these products are not as abundant as the major ones in the breakdown experiment.

There appear to be some inconsistencies within the calculations themselves. For instance, intermediates **1i** and **1m** sit slightly above the preceding transition states relative energy levels, which is counter intuitive. This inconsistency arises due to the nature of the CBS-QB3 single-point calculation. At the B3LYP level of theory, these intermediates sit slightly below the preceding transition states in relative energy. When comparing the CBS-QB3 single-point energies between the transition state and intermediate, the transition state is higher in energy. However, when factoring in the zero-point energy calculated at the B3LYP level of theory, the intermediate energy becomes relatively higher than the transition state, leading to the features observed in Figure 4.3.

4.5.2 – Protonated α-Terpineol

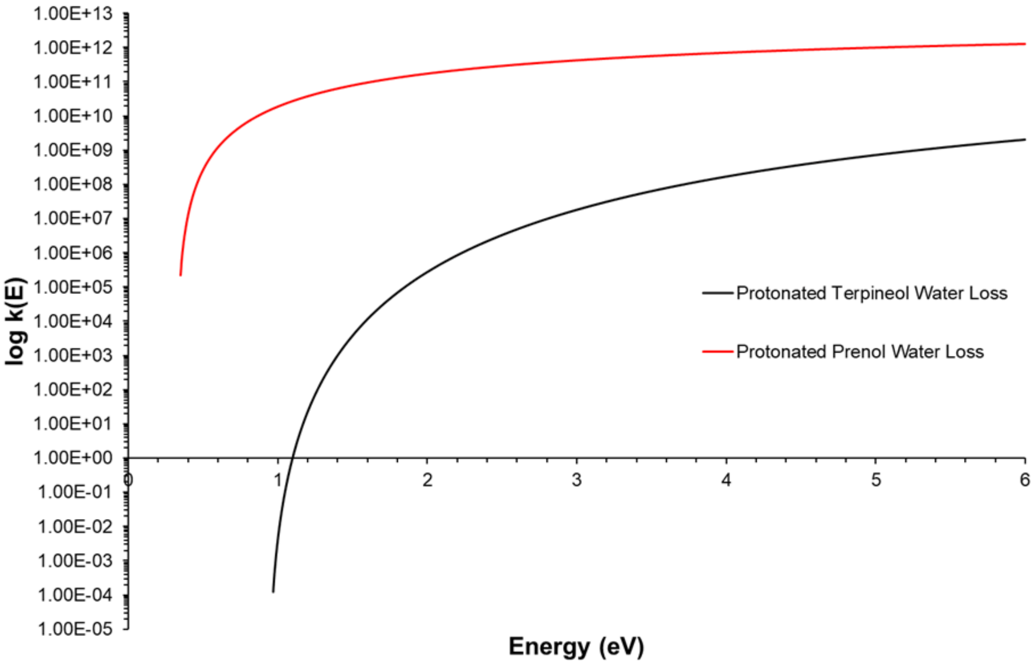

Figure 4.10: RRKM-derived log k(E) vs E curves for the neutral loss of water from the ion-molecule complex of protonated α-terpineol (black curve), compared with the neutral loss of water from the ion-molecule complex of protonated prenol, an open-chain hemiterpene alcohol (red curve).

The chemistry of protonated α-terpineol appears to largely be driven by the initial ion-molecule complex formation through protonation at the oxygen. The barrier for the dissociation of the ion-molecule complex towards products is much lower than other transformations available to the starting protonated structures. However, for the theory to match with the experimental breakdown diagrams, the protonated α-terpineol ion-molecule complex must be stable enough to travel from the ion source of the instrument and survive to reach the collision cell to be activated by CID. RRKM calculations were used to try and illustrate this possibility, by plotting the k(E) vs E curves for the dissociation of water from the ion-molecule complex of α-terpineol, and comparing that with an analogous reaction in prenol, an open chain hemiterpene alcohol that was recently investigated in our group, and those plots have been presented in Figure 4.10. In the case of protonated prenol, the rate of the water loss reaction is so fast that the observation of the water loss channel was relatively low in abundance, suggesting that the protonated prenol ion-molecule complex would dissociate between the ion-source and collision cell. In contrast, the rate of the water loss reaction in the case of protonated α-terpineol is multiple orders of magnitudes slower than that of protonated prenol, suggesting that this ion-molecule complex may be stable enough to reach the collision cell, supporting the observations in the experiment.

4.6 – Conclusions

The underlying aim of this work was to unravel the unimolecular chemistry of protonated limonene and its closely related terpenoid derivative α-terpineol. The CID-MS/MS data revealed that protonated limonene broke apart into four product ions, one of them was most dominant in abundance when compared with the rest, corresponding to the neutral loss of C_4H_8 (observed ion m/z 81, $C_6H_9^+$). The second major reaction pathway, in terms of abundance, corresponded to the neutral loss of C_3H_6 (observed product ion m/z 95, $C_7H_{11}^+$). This pathway was less abundant than the other major pathway, but much more abundant than the two minor pathways. The two minor pathways resulted in the neutral losses of C_2H_4 and C_3H_8 (observed product ions m/z 109, $C_8H_{13}^+$, and m/z 93, $C_7H_9^+$, respectively). In the case of the protonated α-terpineol CID-MS/MS data, it was shown that the rapid loss of water lead to an m/z 137 product ion, likely an isomer of protonated limonene. The data further confirmed this suspicion with the appearance of similar product ions as to those observed in the breakdown of protonated limonene (m/z 81 and 95). Theoretical calculations revealed the underlying mechanisms for the chemical transformations involved in each pathway, described in detail in the previous section. RRKM derived k(E) vs. E curves were useful in differentiating between pathways in the case of C_3H_6 loss and clarifying the rate limiting step leading to the decreased abundance of the C_2H_4 loss pathway. One interesting observation of the results is that the protonated α-terpineol ion-molecule complex with water sits at a relatively lower energy than the individual protonated limonene and water pair. This data could suggest that protonated limonene formed in the gas-phase may preferentially bind with water forming that ion-molecule complex, rather than undergoing unimolecular reactions.

4.7 – Chapter 4 References

(1) Rehman, R.; Hanif, M. A.; Mushtaq, Z.; Al-Sadi, A. M. Biosynthesis of Essential Oils in Aromatic Plants: A Review. *Food Rev. Int.* **2016**, *32* (2), 117–160. https://doi.org/10.1080/87559129.2015.1057841.

(2) Sahu, P.; Bhowmick, A. K.; Kali, G. Terpene Based Elastomers: Synthesis, Properties, and Applications. *Processes* **2020**, *8* (5), 553. https://doi.org/10.3390/pr8050553.

(3) Mewalal, R.; Rai, D. K.; Kainer, D.; Chen, F.; Külheim, C.; Peter, G. F.; Tuskan, G. A. Plant-Derived Terpenes: A Feedstock for Specialty Biofuels. *Trends Biotechnol.* **2017**, *35* (3), 227–240. https://doi.org/10.1016/j.tibtech.2016.08.003.

(4) Guenther, A. B.; Jiang, X.; Heald, C. L.; Sakulyanontvittaya, T.; Duhl, T.; Emmons, L. K.; Wang, X. The Model of Emissions of Gases and Aerosols from Nature Version 2.1 (MEGAN2.1): An Extended and Updated Framework for Modeling Biogenic Emissions. *Geosci. Model Dev.* **2012**, *5* (6), 1471–1492. https://doi.org/10.5194/gmd-5-1471-2012.

(5) Hantson, S.; Knorr, W.; Schurgers, G.; Pugh, T. A. M.; Arneth, A. Global Isoprene and Monoterpene Emissions under Changing Climate, Vegetation, CO 2 and Land Use. *Atmos. Environ.* **2017**, *155*, 35–45. https://doi.org/10.1016/j.atmosenv.2017.02.010.

(6) Enami, S.; Hoffmann, M. R.; Colussi, A. J. Dry Deposition of Biogenic Terpenes via Cationic Oligomerization on Environmental Aqueous Surfaces. *J. Phys. Chem. Lett.* **2012**, *3* (21), 3102–3108. https://doi.org/10.1021/jz301294q.

(7) Ishizuka, S.; Matsugi, A.; Hama, T.; Enami, S. Interfacial Water Mediates Oligomerization Pathways of Monoterpene Carbocations. *J. Phys. Chem. Lett.* **2020**, *11* (1), 67–74. https://doi.org/10.1021/acs.jpclett.9b03110.

(8) Colussi, A. J.; Enami, S.; Ishizuka, S. Hydronium Ion Acidity Above and Below the Interface of Aqueous Microdroplets. *ACS Earth Space Chem.* **2021**, *5* (9), 2341–2346. https://doi.org/10.1021/acsearthspacechem.1c00067.

(9) Tereza Fernandez, M.; Williams, C.; Mason, R. S.; Costa Cabral, B. J. Experimental and Theoretical Proton Affinity of Limonene. *J. Chem. Soc. Faraday Trans.* **1998**, *94* (10), 1427–1430. https://doi.org/10.1039/a800049b.

(10) Hewitt, C. N.; Hayward, S.; Tani, A. The Application of Proton Transfer Reaction-Mass Spectrometry (PTR-MS) to the Monitoring and Analysis of Volatile Organic Compounds in the Atmosphere. *J. Environ. Monit.* **2003**, *5* (1), 1–7. https://doi.org/10.1039/b204712h.

(11) Müller, M.; Mielke, L. H.; Breitenlechner, M.; McLuckey, S. A.; Shepson, P. B.; Wisthaler, A.; Hansel, A. MS/MS Studies for the Selective Detection of Isomeric Biogenic VOCs Using a Townsend Discharge Triple Quadrupole Tandem MS and a PTR-Linear Ion Trap MS. *Atmospheric Meas. Tech.* **2009**, *2* (2), 703–712. https://doi.org/10.5194/amt-2-703-2009.

(12) Frisch, M. J.; Trucks, G. W.; Schlegel, H. B.; Scuseria, G. E.; Robb, M. A.; Cheeseman, J. R.; Scalmani, G.; Barone, V.; Petersson, G. A.; Nakatsuji, H.; Li, X.; Caricato, M.; Marenich, A. V.; Bloino, J.; Janesko, B. G.; Gomperts, R.; Mennucci, B.; Hratchian, H. P.; Ortiz, J. V.; Izmaylov, A. F.; Sonnenberg, J. L.; Williams; Ding, F.; Lipparini, F.; Egidi, F.; Goings, J.; Peng, B.; Petrone, A.; Henderson, T.; Ranasinghe, D.; Zakrzewski, V. G.; Gao, J.; Rega, N.; Zheng, G.; Liang, W.; Hada, M.; Ehara, M.; Toyota, K.; Fukuda, R.; Hasegawa, J.; Ishida, M.; Nakajima, T.; Honda, Y.; Kitao, O.; Nakai, H.; Vreven, T.; Throssell, K.; Montgomery Jr., J. A.; Peralta, J. E.; Ogliaro, F.; Bearpark, M. J.; Heyd, J. J.; Brothers, E. N.; Kudin, K. N.; Staroverov, V. N.; Keith, T. A.; Kobayashi, R.; Normand, J.; Raghavachari, K.; Rendell, A. P.; Burant, J. C.; Iyengar, S. S.; Tomasi, J.; Cossi, M.; Millam, J. M.; Klene, M.; Adamo, C.; Cammi, R.; Ochterski, J. W.; Martin, R. L.; Morokuma, K.; Farkas, O.; Foresman, J. B.; Fox, D. J. Gaussian 16 Rev. C.01, 2016.

(13) Becke, A. D. Density-functional Thermochemistry. III. The Role of Exact Exchange. *J. Chem. Phys.* **1993**, *98* (7), 5648–5652. https://doi.org/10.1063/1.464913.

(14) Lee, C.; Yang, W.; Parr, R. G. Development of the Colle-Salvetti Correlation-Energy Formula into a Functional of the Electron Density. *Phys. Rev. B* **1988**, *37* (2), 785–789. https://doi.org/10.1103/PhysRevB.37.785.

(15) Ochterski, J. W.; Petersson, G. A.; Montgomery, J. A. A Complete Basis Set Model Chemistry. V. Extensions to Six or More Heavy Atoms. *J. Chem. Phys.* **1996**, *104* (7), 2598–2619. https://doi.org/10.1063/1.470985.

(16) Montgomery, J. A.; Frisch, M. J.; Ochterski, J. W.; Petersson, G. A. A Complete Basis Set Model Chemistry. VI. Use of Density Functional Geometries and Frequencies. *J. Chem. Phys.* **1999**, *110* (6), 2822–2827. https://doi.org/10.1063/1.477924.

(17) Baer, T.; Hase, W. L. *Unimolecular Reaction Dynamics: Theory and Experiments*; Oxford University Press on Demand, 1996; Vol. 31.

(18) Baer, T.; Mayer, P. M. Statistical Rice-Ramsperger-Kassel-Marcus Quasiequilibrium Theory Calculations in Mass Spectrometry. *J. Am. Soc. Mass Spectrom.* **1997**, *8* (2), 103–115. https://doi.org/10.1016/S1044-0305(96)00212-7.

(19) Beyer, T.; Swinehart, D. F. Algorithm 448: Number of Multiply-Restricted Partitions. *Commun. ACM*, 1973, *16*, 379.

Chapter 5 – Protonated Myrcene and Linalool

Based on the publication Buenger, E. W.; Mayer, P. M. Where You Protonate Matters: Deciphering the Unimolecular Chemistry of Protonated Myrcene and Linalool. *J Mass Spectrom* **2024**, *59* (10), e5096. https://doi.org/10.1002/jms.5096.

Contribution Statement

E. White Buenger carried out the experiments, computational studies, prepared and revised the manuscript for submission. P. M. Mayer conceptualized the idea, supervised the work and revised the manuscript.

5.1 – Introduction

Terpenes represent a diverse family of organic molecules consisting of the C_5H_8 building block. Compounds that are structurally related but slightly modified from this core motif are called terpenoids; for instance, through the incorporation of oxygenated functional groups. Monoterpenes and monoterpenoids are compounds that are based on the $C_{10}H_{16}$ framework and are naturally produced by plants as secondary metabolites. Their primary function has been proposed to be protection against predators,[1] and recently there has been evidence that these compounds may also signal danger in plant-to-plant signaling processes.[2] The abundance of monoterpenes is not limited to the natural world as these compounds are also increasingly used throughout industrial processes, including the manufacture of value-added foods,[3] fragrances,[4] pharmaceuticals,[5] and fuel products.[6] Through both natural and anthropogenic processes, monoterpenes and their derivatives are released into the atmosphere as volatile organic compounds (VOCs). It has been estimated that the annual natural global emission of VOCs is in the range of 700-1000 Tg per year, the majority of this mass consisting of the hemiterpene isoprene (C_5H_8). However, natural monoterpene VOC emissions are also significant (estimated in the range of 26-156 Tg per year).[7] Myrcene is an example of an acyclic monoterpene, featuring three carbon-carbon double bonds and linalool is a monoterpene alcohol derivative of myrcene, where water has been added across the central point of unsaturation in myrcene (Figure 5.1). The primary and generally established anthropogenic use of these two compounds is in the manufacture of fragrances and flavouring agents due to their pleasantly sweet, floral aromas.[8,9] Myrcene has been targeted as a potential intermediate in the broader value-added hydrocarbon chemical manufacturing process currently dominated by petrochemical products, as it fills similar roles but can be sourced from renewable methods.[10] The majority of monoterpene emissions have been reported to come from natural sources due to their abundance in biomass; however, recent evidence suggests that anthropogenic activity is also releasing significant sources of monoterpenes into the atmosphere.[11] This emission of monoterpenes is impactful in the atmosphere as it has previously been demonstrated that these compounds contribute towards the formation of secondary organic aerosols, which can affect air quality and climate.[12] Thus, it is of interest for researchers to uncover the chemistry of myrcene and linalool in the gas phase.

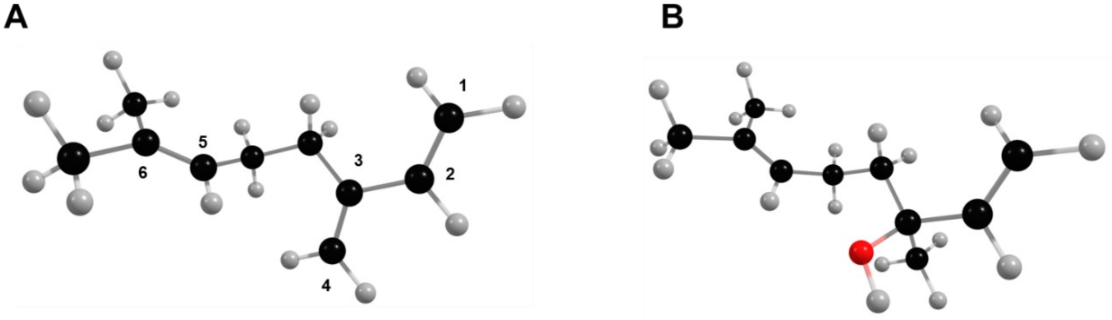

Figure 5.1: Optimized minimum energy structures obtained for (A) neutral myrcene and (B) neutral linalool calculated at the B3LYP/6-311+G(d,p) level of theory. The numbers associated with the myrcene structure indicate carbons bearing a double bond.

To date, most of the research around the atmospheric chemistry of myrcene and linalool has focused on the oxidation of these compounds by common environmental oxidants like the hydroxyl radical, ozone, or NO_x. Myrcene has been estimated to have an atmospheric lifetime of approximately 1 hour before undergoing oxidation reactions.[13] The oxidation products of myrcene were determined to be primarily carbonyl-containing compounds like formaldehyde, acetone, and 4-vinyl-4-pentanal, resulting from a series of oxidations involving peroxy radicals as intermediates in the process.[14,15] The oxidation of linalool has similarly been shown to produce acetone and formaldehyde; however, higher molecular weight products 4-hydroxy-4-methyl-5-hexen-1-al and its equivalent substituted 5-hydroxytetrafuran differ slightly from the myrcene oxidation products as a result of the additional hydroxy group.[16,17] An underappreciated aspect of myrcene and linalool gas-phase chemistry is protonation and how these molecules break apart after becoming protonated. A pair of studies investigated the reactions of monoterpenes using selected ion flow tube mass spectrometry, where they reacted high energy cations (H_3O^+, NO^+, and O_2^+) with monoterpenes, including myrcene.[18,19] Although these studies were primarily focused on determining the rate constants between the higher energy cations and the monoterpenes, they also briefly described the product ions that were observed from the breakdown of protonated myrcene ($C_{10}H_{17}^+$), predominantly $C_6H_9^+$ (neutral loss of C_4H_8) with minor amounts of $C_7H_{11}^+$ and $C_5H_9^+$ (neutral losses of C_3H_6 and C_5H_8, respectively).[18,19] A similar experiment was performed using protonated water and ethanol clusters to react with linalool to determine the rate constant of these reactions.[20] They also reported on product ions that were observed from these reactions, which were dominated by the presence of $C_{10}H_{17}^+$ and $C_6H_9^+$.[20] The same group published a study that focused more on the reaction products of the protonated monoterpenes where they used NO^+ as a chemical ionization method to protonate compounds including myrcene and linalool.[21] They observed rich fragmentation leading to a variety of C_7 and C_6-containing products in the case of protonated myrcene.[21] Although similar products were observed in the case of protonated linalool, there was an additional presence of C_9 and C_8 products. However, it should be noted that the molecular ion of linalool that was mass selected in this study was m/z 137, which would correspond to the dehydrated protonated linalool.[21]

In this work, we aim to improve upon the understanding of the unimolecular dissociation of protonated myrcene and linalool. Previous studies focused largely on determining the rate constants of reactions between high-energy protonated small molecules and monoterpenes, with some discussion revolving around the products observed. However, there has been little focus on deciphering the mechanism by which these protonated monoterpenes break apart into products. Our work will combine experimental and theoretical methods to provide a comprehensive picture of the primary dissociation channels by which protonated myrcene and linalool break apart in the gas phase. Conventional tandem mass spectrometry performed on a triple quadrupole instrument will enable the formation and isolation of the protonated compounds, and fragmentation in a collision cell at controlled energy steps in the presence of an inert gas will allow for the identification of their unimolecular breakdown products. The experimental observations will be supported with density functional theory calculations that will unravel the mechanism by which the protonated myrcene and linalool reach the observed products in the experiment.

5.2 – Methods

5.2.1 – Sample Preparation

Myrcene was purchased from Fisher Scientific (>90%, Ottawa, Ontario, CA). Linalool was purchased from TCI America (>96%, Portland, Oregon, USA). Both compounds were used as purchased, without further purification, prepared as individual solutions in methanol, and diluted to 100 μg/mL prior to injection into the mass spectrometer.

5.2.2 – Tandem Mass Spectrometry

Solutions were introduced into the triple quadrupole mass spectrometer (Waters Micromass Ultima, Manchester, UK) using a syringe pump operating at a flow rate of 50 μL/min. An atmospheric pressure chemical ionization (APCI) source was used to generate protonated myrcene and linalool, with the probe set to a temperature of 200 °C, the source operating at 100 °C and the corona discharge needle set to 10 μA. An electrospray ionization (ESI) source was also used to form protonated linalool, where the source and heater temperatures were both set to 120 °C, and the capillary voltage was set to 3.0 kV. Both APCI and ESI were operated in the positive ionization mode to produce protonated molecular ions. The molecular ions were mass-selected according to their m/z (137 for protonated myrcene, 155 for protonated linalool) with the first quadrupole, underwent collisions with argon gas in the collision cell, and the product ions were filtered in the final quadrupole. The collision-induced dissociation (CID) experiment was performed by reducing the main molecular ion beam signal intensity by 50% through the addition of argon gas in the collision cell. The CID experiments were performed using 0-20 eV of collision energy (laboratory frame, E_{Lab}), at intervals of 1 eV.

5.2.3 – Breakdown Diagrams

The collection of CID data was compiled into breakdown diagrams, where the relative abundance of the ions observed in the CID mass spectra are plotted as a function of increasing collision energy. To compare the breakdown behaviour of different ions more accurately, the collision energy applied by the instrument (E_{Lab}) is first converted to the centre-of-mass frame of reference (E_{CoM}). This conversion accounts for differences in the efficiency of energy transfer during the collisional activation, according to the equation below:

$$E_{COM} = E_{Lab}\left(\frac{m_{Ar}}{m_{Ar} + m_I}\right)$$

where m_{Ar} is the mass of argon, and m_I is the mass of the ion undergoing CID.

5.2.4 – Computational Methods

All calculations (geometry optimizations, vibrational frequency, and intrinsic reaction coordinate) were performed with the GAUSSIAN 16 suite of programs at the B3LYP/6-311+G(d,p) level of theory.[22–24] The B3LYP output files were used for single-point energy calculations using the CBS-QB3 composite method, to provide more accurate energy values.[25,26] Transition state structures featuring a single negative vibrational mode were verified using intrinsic reaction coordinate calculations. The optimized geometries and internal energies obtained through these sets of calculations were used to produce minimum energy reaction pathways (MERP). In these models, the pathway from reactants to products was mapped through the individual transformations involved (transition states, intermediates, and ion-molecule complexes). All relative energies are reported at 0 K and all processes are described in terms of energy (eV). The structure marked as zero energy is considered the baseline to which others are compared.

5.3 – Results and Discussion – Mass Spectrometry

Representative data obtained from one of the CID experiments have been presented in Figure 5.2. Panel A shows a mass spectrum of protonated myrcene with 10 eV of collision energy. The relevant fragmentation products predicted to arise from unimolecular chemistry, as well as the molecular ion, have been indicated on the plot. It should be noted that the peak at 119 m/z was determined not to be a fragmentation product, since the neutral loss of 18 is an unrealistic product ion channel for protonated myrcene. Rather the appearance of this peak likely arises from some form of contaminant in the commercial myrcene that was co-isolated at m/z 137, which led to the neutral loss of water giving rise to the observed ion at m/z 119. The mass spectra presented in panels B and C of Figure 5.2 are examples of the ions observed in the breakdown of protonated linalool at the same collision energy, albeit from different ionization sources (APCI in panel B and ESI in panel C). There is little difference between the two mass spectra aside from the slightly greater fragmentation observed in the ESI mass spectrum, suggesting that the ESI source in our instrument produces slightly more energetic ions relative to APCI.

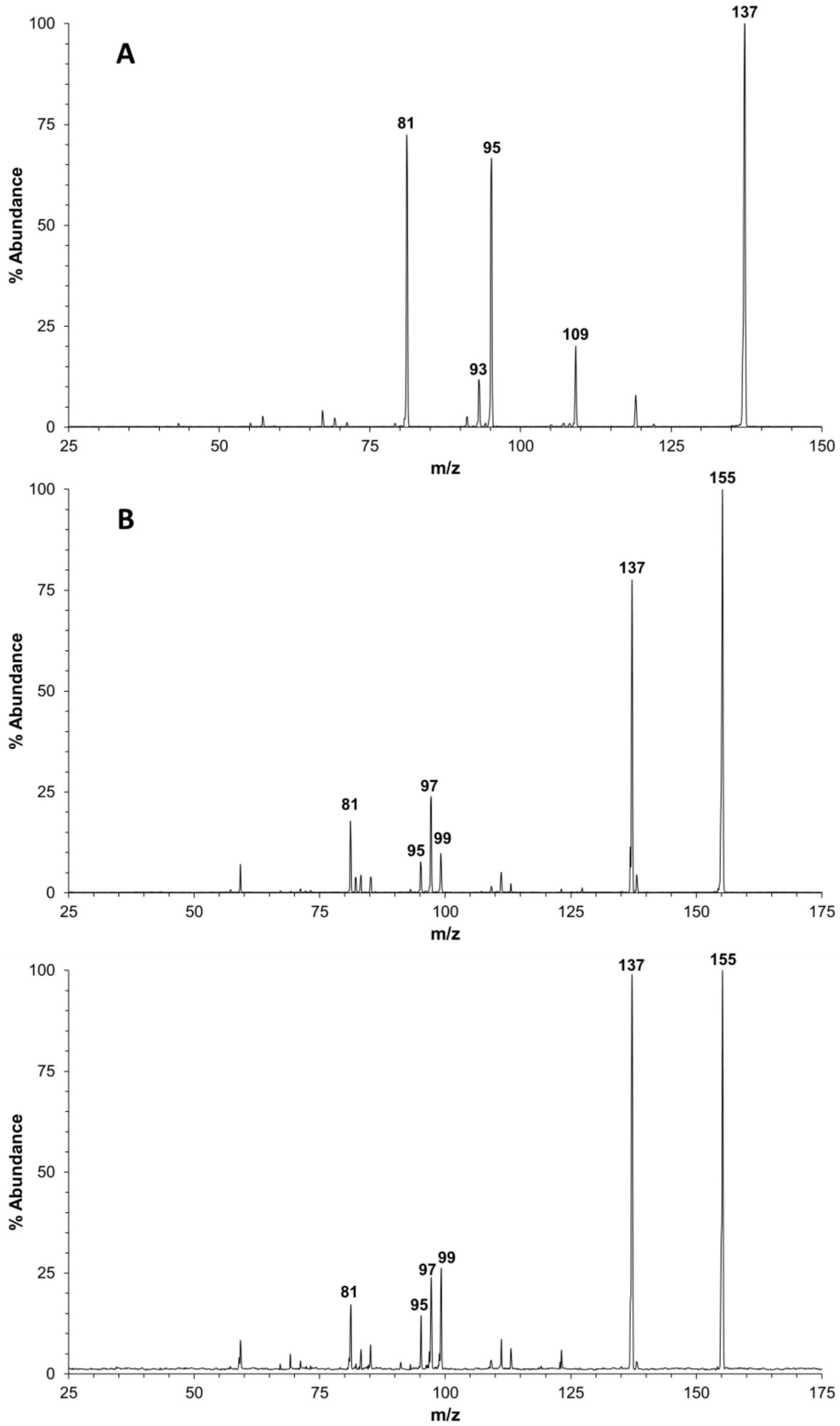

Figure 5.2: Representative CID-MS/MS spectra obtained from protonated myrcene (**A**, m/z 137, E_{Lab} = 10 eV) and protonated linalool ionized using APCI (**B**, m/z 155, E_{Lab} = 6 eV) and ESI (**C**, m/z 155, E_{Lab} = 6 eV).

The CID-MS/MS spectra were compiled into breakdown diagrams, shown in Figure 5.3. In the case of protonated myrcene (panel A), there are two major and two minor product ions. The two major product ions, m/z 95 and 81, correspond respectively to the neutral losses of C_3H_6 and C_4H_8 from protonated myrcene. At low collision energies (E_{CoM} = 0-2 eV) m/z 81 is somewhat greater in abundance when compared with m/z 95; however, at higher collision energies this trend is inverted ($E_{CoM} > 2$ eV). The two minor product ions were observed at m/z 109 and 93, corresponding to the neutral losses of C_2H_4 and C_3H_8 from protonated myrcene. Both fragmentation channels are relatively competitive with one another, with a slight bias towards the m/z 109 pathway at moderate collision energies (E_{CoM} = 1.5-3.5 eV).

The breakdown diagrams obtained from protonated linalool are presented in panels B and C of Figure 5.3. There is one dominant fragmentation pathway, loss of water, to form m/z 137. As the collision energy increases the m/z 137 peak begins to decrease in abundance, and the appearance of product ions at m/z 95 and 81 are observed at increasing abundance. These results can be interpreted as the protonated linalool readily losing neutral water and the resulting ion at m/z 137 resembling protonated myrcene. Two minor product ions observed at m/z 99 and 97 also arise directly from the protonated linalool cation. These product ions were determined to result from the neutral losses of C_4H_8 and C_3H_6O, respectively.

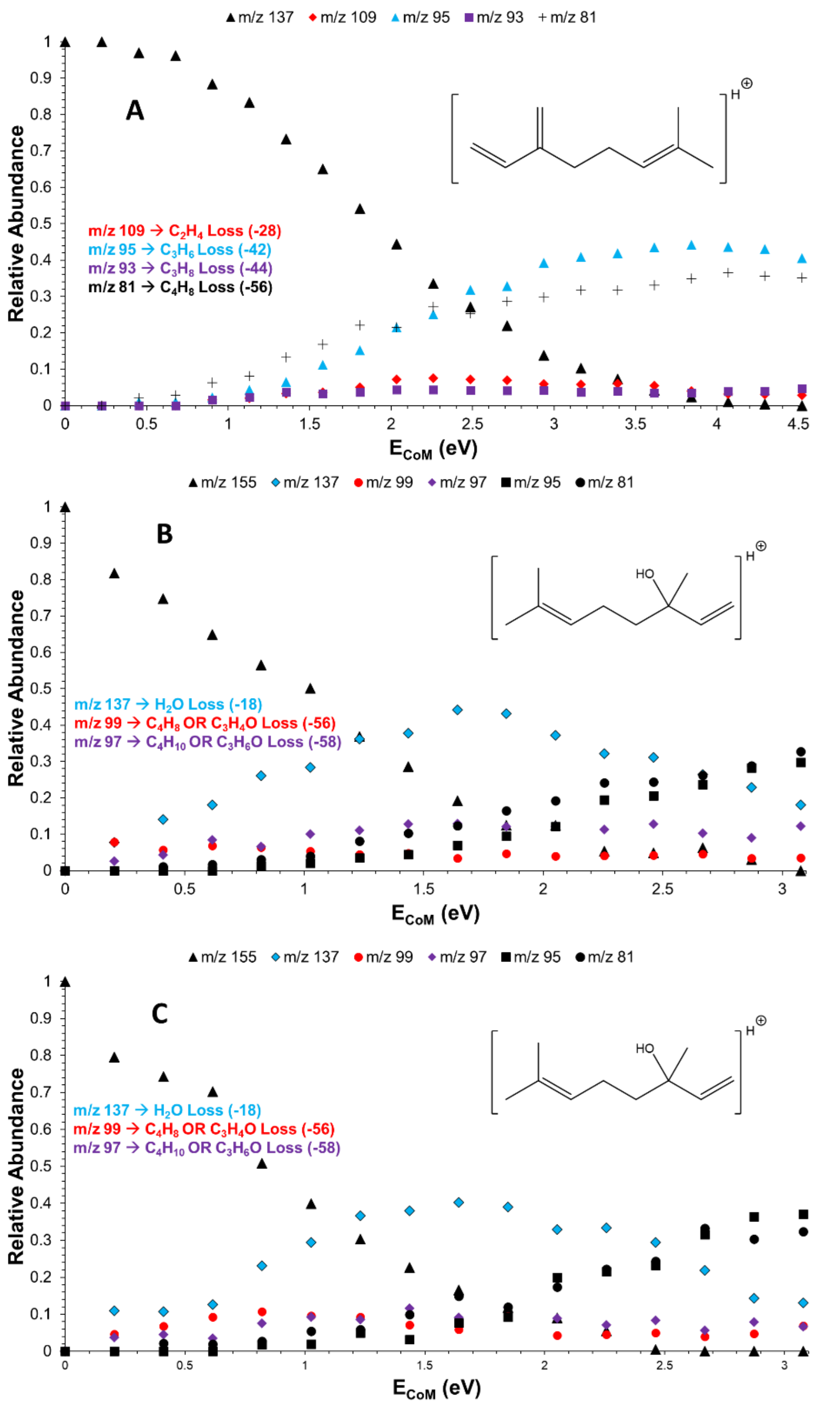

Figure 5.3: CID breakdown curves obtained from protonated myrcene (**A**), and protonated linalool using APCI (**B**) and ESI (**C**). The data was consistent across two separate measurement days.

5.4 – Results and Discussion – Calculated Reaction Mechanisms

5.4.1 – Protonated Myrcene – Initial Protonation

Six different positions on the neutral myrcene molecule can accept a proton, corresponding to the carbons that bear a double bond highlighted in Figure 5.1. DFT calculations revealed four optimized structures that arise from the protonation of these six positions, presented in Figure 5.4. The structure labeled as the relative zero in Figure 5.4 (**1a**) results from protonation at the carbons labeled 1 and 2 in Figure 5.1. Protonation at the carbons labeled 3 and 4 leads to the structure **1b** with a relative energy of -0.04 eV. Carbon 5 leads to structure **1h** at 0.85 eV, while carbon 6 leads to structure **1e** at -0.09 eV. The energetic differences between **1a**, **1b**, and **1e** are negligible compared to **1h**, suggesting that the former three structures are equally populated in the ion source, while the latter remains largely unpopulated. Since **1a** and **1b** can arise from multiple protonation sites, these structures would be twice as populated as **1e**. Thus, it can be predicted that an approximate 2:2:1 ratio of **1a**:**1b**:**1e** would be formed in the ion source at the start of the experiment.

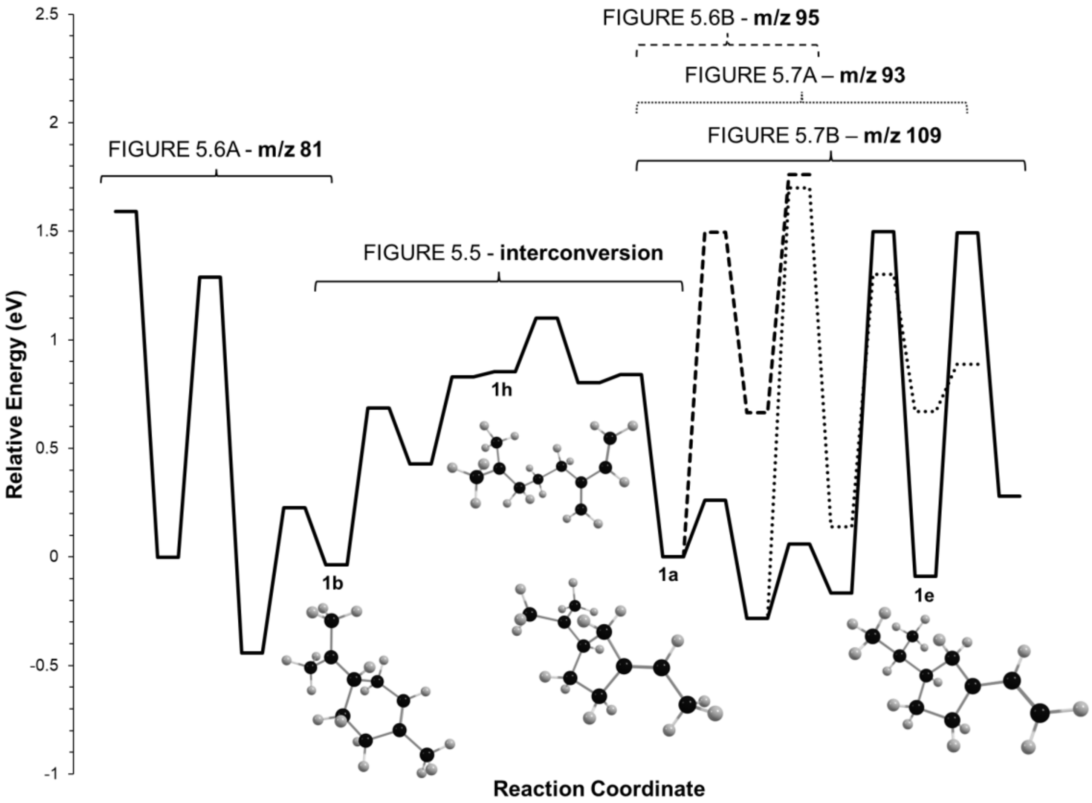

Figure 5.4: CBS-QB3(sp)//B3LYP/6-311+G(d,p) calculated minimum energy reaction pathway for protonated myrcene, including all products observed, designed to allow for comparison between pathways. Positions along the pathway that may be produced through the direct protonation of neutral myrcene have been highlighted with structural features. For more detailed information regarding individual reaction mechanisms, see Figures 5.5-5.7.

5.4.2 – Protonated Myrcene – Reaction Pathways

Figure 5.5 shows the conversion between the two starting protonated structures **1a** and **1b**. The process takes the 5-membered ring structure **1a** and converts it to the 6-membered ring structure **1b**. The mechanism begins from either side through a bond elongation transition state (**TS1b-1i** or **TS1a-1g**), leading to open chain intermediates **1i** and **1g**, sitting at 0.43 and 0.80 eV, respectively. These structures are similar, although they differ in the position of the CH_3-bearing carbon in the n-butyl-like moiety. From **1i**, the reaction proceeds to **1h** through **TS1h-1i**, where a 1,5-H shift transfers one of the n-butyl CH_3 protons over to the CH central carbon. From the other side, **1h** can be reached from **1g** through the transition state **TS1g-1h** undergoing a 1,6-H shift in this case. The open chain intermediate **1h** sits in the middle of this process at a relative energy of 0.85 eV, and may be populated in the ion source directly, but will not be kinetically stable.

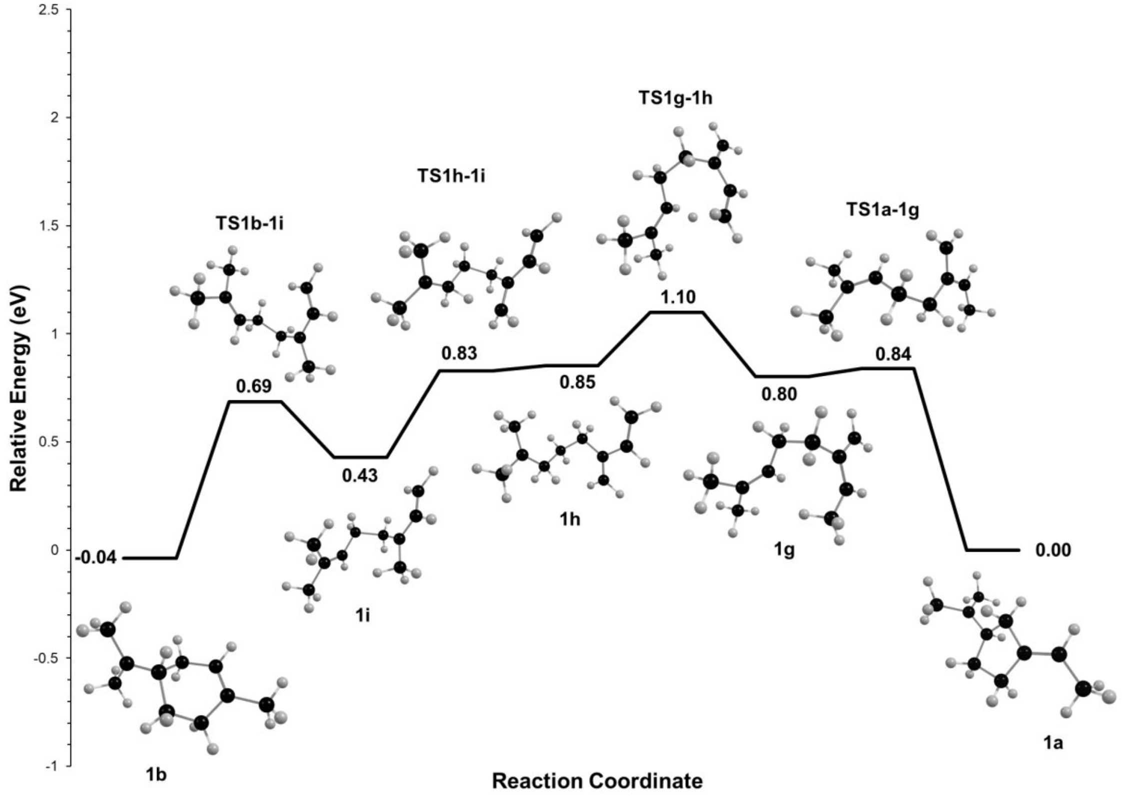

Figure 5.5: CBS-QB3(sp)//B3LYP/6-311+G(d,p) calculated minimum energy reaction pathway for converting **1a** to **1b**.

Figure 5.6 shows the reaction pathways associated with the two major product ions. Panel **A** describes the formation of m/z 81 with the associated neutral loss of C_4H_8. This pathway begins from the protonated myrcene structure **1b** and proceeds towards the 7-

membered ring intermediate **1c** through **TS1b-1c** with a relatively small 0.23 eV barrier. **1c** proceeds towards an ion-molecule complex through **TS-81IMC**, where the 7-membered ring undergoes a ring-pinch type reaction that produces a 5-membered ring **81IMC**, with a terminal isobutyl group. The ion-molecule complex can dissociate towards products through elongation of the bond that is holding the isobutyl group to the 5-membered ring, providing the observed products m/z 81 and C_4H_8. The pathway that leads towards the production of the other major products observed, m/z 95 and C_3H_6, is presented in Figure 5.6B. Following the formation of **1a** the reaction proceeds towards m/z 95 through the transition state **TS-95IMC** where one of the methyl hydrogens in the propyl moiety transfers to the central carbon, leading to **95IMC**, which then dissociates to yield the m/z 95 and C_3H_6.

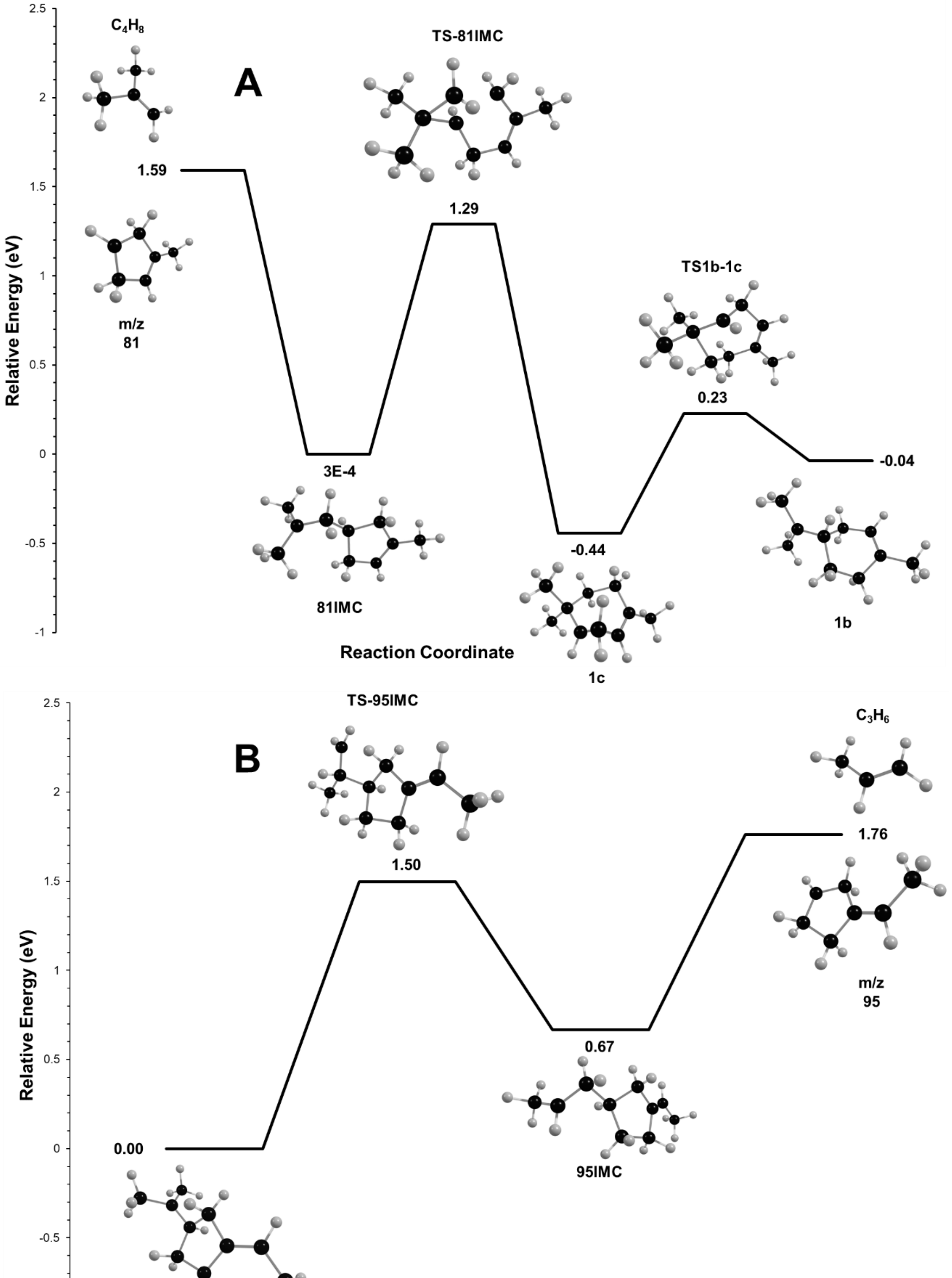

Figure 5.6: CBS-QB3(sp)//B3LYP/6-311+G(d,p) calculated minimum energy reaction pathways for protonated myrcene featuring structural details of the two major product ions observed: **A**) pathway leading to m/z 81, **B**) pathway leading to m/z 95.

The first of the minor product ion pathways to be discussed in detail is presented in Figure 5.7A, leading to m/z 93 (loss of C_3H_8). This pathway begins from **1a** and proceeds towards intermediate **1d** over a small barrier of 0.26 eV where one of the ring hydrogens migrates to the tertiary carbon in the propyl group. The reaction continues from **1d** over two high energy barriers **TS1d-1e** and **TS1e-m/z 93**. One of the hydrogens on the ethyl CH_3 group transfers onto the CH carbon within the 5-membered ring, leading to **1e**. This intermediate may also be produced directly in the ion source, as discussed in the previous section. The reaction can proceed to products from **1e** through the transition state **TS1e-m/z 93**, with the transfer of a ring-H atom to the departing neutral.

The final product ion observed in the experiment, m/z 109, and its reaction pathway are shown in Figure 5.7B. This pathway begins from **1a** through **TS1a-1d** to **1d** as described in the m/z 93 pathway. The pathway diverges from **1d** through **TS1d-1f** with a relative energy barrier of 1.70 eV, where one of the hydrogens in the CH_3 group of the ethyl moiety undergoes a 1,2-H shift to produce the intermediate **1f**, having a C_2H_4 group attached to the 5-membered ring. The pathway proceeds from **1f** through **TS1f-109IMC** where the loose CH_2 of the ethyl moiety associates more closely with the ring structure, leading to the ion-molecule complex **109IMC**. The relatively weakly bound C_2H_4 neutral loss product can be released to form the observed product ion m/z 109.

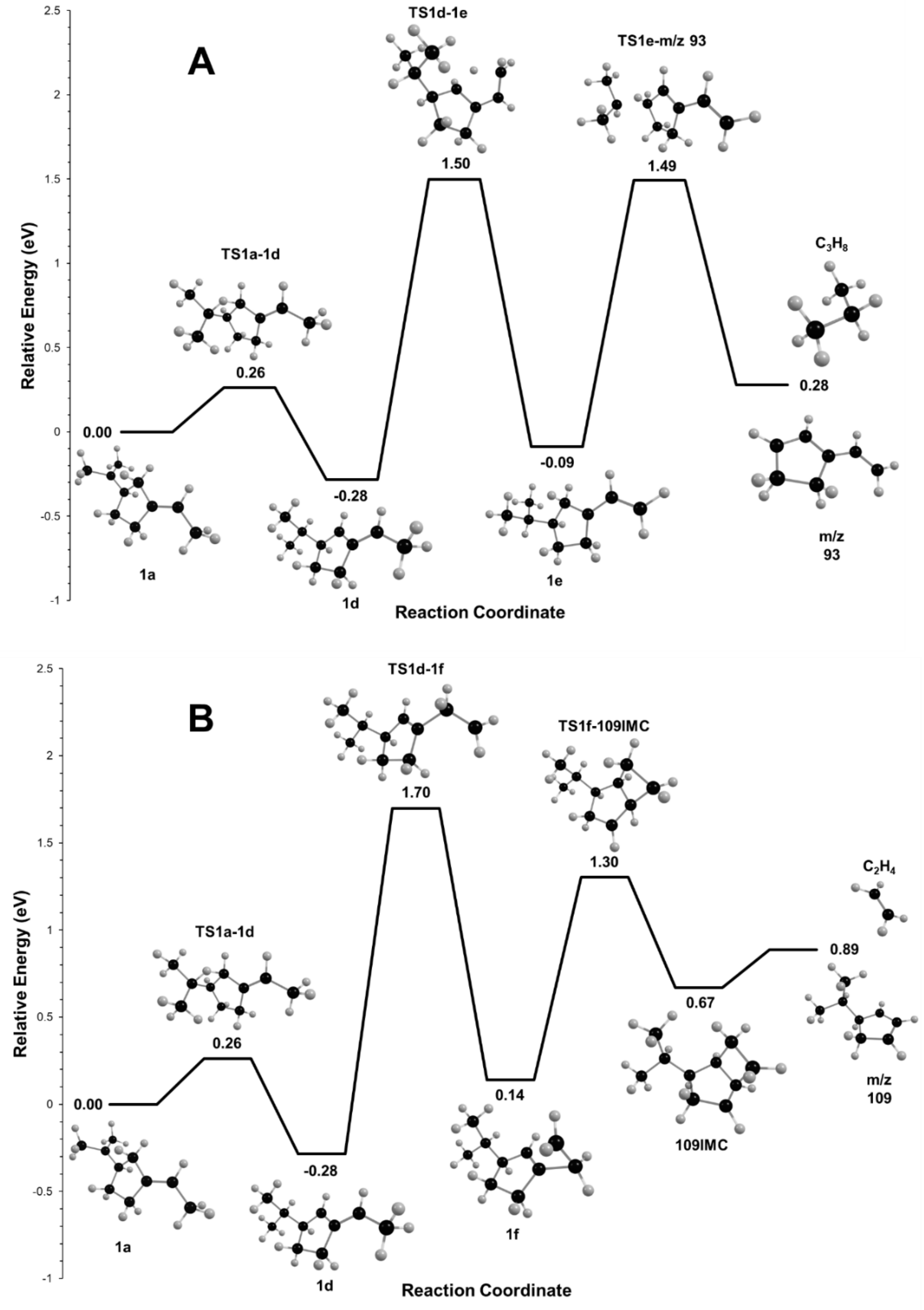

Figure 5.7: CBS-QB3(sp)//B3LYP/6-311+G(d,p) calculated minimum energy reaction pathways for protonated myrcene featuring structural details of the two minor product ions: **A**) pathway leading to m/z 93, **B**) pathway leading to m/z 109.

5.4.3 – Protonated Myrcene – Relating Theory to Experiment

When considering how the experimental results relate to the theoretically calculated reaction pathways it is worth recalling the initial site of protonation, which is expected to provide a roughly 2:2:1 ratio of **1a**:**1b**:**1e**. From the perspective of ions that begin at **1a**, the most likely product ion is m/z 95 via **TS-95IMC**. There also will be competition going through **TS1a-1d**, splitting the initial **1a** population partially into **1d**. This initial equilibrium between **1a** and **1d** could explain why m/z 95 is less abundant when compared with the other major product ion, m/z 81. The proportion of ions that initially populate **1b** will nearly exclusively proceed towards the m/z 81 product ion, due to the relatively lower energy barriers involved along that pathway (Figure 5.6B), when compared to going through the ring opening and closing processes involved in the transformation towards **1a** (Figure 5.5). Thus, at lower collision energies, m/z 81 should be more abundant than m/z 95, based on the calculations, which is consistent with the experimental data. As the collision energy increases, access towards the higher energy barrier products of the m/z 109 and m/z 93 ions can be more readily achieved. However, the population of ions that initially reside in **1e** could repopulate **1a** and form m/z 93. This observation could explain why the m/z 95 major product ion outcompetes the m/z 81 major product ion at higher collision energies, as **1a** gets repopulated.

5.4.4 – Protonated Linalool – Reaction Pathways and Relation to Experiment

The structure of linalool is closely related to myrcene, differing slightly by the incorporation of a water molecule across the C3 and C4 carbons of myrcene, as labeled in Figure 5.1. The addition of water is such that the hydroxyl group is added to C3, while the remaining hydrogen is added to C4. Thus, five positions on linalool could reasonably become protonated: the unsaturated carbons (C1, C2, C5, C6 as labeled on myrcene), and the oxygen. Four optimized structures were obtained through DFT calculations of protonation at each of these protonation sites, three of which were found to be relevant for the reaction pathways of protonated linalool.

The calculated minimum energy reaction pathways determined for protonated linalool have been presented in Figure 5.8. The three structures that are initially populated by protonation in the ion source are **2a**, **2e**, and **2**, the former of which results from protonation on the oxygen, while the latter two are two different configurations that arise from protonation at C2. The most stable of these protonated structures, **2**, is set as the relative zero energy and would be the most populated structure formed in the ion source. Both **2a** and **2e** are higher in energy relative to **2** by approximately 0.6-0.8 eV, although it is possible that a small fraction of these could also be formed in the ion source and isolated in the collision cell.

The calculated reaction pathway that describes the neutral loss of water from **2** can be seen on the right side of Figure 5.8A. The reaction begins from **2** through a 1,5-H shift in which a proton from the CH_2 group is transferred onto the oxygen through a small barrier of 0.80 eV, leading to the intermediate **2a**. The reaction proceeds forward from **2a** through another relatively low barrier where the C-O bond of the water moiety formed in the last step is bond elongated, releasing the neutral loss of water and the ion observed at m/z 137. The optimized structure for m/z 137 resulting from the neutral loss of water from linalool closely resembles myrcene ion **1b**, which could reasonably undergo secondary fragmentation before exiting the collision cell, leading to the product ions observed at m/z

95 and 81. Any **2a** that was formed in the ion source is most likely to proceed along this pathway and contribute towards the formation of m/z 137.

The minor pathway that leads towards the neutral loss of C_3H_6O from **2** has been shown on the left side of Figure 5.8A. This reaction starts from **2** with a 1,4-H shift taking the hydrogen bound to the oxygen in **2** and shifting it over to the acyclic CH_2 carbon, leading to the 7-membered ring intermediate **2b** before quickly re-arranging to **2c** and then shifting the newly formed CH_3 group over to the adjacent tertiary carbon, ultimately landing at the more stable intermediate **2d**. The reaction can go onwards to products from **2d** by rearrangement to simultaneously break the C-O and C-CH_2 bonds to form a new HC-CH_2 bond, leading to the 5-membered ring product ion and the neutral loss of C_3H_6O. This pathway competes with the water loss pathway out of the initial population of protonated **2**. Based on the energetic difference between the initial transition states, it is reasonable that the majority of **2** proceeds toward the water loss channel, aligning with what was observed in the breakdown experiment. On the other hand, the small fraction of **2** that would overcome **TS2-2b** would be unlikely to return towards **2**, continuing onwards towards the acetone loss pathway and explaining its minor presence in the experiment.

The other minor reaction pathway was determined to lead towards the neutral loss of C_4H_8 directly from protonated linalool, leading to m/z 99 and this pathway has been shown on the right side of Figure 5.8B. The reaction begins from **2** towards **2a** as previously described, then continues towards **2e** via a 1,5-H shift where a hydrogen from the oxygen is transferred to the nearby CH carbon. The reaction continues towards products from **2e** through a relatively high transition state **TS2e-2f** with an energy barrier of 2.57 eV, where the neutral loss product C_4H_8 is released by a 1,2-H shift which produces a terminal CH_3 group, ultimately leading to m/z 99, landing at a relatively high 1.90 eV. Due to the high energetics involved, this pathway is unlikely to occur. However, the initial ion population consists entirely of structures that feed into the C_4H_8 neutral loss pathway, and the energetics of conversion between **2**, **2a**, and **2e**, are relatively low, there is a possibility that a small fraction of ions undergoing CID could overcome the relatively massive **TS2e-2f** barrier. This fact could explain the small abundance of m/z 99 observed in the experiment.

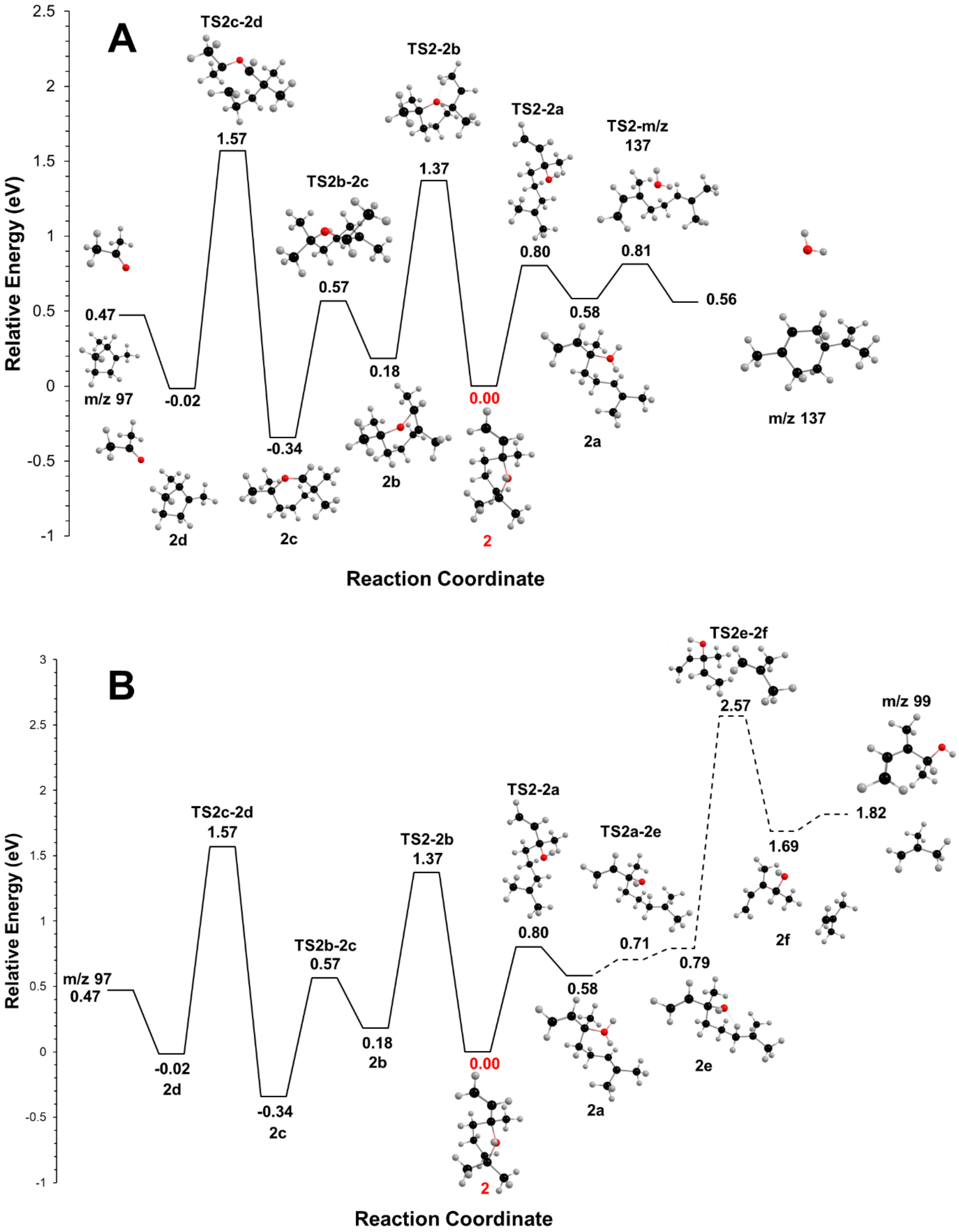

Figure 5.8: CBS-QB3(sp)//B3LYP/6-311+G(d,p) calculated minimum energy reaction pathways for the product ions observed in the breakdown of protonated linalool (**2**): (**A**) m/z 97 and 137, (**B**) m/z 99.

5.5 – Conclusion

The unimolecular chemistry of protonated myrcene and linalool was found to be greatly dependent on the initial site of protonation. Of the six possible protonation sites in myrcene, four resulted in equilibrium ion structures. The two major (m/z 85 and 91) and two minor (m/z 93 and 109) observed reaction products are generated from three distinct protomers. Similarly, protonated linalool can be formed in three significant protomers. The lowest energy one interestingly does not involve direct protonated at the hydroxyl group, but rather at the CH group of the central double bond. This results in bond migration to form a six-member ring with a protonated ether. This is the main ion that survives transit from the ion source to the collision cell.

5.6 – Chapter 5 References

(1) Gershenzon, J.; Dudareva, N. The Function of Terpene Natural Products in the Natural World. *Nat. Chem. Biol.* **2007**, *3* (7), 408–414. https://doi.org/10.1038/nchembio.2007.5.

(2) Riedlmeier, M.; Ghirardo, A.; Wenig, M.; Knappe, C.; Koch, K.; Georgii, E.; Dey, S.; Parker, J. E.; Schnitzler, J.-P.; Vlot, A. C. Monoterpenes Support Systemic Acquired Resistance within and between Plants. *Plant Cell* **2017**, *29* (6), 1440–1459. https://doi.org/10.1105/tpc.16.00898.

(3) De Alvarenga, J. F. R.; Genaro, B.; Costa, B. L.; Purgatto, E.; Manach, C.; Fiamoncini, J. Monoterpenes: Current Knowledge on Food Source, Metabolism, and Health Effects. *Crit. Rev. Food Sci. Nutr.* **2023**, *63* (10), 1352–1389. https://doi.org/10.1080/10408398.2021.1963945.

(4) Jiang, H.; Wang, X. Biosynthesis of Monoterpenoid and Sesquiterpenoid as Natural Flavors and Fragrances. *Biotechnol. Adv.* **2023**, *65*, 108151. https://doi.org/10.1016/j.biotechadv.2023.108151.

(5) Zielińska-Błajet, M.; Feder-Kubis, J. Monoterpenes and Their Derivatives—Recent Development in Biological and Medical Applications. *Int. J. Mol. Sci.* **2020**, *21* (19), 7078. https://doi.org/10.3390/ijms21197078.

(6) Woodroffe, J.-D.; Lupton, D. V.; Garrison, M. D.; Nagel, E. M.; Siirila, M. J.; Harvey, B. G. Synthesis and Fuel Properties of High-Energy Density Cyclopropanated Monoterpenes. *Fuel Process. Technol.* **2021**, *222*, 106952. https://doi.org/10.1016/j.fuproc.2021.106952.

(7) Acosta Navarro, J. C.; Smolander, S.; Struthers, H.; Zorita, E.; Ekman, A. M. L.; Kaplan, J. O.; Guenther, A.; Arneth, A.; Riipinen, I. Global Emissions of Terpenoid VOCs from Terrestrial Vegetation in the Last Millennium. *J. Geophys. Res. Atmospheres* **2014**, *119* (11), 6867–6885. https://doi.org/10.1002/2013JD021238.

(8) Surendran, S.; Qassadi, F.; Surendran, G.; Lilley, D.; Heinrich, M. Myrcene—What Are the Potential Health Benefits of This Flavouring and Aroma Agent? *Front. Nutr.* **2021**, *8*, 699666. https://doi.org/10.3389/fnut.2021.699666.

(9) Aprotosoaie, A. C.; Hăncianu, M.; Costache, I.; Miron, A. Linalool: A Review on a Key Odorant Molecule with Valuable Biological Properties. *Flavour Fragr. J.* **2014**, *29* (4), 193–219. https://doi.org/10.1002/ffj.3197.

(10) Behr, A.; Johnen, L. Myrcene as a Natural Base Chemical in Sustainable Chemistry: A Critical Review. *ChemSusChem* **2009**, *2* (12), 1072–1095. https://doi.org/10.1002/cssc.200900186.

(11) Peng, Y.; Mouat, A. P.; Hu, Y.; Li, M.; McDonald, B. C.; Kaiser, J. Source Appointment of Volatile Organic Compounds and Evaluation of Anthropogenic Monoterpene Emission Estimates in Atlanta, Georgia. *Atmos. Environ.* **2022**, *288*, 119324. https://doi.org/10.1016/j.atmosenv.2022.119324.

(12) Xu, L.; Pye, H. O. T.; He, J.; Chen, Y.; Murphy, B. N.; Ng, N. L. Experimental and Model Estimates of the Contributions from Biogenic Monoterpenes and Sesquiterpenes to Secondary Organic Aerosol in the Southeastern United States. *Atmospheric Chem. Phys.* **2018**, *18* (17), 12613–12637. https://doi.org/10.5194/acp-18-12613-2018.

(13) Kim, D.; Stevens, P. S.; Hites, R. A. Rate Constants for the Gas-Phase Reactions of OH and O_3 with β-Ocimene, β-Myrcene, and α- and β-Farnesene as a Function of Temperature. *J. Phys. Chem. A* **2011**, *115* (4), 500–506. https://doi.org/10.1021/jp111173s.

(14) Böge, O.; Mutzel, A.; Iinuma, Y.; Yli-Pirilä, P.; Kahnt, A.; Joutsensaari, J.; Herrmann, H. Gas-Phase Products and Secondary Organic Aerosol Formation from the Ozonolysis and Photooxidation of Myrcene. *Atmos. Environ.* **2013**, *79*, 553–560. https://doi.org/10.1016/j.atmosenv.2013.07.034.

(15) Tan, Z.; Hantschke, L.; Kaminski, M.; Acir, I.-H.; Bohn, B.; Cho, C.; Dorn, H.-P.; Li, X.; Novelli, A.; Nehr, S.; Rohrer, F.; Tillmann, R.; Wegener, R.; Hofzumahaus, A.; Kiendler-Scharr, A.; Wahner, A.; Fuchs, H. Atmospheric Photo-Oxidation of Myrcene: OH Reaction Rate Constant, Gas-Phase Oxidation Products and Radical Budgets. *Atmospheric Chem. Phys.* **2021**, *21* (20), 16067–16091. https://doi.org/10.5194/acp-21-16067-2021.

(16) Shu, Y.; Kwok, E. S. C.; Tuazon, E. C.; Atkinson, R.; Arey, J. Products of the Gas-Phase Reactions of Linalool with OH Radicals, NO $_3$ Radicals, and O $_3$. *Environ. Sci. Technol.* **1997**, *31* (3), 896–904. https://doi.org/10.1021/es960651o.

(17) Bernard, F.; Daële, V.; Mellouki, A.; Sidebottom, H. Studies of the Gas Phase Reactions of Linalool, 6-Methyl-5-Hepten-2-Ol and 3-Methyl-1-Penten-3-Ol with O $_3$ and OH Radicals. *J. Phys. Chem. A* **2012**, *116* (24), 6113–6126. https://doi.org/10.1021/jp211355d.

(18) Schoon, N.; Amelynck, C.; Vereecken, L.; Arijs, E. A Selected Ion Flow Tube Study of the Reactions of H3O+, NO+ and O2+ with a Series of Monoterpenes. *Int. J. Mass Spectrom.* **2003**, *229* (3), 231–240. https://doi.org/10.1016/S1387-3806(03)00343-9.

(19) Wang, T.; Španěl, P.; Smith, D. Selected Ion Flow Tube, SIFT, Studies of the Reactions of H3O+, NO+ and O2+ with Eleven C10H16 Monoterpenes. *Int. J. Mass Spectrom.* **2003**, *228* (1), 117–126. https://doi.org/10.1016/S1387-3806(03)00271-9.

(20) Dhooghe, F.; Amelynck, C.; Rimetz-Planchon, J.; Schoon, N.; Vanhaecke, F. FA-SIFT Study of Reactions of Protonated Water and Ethanol Clusters with α-Pinene and Linalool in View of Their Selective Detection by CIMS. *Int. J. Mass Spectrom.* **2010**, *290* (2–3), 106–112. https://doi.org/10.1016/j.ijms.2009.12.010.

(21) Rimetz-Planchon, J.; Dhooghe, F.; Schoon, N.; Vanhaecke, F.; Amelynck, C. Chemical Ionization by [NO] $^+$ and Subsequent Collision-induced Dissociation for the Selective On-line Detection of Monoterpenes and Linalool. *Rapid Commun. Mass Spectrom.* **2011**, *25* (5), 647–654. https://doi.org/10.1002/rcm.4901.

(22) Frisch, M. J.; Trucks, G. W.; Schlegel, H. B.; Scuseria, G. E.; Robb, M. A.; Cheeseman, J. R.; Scalmani, G.; Barone, V.; Petersson, G. A.; Nakatsuji, H.; Li, X.; Caricato, M.; Marenich, A. V.; Bloino, J.; Janesko, B. G.; Gomperts, R.; Mennucci, B.; Hratchian, H. P.; Ortiz, J. V.; Izmaylov, A. F.; Sonnenberg, J. L.; Williams; Ding, F.; Lipparini, F.; Egidi, F.; Goings, J.; Peng, B.; Petrone, A.; Henderson, T.; Ranasinghe, D.; Zakrzewski, V. G.; Gao, J.; Rega, N.; Zheng, G.; Liang, W.; Hada, M.; Ehara, M.; Toyota, K.; Fukuda, R.; Hasegawa, J.; Ishida, M.; Nakajima, T.; Honda, Y.; Kitao, O.; Nakai, H.; Vreven, T.; Throssell, K.; Montgomery Jr., J. A.; Peralta, J. E.; Ogliaro, F.; Bearpark, M. J.; Heyd, J. J.; Brothers, E. N.; Kudin, K. N.; Staroverov, V. N.; Keith, T.

A.; Kobayashi, R.; Normand, J.; Raghavachari, K.; Rendell, A. P.; Burant, J. C.; Iyengar, S. S.; Tomasi, J.; Cossi, M.; Millam, J. M.; Klene, M.; Adamo, C.; Cammi, R.; Ochterski, J. W.; Martin, R. L.; Morokuma, K.; Farkas, O.; Foresman, J. B.; Fox, D. J. Gaussian 16 Rev. C.01, 2016.

(23) Becke, A. D. Density-functional Thermochemistry. III. The Role of Exact Exchange. *J. Chem. Phys.* **1993**, *98* (7), 5648–5652. https://doi.org/10.1063/1.464913.

(24) Lee, C.; Yang, W.; Parr, R. G. Development of the Colle-Salvetti Correlation-Energy Formula into a Functional of the Electron Density. *Phys. Rev. B* **1988**, *37* (2), 785–789. https://doi.org/10.1103/PhysRevB.37.785.

(25) Ochterski, J. W.; Petersson, G. A.; Montgomery, J. A. A Complete Basis Set Model Chemistry. V. Extensions to Six or More Heavy Atoms. *J. Chem. Phys.* **1996**, *104* (7), 2598–2619. https://doi.org/10.1063/1.470985.

(26) Montgomery, J. A.; Frisch, M. J.; Ochterski, J. W.; Petersson, G. A. A Complete Basis Set Model Chemistry. VI. Use of Density Functional Geometries and Frequencies. *J. Chem. Phys.* **1999**, *110* (6), 2822–2827. https://doi.org/10.1063/1.477924.

Chapter 6 – Protonated α-Pinene and β-Pinene

Based on the publication Buenger, E. W.; Mayer, P. M. The Site of Protonation Affects the Dissociation of Protonated α- and β-Pinene Ions. *Rapid Comm Mass Spectrometry* **2025**, *39* (6), e9978. https://doi.org/10.1002/rcm.9978.

Contribution Statement

E. White Buenger carried out the experiments, computational studies, prepared and revised the manuscript for submission. P. M. Mayer conceptualized the idea, supervised the work and revised the manuscript.

6.1 – Introduction

Monoterpenes are produced naturally through biosynthetic pathways available across a variety of plant species.[1] These compounds constitute the majority component of plant essential oils, an extract that captures and concentrates the plant's unique aroma and/or flavour. Aside from their natural production and function in plants, humans make extensive use of monoterpenes across a variety of industries.[2–5] Pinene is one of the most abundant monoterpenes and features a unique [6+4]-bicyclic structure that has two prominent isomers: the α isomer bearing an endocyclic double bond, and the β isomer bearing an exocyclic one (Figure 6.1). Anthropogenically, the pinene isomers offer an excellent starting point for the organic synthesis of more complex natural products and pharmaceuticals.[6] In addition, there has been evidence showing that the pinene isomers themselves have broad-ranging therapeutic effects.[7] A significant consequence resulting from both natural and human sources of monoterpene production is the emission of gaseous terpenes into the atmosphere, estimated to be in the range of 26-156 Tg per year, of which the pinene isomers contribute a large portion.[8] Atmospheric reactions of pinene include a wide variety of oxidation reactions that contribute towards secondary organic aerosol formation.[9–13]

There remain relatively unexplored avenues of pinene chemistry, for instance, protonation of gaseous pinenes and reactions that result from this protonation. It has been demonstrated that α-pinene can react on the surface of acidic aerosols, leading to the occurrence of polymerization reactions.[14] Another study demonstrated that the abundance of pinene isomers can be observed to decrease on the surface of sulfuric acid solutions, coinciding with the appearance of a smaller mass product, suggesting that the acidic solution may protonate the pinenes and subsequently lead towards fragmentation.[15] It has also been reported that gaseous pinene may protonate on the surface of acidic water and ethanol clusters, leading to the stabilization of a protonated pinene-water cluster complex, which may undergo further reactions.[16,17]

It has previously been shown that the site of protonation can significantly impact the fragmentation of organic molecules in mass spectrometry, where there are multiple sites within the molecule that can accept a proton.[18,19] A few research groups have attempted to perform positively charged mass spectrometry experiments involving protonated terpenes. One paper showed that there was minimal differences between the pinene isomers with regard to product ion abundances, with a dominant m/z 137 precursor ion and m/z 81 product ion, and included the presence of some minor products at m/z 138, 95, and 82.[20] However, this paper was more focused on manipulating experimental parameters and noting observational differences, as well as determining reaction rate constants between monoterpenes and hydronium ions, rather than rationalizing the appearance of observed product ions. Another group attempted to use proton transfer mass spectrometry to differentiate isomeric monoterpenes, including α-, and β-pinene, noting marginal differences owing to the position of the double bond.[21] Research that has come out of our group has demonstrated that the site of protonation can have a significant impact on the fragmentation of protonated terpenes.[22–24] This work will aim to further understand the chemistry that occurs following the protonation of the two most abundant isomers of pinene, through a combination of tandem mass spectrometry and density functional theory calculations.

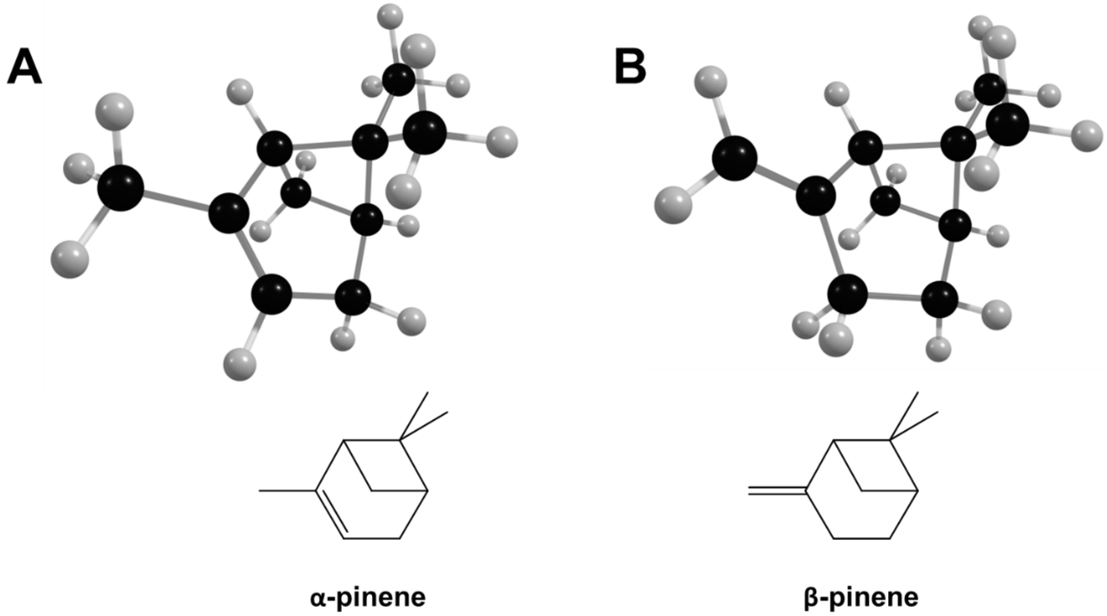

Figure 6.1: Optimized minimum energy structures obtained for (**A**) neutral α-pinene and (**B**) neutral β-pinene calculated at the B3LYP/6-311+G(d,p) level of theory. 2-dimensional stick diagrams have been included to assist with visual clarity of the double bond position.

6.2 – Methods

6.2.1 – Sample Preparation

Both compounds were used as purchased, without further purification, prepared as individual solutions in methanol, and diluted to 100 µg/mL prior to injection into the mass spectrometer.

6.2.2 – Tandem Mass Spectrometry

Solutions were introduced into the Waters Quattro Ultima triple quadrupole mass spectrometer (Waters, Manchester, UK) using a syringe pump operating at a flow rate of 50 µL/min. An atmospheric pressure chemical ionization (APCI) source was used to generate protonated α-pinene and protonated β-pinene, with the probe set to a temperature of 200 °C, the source operating at 100 °C and the corona discharge needle set to 10 µA, operating in the positive ionization mode. Desolvation gas (N_2) was set to a flow rate of 36 L/hour. The collision-induced dissociation (CID) experiment was performed by reducing the main precursor ion beam signal intensity by 50% through the addition of argon gas in the collision cell. The CID experiments were performed using 0-20 eV of collision energy (laboratory frame, E_{Lab}), at intervals of 1 eV.

6.2.3 – Breakdown Diagrams

The collection of CID data was compiled into breakdown diagrams, where the relative abundance of the ions observed in the CID mass spectra are plotted as a function of increasing collision energy. To compare the breakdown behaviour of different ions more accurately, the collision energy applied by the instrument (E_{Lab}) is first converted to the centre-of-mass frame of reference (E_{CoM}). This conversion accounts for differences in the efficiency of energy transfer during the collisional activation, according to the following equation shown below:

$$E_{COM} = E_{Lab}\left(\frac{m_{Ar}}{m_{Ar} + m_I}\right)$$

where m_{Ar} is the mass of argon, and m_I is the mass of the ion undergoing CID.

6.2.4 – Computational Methods

All calculations (geometry optimizations, vibrational frequency, and intrinsic reaction coordinate) were performed with the GAUSSIAN 16 suite of programs at the B3LYP/6-311+G(d,p) level of theory.[25–27] The B3LYP output files were used for single-point energy calculations using the CBS-QB3 composite method, to provide more accurate energy values.[28,29] Transition state structures featuring a single negative vibrational mode were verified using intrinsic reaction coordinate calculations. The optimized geometries and internal energies obtained through these sets of calculations were used to produce minimum energy reaction pathways (MERP). In these models, the pathway from reactants to products was mapped through the individual transformations involved (transition states, intermediates, and ion-molecule complexes). All relative energies are reported at 0 K and all processes are described in terms of energy (eV). The structure marked as zero energy is considered the baseline to which others are compared.

6.3 – Results and Discussion

6.3.1 – Mass Spectrometry and Breakdown Diagrams

Representative mass spectra that were obtained during the collection of CID-MS/MS experiments performed on protonated α-, and β-pinene are presented in Figure 6.2, labeled with the precursor ion (m/z 137), and the most prominent product ions at m/z 81, 95, and 109. There is little difference between the fragmentation of the two protonated pinene isomers. There appears to be a slightly greater abundance of m/z 95 in the fragmentation of protonated α-pinene when compared to protonated β-pinene. Numerous minor product ions can be seen in both spectra, although there appears to be a greater variety of minor fragments observed in the case of α-pinene, and the abundance of these ions does not exceed 1%. The CID-MS/MS mass spectra were compiled into breakdown diagrams, shown in Figure 6.3. At low collision energy (under 1 eV), m/z 81 is the only ion observed for both protonated pinenes. The m/z 95 product ion begins to appear at approximately 1 eV and is slightly more abundant in protonated α-pinene as the collision energy increases. The most abundant of the minor product ions, m/z 109, was included in the breakdown diagram, and can be observed between 2-5 eV, however, its abundance does not exceed 3% at any point throughout the experiment.

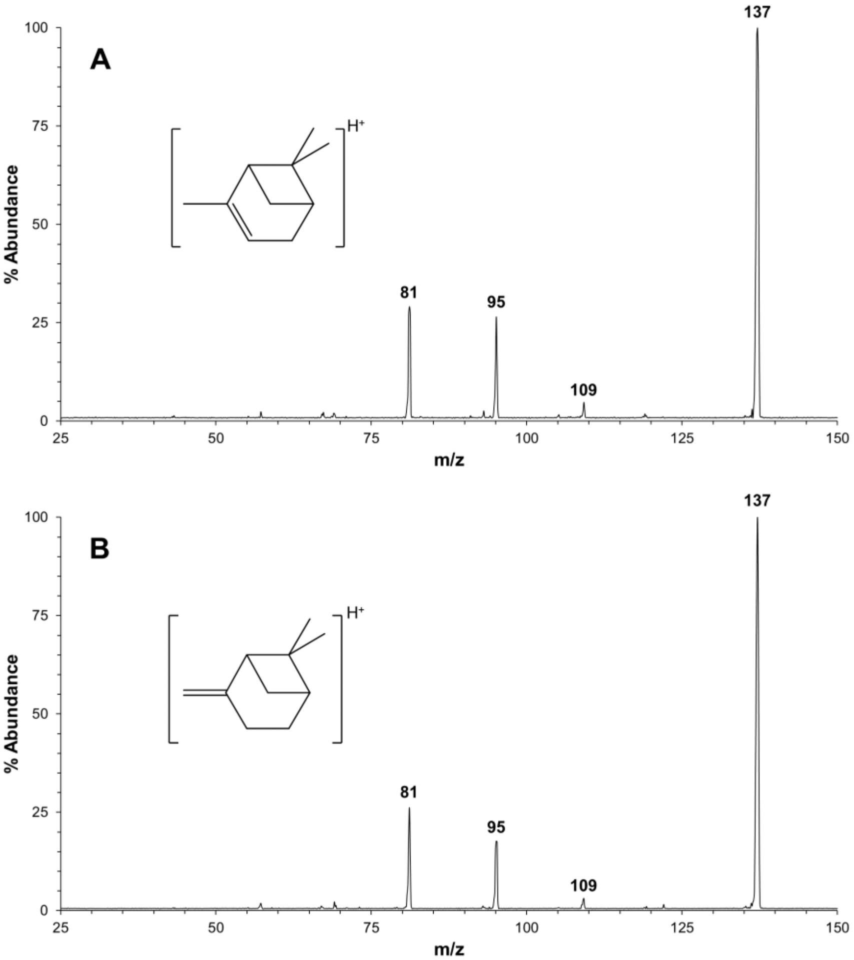

Figure 6.2: Representative CID-MS/MS spectra obtained from (**A**) protonated α-pinene and (**B**) protonated β-pinene, where the collision energy was set to 10 eV in both cases.

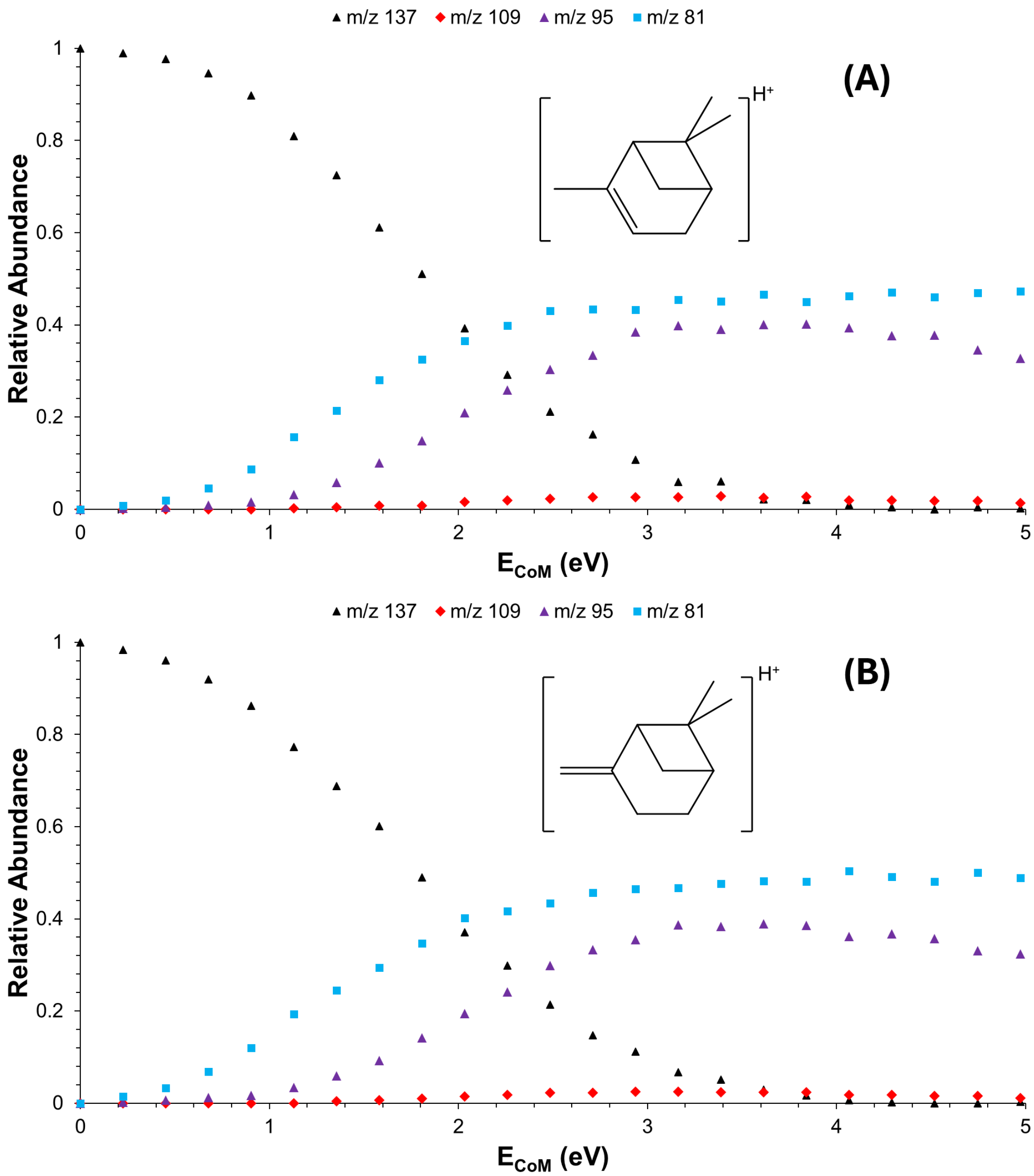

Figure 6.3: CID breakdown curves obtained from protonated α-pinene (**A**), and protonated β-pinene (**B**). The data was consistent across two separate measurement days.

6.3.2 – Calculated Reaction Pathways

The calculated reaction pathways for m/z 81 and 95 are presented in Figure 6.4. Both compounds are represented within the Figure, although they differ by which species along the path they populate in the ion source. In the case of m/z 95, the reaction begins through protonation of neutral α-pinene at the CH_2 carbon of the four-membered ring, leading to structure **1a**, set as the relative zero energy structure for the reaction pathways. The reaction proceeds through **TS1a-1b** where one of the protons from the CH_3 group formed in the previous step undergoes a 1,4-H shift, leading to the structure **1b**, featuring a four-membered ring. From **1b**, the reaction proceeds through a sequence of low energy barrier bond stretching transition states that ultimately lead to structure **1e**, where the four-membered ring has been broken to yield an exocyclic propyl moiety and sits at a relative 0.30 eV. From the intermediate **1e** the reaction continues towards the ion-molecule complex through the transition state **TS1e-1f** with a relative energy barrier of 1.64 eV where the exocyclic propyl undergoes a 1,2-H shift, landing at **1f** sitting at a relative 0.88 eV. The reaction completes through dissociation of the two species that produce the neutral loss of C_3H_6 and the observed ion at m/z 95, collectively landing at a relative 1.97 eV.

The pathway leading to m/z 81 can also be observed in Figure 6.4, labeled in purple. This reaction pathway begins from the intermediate **1b**, which passes a lower energy transition state **TS1b-1c** at 1.16 eV, where one of the CH_2 carbons part of the four-membered ring can undergo a 1,2-H shift, leading to the ion-molecule complex **1c**. The reaction completes through the loss of neutral C_4H_8, leaving the observed ion at m/z 81, a structure that resembles protonated methylcyclopentadiene.

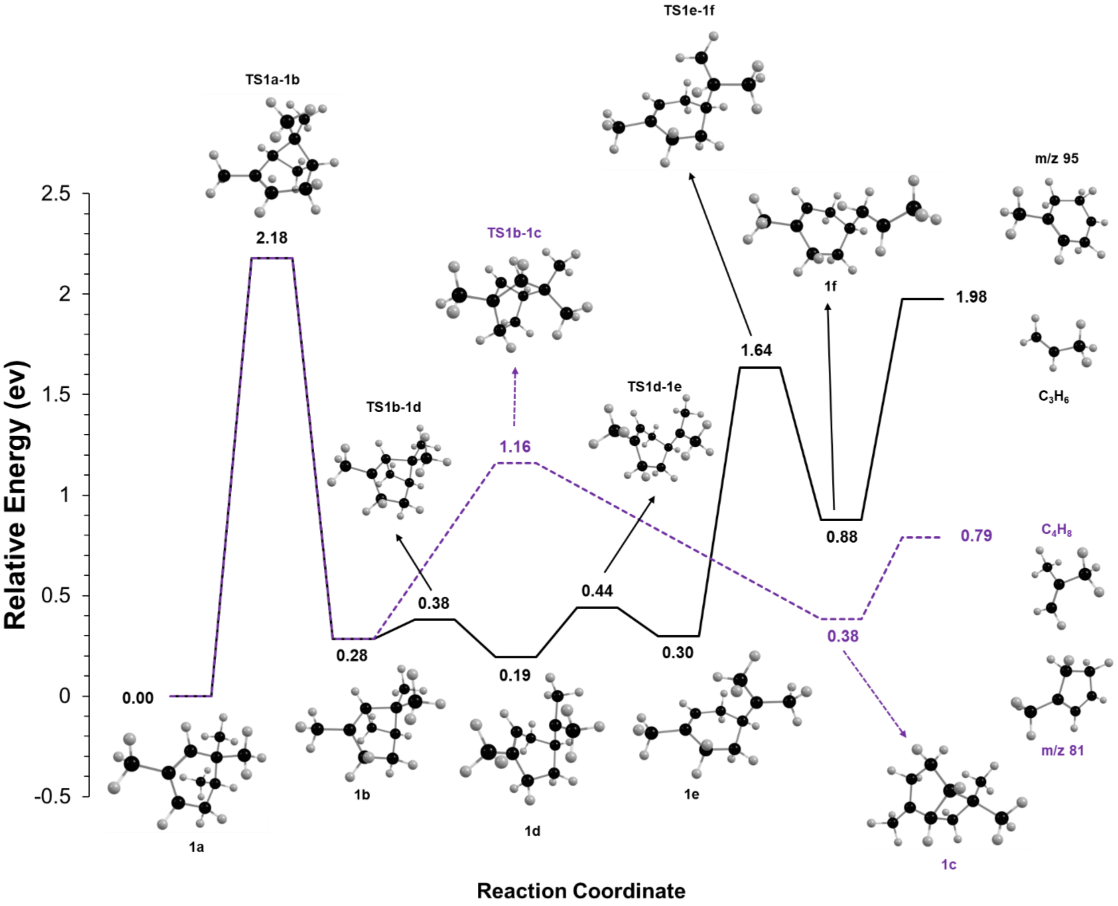

Figure 6.4: CBS-QB3(sp)//B3LYP/6-311+G(d,p) calculated minimum energy reaction pathways that include the major product ions observed in the breakdown of both protonated α-pinene and protonated β-pinene. The pathways have been differentiated by colour, where the black pathway leads towards m/z 95 and C_3H_6 loss and the purple pathway leads towards m/z 81 and C_4H_8 loss.

6.3.3 – Relating Calculated Mechanisms to Experimental Breakdown

The CID-MS/MS experiment of the protonated pinenes can first be related to the theoretically calculated minimum energy reaction pathways by the initial site of protonation of each of the neutral pinene species. In each of the two neutral pinene isomers, five carbons may reasonably accept a proton in the ion source, including the double-bond bearing carbons and the carbons of the four-membered ring system (Figure 6.1). For α-pinene, four structures may be produced via protonation of these five carbons, two of which are represented in the minimum energy reaction pathways as **1a**, and **1b** (Figure 6.4 & Figure 6.5). Thus, the initial protonation of α-pinene would be expected to nearly exclusively populate **1a**, with a fractional proportion of **1b** being produced. In comparison, the β-pinene isomer has four protonated structures that may be formed from protonation at the five positions, however only one of these structures is found on the minimum energy reaction pathway (**1b**). The remaining structures are relatively higher in energy, only βS3 has the possibility of being marginally populated following protonation and has been determined not to contribute towards the observed reaction pathways (Figure 6.6). Thus, the chemistry of protonation of β-pinene would exclusively start from populated structure **1b** on the reaction surface. This difference in starting point along the reaction coordinate for each of the isomers explains the slightly different relative abundances of m/z 81 and 95 in the protonated β-pinene breakdown (Figure 6.3). **1b** can immediately access the key transition state **TS1b-1e** that leads towards the m/z 81 ion, compared with **1a** which must first overcome the energetically higher **TS1a-1b** to access the two fragmentation channels (Figure 6.4). Dissociating protonated α-pinene ions thus have a higher average internal energy, leading to slightly more m/z 95 forming.

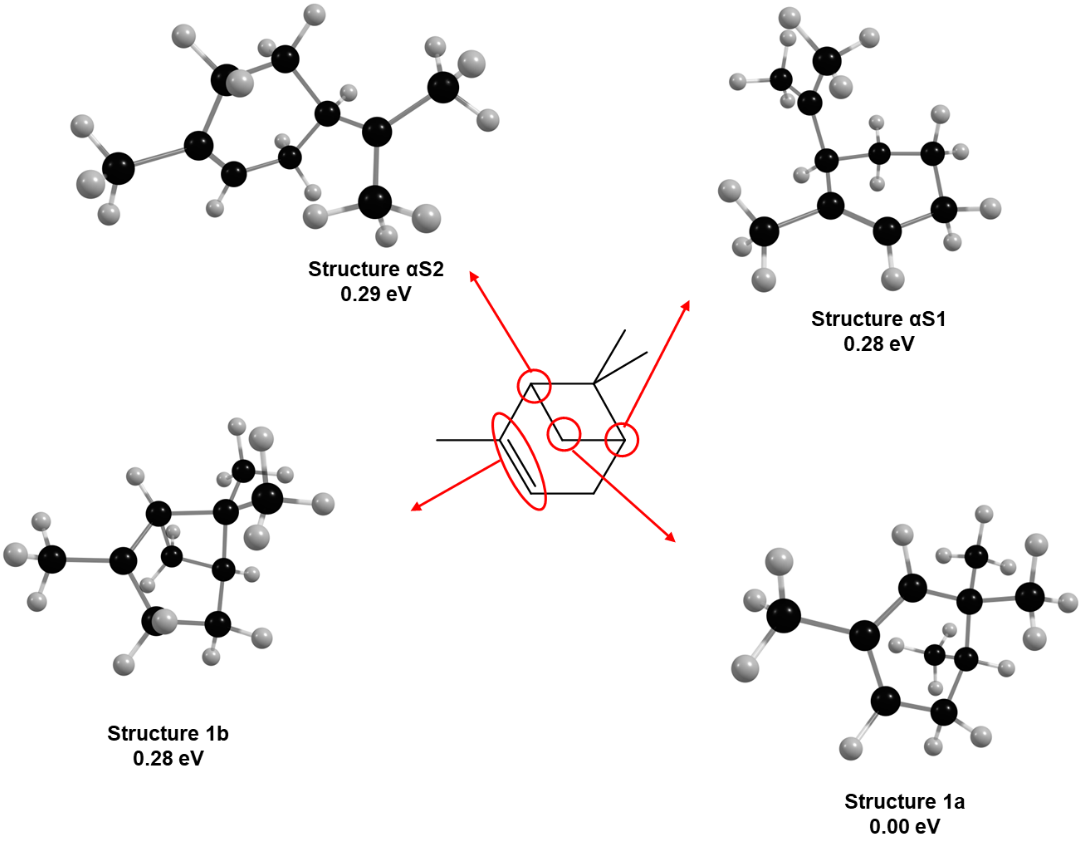

Figure 6.5: Map for the possible structures produced in the ion source during the protonation of α-pinene. Sites of protonation have been associated with the corresponding structure. Energy levels are set relative to structure **1a** from Figure 6.4.

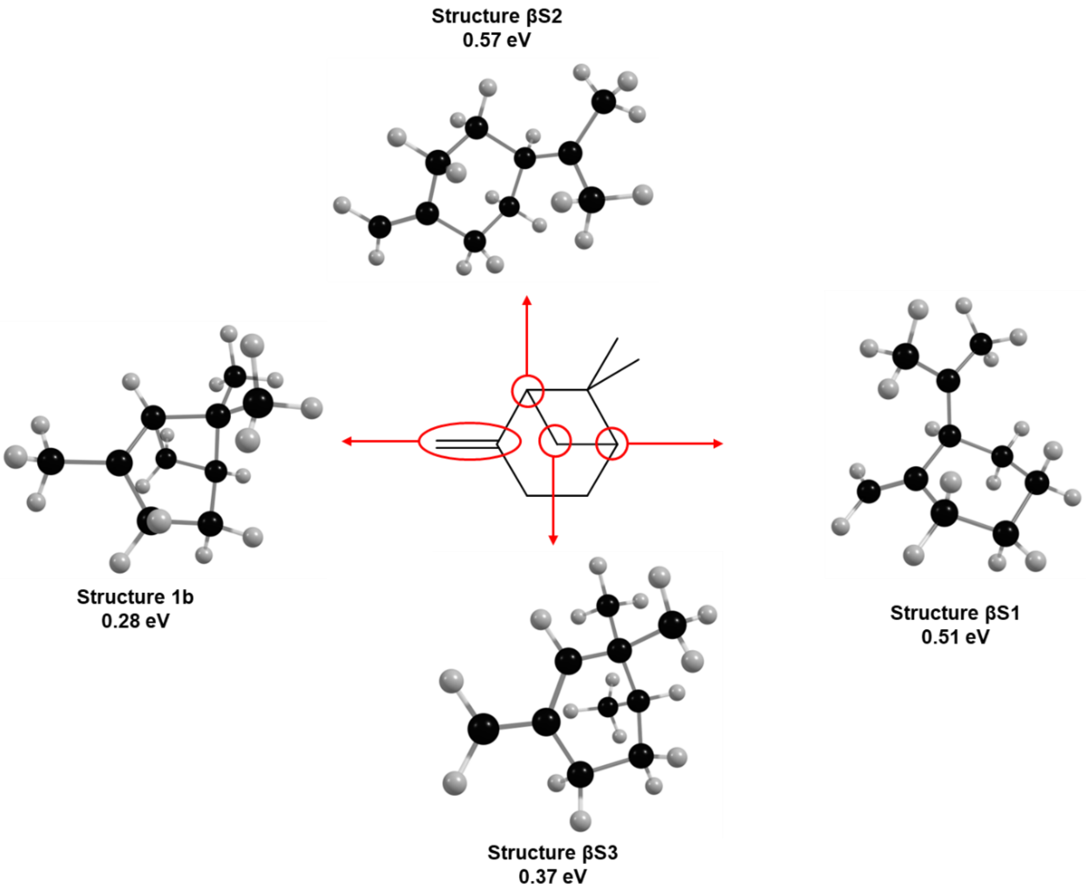

Figure 6.6: Map for the possible structures produced in the ion source during the protonation of β-pinene. Sites of protonation have been associated with the corresponding structure. Energy levels are set relative to structure **1a** from Figure 6.4.

6.4 – Conclusion

The unimolecular chemistry of the protonated bicyclic monoterpenes α-pinene and β-pinene were investigated using a combined experimental and theoretical approach, encompassing CID-MS/MS and density functional theory calculations. The CID breakdown experiments led to nearly identical fragmentation for both isomers, with subtle differences. Two prominent product ion pathways were observed at m/z 95 and 81, corresponding to the neutral losses of propene and isobutylene, respectively. Calculations revealed that the observed products for each protonated isomer were dependent upon the site of protonation. The α-isomer initially populates a slightly more stable structure which requires an initial transformation before reaching the reactive intermediate **1b**, whereas the β-isomer initially populates **1b** directly. This extra step may explain the two isomers' different relative fragment ion abundances.

6.5 – Chapter 6 References

(1) Cheng, A.; Lou, Y.; Mao, Y.; Lu, S.; Wang, L.; Chen, X. Plant Terpenoids: Biosynthesis and Ecological Functions. *J. Integr. Plant Biol.* **2007**, *49* (2), 179–186. https://doi.org/10.1111/j.1744-7909.2007.00395.x.

(2) Woodroffe, J.-D.; Lupton, D. V.; Garrison, M. D.; Nagel, E. M.; Siirila, M. J.; Harvey, B. G. Synthesis and Fuel Properties of High-Energy Density Cyclopropanated Monoterpenes. *Fuel Process. Technol.* **2021**, *222*, 106952. https://doi.org/10.1016/j.fuproc.2021.106952.

(3) De Alvarenga, J. F. R.; Genaro, B.; Costa, B. L.; Purgatto, E.; Manach, C.; Fiamoncini, J. Monoterpenes: Current Knowledge on Food Source, Metabolism, and Health Effects. *Crit. Rev. Food Sci. Nutr.* **2023**, *63* (10), 1352–1389. https://doi.org/10.1080/10408398.2021.1963945.

(4) Sarkic, A.; Stappen, I. Essential Oils and Their Single Compounds in Cosmetics—A Critical Review. *Cosmetics* **2018**, *5* (1), 11. https://doi.org/10.3390/cosmetics5010011.

(5) Koziol, A.; Stryjewska, A.; Librowski, T.; Salat, K.; Gawel, M.; Moniczewski, A.; Lochynski, S. An Overview of the Pharmacological Properties and Potential Applications of Natural Monoterpenes. *Mini-Rev. Med. Chem.* **2015**, *14* (14), 1156–1168. https://doi.org/10.2174/1389557514666141127145820.

(6) Nyamwihura, R. J.; Ogungbe, I. V. The Pinene Scaffold: Its Occurrence, Chemistry, Synthetic Utility, and Pharmacological Importance. *RSC Adv.* **2022**, *12* (18), 11346–11375. https://doi.org/10.1039/D2RA00423B.

(7) Salehi, B.; Upadhyay, S.; Erdogan Orhan, I.; Kumar Jugran, A.; L.D. Jayaweera, S.; A. Dias, D.; Sharopov, F.; Taheri, Y.; Martins, N.; Baghalpour, N.; C. Cho, W.; Sharifi-Rad, J. Therapeutic Potential of α- and β-Pinene: A Miracle Gift of Nature. *Biomolecules* **2019**, *9* (11), 738. https://doi.org/10.3390/biom9110738.

(8) Acosta Navarro, J. C.; Smolander, S.; Struthers, H.; Zorita, E.; Ekman, A. M. L.; Kaplan, J. O.; Guenther, A.; Arneth, A.; Riipinen, I. Global Emissions of Terpenoid VOCs from Terrestrial Vegetation in the Last Millennium. *J. Geophys. Res. Atmospheres* **2014**, *119* (11), 6867–6885. https://doi.org/10.1002/2013JD021238.

(9) Iyer, S.; Rissanen, M. P.; Valiev, R.; Barua, S.; Krechmer, J. E.; Thornton, J.; Ehn, M.; Kurtén, T. Molecular Mechanism for Rapid Autoxidation in α-Pinene Ozonolysis. *Nat. Commun.* **2021**, *12* (1), 878. https://doi.org/10.1038/s41467-021-21172-w.

(10) Peeters, J.; Vereecken, L.; Fantechi, G. The Detailed Mechanism of the OH-Initiated Atmospheric Oxidation of α-Pinene: A Theoretical studyElectronic Supplementary Information Available. See Http:/Sol;Www.Rsc.Org/Suppdata/Cp/B1/B106555f/. This Information Is Also Available Directly from the Authors at Http://Arrhenius.Chem.Kuleuven.Ac.Be/Labpeeters. *Phys. Chem. Chem. Phys.* **2001**, *3* (24), 5489–5504. https://doi.org/10.1039/b106555f.

(11) Ma, S. X.; Rindelaub, J. D.; McAvey, K. M.; Gagare, P. D.; Nault, B. A.; Ramachandran, P. V.; Shepson, P. B. α-Pinene Nitrates: Synthesis, Yields and Atmospheric Chemistry. *Atmospheric Chem. Phys.* **2011**, *11* (13), 6337–6347. https://doi.org/10.5194/acp-11-6337-2011.

(12) Nah, T.; Sanchez, J.; Boyd, C. M.; Ng, N. L. Photochemical Aging of α-Pinene and β-Pinene Secondary Organic Aerosol Formed from Nitrate Radical Oxidation. *Environ. Sci. Technol.* **2016**, *50* (1), 222–231. https://doi.org/10.1021/acs.est.5b04594.

(13) Zhang, D.; Zhang, R. Ozonolysis of α-Pinene and β-Pinene: Kinetics and Mechanism. *J. Chem. Phys.* **2005**, *122* (11), 114308. https://doi.org/10.1063/1.1862616.

(14) Liggio, J.; Li, S.; Brook, J. R.; Mihele, C. Direct Polymerization of Isoprene and A-pinene on Acidic Aerosols. *Geophys. Res. Lett.* **2007**, *34* (5), 2006GL028468. https://doi.org/10.1029/2006GL028468.

(15) Liu, Z.; Ge, M.; Yin, S.; Wang, W. Uptake and Reaction Kinetics of α-Pinene and β-Pinene with Sulfuric Acid Solutions. *Chem. Phys. Lett.* **2010**, *491* (4–6), 146–150. https://doi.org/10.1016/j.cplett.2010.04.004.

(16) Dhooghe, F.; Amelynck, C.; Rimetz-Planchon, J.; Schoon, N.; Vanhaecke, F. FA-SIFT Study of Reactions of Protonated Water and Ethanol Clusters with α-Pinene and Linalool in View of Their Selective Detection by CIMS. *Int. J. Mass Spectrom.* **2010**, *290* (2–3), 106–112. https://doi.org/10.1016/j.ijms.2009.12.010.

(17) Poštulka, J.; Slavíček, P.; Domaracka, A.; Pysanenko, A.; Fárník, M.; Kočišek, J. Proton Transfer from Pinene Stabilizes Water Clusters. *Phys. Chem. Chem. Phys.* **2019**, *21* (26), 13925–13933. https://doi.org/10.1039/C8CP05959D.

(18) Tu, Y.-P. Dissociative Protonation Sites: Reactive Centers in Protonated Molecules Leading to Fragmentation in Mass Spectrometry. *J. Org. Chem.* **2006**, *71* (15), 5482–5488. https://doi.org/10.1021/jo060439v.

(19) Hu, N.; Tu, Y.-P.; Liu, Y.; Jiang, K.; Pan, Y. Dissociative Protonation and Proton Transfers: Fragmentation of α, β-Unsaturated Aromatic Ketones in Mass Spectrometry. *J. Org. Chem.* **2008**, *73* (9), 3369–3376. https://doi.org/10.1021/jo702464b.

(20) Tani, A.; Hayward, S.; Hewitt, C. N. Measurement of Monoterpenes and Related Compounds by Proton Transfer Reaction-Mass Spectrometry (PTR-MS). *Int. J. Mass Spectrom.* **2003**, *223–224*, 561–578. https://doi.org/10.1016/S1387-3806(02)00880-1.

(21) Misztal, P. K.; Heal, M. R.; Nemitz, E.; Cape, J. N. Development of PTR-MS Selectivity for Structural Isomers: Monoterpenes as a Case Study. *Int. J. Mass Spectrom.* **2012**, *310*, 10–19. https://doi.org/10.1016/j.ijms.2011.11.001.

(22) White Buenger, E.; Mayer, P. M. Unraveling the Unimolecular Ion Chemistry of Protonated Isoprene and Prenol. *J. Am. Soc. Mass Spectrom.* **2024**, *35* (1), 31–39. https://doi.org/10.1021/jasms.3c00297.

(23) White Buenger, E.; Mansour, K.; Mayer, P. M. Exploring the Unimolecular Chemistry of Protonated Limonene and α-Terpineol. *Int. J. Mass Spectrom.* **2024**, *498*, 117204. https://doi.org/10.1016/j.ijms.2024.117204.

(24) Buenger, E. W.; Mayer, P. M. Where You Protonate Matters: Deciphering the Unimolecular Chemistry of Protonated Myrcene and Linalool. *J. Mass Spectrom.* **2024**, *59* (10), e5096. https://doi.org/10.1002/jms.5096.

(25) Frisch, M. J.; Trucks, G. W.; Schlegel, H. B.; Scuseria, G. E.; Robb, M. A.; Cheeseman, J. R.; Scalmani, G.; Barone, V.; Petersson, G. A.; Nakatsuji, H.; Li, X.; Caricato, M.; Marenich, A. V.; Bloino, J.; Janesko, B. G.; Gomperts, R.; Mennucci, B.; Hratchian, H. P.; Ortiz, J. V.; Izmaylov, A. F.; Sonnenberg, J. L.; Williams; Ding, F.; Lipparini, F.; Egidi, F.; Goings, J.; Peng, B.; Petrone, A.; Henderson, T.; Ranasinghe, D.; Zakrzewski, V. G.; Gao, J.; Rega, N.; Zheng, G.; Liang, W.; Hada, M.; Ehara, M.; Toyota, K.; Fukuda, R.; Hasegawa, J.; Ishida, M.; Nakajima, T.; Honda, Y.; Kitao, O.;

Nakai, H.; Vreven, T.; Throssell, K.; Montgomery Jr., J. A.; Peralta, J. E.; Ogliaro, F.; Bearpark, M. J.; Heyd, J. J.; Brothers, E. N.; Kudin, K. N.; Staroverov, V. N.; Keith, T. A.; Kobayashi, R.; Normand, J.; Raghavachari, K.; Rendell, A. P.; Burant, J. C.; Iyengar, S. S.; Tomasi, J.; Cossi, M.; Millam, J. M.; Klene, M.; Adamo, C.; Cammi, R.; Ochterski, J. W.; Martin, R. L.; Morokuma, K.; Farkas, O.; Foresman, J. B.; Fox, D. J. Gaussian 16 Rev. C.01, 2016.

(26) Becke, A. D. Density-functional Thermochemistry. III. The Role of Exact Exchange. *J. Chem. Phys.* **1993**, *98* (7), 5648–5652. https://doi.org/10.1063/1.464913.

(27) Lee, C.; Yang, W.; Parr, R. G. Development of the Colle-Salvetti Correlation-Energy Formula into a Functional of the Electron Density. *Phys. Rev. B* **1988**, *37* (2), 785–789. https://doi.org/10.1103/PhysRevB.37.785.

(28) Ochterski, J. W.; Petersson, G. A.; Montgomery, J. A. A Complete Basis Set Model Chemistry. V. Extensions to Six or More Heavy Atoms. *J. Chem. Phys.* **1996**, *104* (7), 2598–2619. https://doi.org/10.1063/1.470985.

(29) Montgomery, J. A.; Frisch, M. J.; Ochterski, J. W.; Petersson, G. A. A Complete Basis Set Model Chemistry. VI. Use of Density Functional Geometries and Frequencies. *J. Chem. Phys.* **1999**, *110* (6), 2822–2827. https://doi.org/10.1063/1.477924.

Chapter 7 – Isoprene Pyrolysis

Based on the publication Buenger, E. W.; Bodi, A.; Burgos-Paci, M. A.; Mayer, P. M. Cyclopentene and Cyclopentadiene Formation in Isoprene Pyrolysis. *Phys. Chem. Chem. Phys.* **2024**, *26* (36), 23971–23978. https://doi.org/10.1039/D4CP02798A.

Contribution Statement

E. White Buenger processed the data, performed computational studies, and prepared the manuscript for submission. A. Bodi performed the experiments and offered technical support as part of the SLS facility. P. M. Mayer conceptualized the idea and supervised the work. All authors contributed towards revisions of the submitted manuscript.

7.1 – Introduction

Isoprene (2-methyl-1,3-butadiene) is a reactive volatile substance of relevance in phytochemistry, atmospheric and industrial chemistry,[1–3] and has been identified as the most abundant non-methane biogenic volatile organic compound (BVOC), making up approximately 500 Tg carbon yr^{-1} out of the total 1150 Tg carbon yr^{-1} emissions, single-handedly representing nearly half of the atmospheric carbon flux.[4,5] The reactions involved in the consumption of isoprene in the atmosphere are not fully understood; however, evidence has shown that they are dominantly oxidized by atmospheric oxidants, such as the hydroxyl radical and NO_x/SO_x species.[6] Wildfires also contribute to natural VOC emissions; of the four phases involved in the burning of biomass, the initial distillation phase has been shown to release terpenes, including isoprene.[7] In addition to the natural processes described, there are also substantial anthropogenic isoprene sources. The most prevalent synthetic use of isoprene is in the synthesis of rubbers for tires and other polymers,[8] and it has also been identified as a key component in the manufacturing process of certain biofuels and biologically derived rubbers.[9–11] In the light of the natural isoprene combustion in wildfires and the controlled pyrolysis of polymeric isoprene, there is a clear need for understanding how isoprene breaks apart at high temperatures. Also, from a fundamental point of view, understanding the thermal decomposition mechanism of isoprene is challenging because of the multitude of reaction channels available due to the presence of conjugated double bonds.

Early studies on isoprene pyrolysis were primarily interested in identifying carcinogenic components of cigarette smoke.[12–14] More recently, mechanistic studies have been published addressing the unimolecular thermal decomposition of isoprene, instead of the bimolecular formation of larger hydrocarbons polycyclic aromatic hydrocarbons (PAHs). Weber and Zhang performed pyrolysis experiments at varying temperatures and identified the products using vacuum ultraviolet single-photon ionization time-of-flight mass spectrometry at 10.48 eV.[15] They observed ions at m/z 78, 68, 53, 52, in the range of m/z 42–39, at m/z 28, and 15, with the abundance of each varying as a function of pyrolysis temperature.[15] These peaks in the mass spectra were assigned molecular identities, which were then supported with quantum chemical reaction path calculations leading to the assumed pyrolysis products.[15] Grajales-González *et al.* developed a kinetic model on the pyrolysis of isoprene based on the available literature and their experimental work using shock tube pyrolysis and jet-stirred reactors, supported by theoretical calculations.[16] The shock tube reaction products were deduced by GC-FID after the experiment. Chen *et al.* also published a kinetic model to describe the temperature-dependence of isoprene pyrolysis reactions, based on isoprene pyrolysis in a flow tube reactor and product analysis using (dissociative) photoionization.[17] Through a combination of interpreting their experimental results with computational chemistry and a collection of rate constants derived from the literature, they were able to develop a computational model that described the thermal breakdown of isoprene comparable to the model developed by Grajales-Gonzales *et al.*[16,17] The molecular assignments were based on IE values. As the experimental photoionization spectra forming the basis of the assignment have not been published, it is difficult to follow the reasoning of the authors. This is particularly concerning because the interpretation of photoionization spectra is hampered when multiple species may be present, or when dissociative ionization of higher m/z ions also contributes to lower m/z peaks.

We have employed imaging photoelectron photoion spectroscopy (iPEPICO)[18,19] to transcend these experimental limitations and identify the early unimolecular pyrolysis products of isoprene unambiguously. iPEPICO is known for its ability to separate and identify isomeric species based on their IE and photoelectron spectra,[20] and to separate molecular ionization from ion dissociative processes.[21,22]

7.2 – Methods

The experiments were carried out at the Swiss Light Source (SLS, Paul Scherrer Institut, Villigen, Switzerland) using the imaging photoelectron photoion coincidence endstation (CRF-PEPICO) at the VUV beamline, the details of which have been described thoroughly elsewhere,[18,19] and a scheme describing the experiment and the data collected has been published by Bodi *et al.*[23] Pyrolysis was carried out using the high-temperature pyrolysis microreactor previously described for this endstation.[24] Synchrotron radiation was dispersed using a 150 grooves/mm grating with 5 meV energy resolution. The higher harmonics of the grating were filtered out using a differentially pumped gas filter filled with 9 mbar of a Ne:Ar mixture over 10 cm optical length. The resulting monochromatic VUV radiation photoionized molecules in a 2×2 mm^2 interaction region. Both photoions and photoelectrons were velocity-mapped on imaging RoentDek delay line detectors. The electrons were time- and position-stamped at the detector, and the delayed, coincident photoion signal was evaluated to obtain the time-of-flight mass spectrum. Threshold photoelectrons are detected at the centre of the electron detector, whereas non-zero-kinetic energy ("hot") electrons are detected according to their off-axis momentum. Hot electrons without an initial lateral momentum component also have a trajectory to hit the centre spot. The mass spectrum based on electrons detected in a ring around the centre spot was used to subtract the hot electron contamination from the centre signal and obtain the threshold photoionization mass spectrum.[25] Plotting the normalized intensity of a peak with a particular m/z ratio from the threshold ionization mass spectra as a function of photon energy yields the photoion mass-selected TPES (ms-TPES).[20]

Pyrolysis experiments were performed by passing argon, at a pressure of 1 bar and a flow rate of 1 standard cubic centimetres per minute (sccm), over a vial containing isoprene at room temperature. The room temperature vapor pressure of isoprene is ca. 780 mbar.[26] This mixture was then diluted with 20 sccm of argon to produce a beam with approximately 2.5% isoprene, which expanded through a 200 μm pinhole into the 3 cm long, 1 mm internal diameter, resistively heated SiC pyrolysis microreactor. Reactor surface temperatures have been derived based on a previously observed power dependence measured in an identical pyrolysis setup by a type C thermocouple, defined by the equation below:

$$T/^{\circ}\mathrm{C} = P/\mathrm{W} \times 14.27 + 303$$

Where T is the reactor temperature and P is the heating power. The reactor temperature is considered to represent the gas temperature inside the reactor to within 100 ºC.[27] The pressure and residence time in the reactor has been estimated to be 10–40 mbar and up to 100 μs, respectively.[27,28] The reactor is placed in the source vacuum chamber, where the pressure was ~ 5×10^{-5} mbar during measurements. The molecular beam exiting the pyrolysis reactor passed through a 2 mm diameter skimmer into the detection chamber, kept at a pressure of 10^{-6} mbar during measurements. The reactor can be heated to temperatures between 200 and 2000 °C to explore the distribution of pyrolysis products as a function of temperature by recording the ms-TPES of the pyrolysis products. Isoprene was studied at 1400 °C.

Rovibrational cooling in the expansion from such microreactors has been found to be limited,[29] because of the low preexpansion pressure at the reactor nozzle.[27] The total ionization signal is therefore due in part to the barely cooled molecular beam and in part to room-temperature species that underwent collisional cooling in the ionization chamber. These fractions are typically commensurate, which leads to an intermediate "effective temperature" as far as the internal energy distribution of the sample is concerned. Furthermore, previous studies with these types of reactors have concluded that the role of unimolecular vs. bimolecular reactions is largely molecule-dependent, with bimolecular reactions increasing with sample pressure. Reactions involving 0.2% propionic acid in argon and 0.3% furfural in helium gave results consistent with primarily unimolecular chemistry,[30,31] while benzaldehyde pyrolysis at similar concentrations evidenced bimolecular chemistry,[30] and so did analogous acetone pyrolysis experiments.[32] Our previous work on the pyrolysis of methyl-, ethyl- and methylchloroformate did not show evidence for a meaningful amount of bimolecular reactions.[21,22]

All structures were optimized using density functional theory (DFT) with B3LYP/6-311+G(d,p) level of theory using the Gaussian 16 software suite.[33] Franck–Condon (FC) simulations were carried out at the optimized geometries for the pyrolysis products using Gaussian 16. Single-point energy calculations with the CBS-QB3 composite method[34,35] were carried out for improved energetics.

7.3 – Results and Discussion

Figures 7.1 and 7.2 summarize the mass-selected threshold photoelectron spectra (ms-TPES) obtained in isoprene pyrolysis. The all-electron mass spectrum at 12 eV photon energy and a pyrolysis temperature of 1400 °C is shown in Figure 7.3. The peaks at m/z 67 and 53 are dominant but are not due to the ionization of neutrals with 67 and 53 Da. Instead, they are the result of isoprene dissociative ionization at this photon energy.[36]

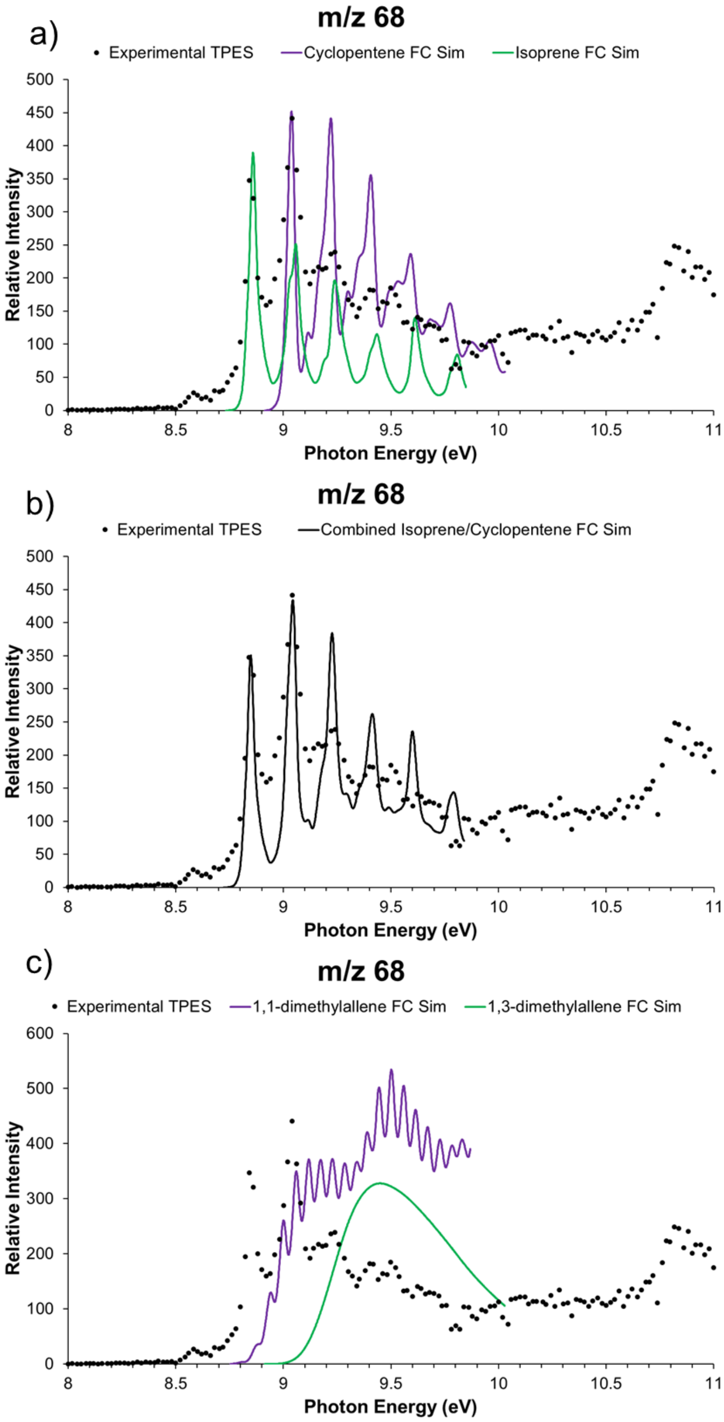

Figure 7.1: Mass-selected TPES for m/z 68 (data points). Franck–Condon simulations (solid lines with the origin transition shifted to 8.85 and 9.01 eV for isoprene and cyclopentadiene, respectively) show the contributions of (a) isoprene and cyclopentene, (b) the sum reproduction of the experimental spectrum. As shown in (c), dimethylallenes do not contribute to the ms-TPES above the photoionization detection limit.

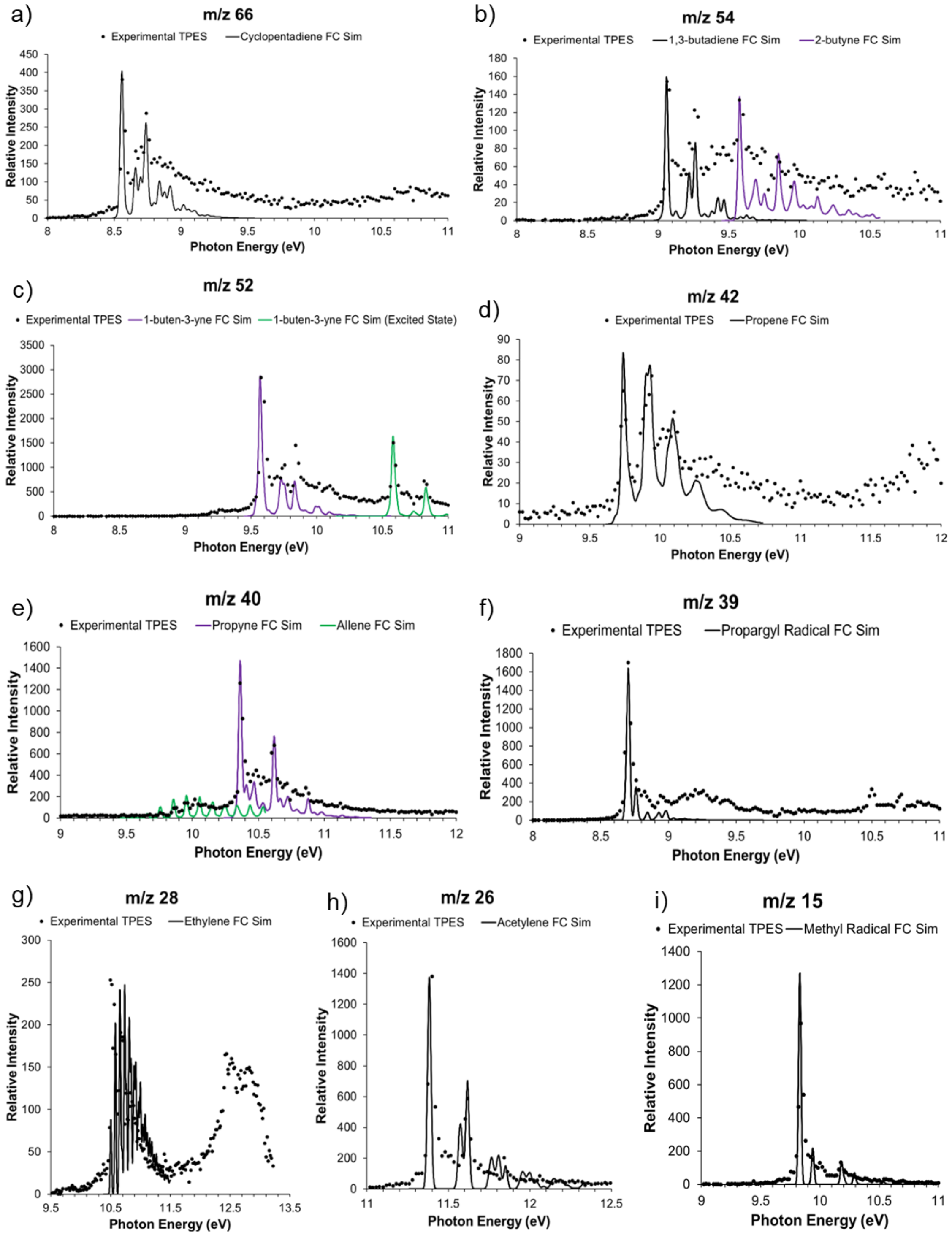

Figure 7.2: ms-TPES for all other species observed in this study. FC-simulations, overlaid in solid lines, have been adjusted to match the experimentally reported IEs in ref. 42.

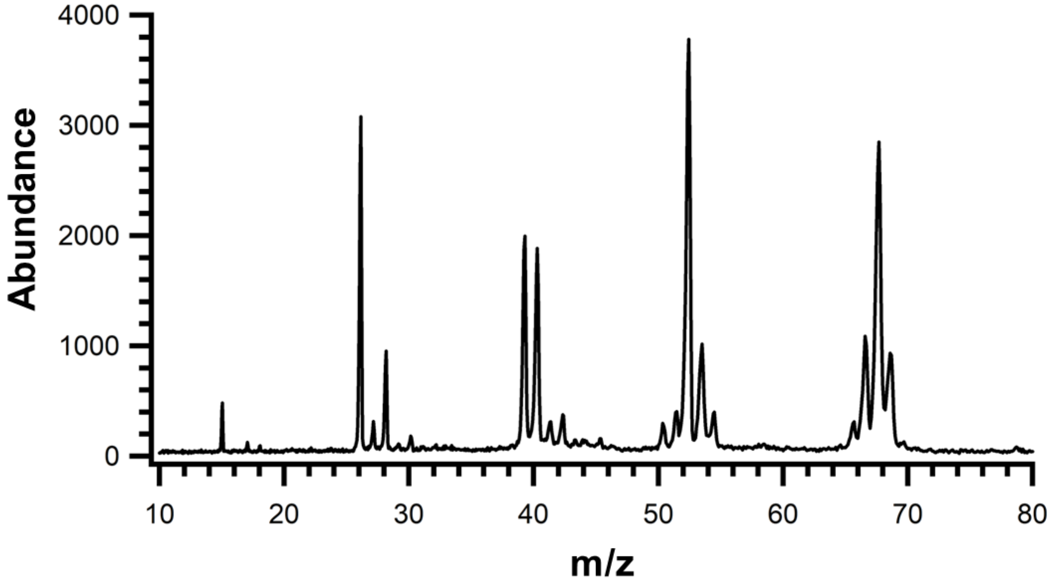

Figure 7.3: Mass spectrum at 1400 ºC and 12 eV photon energy in coincidence with all electrons (not only threshold ionization). Note that some ions, such as m/z 67 and 53, are dissociation products of m/z 68 and NOT due to the ionization of a neutral 67 Da species.

7.3.1 – m/z 68 and m/z 66

While it is tempting to assign m/z 68 to isoprene surviving the furnace, the ms-TPES strongly suggests the presence of a unimolecular isomerization product of isoprene, cyclopentene (Figure 7.1a). The most straightforward clue is that the Franck–Condon simulation of both isomers predicts the origin transition to be the strongest, but the second peak is the most intense in the recorded band. The photoelectron spectra of both isoprene[37] and cyclopentene[38] also display the origin band to be the most intense leaving no doubt as to the presence of two species. Assuming that the electronic oscillator strengths for threshold ionization into the ground electronic state of isoprene and cyclopentene are approximately equal, the spectrum indicates comparable abundances for isoprene and cyclopentene as carriers of the m/z 68 signal, as the sum of the two FC envelopes produces good agreement with the experimental spectrum (Figure 7.1b). This is the first time cyclopentene has been identified as a product in isoprene pyrolysis. Because of its large abundance, it is likely an important precursor in the formation of larger polycyclic aromatic hydrocarbons, as well.[13,14] According to the Active Thermochemical Tables,[39] isoprene is ca. 30 kJ mol^{-1} higher in energy than cyclopentene. Therefore, thermal equilibrium at 1000 K would imply a more than 30-fold excess of cyclopentene. Both isoprene and cyclopentene cations are stable with regard to fragmentation over an energy range of ca. 2 eV.[40] Therefore, dissociative ionization is unlikely to affect the detected abundances of even hot neutrals at the ionization onset. Instead, the comparable isoprene vs. cyclopentene abundance hints at kinetically hindered isomerization or, more likely, a comparably or even more important cyclopentene sink in the form of sequential pyrolysis reactions. Thus, cyclopentene detection suggests that it plays a crucial role in the unimolecular thermal decomposition of isoprene, at least until higher energy but also higher activation entropy processes from isoprene, e.g., bond cleavage outcompetes isomerization. Simple methyl radical loss from isoprene has been calculated to require 372 kJ mol^{-1},[15] so there is an internal energy window in which isomerization to cyclopentene will be competitive.

The comparison of the 1,1- and 1,3-dimethylallene FC spectra with the experimental ms-TPES shows that dimethylallenes are below the photoionization detection limit in the product distribution (Figure 7.1c). However, as their ionization energy lies higher than that of isoprene and cyclopentadiene, the detection limit is rather high. Enlisting alternative analytical tools to look for trace amounts of methylallenes would nevertheless likely be a futile endeavour, as these isomers are over 50 kJ mol^{-1} higher in energy than isoprene,[41] implying a vanishingly small abundance even in thermal equilibrium. While this does not preclude the participation of these isomers in the decomposition mechanism, it does call into question the assignment of these and related allene species in the pyrolysis of isoprene suggested by Weber and Zhang.[15] We calculated the energies of two further C_5H_8 isomers, which could easily be involved in the pyrolysis mechanism, methylcyclobutene and methylenecyclobutane, to lie 45 and 48 kJ mol^{-1} above isoprene, respectively. Thus, neither is likely to have significant concentrations even in thermal equilibrium. Evidence for cyclopentadiene formation (m/z 66 ms-TPES, Figure 7.2a) is also consistent with the involvement of cyclopentene as it is the primary pyrolysis product thereof by H_2 loss.[42]

Concerning the isomerization of isoprene to cyclopentene, Wellington determined that vinylcyclopropene preferentially rearranges to cyclopentene,[43] while Crane and Rose[44] studied the high-energy isomerization of vinylcyclopropane, and reported rate constants to pentadiene isomers as well. The simulated TPES for cis- and trans-1,3-pentadiene are not consistent with the experimental data, Figure 7.5. As cyclopentene is the most stable isomer by ca. 30 mol^{-1}, it will dominate the isomer distribution in thermal equilibrium. Indeed, the rate constants reported by Wellington for cyclopentene formation from vinylcyclopropane can be extrapolated to 1.3×10^7 s^{-1} at 1400 °C. Thus, if isoprene can rearrange to vinylcyclopropane, it will quantitatively yield cyclopentene. To search for the missing step, we explored the interconversion of isoprene to vinylcyclopropane and on to cyclopentene and cyclopentadiene computationally at the CBS-QB3(sp)//B3LYP/6-311+G(d,p) level of theory (Figure 7.4).

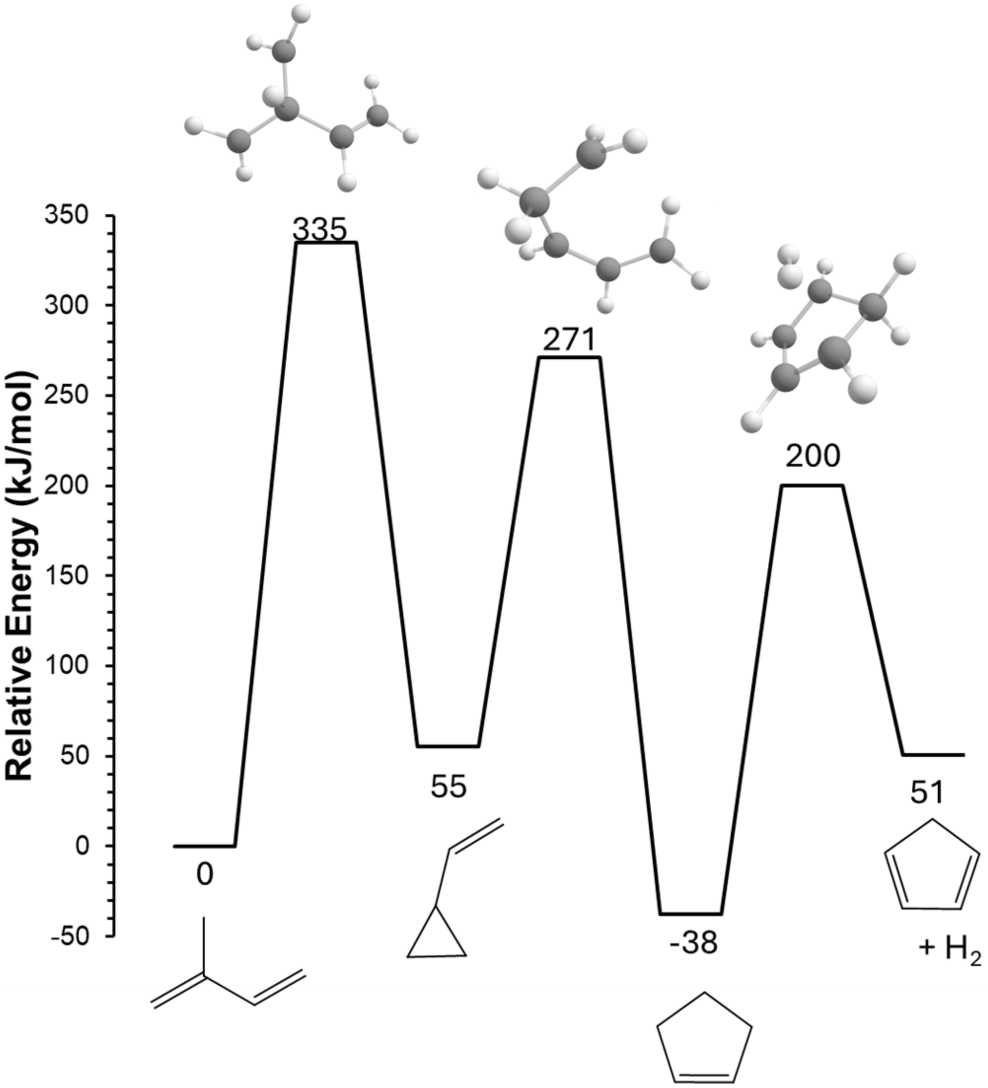

Figure 7.4: Minimum energy reaction pathway for the isomerization of isoprene to cyclopentene, and the subsequent H_2 elimination from the latter. CBS-QB3(sp)//B3LYP/6-311+G(d,p) level of theory.

The highest barrier in the process is the initial ring-closing of isoprene to vinylcyclopropane at 335 kJ mol^{-1} (80 kcal mol^{-1}), involving a 1,3-H-shift and ring-closing. This value is comparable to the threshold of the alternative isomerization pathways as calculated by Chen *et al.*[17] and is significantly lower than the decomposition product energies quoted in the literature. The vinylcyclopropane formed in this step is energetic enough that it will promptly ring-expand and rearrange into cyclopentene over a barrier of 216 kJ mol^{-1} relative to the vinylcyclopropane minimum. Thus, vinylcyclopropane is only a short-lived intermediate in this isomerization. Molecular hydrogen loss from cyclopentene also takes place over a barrier of only 238 kJ mol^{-1} with respect to cyclopentene, which, in absolute terms, lies lower than the other transition states in the mechanism. Therefore, in the low-pressure limit, this reaction path is expected to yield cyclopentadiene and hydrogen quantitatively. The fact that cyclopentene is observable along with cyclopentadiene (Figure 7.2a) suggests that the tight H_2-formation transition state leads to low enough dissociation rates so that cyclopentene can be collisionally rethermalized and stabilized in the reactor.

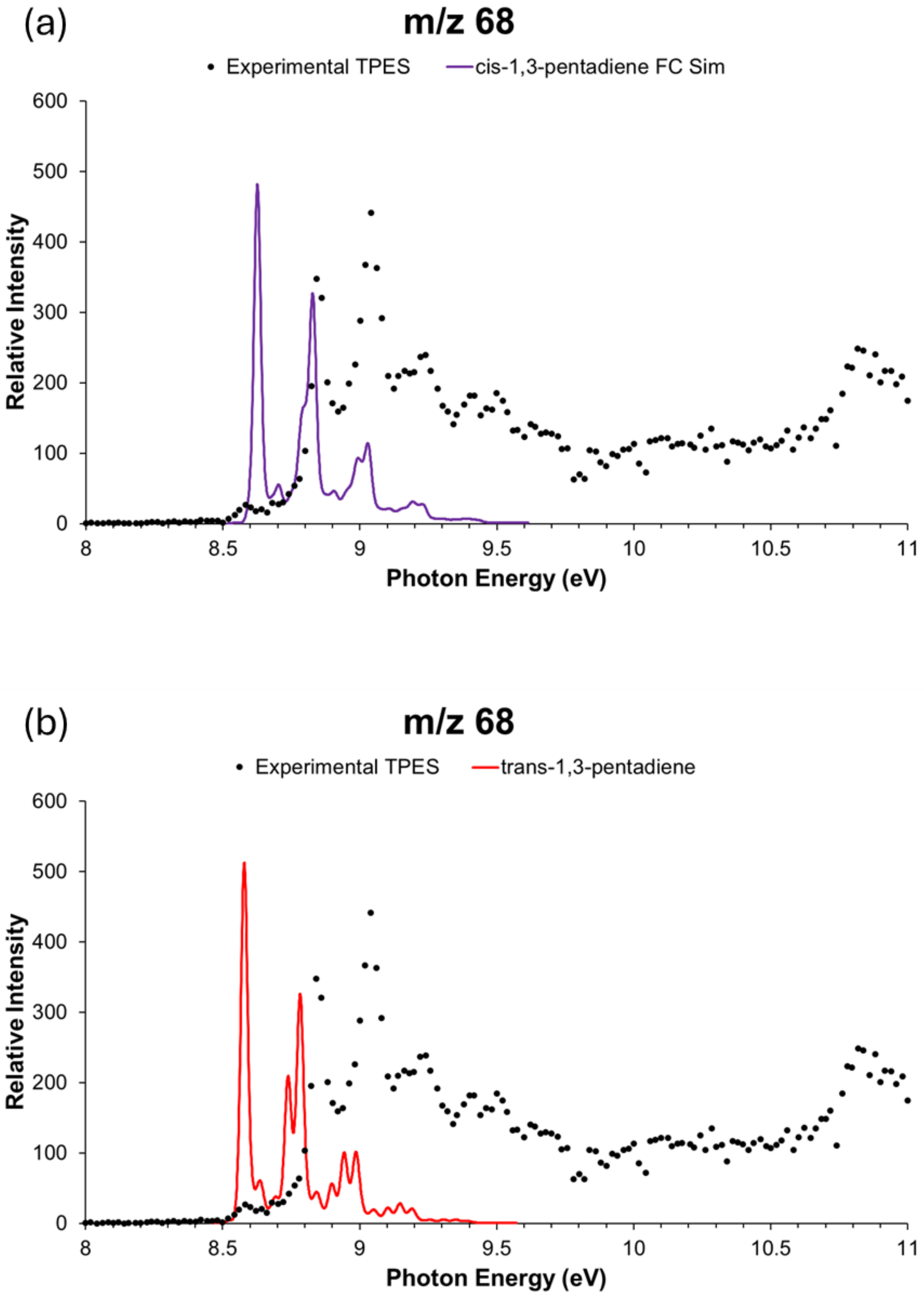

Figure 7.5: Comparison of the FC simulation for (a) cis- and (b) trans-1,3-pentadiene with the experimental ms-TPES of m/z 68. The FC simulations were moved to the experimentally-reported IE values.[42]

7.3.2 – C_1-C_4 Products

The ms-TPES in Figure 7.2b-f show many of the anticipated four and three carbon-containing products from isoprene pyrolysis. We observe 1,3-butadiene and 2-butyne (Figure 7.2b), but not 1-butyne or methylallene (Figure 7.6). The only 52 Da isomer we positively assign is 1-buten-3-yne (m/z 52 ms-TPES, Figure 7.2c) which displays both a ground and excited state vibrational structure in the ms-TPES. Again, there is neither evidence for the methylallenyl-H suggested by Weber and Zhang,[15] nor for 1,2,3-butatriene postulated by Chen and co-workers (Figure 7.7).[17] Figure 7.8 displays the optimized geometries of neutral 1-buten-3-yne together with its ground and first excited state ions. The main excitations in the ground state Franck–Condon simulation are two in-plane deformations of the ethene moiety centred at 9.75 eV and the asymmetric stretch of the linear portion of the molecule at ~ 9.85 eV. These are consistent with the change in geometry upon ionization (Figure 7.8) which shows bond length changes around the substituted ethyne carbon atom. The excited state FC simulation shows one main excitation corresponding to the stretching of the C−H bond that goes from 1.087 Å to 1.098 Å in the excited state. There are fewer skeletal C−C bond length changes between the neutral and excited state than between the neutral and ground ion state.

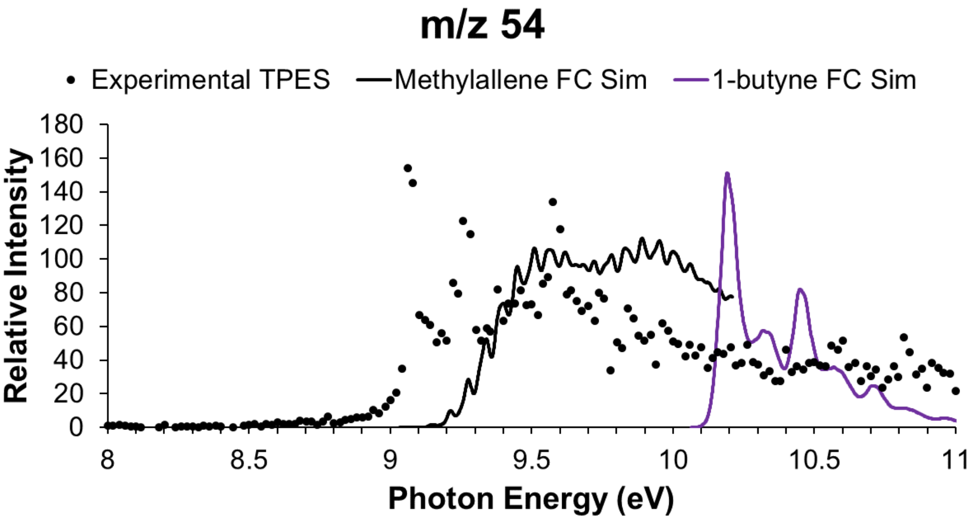

Figure 7.6: Comparison of the FC simulation for methylallene and 1-butyne with the experimental ms-TPES of m/z 54. The FC simulations were moved to the experimentally-reported IE values.[42]

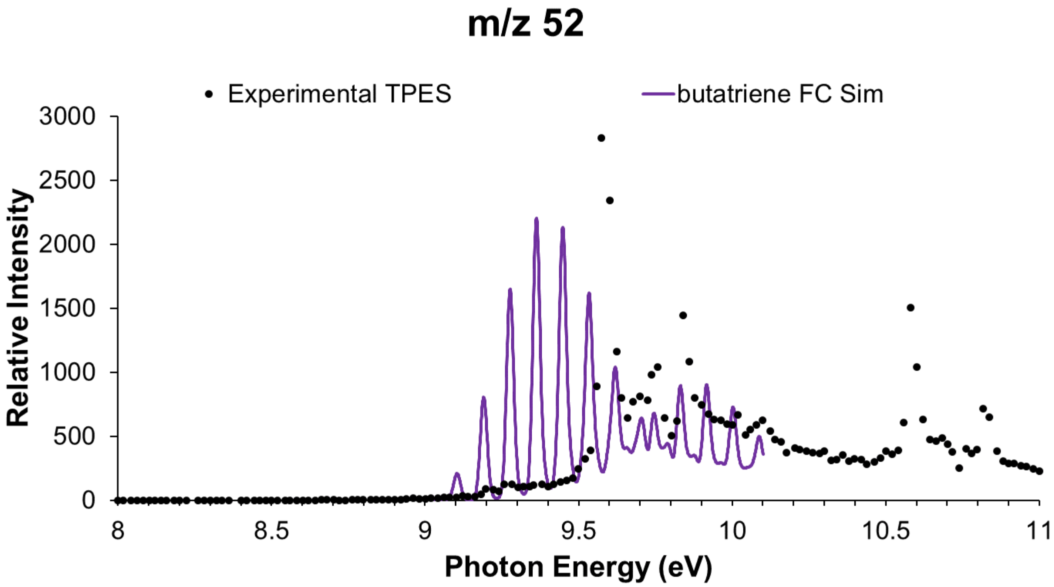

Figure 7.7: Comparison of the FC simulation for butatriene with the experimental ms-TPES of m/z 52. The simulation was adjusted to match the experimental IE of 9.14 eV reported in ref. 41.

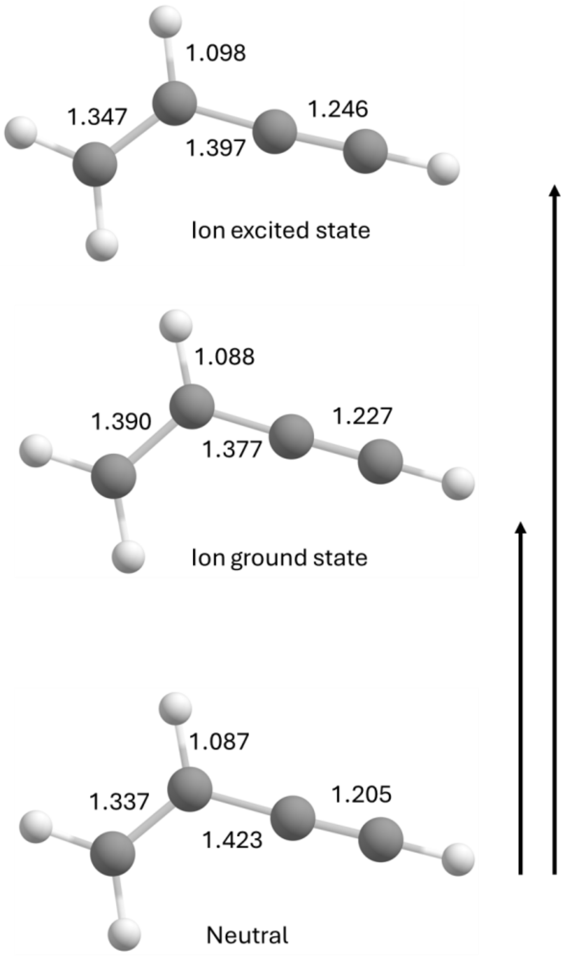

Figure 7.8: Optimized geometries of the neutral, ground ionic and excited ion states of 1-butene-3-yne. Bond lengths in Å.

Three-carbon-containing products include propene (Figure 7.2d, m/z 42 ms-TPES) and propyne (Figure 7.2e, m/z 40 ms-TPES) and only very weak evidence of allene (Figure 7.2e). Propyne is consistent with the co-observation of the propargyl radical (Figure 7.2f, m/z 39 ms-TPES). Two- and one-carbon species observed include the anticipated ethylene (Figure 7.2g, m/z 28 ms-TPES), acetylene (Figure 7.2h, m/z 26 ms-TPES), methane (Figure 7.9) and the methyl radical (Figure 7.2i, m/z 15 ms-TPES). In the ms-TPES of m/z 28, the broad band above 11.5 eV is due to dissociative ionization of a higher molecular weight species.[21,22]

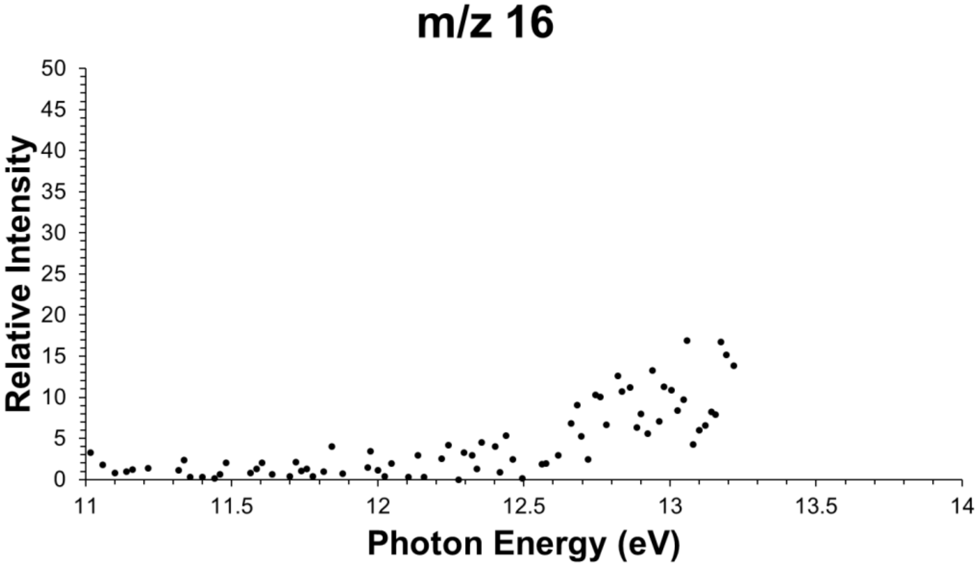

Figure 7.9: ms-TPES of m/z 16, suspected to be methane.

7.3.3 – Bimolecular Reactions

There is a minute m/z 78 signal suggestive of benzene formation (Figure 7.10), indicating that bimolecular reactions are not completely suppressed at the used sample dilution in the reactor. However, the general absence of heavier, energetically favored condensation products indicates that the overwhelming majority of the observed chemistry is due to unimolecular fragmentation in the pyrolysis reactor. Weber suggests that benzene formation is from the dimerization of C_3H_3 radicals, but this is unlikely in the present experiment in terms of the rate constant (1×10^{-12} cm^3 $molec^{-1}$ s^{-1}), radical density (ca. 10^{14} molecules cm^{-3}) and time scale of the experiment.

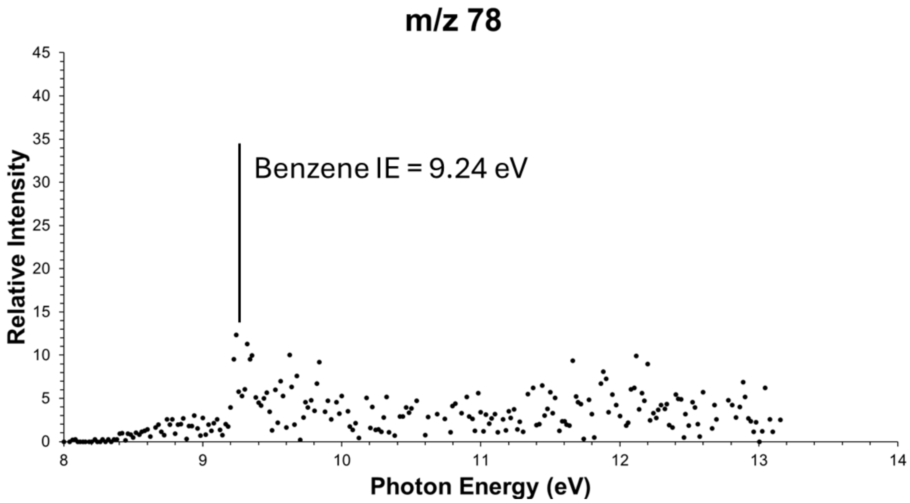

Figure 7.10: ms-TPES of m/z 78, suspected to contain benzene.

7.3.4 – Reaction Summary

In summary, based on the experimentally observed mass-selected TPES, it has been demonstrated that a major unimolecular route in the pyrolysis of isoprene is isomerization, via vinylcyclopropane, to cyclopentene. Cyclopentene is then responsible for the observation of cyclopentadiene.

R1.

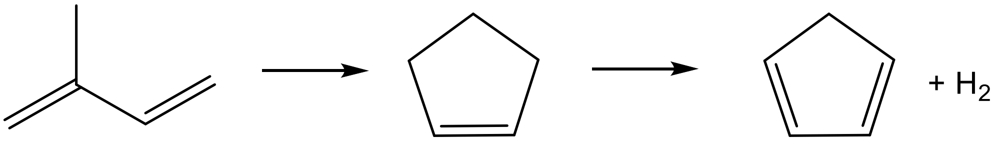

isoprene (m/z 68) cyclopentene (m/z 68) cyclopentadiene (m/z 66)

Isoprene itself can also fragment into the C_1–C_4 products, ostensibly by pathways related to the formation of the observed products (ms-TPES m/z listed). Given that loss of neutral CH_2 is energetically unlikely, it is more likely m/z 54 results from the loss of CH_3 (see R2) followed by H addition (R3).

R2. $C_5H_8 \rightarrow CH_3$ (*m*/*z* 15) + C_4H_5 (*m*/*z* 53)

R3. $C_4H_5 + H \rightarrow C_4H_6$ (*m*/*z* 54, 1,3-butadiene and 2-butyne)

In the mass spectrum, m/z 53 is dominated by the dissociation of the isoprene radical cation and between this and presumably fast H addition, its ms-TPES could not be discerned due to a low concentration.

R4. $C_5H_8 \rightarrow CH_4$ (*m*/*z* 16) + C_4H_4 (*m*/*z* 52, 1-butene-3-yne)

R5. $C_5H_8 \rightarrow C_2H_2$ (*m*/*z* 26) + C_3H_6 (*m*/*z* 42, propene)

R6. $C_5H_8 \rightarrow C_2H_4$ (*m*/*z* 28) + C_3H_4 (*m*/*z* 40, propyne)

R7. $C_5H_8 \rightarrow C_2H_5 + C_3H_3$ (*m*/*z* 39, propargyl radical)

The ethyl radical exhibits a broad, ill-defined TPES,[45] due to the large geometry change that occurs upon ionization and is difficult to discern in the current experiment.

7.4 – Conclusion

Photoion mass-selected threshold photoelectron spectra recorded by photoelectron photoion coincidence spectroscopy for the thermal decomposition products of isoprene identified a major, but previously unobserved, reaction, the isomerization of isoprene to cyclopentene. A mechanism for the interconversion, via vinylcyclopropane, was calculated and found to be energetically consistent with the energy demands calculated for other decomposition mechanisms by Chen et al.[17] In contrast to previous assignments, no allene-derived species (dimethylallene, methylallene, allene) were observed in the threshold photoelectron spectra. 1-buten-3-yne was found to be the only significant product with 52 Da and its ms-TPES also displayed bands due to the first excited state of the molecule. Several other previously hypothesized products were not observed, either, leading to a simplified picture of the potential reactions (see R1-R7). We believe the current results provide a more definitive assignment of the pyrolysis products and that previously derived kinetic models of the thermal degradation of isoprene need to be revisited.

7.5 – Chapter 7 References

(1) Monson, R. K.; Weraduwage, S. M.; Rosenkranz, M.; Schnitzler, J.-P.; Sharkey, T. D. Leaf Isoprene Emission as a Trait That Mediates the Growth-Defense Tradeoff in the Face of Climate Stress. *Oecologia* **2021**, *197* (4), 885–902. https://doi.org/10.1007/s00442-020-04813-7.

(2) DiMaria, C. A.; Jones, D. B. A.; Worden, H.; Bloom, A. A.; Bowman, K.; Stavrakou, T.; Miyazaki, K.; Worden, J.; Guenther, A.; Sarkar, C.; Seco, R.; Park, J.; Tota, J.; Alves, E. G.; Ferracci, V. Optimizing the Isoprene Emission Model MEGAN With Satellite and Ground-Based Observational Constraints. *J. Geophys. Res. Atmospheres* **2023**, *128* (4), e2022JD037822. https://doi.org/10.1029/2022JD037822.

(3) Batten, R.; Karanjikar, M.; Spatari, S. Bio-Based Polyisoprene Can Mitigate Climate Change and Deforestation in Expanding Rubber Production. *Fermentation* **2021**, *7* (4), 204. https://doi.org/10.3390/fermentation7040204.

(4) Guenther, A. B.; Jiang, X.; Heald, C. L.; Sakulyanontvittaya, T.; Duhl, T.; Emmons, L. K.; Wang, X. The Model of Emissions of Gases and Aerosols from Nature Version 2.1 (MEGAN2.1): An Extended and Updated Framework for Modeling Biogenic Emissions. *Geosci. Model Dev.* **2012**, *5* (6), 1471–1492. https://doi.org/10.5194/gmd-5-1471-2012.

(5) Santos, F.; Longo, K.; Guenther, A.; Kim, S.; Gu, D.; Oram, D.; Forster, G.; Lee, J.; Hopkins, J.; Brito, J.; Freitas, S. Biomass Burning Emission Disturbances of Isoprene Oxidation in a Tropical Forest. *Atmospheric Chem. Phys.* **2018**, *18* (17), 12715–12734. https://doi.org/10.5194/acp-18-12715-2018.

(6) Wennberg, P. O.; Bates, K. H.; Crounse, J. D.; Dodson, L. G.; McVay, R. C.; Mertens, L. A.; Nguyen, T. B.; Praske, E.; Schwantes, R. H.; Smarte, M. D.; St Clair, J. M.; Teng, A. P.; Zhang, X.; Seinfeld, J. H. Gas-Phase Reactions of Isoprene and Its Major Oxidation Products. *Chem. Rev.* **2018**, *118* (7), 3337–3390. https://doi.org/10.1021/acs.chemrev.7b00439.

(7) Sekimoto, K.; Koss, A. R.; Gilman, J. B.; Selimovic, V.; Coggon, M. M.; Zarzana, K. J.; Yuan, B.; Lerner, B. M.; Brown, S. S.; Warneke, C.; Yokelson, R. J.; Roberts, J. M.; De Gouw, J. High- and Low-Temperature Pyrolysis Profiles Describe

Volatile Organic Compound Emissions from Western US Wildfire Fuels. *Atmospheric Chem. Phys.* **2018**, *18* (13), 9263–9281. https://doi.org/10.5194/acp-18-9263-2018.

(8) Isikgor, F. H.; Becer, C. R. Lignocellulosic Biomass: A Sustainable Platform for the Production of Bio-Based Chemicals and Polymers. *Polym. Chem.* **2015**, *6* (25), 4497–4559. https://doi.org/10.1039/C5PY00263J.

(9) Melis, A. Photosynthesis-to-Fuels: From Sunlight to Hydrogen, Isoprene, and Botryococcene Production. *Energy Env. Sci* **2012**, *5* (2), 5531–5539. https://doi.org/10.1039/C1EE02514G.

(10) Wang, S.; Wang, Z.; Wang, Y.; Nie, Q.; Yi, X.; Ge, W.; Yang, J.; Xian, M. Production of Isoprene, One of the High-Density Fuel Precursors, from Peanut Hull Using the High-Efficient Lignin-Removal Pretreatment Method. *Biotechnol. Biofuels* **2017**, *10* (1), 297. https://doi.org/10.1186/s13068-017-0988-5.

(11) Riazi, B.; Karanjikar, M.; Spatari, S. Renewable Rubber and Jet Fuel from Biomass: Evaluation of Greenhouse Gas Emissions and Land Use Trade-Offs in Energy and Material Markets. *ACS Sustain. Chem. Eng.* **2018**, *6* (11), 14414–14422. https://doi.org/10.1021/acssuschemeng.8b03098.

(12) Gil-Av, E.; Shabtai, J. Precursors of Carcinogenic Hydrocarbons in Tobacco Smoke. *Nature* **1963**, *197* (4872), 1065–1066. https://doi.org/10.1038/1971065a0.

(13) Badger, G. M.; Donnelly, J. K.; Spotswood, T. M. The Formation Of Aromatic Hydrocarbons At High Temperatures. *Aust. J. Chem.* **1966**, *19* (6), 1023–1043.

(14) Oro, Juan.; Han, Jerry.; Zlatkis, Albert. Application of High-Resolution Gas Chromatography-Mass Spectrometry to the Analysis of the Pyrolysis Products of Isoprene. *Anal. Chem.* **1967**, *39* (1), 27–32. https://doi.org/10.1021/ac60245a035.

(15) Weber, K. H.; Zhang, J. Mechanistic Study of Thermal Decomposition of Isoprene (2-Methyl-1,3-Butadiene) Using Flash Pyrolysis Supersonic Jet VUV Photoionization Mass Spectrometry. *J. Phys. Chem. A* **2007**, *111* (45), 11487–11492. https://doi.org/10.1021/jp075689+.

(16) Grajales-González, E.; Kukkadapu, G.; Nagaraja, S. S.; Shao, C.; Monge-Palacios, M.; Chavarrio, J. E.; Wagnon, S. W.; Curran, H. J.; Pitz, W. J.; Mani Sarathy, S. An Experimental and Kinetic Modeling Study of the Pyrolysis of Isoprene, a Significant

Biogenic Hydrocarbon in Naturally Occurring Vegetation Fires. *Combust. Flame* **2022**, *242*, 112206. https://doi.org/10.1016/j.combustflame.2022.112206.

(17) Chen, G.; Ding, W.; Cheng, Z.; Wang, J.; Xing, L.; Li, W.; He, Y.; Lin, F.; Yang, J.; Zhao, L.; Yan, B. Experimental and Kinetic Modeling Studies of Isoprene Pyrolysis at Low and Atmospheric Pressures. *Combust. Flame* **2022**, *246*, 112445. https://doi.org/10.1016/j.combustflame.2022.112445.

(18) Bodi, A.; Hemberger, P.; Gerber, T.; Sztáray, B. A New Double Imaging Velocity Focusing Coincidence Experiment: *I* 2PEPICO. *Rev. Sci. Instrum.* **2012**, *83* (8), 083105. https://doi.org/10.1063/1.4742769.

(19) Sztáray, B.; Voronova, K.; Torma, K. G.; Covert, K. J.; Bodi, A.; Hemberger, P.; Gerber, T.; Osborn, D. L. CRF-PEPICO: Double Velocity Map Imaging Photoelectron Photoion Coincidence Spectroscopy for Reaction Kinetics Studies. *J. Chem. Phys.* **2017**, *147* (1), 013944. https://doi.org/10.1063/1.4984304.

(20) Hemberger, P.; Bodi, A.; Bierkandt, T.; Köhler, M.; Kaczmarek, D.; Kasper, T. Photoelectron Photoion Coincidence Spectroscopy Provides Mechanistic Insights in Fuel Synthesis and Conversion. *Energy Fuels* **2021**, *35* (20), 16265–16302. https://doi.org/10.1021/acs.energyfuels.1c01712.

(21) Lowe, B.; Cardona, A. L.; Salas, J.; Bodi, A.; Burgos Paci, M. A.; Mayer, P. M. Probing the Pyrolysis of Methyl Formate in the Dilute Gas Phase by Synchrotron Radiation and Theory. *J. Mass Spectrom.* **2022**, *57* (6), e4868. https://doi.org/10.1002/jms.4868.

(22) Lowe, B.; Cardona, A. L.; Bodi, A.; Mayer, P. M.; Burgos Paci, M. A. The Unimolecular Chemistry of Methyl Chloroformate Ions and Neutrals: A Story of Near-Threshold Decomposition. *J. Am. Soc. Mass Spectrom.* **2023**, *34* (12), 2831–2839. https://doi.org/10.1021/jasms.3c00334.

(23) Bodi, A.; Hemberger, P.; Pérez-Ramírez, J. Photoionization Reveals Catalytic Mechanisms. *Nat. Catal.* **2022**, *5* (10), 850–851. https://doi.org/10.1038/s41929-022-00847-7.

(24) Hemberger, P.; Custodis, V. B. F.; Bodi, A.; Gerber, T.; Van Bokhoven, J. A. Understanding the Mechanism of Catalytic Fast Pyrolysis by Unveiling Reactive

Intermediates in Heterogeneous Catalysis. *Nat. Commun.* **2017**, *8* (1), 15946. https://doi.org/10.1038/ncomms15946.

(25) Sztáray, B.; Baer, T. Suppression of Hot Electrons in Threshold Photoelectron Photoion Coincidence Spectroscopy Using Velocity Focusing Optics. *Rev. Sci. Instrum.* **2003**, *74* (8), 3763–3768. https://doi.org/10.1063/1.1593788.

(26) Acree, W. E.; Chickos, J., S. Phase Transition Enthalpy Measurements of Organic and Organometallic Compounds. In *NIST Chemistry WebBook, NIST Standard Reference Database Number 69,*; Linstrom, P. J., Mallard, W. G., Eds.; National Institute of Standards and Technology: Gaithersburg, MD, 20899.

(27) Guan, Q.; Urness, K. N.; Ormond, T. K.; David, D. E.; Barney Ellison, G.; Daily, J. W. The Properties of a Micro-Reactor for the Study of the Unimolecular Decomposition of Large Molecules. *Int. Rev. Phys. Chem.* **2014**, *33* (4), 447–487. https://doi.org/10.1080/0144235X.2014.967951.

(28) Grimm, S.; Baik, S.-J.; Hemberger, P.; Bodi, A.; Kempf, A. M.; Kasper, T.; Atakan, B. Gas-Phase Aluminium Acetylacetonate Decomposition: Revision of the Current Mechanism by VUV Synchrotron Radiation. *Phys. Chem. Chem. Phys.* **2021**, *23* (28), 15059–15075. https://doi.org/10.1039/D1CP00720C.

(29) Hemberger, P.; Wu, X.; Pan, Z.; Bodi, A. Continuous Pyrolysis Microreactors: Hot Sources with Little Cooling? New Insights Utilizing Cation Velocity Map Imaging and Threshold Photoelectron Spectroscopy. *J. Phys. Chem. A* **2022**, *126* (14), 2196–2210. https://doi.org/10.1021/acs.jpca.2c00766.

(30) Vasiliou, A. K.; Kim, J. H.; Ormond, T. K.; Piech, K. M.; Urness, K. N.; Scheer, A. M.; Robichaud, D. J.; Mukarakate, C.; Nimlos, M. R.; Daily, J. W.; Guan, Q.; Carstensen, H.-H.; Ellison, G. B. Biomass Pyrolysis: Thermal Decomposition Mechanisms of Furfural and Benzaldehyde. *J. Chem. Phys.* **2013**, *139* (10), 104310. https://doi.org/10.1063/1.4819788.

(31) Rogers, C. O.; Lockwood, K. S.; Nguyen, Q. L. D.; Labbe, N. J. Diol Isomer Revealed as a Source of Methyl Ketene from Propionic Acid Unimolecular Decomposition. *Int. J. Chem. Kinet.* **2021**, *53* (12), 1272–1284. https://doi.org/10.1002/kin.21532.

(32) Zaleski, D. P.; Sivaramakrishnan, R.; Weller, H. R.; Seifert, N. A.; Bross, D. H.; Ruscic, B.; Moore, K. B.; Elliott, S. N.; Copan, A. V.; Harding, L. B.; Klippenstein, S. J.; Field, R. W.; Prozument, K. Substitution Reactions in the Pyrolysis of Acetone Revealed through a Modeling, Experiment, Theory Paradigm. *J. Am. Chem. Soc.* **2021**, *143* (8), 3124–3142. https://doi.org/10.1021/jacs.0c11677.

(33) Frisch, M. J.; Trucks, G. W.; Schlegel, H. B.; Scuseria, G. E.; Robb, M. A.; Cheeseman, J. R.; Scalmani, G.; Barone, V.; Petersson, G. A.; Nakatsuji, H.; Li, X.; Caricato, M.; Marenich, A. V.; Bloino, J.; Janesko, B. G.; Gomperts, R.; Mennucci, B.; Hratchian, H. P.; Ortiz, J. V.; Izmaylov, A. F.; Sonnenberg, J. L.; Williams; Ding, F.; Lipparini, F.; Egidi, F.; Goings, J.; Peng, B.; Petrone, A.; Henderson, T.; Ranasinghe, D.; Zakrzewski, V. G.; Gao, J.; Rega, N.; Zheng, G.; Liang, W.; Hada, M.; Ehara, M.; Toyota, K.; Fukuda, R.; Hasegawa, J.; Ishida, M.; Nakajima, T.; Honda, Y.; Kitao, O.; Nakai, H.; Vreven, T.; Throssell, K.; Montgomery Jr., J. A.; Peralta, J. E.; Ogliaro, F.; Bearpark, M. J.; Heyd, J. J.; Brothers, E. N.; Kudin, K. N.; Staroverov, V. N.; Keith, T. A.; Kobayashi, R.; Normand, J.; Raghavachari, K.; Rendell, A. P.; Burant, J. C.; Iyengar, S. S.; Tomasi, J.; Cossi, M.; Millam, J. M.; Klene, M.; Adamo, C.; Cammi, R.; Ochterski, J. W.; Martin, R. L.; Morokuma, K.; Farkas, O.; Foresman, J. B.; Fox, D. J. Gaussian 16 Rev. C.01, 2016.

(34) Ochterski, J. W.; Petersson, G. A.; Montgomery, J. A. A Complete Basis Set Model Chemistry. V. Extensions to Six or More Heavy Atoms. *J. Chem. Phys.* **1996**, *104* (7), 2598–2619. https://doi.org/10.1063/1.470985.

(35) Montgomery, J. A.; Frisch, M. J.; Ochterski, J. W.; Petersson, G. A. A Complete Basis Set Model Chemistry. VI. Use of Density Functional Geometries and Frequencies. *J. Chem. Phys.* **1999**, *110* (6), 2822–2827. https://doi.org/10.1063/1.477924.

(36) Ma, Q.; Huang, M.; Liu, X.; Gai, Y.; Lin, X.; Yang, C.; Sheng, L.; Shan, X.; Zhang, W. Theoretical Study of Isoprene Dissociative Photoionization. *Chin. J. Chem. Phys.* **2017**, *30* (1), 43–49. https://doi.org/10.1063/1674-0068/30/cjcp1606131.

(37) Martins, G.; Ferreira-Rodrigues, A. M.; Rodrigues, F. N.; De Souza, G. G. B.; Mason, N. J.; Eden, S.; Duflot, D.; Flament, J.-P.; Hoffmann, S. V.; Delwiche, J.; Hubin-Franskin, M.-J.; Limão-Vieira, P. Valence Shell Electronic Spectroscopy of Isoprene Studied by Theoretical Calculations and by Electron Scattering, Photoelectron, and

Absolute Photoabsorption Measurements. *Phys. Chem. Chem. Phys.* **2009**, *11* (47), 11219. https://doi.org/10.1039/b916620c.

(38) Bodi, A.; Hemberger, P.; Osborn, D. L.; Sztáray, B. Mass-Resolved Isomer-Selective Chemical Analysis with Imaging Photoelectron Photoion Coincidence Spectroscopy. *J. Phys. Chem. Lett.* **2013**, *4* (17), 2948–2952. https://doi.org/10.1021/jz401500c.

(39) Branko, R.; Bross, D. H. *Active Thermochemical Tables (ATcT) Values Based on Ver. 1.130 of the Thermochemical Network.*; Argonne National Laboratory, 2023.

(40) Lias, S. G.; Liebman, J. F. Ion Energetics Data. In *NIST Chemistry WebBook, NIST Standard Reference Database Number 69*; Linstrom, P. J., Mallard, W. G., Eds.; National Institute of Standards and Technology: Gaithersburg, MD, 20899.

(41) Hussein, Y. A.; Liebman, J. F.; Stein, S. E. Neutral Thermochemical Data. In *NIST Chemistry WebBook, NIST Standard Reference Database Number 69*; Linstrom, P. J., Mallard, W. G., Eds.; National Institute of Standards and Technology: Gaithersburg, MD, 20899.

(42) Knecht, D. A. Thermal Decomposition of Cyclopentene and Cyclopentene-D8 in the Gas Phase. *J. Am. Chem. Soc.* **1973**, *95* (24), 7933–7938. https://doi.org/10.1021/ja00805a001.

(43) Wellington, C. A. The Thermal Isomerization Of Vinylcyclopropane. *J. Phys. Chem.* **1962**, *66* (9), 1671–1674. https://doi.org/10.1021/j100815a026.

(44) Crane, P. M.; Rose, T. L. Reactions of Singlet Methylene with Butadiene. High Energy Isomerizations of Vinylcyclopropane. *J. Phys. Chem.* **1975**, *79* (5), 403–409. https://doi.org/10.1021/j100572a001.

(45) Genossar-Dan, N.; Atlas, S.; Fux, D.; Har Lavan, S.; Zamir, U.; Rozenberg, I.; Lam Nguyen, T.; Hemberger, P.; Baraban, J. H. Direct Observation of the Ethyl Radical in the Pyrolysis of Ethane. *Angew. Chem. Int. Ed.* **2023**, *62* (32), e202305881. https://doi.org/10.1002/anie.202305881.

Chapter 8 – Monoterpene Pyrolysis

Based on the publication Buenger, E. W.; Bodi, A.; Burgos-Paci, M. A.; Mayer, P. M. Monoterpene Flash Pyrolysis Reveals Weakly Coupled Mechanistic Domains and Fleeting Biradical Intermediates. *Phys. Chem. Chem. Phys.* **2025**, *27* (43), 23400–23409. https://doi.org/10.1039/D5CP03144C.

Contribution Statement

E. White Buenger processed the data, performed computational studies, and prepared the manuscript for submission. A. Bodi performed the experiments and offered technical support as part of the SLS facility. P. M. Mayer conceptualized the idea and supervised the work. All authors contributed towards revisions of the submitted manuscript.

8.1 – Introduction

Terpenes are abundant, naturally occurring hydrocarbons, built up by isoprene (C_5H_8) moieties. Monoterpenes ($C_{10}H_{16}$) consist of two isoprene units and exhibit a wide array of isomeric structures due to the three degrees of unsaturation in isoprene and the frequent formation of stereocenters during isoprene coupling, which gives rise to optical isomerism. Representative examples include the acyclic myrcene, the monocyclic limonene, and the bicyclic α-pinene, highlighting the monoterpenes' structural diversity. They are relatively volatile and readily enter the gas phase, i.e., the atmosphere, when they are emitted into the environment, where they are consumed primarily through oxidation reactions with environmental oxidants, such as ozone.[1] In addition to the natural abundance and emission of terpenes, they are relevant in the food,[2] fragrance,[3] and pharmaceutical industries.[4] As fossil fuels are phased out, we turn to alternative sources of renewable energy, and monoterpenes have been considered a viable option.[5,6] The increasing intensity of forest fires worldwide due to climate change[7] as well as the prospective use case for monoterpenes as fuels means that monoterpene emissions, atmospheric oxidation,[8] and pyrolysis are expected to grow. This puts their reactivity, and particularly the pyrolysis mechanism of the most abundant monoterpenes, into research focus.

There have been numerous reports on waste tire pyrolysis, in which polyisoprene is broken down to obtain limonene,[9] to maximize limonene selectivity for economic purposes.[10] However, fundamental studies concerning limonene pyrolysis remain few and far between. Pines and Ryer investigated limonene pyrolysis at atmospheric pressure and 450 °C and observed a variety of substituted benzenes, and small amounts of isoprene and volatile gases, namely hydrogen, methane, ethane, ethylene, and propene. They proposed that biradical intermediates are first formed by homolytic bond cleavage and go on to yield the final pyrolysis products.[11] More recently, Zheng *et al.* investigated limonene pyrolysis along with that of β-pinene and myrcene and identified limonene isomerization products and minimal decomposition in the 540–600 °C temperature range, although the proportion of isoprene and non-identified products increased with temperature.[12] Bierkandt *et al.* studied limonene combustion and pyrolysis in a flow tube reactor in the 400–1000 °C range and observed small quantities of substituted benzenes, and larger quantities of benzene and isoprene, as well as small combustion intermediates including acetylene and ethylene as pyrolysis products.[13] They also rationalized the pyrolysis mechanism by invoking the consensus biradical intermediates.

Early reports on pinene pyrolysis have shown that the α- and β-isomers yield different thermal isomerization products at intermediate temperatures, with α-pinene forming alloocimene and β-pinene providing predominantly myrcene.[14] Similar to the mechanism proposed for limonene, pinene isomers were suggested to rearrange towards the observed product through biradical intermediates.[14] Crowley and Traynor performed α-pinene pyrolysis at 420 °C and observed a variety of monoterpene isomers resulting from rearrangements, as well as the formation of methyl substituted benzene compounds.[15] Gajewski *et al.* studied the pyrolysis of deuterium-labeled α-pinene and also followed the racemization kinetics. The observation primarily relates to the relative rate of internal rotation vs. ring opening and closure. They concluded that a C_S biradical intermediate is the most straightforward explanation for the observations and, thus, evidence for the formation of biradical intermediates in the thermal rearrangement of α-pinene in the range of 220–260 °C.[16] Stolle, Ondrushcka and Findeisen published a study that focused on the rearrangement of α-pinene to limonene and ocimene over the range of 250–500 °C during the course of a pyrolysis experiment with GC analysis.[17] Analogous studies on β-pinene pyrolysis aimed at rationalizing the formation of myrcene, a product that is not observed in the pyrolysis of α-pinene. Kolicheski *et al*. published a study on producing myrcene through the pyrolysis of β-pinene and observed the formation of predominantly myrcene, but also limonene, and 1[7],8 *p*-menthadiene as isomerization products, as well as smaller quantities of consecutive smaller fragmentation products over the 350–550 °C temperature range.[18] It has been suggested that the formation of myrcene from β-pinene is an endothermic but, based on its observation, necessarily entropically favourable and irreversible process at sufficiently high temperatures.[18] The proposed mechanisms for the rearrangement and the pathway for the dissociation of myrcene to butadiene and pentadiene, however, have since been questioned by other researchers in the field.[19] Coudour *et al*. identified α-pinene pyrolysis products by GC-MS at yet higher temperatures, detecting butene, isoprene, benzene, and other associated aromatic compounds at 800 °C without delving into mechanistic details.[20]

A common emphasis in monoterpene pyrolysis studies has been their rearrangement and interconversion, not so much the identification of decomposition products. The moderate temperature regimes applied in most studies are conducive to rearrangement, but not to fragmentation. However, as pyrolysis temperature rises into the range characteristic of fuel-rich wildfire conditions with residual woody fuel, the proportion of monoterpene dissociation products increases.[13]

In this work, we will carry out high-temperature pyrolysis experiments with photoelectron photoion coincidence spectroscopy detection, supplemented by theoretical calculations to identify the dissociation products obtained through the pyrolysis of selected representative monoterpenes, namely limonene, α-pinene, and β-pinene. In the competition between low activation energy and activation entropy vs. high activation energy and activation entropy processes, high temperatures, characteristic of wildfires, will favor the latter. This is expected to complement previous studies carried out at lower temperatures and higher reaction times.

8.2 – Methods

8.2.1 – Pyrolysis Experiments

Pyrolysis experiments were carried out on the VUV beamline at the Swiss Light Source (SLS, Paul Scherrer Institute, Villigen, Switzerland) using the imaging photoelectron photoion coincidence endstation[21–23] and a high-temperature pyrolysis microreactor,[24] as described previously in Chapter 7.2. After photoionization, imaging RoentDek delay line detectors were employed to velocity-map photoions and photoelectrons, which were time- and position-stamped. The electron event was used as the start of the time-of-flight timer for the photoions. Photoelectrons having initially zero kinetic energy (threshold electrons) are detected at the centre of the electron imaging detector, whereas kinetic energy ("hot") electrons are detected off-axis according to their initial lateral momentum. Hot electrons with an initial trajectory along the extraction axis also hit the centre spot. These events were subtracted from the centre mass spectra by subtracting the mass spectrum based on electrons detected in a ring around the centre spot to obtain threshold ionization mass spectra, i.e., ions in coincidence with truly threshold electrons.[25] Plotting the intensity of a mass spectral peak with a particular m/z ratio from the threshold ionization mass spectrum as a function of photon energy yields the photoion mass-selected threshold photoelectron spectrum (ms-TPES).[26]

Pyrolysis experiments were performed by passing argon, at a pressure of 1 bar and a flow rate of 1 standard cubic centimetres per minute (sccm), over a vial containing the terpene at room temperature. The room temperature vapour pressure of the three terpenes is ca. 4–6 mbar.[27] This mixture was then diluted with 20 sccm of argon to produce a beam with approximately 0.5% terpene, which expanded through a 200 μm pinhole into the 3 cm long, 1 mm internal diameter, resistively heated SiC pyrolysis microreactor. Reactor surface temperatures have been derived based on a previously observed power dependence measured in the pyrolysis setup by a type C thermocouple (1):

$$(1) \qquad T/°\mathrm{C} = P/\mathrm{W} \times 14.27 + 303$$

Where T is the reactor temperature and P is the heating power. The reactor temperature is considered to represent the gas temperature inside the reactor to within 100 °C.[28] The pressure and residence time in the reactor has been estimated to be 10–40 mbar and up to 100 μs, respectively.[28,29] The reactor is placed in the source vacuum chamber, where the pressure was ~ 5 × 10^{-5} mbar during measurements. The molecular beam exiting the pyrolysis reactor passed through a 2 mm diameter skimmer into the detection chamber, kept at a pressure of 10^{-6} mbar during measurements. The reactor can be heated to temperatures between 200 and 2000 °C to explore the distribution of pyrolysis products as a function of temperature by recording ms-TPES. The terpenes were studied at 950 °C.

Rovibrational cooling in the expansion from such microreactors has been found to be limited,[30] because of the low preexpansion pressure at the reactor nozzle.[28] The total ionization signal is therefore due in part to the barely cooled molecular beam and in part to room-temperature species that underwent collisional cooling with wall surfaces in the ionization chamber. These fractions are typically commensurate, which leads to an intermediate "effective temperature" as far as the internal energy distribution of the sample is concerned. Furthermore, previous studies with these types of reactors have concluded that the role of unimolecular vs. bimolecular reactions is molecule-dependent, with bimolecular reactions increasing with sample pressure. Reactions involving 0.2% propionic acid in argon and 0.3% furfural in helium gave results consistent with primarily unimolecular chemistry,[31,32] while benzaldehyde pyrolysis at similar concentrations evidenced bimolecular chemistry,[31] and so did analogous acetone pyrolysis experiments.[33] Our previous work on the pyrolysis of methyl-, ethyl- and methylchloroformate did not show evidence for a meaningful amount of bimolecular reactions.[34,35]

8.2.2 – Computational Methods

Closed-shell singlet structures were optimized using density functional theory (DFT) with B3LYP/6-311+G(d,p) level of theory using the Gaussian 16 software suite.[36]

Minimum-energy reaction paths and transition states were located using relaxed internal coordinate scans and the Synchronous Transit-Guided Quasi-Newton (STQN) method.[37] Single-point energy calculations with the CBS-QB3 composite method[38,39] were carried out for improved energetics, and are reported in the potential energy figures. There were noticeable discrepancies between, for example, the B3LYP and CBS-QB3 energies for β-pinene and myrcene. Myrcene is less stable by ca. 40 kJ/mol according to CBS-QB3 but only by 7 kJ/mol according to B3LYP/6-311+G(d,p). G4, M06-2X/6-311++G(d,p) and ωB97-XD/def2-TZVPP calculations confirmed the CBS-QB3 results. As B3LYP geometries feature in CBS-QB3 and G4 calculations, as well, we conclude that B3LYP geometries are acceptable, but B3LYP energetics are likely untrustworthy for these monoterpenes. Franck–Condon (FC) simulations of the ground-state ms-TPES bands of pyrolysis product candidates were also carried out using B3LYP geometries in Gaussian 16. Optimized structures in Figures 8.2 and 8.3 have been uploaded to the ioChem BD database, available at the following directory: https://iochem-bd.bsc.es/browse/review-collection/100/478924/ed8df8b822789fef9ca2906e

Biradicals were previously proposed to play a crucial role in the conversion of monoterpenes and are characterized by two, barely coupled radical centers. The biradical energies were obtained for the triplet state using CBS-QB3. As the singlet and triplet states are quasi-degenerate, the reaction path from the singlet monoterpene to the biradical minimum may proceed on the closed-shell singlet, the open-shell singlet, or triplet surface. Therefore, we also carried out broken-symmetry open-shell singlet and triplet path calculations to determine if the open-shell potential energy surface influences unimolecular monoterpene reactivity both towards the biradicals and along the other reaction steps.

Open-shell singlets (OSS) were addressed in unrestricted DFT calculations with α/β symmetry breaking by mixing β HOMO and LUMO orbitals in the initial guess, which relaxed into the closed-shell DFT result when the OSS configuration was higher in energy than the closed-shell one and yielded an open-shell solution otherwise. When symmetry-breaking led to a meaningful change in energy, OSS geometry optimizations were carried out to re-optimize the transition state geometries on the OSS surface. As B3LYP energies were found unsatisfactory and composite method calculations are not trivially applicable to these states, we evaluated the transition state energetics at the ωB97-XD/def2-TZVPP level of theory, referencing it to the related monoterpene on the potential energy surface. The broken-symmetry solution is contaminated by the triplet wave function, as seen by typical $\langle S^2 \rangle$ values of 0.7–1.0 instead of the expected 0 for a singlet. To obtain the pure singlet energy, we computed the triplet energy at the symmetry-broken optimized geometries using restricted open-shell Kohn–Sham (ROKS) ωB97-XD/def2-TZVPP calculations, and used the Yamaguchi spin decontamination correction:[40–42]

$$(2) \qquad E_{\mathrm{OSS}} = E_{\mathrm{BS}} - \frac{\langle S^2 \rangle_{\mathrm{BS}}}{2 - \langle S^2 \rangle_{\mathrm{BS}}} (E_{\mathrm{T}} - E_{\mathrm{BS}})$$

where E_{OSS} is the derived open-shell singlet energy, E_{T} is the ROKS triplet energy, E_{BS} is the broken-symmetry singlet energy and $\langle S^2 \rangle_{\mathrm{BS}}$ is the expectation value of the spin-squared operator in the broken-symmetry calculation. As discussed by David et al.,[43] this approach is expected to yield reliable results as long as the spin polarization of the supposedly closed-shell orbitals is minor, *i.e.,* up to $\langle S^2 \rangle \approx 1$, as was the case here. Nonetheless, the activation energies thus computed are expected to be markedly less accurate than the closed-shell and triplet biradical CBS-QB3 energies.

8.3 – Results and Discussion

8.3.1 – Experimental ms-TPES and Pyrolysis Product Identification

All recorded photoion mass-selected TPES can be found in the Appendix (Chapter 10). In Figure 8.1, the ms-TPES for m/z 68 from each of the three precursors is used as an example, together with a Franck–Condon simulation, in this case for isoprene.

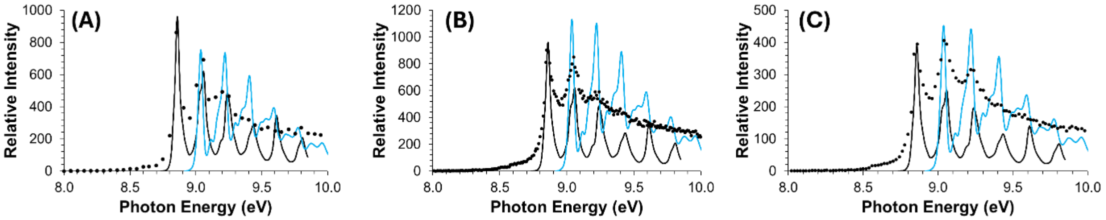

Figure 8.1: ms-TPES (markers) for m/z 68 obtained from the pyrolysis of (A) limonene, (B) α-pinene, (C) β-pinene. The FC simulations of isoprene (black line) and cyclopentadiene (blue line) have been overlaid on top of each ms-TPES. The product observed at m/z 68 has, thus, been identified as predominantly isoprene.

It is evident that limonene, α- and β-pinene all produced isoprene upon pyrolysis, but the intensity of the second peak in the ms-TPES and the more gradual drop in signal intensity suggest that an additional species contributes to the m/z 68 peak in the case of α- and β-pinene. In our earlier work on isoprene pyrolysis, we observed evidence for the formation of cyclopentene, which ionizes at 9 eV and contributes the stronger band at that energy in the TPES, which may therefore be a monoterpene pyrolysis product to account for the enhancement of the 9 eV peak.[44]

Table 8.1: Fractional abundances (in %) of the identified flash pyrolysis products of α-pinene, β-pinene, and limonene at 950 °C, assigned by ms-TPES. Abundances are based on cross-section corrected mass spectral signals of the ground-state TPES band (see text). The basis vectors ($\mathbf{w}_i$, renormalized to 100% in sum) from the non-negative matrix factorization, representing the mechanistic domains with their coefficients in the monoterpene pyrolysis ($\mathbf{h}_i$) giving each domain's contribution to pyrolysis. Coefficients for a two-component factorization are also given ($\mathbf{h}'_i$).

Compound	*Identity*	*α-pinene*	*β-pinene*	*limonene*	$\mathbf{w}_1$	$\mathbf{w}_2$	$\mathbf{w}_3$
C_9H_{12}	Trimethylbenzene	**11.4**	0.9	1.6	0.4	11.8	1.2
C_8H_{10}	Xylene	**39.6**	2.4	7.7	3.8	**41.2**	0.7
C_7H_8	Toluene	**20.1**	2.4	6.3	4.6	**20.9**	0.2
C_6H_8	Cyclohexadiene	1.8	0.2	0.2	0.0	1.9	0.4
C_6H_6	Benzene	0.5	0.7	0.5	0.5	0.5	0.9
C_5H_8	Isoprene/(cyclopentene)	**7.3**	**25.6**	**48.6**	**53.5**	6.7	0.0
C_5H_6	Cyclopentadiene	1.4	**15.0**	11.0	**12.2**	0.8	**17.8**
C_4H_6	1,3-butadiene	1.3	4.6	2.3	2.4	1.1	6.7
C_4H_4	1-buten-3-yne	0.3	2.2	2.7	3.0	0.2	1.5
C_3H_6	Propene	2.5	1.2	1.7	1.6	2.6	0.8
$C_3H_5^{\cdot}$	Propenyl radical	0.3	0.7	0.4	0.4	0.3	1.0
C_3H_4	Propyne	0.7	1.3	0.6	0.6	0.7	2.0
$C_3H_3^{\cdot}$	Propargyl radical	1.4	**30.1**	7.3	8.1	0.0	**50.9**
C_2H_4	Ethene	1.9	5.8	1.8	1.8	1.7	9.6
C_2H_2	Ethyne	0.5	2.0	1.3	1.4	0.4	2.6
$CH_3^{\cdot}$	Methyl radical	**9.1**	4.8	6.1	5.7	**9.3**	3.9
NMF coefficients for precursor products		$\mathbf{h}'_1$	$\mathbf{h}'_2$		$\mathbf{h}_1$	$\mathbf{h}_2$	$\mathbf{h}_3$
α-pinene		0.00	**0.98**		0.02	**0.96**	0.02
β-pinene		**0.82**	0.00		**0.48**	0.01	**0.52**
limonene		**0.97**	0.18		**0.90**	0.11	0.00

Table 8.1 summarizes the products observed and confirmed by FC-simulation in the pyrolysis of each terpene precursor. Aside from these peaks, up to half of the overall mass spectral signal intensity was spread over an abundance of minor peaks that could not

be individually assigned. However, the major peaks can be expected to deliver a valid overall picture of the unimolecular pyrolysis chemistry of the samples to understand commonalities and differences. The fractional abundance of the confirmed products, listed in Table 8.1, was approximated as the intensity of the origin band in the ms-TPES, divided by the known photoionization cross sections,[45] and normalized to the sum of their total renormalized signal. Based on cursory inspection of the major products, limonene primarily dissociates into isoprene, while α- and β-pinene exhibit distinct chemistries. β-Pinene forms primarily C_5H_8 (isoprene and cyclopentene), C_4H_4 (1-buten-3-yne), and a large amount of $C_3H_3^{\cdot}$ (propargyl radical), while α-pinene is the "busiest" of the three terpenes, exhibiting a variety of pyrolysis products, with methyl radicals being the predominant one.

8.3.2 – Product Matrix Factorization

If monoterpenes were to promptly interconvert before decomposing at the high pyrolysis temperature of 950 °C, we would see the same products emanating from the reactor, independent of the precursor monoterpene. Although this is not the case, there are similarities between the experimental α-pinene, β-pinene, and limonene product vectors in Table 8.1. A simple measure of the similarity between the product distributions is the angle between the product vectors, computed using cosine similarity after normalizing each distribution. At 0°, the distributions are identical and at 90°, they are orthogonal to each other. The angles are 77° (α-pinene vs. β-pinene), 69° (α-pinene vs. limonene), and 40° (β-pinene vs. limonene). This suggests that parts of the mechanism are shared, especially between β-pinene and limonene.

Non-negative matrix factorization (NMF, as implemented in scikit-learn)[46] is motivated by the idea that complex observations can be explained as an additive, strictly non-negative combination of parts. These are obtained as basis vectors and coefficients that reconstruct the measured data, *i.e.,* the product abundances, best.[47] Because the factors cannot take negative values, each column ($\mathbf{w}_i$) naturally represents a chemically plausible mechanistic domain, and the coefficient vectors ($\mathbf{h}_i$) quantify said domain's contribution to pyrolysis. Evidence for mechanistic coupling appears when a precursor's weights are spread over more than one domain rather than concentrated in a single one. This parts-based decomposition has previously been used to interpret chemistry: positive matrix factorization work by Paatero and Tapper contributed to source apportionment in environmental chemistry,[48] and Puliyanda et al. recently used joint NMF to unravel coupled versus uncoupled reaction pathways in heavy-oil upgrading.[49]

If each sample is trivially assigned to its own domain, we obtain a mathematically valid and exact but chemically uninformative decomposition with an identity matrix for the coefficients. Starting from a random or perturbed initial guess, the NMF algorithm will converge to a chemically interpretable local minimum. To avoid over-interpreting a single random initialization, we ran NMF many times with different random seeds and chose the most representative decomposition within 1–2% of the best error, i.e., one with basis profiles most similar to the other solutions. The solutions were easily reproducible and largely insensitive to initialization.

However, the first question is whether a two-component factorization reproduces the experiment well enough. The coefficients in the rank-2 factorization ($\mathbf{h}'_i$ in Table 8.1) suggest strong coupling between β-pinene and limonene products, and the rest of the limonene chemistry is approximated by α-pinene contributions. This, however, is a poor fit with a Euclidean reconstruction error (normalized by the Euclidean norm of the data matrix) of 27%, which shows that a third domain is necessary for a suitable reproduction of the product matrix. The three-factor basis vectors and their coefficients are also given in Table 8.1. Limonene and α-pinene have their own mechanistic domains ($\mathbf{w}_1$ and $\mathbf{w}_2$) in this factorization, while β-pinene chemistry is half unique ($\mathbf{w}_3$) and half coupled to limonene's domain. This provides a preliminary estimate on where the reactive flux branches out. Apparently, β-pinene will in part isomerize to limonene, but the decomposition of the other monoterpenes takes place mostly before interconversion, at least at 950 °C. If the isomerization barriers are lower in energy but associated with a lower activation entropy than the decomposition transition states, isomerization may compete more effectively at lower temperatures. Computational chemistry can be used to map the reaction paths and provide further, more tangible insights into the different mechanistic domains.

8.3.3 – Calculated Minimum Energy Reaction Pathways

Mechanistic suggestions in the literature invoke biradicals as central early intermediates in the interconversion and decomposition of these three species. Computationally, homolytic bond breaking in a closed-shell molecule yields a biradical system, but unimolecular rearrangements may take place on the closed-shell singlet surface, as well. As the second is easier to address computationally, we first tackled the pathways on the closed-shell singlet surface. Inspired by the singlet paths, we then followed the reaction paths on the triplet surface and evaluated open-shell singlet energies for the transition states and intermediates. While we aimed to locate the lowest-lying channels using constrained bond length and angle scans as well as synchronous transit-guided quasi-

Newton optimizations, per the dimensionality of the system, only a small part of the potential energy surface could be explored. However, due to the lack of a fast and robust level of theory to yield reliable energies across the potential energy surface, it is unlikely that a more aggressive PES exploration strategy using a less expensive level of theory would have yielded better results. Therefore, this balanced approach likely provides a reasonable first guess for the unimolecular thermal decomposition mechanism of monoterpenes.

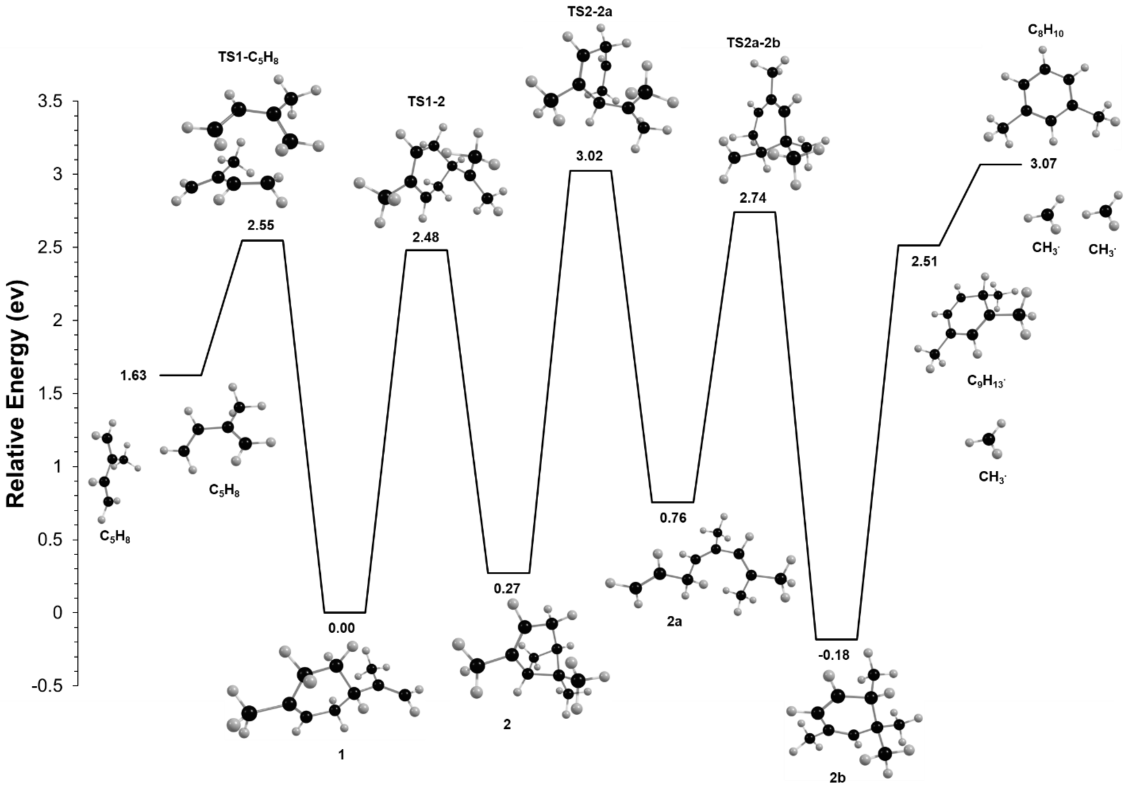

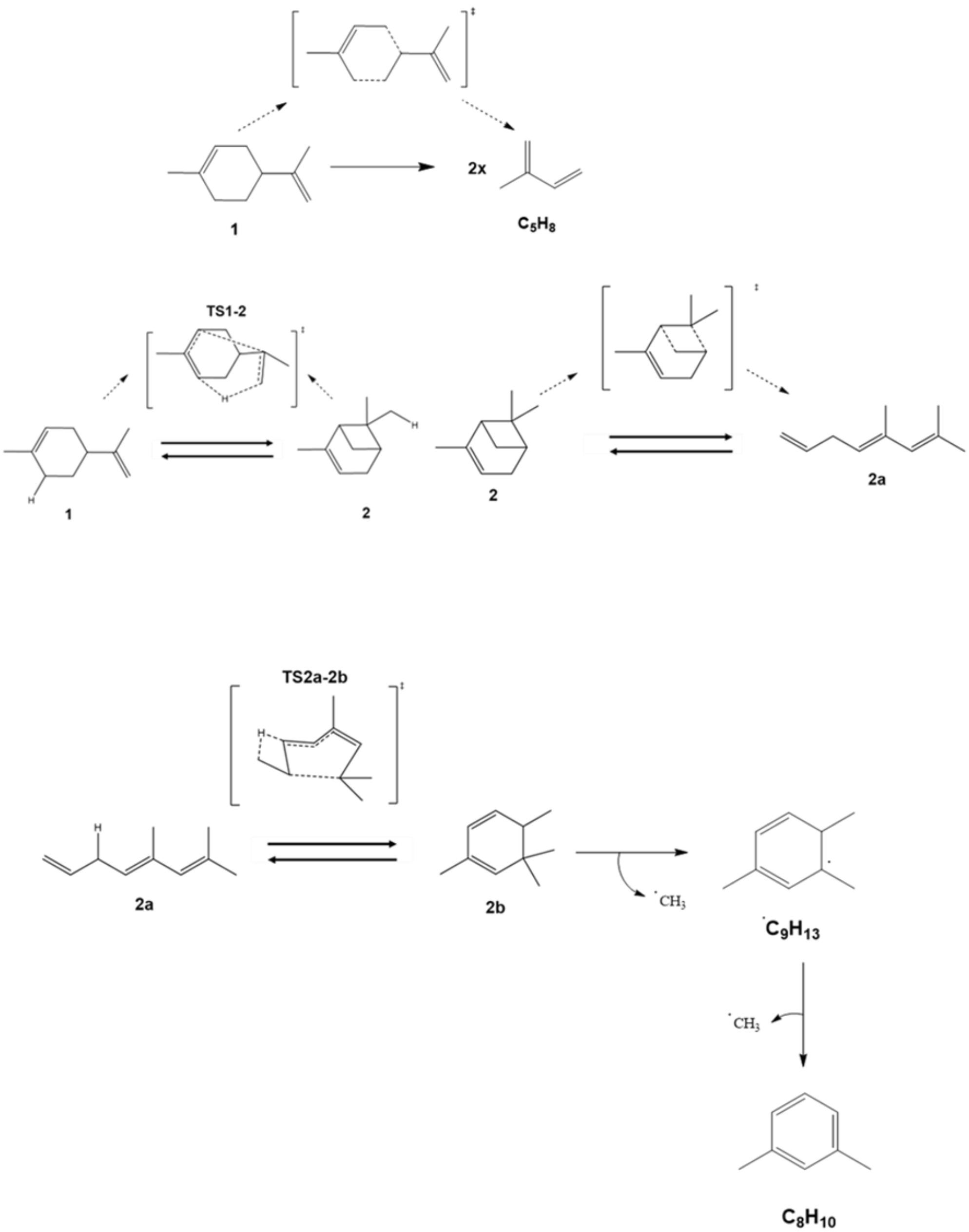

Figure 8.2: Minimum energy reaction pathway calculated at the CBS-QB3//B3LYP/6-311+G(d,p) level of theory, involving limonene (**1**) and α-pinene (**2**). The pathway from 1 towards the left yields two isoprene molecules (C_5H_8). Towards the right, it connects limonene to 2, followed by sequential losses of methyl radical to yield aromatics. Energies indicated are relative to that of **1**. A 2D schematic has been included.

The minimum energy reaction pathway for limonene fragmentation is shown in Figure 8.2. The reaction towards the left is straightforward, beginning from limonene (**1**) and going over a 2.55 eV barrier (**TS1-C_5H_8**), where the cyclohexene ring is broken near the propenyl group in a retro-Diels–Alder reaction, leading to the release of two isoprene molecules (C_5H_8). This is a closed-shell fragmentation pathway with no open-shell or biradical character. Limonene can, however, also undergo isomerization by H-transfer to form a biradical. The energy of this closed-shell transition state is only 2.50 eV but the biradical is not stabilized significantly after the H atom is transferred and exhibits an energy of 1.85 eV (see potential energy surface in Figure 8.3). Thus, while biradical formation is energetically allowed prior to isoprene formation in limonene, it represents a dead end in the mechanism. Limonene's facile dissociation to isoprene also explains the dominant abundance of isoprene observed experimentally in limonene pyrolysis.

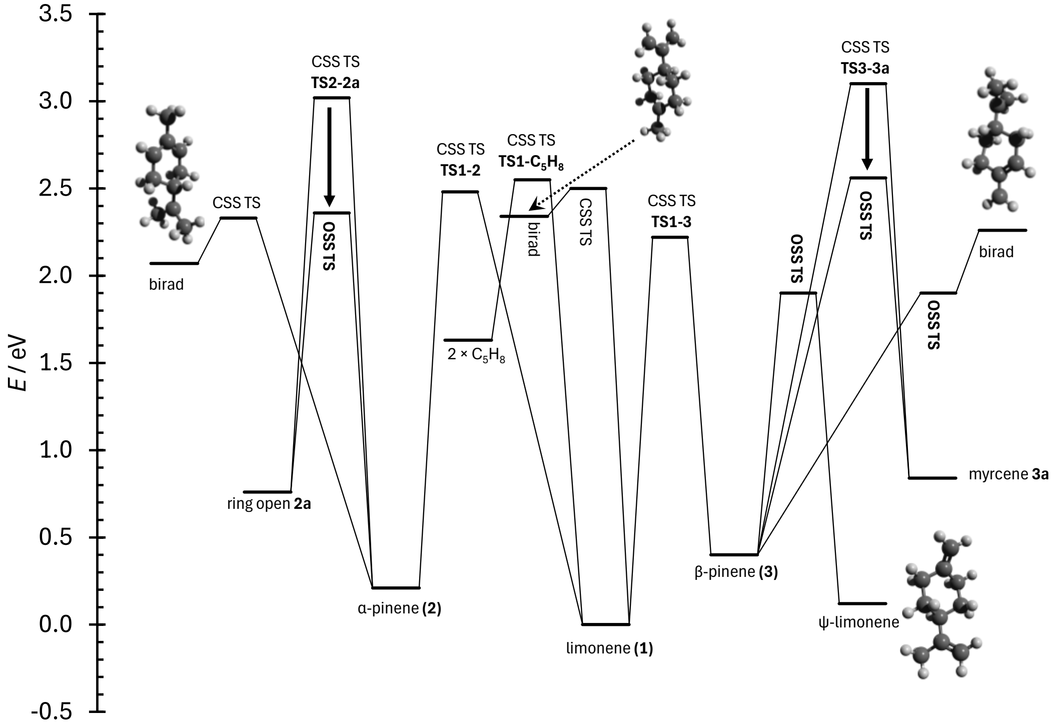

Figure 8.3: Potential energy surface including the open-shell singlet (OSS) ring-opening transition states. The stabilization they represent with respect to the closed-shell analogues (solid arrows) as well as the initial closed-shell (CSS) stationary points discussed in the main text are also shown. The OSS TS energies were computed using DFT as discussed in the Methods section, relative to the corresponding monoterpene energy. CBS-QB3 energies are shown for the closed-shell stationary points, while the biradical energies are the result of triplet CBS-QB3 calculations. The biradical structures are also plotted.

Moving towards the right in Figure 8.2 and towards the left in Figure 8.3, limonene is connected to α-pinene by an isomerization transition state **TS1-2**, where the methyl group on the propyl moiety undergoes a 1,5-H shift and forms the C–C bridge in α-pinene. This closed-shell transition state lies at 2.33 eV, slightly lower than the 2.55 eV transition state to isoprene formation. Based on the experimental observation and the product matrix factorization, limonene barely couples to the α-pinene reactions. The limonene fragmentation (**TS1-C_5H_8**) and the **TS1-2** isomerization transition states are broadly comparable in energy, but **TS1-2** is associated with a lower activation entropy (−20 vs +25 J K^{-1} mol^{-1} for **TS1-C_5H_8**), which allows the retro-Diels–Alder fragmentation to outcompete limonene isomerization to α-pinene at high temperatures.

Moving from structure **2**, α-pinene, towards the right, an open-chain intermediate **2a** is produced via elongation of one of the C–C bonds in the bicyclic bridge feature. The associated transition state, **TS(2-2a)**, is rather high in energy at 3.02 eV. Indeed, a single-point triplet-singlet gap calculation at this geometry yielded a splitting of only 0.17 eV. Only the open-shell singlet transition state, at ca. 2.36 eV (see Figure 8.3), makes the formation of the per se closed-shell intermediate **2a** competitive. **2a** may then re-cyclize by association of the terminal alkene and the central CH carbon, leading to tetramethylcyclohexadiene **2b**. Sequential bond dissociation of CH_3 groups leads to the production of the trimethylcyclohexadienyl radical and xylene, releasing two methyl radicals. This path explains the observation of the strong methyl radical signal as well as aromatic products in α-pinene pyrolysis.

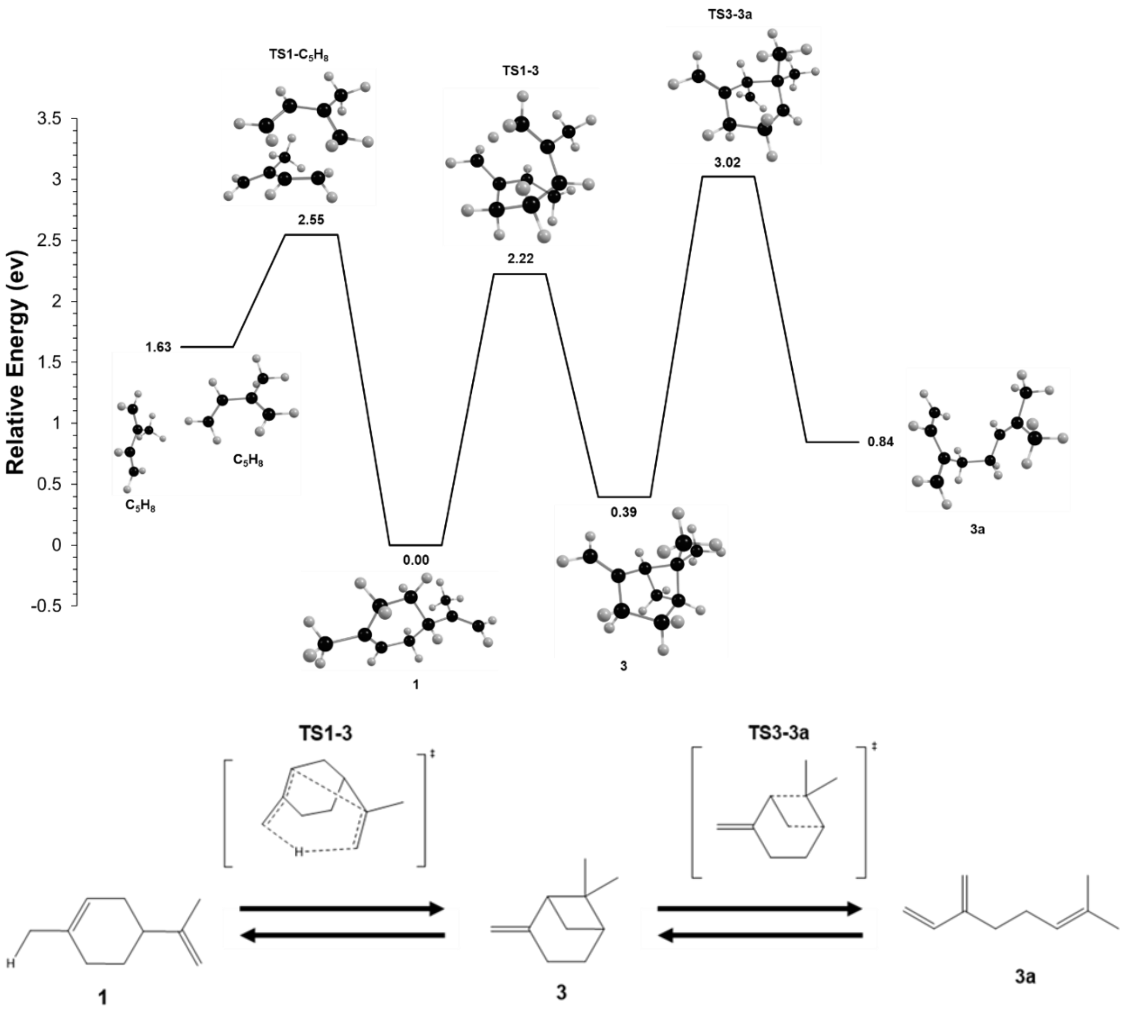

Figure 8.4: Minimum energy reaction pathway calculated at the CBS-QB3//B3LYP/6-311+G(d,p) level of theory, involving limonene (**1**) and β-pinene (**3**). Isoprene formation from **1** is the same as in Figure 8.2. The transition state towards the right connects limonene and β-pinene, which can also rearrange to myrcene (**3a**). Energy values are relative to that of limonene. A 2D schematic has been included.

Minimum energy reaction pathways calculated to account for β-pinene pyrolysis are shown in Figure 8.4. Much like α-pinene, β-pinene (**3**) can also isomerize to limonene (and thus make isoprene) through **TS1-3**, which lies only at 2.22 eV. One of the CH_3 hydrogens undergoes a 1,5-H shift towards the exocyclic CH_2, resulting in **1**. The low energy of this closed-shell rearrangement transition state explains the observation of isoprene and the strong coupling between the β-pinene and limonene pyrolysis chemistry indicated by NMF, as well. Starting to the right from **3**, a rearrangement reaction is seen involving the dissociation of the bond between bicyclic bridging carbons, **TS3-3a**, at an energy of 3.02 eV. This β-pinene rearrangement is analogous to the one calculated in α-pinene, but it leads to **3a,** myrcene, due to the position of the double bond. We did not detect myrcene in β-pinene pyrolysis, and do not have data on myrcene pyrolysis under comparable conditions, but propargyl radicals, an abundant product in the β-pinene reaction domain, represent a likely sequential fragmentation product of myrcene. Because of the linear chain and the comparable bond energies in myrcene, its pyrolysis mechanism is expected to be convoluted, and we did not endeavor to unveil it solely computationally. While this path over a closed-shell transition state leads to a major pyrolysis product of β-pinene known in the literature, its activation energy is prohibitively high.

Although the triplet single-point energy at **TS3-3a** was found to be 0.25 eV higher, an open-shell rearrangement transition state was found at 2.56 eV (Figure 8.3). In fact, we also located a lower-lying open-shell path, with a much lower barrier of ca. 1.90 eV, leading to ψ-limonene. This activation energy is slightly lower than the 2.22 eV isomerization activation energy to limonene. β-Pinene can be thermally converted to 80% myrcene at 450 °C with 11% limonene as co-product, and ψ-limonene is not a major pyrolysis product.[50] Therefore, the overall activation energy to myrcene formation cannot be significantly higher than ca. 2 eV, the closed-shell transition state **TS3-3a** to limonene formation, which is followed dominantly by isoprene release. In fact, the economically feasible conversion of β-pinene to myrcene at lower temperatures, combined with the NMF result of ca. 50:50 β-pinene and limonene mechanistic contributions to the β-pinene flash pyrolysis products tells us that isomerization is dominant at low energies and outcompeted by the looser but higher-energy isomerization process to limonene at our elevated temperatures and short reaction times. Therefore, the transition state to myrcene formation should be tighter and at a lower energy than the isomerization transition state to limonene. Consequently, either the true transition state to myrcene is lower than the OSS transition state we located at 2.56 eV, or ψ-limonene is an intermediate on the way to myrcene formation. In the absence of pyrolysis data on ψ-limonene, we have not explored its thermal decomposition pathways further. These insights and the open-shell transition states driving some of the discussed decomposition paths call for a discussion of the "biradical" intermediates as invoked ubiquitously in the mechanistic discussions of terpene pyrolysis in the literature.

8.3.4 – On the Role of Biradicals

Apart from the open-shell singlet ring-opening transition states discussed above, triplet and OSS minima and transition states along the potential energy surfaces in Figures 8.2 and 8.3 were found to be, in part significantly, higher in energy than the closed-shell singlets. The central biradical intermediates proposed by, e.g., Gajewski *et al.*[16] are distinct from the structures along our PES and correspond to ring-opening of the bicyclic α- and β-pinene to a configuration with two hypovalent carbons with remote radical centers and quasi-degenerate open-shell singlet and triplet electronic configurations. We have also considered the biradical isomer of limonene by H-transfer and found that the biradicals' energy was in the 1.85–1.90 eV range relative to limonene. The corresponding isomerization transition states were found to be on the closed-shell surface at 2.33 eV for α-pinene and at 2.50 eV for limonene. While the former corresponds to a bond breaking, biradical formation in limonene requires a H-transfer, therefore a tight transition state. For β-pinene, an OSS transition state was found at a remarkably low energy of 1.90 eV, suggesting that biradical formation is kinetically allowed at its energetic threshold of 2.26 eV. Thus, biradical formation is generally energetically allowed in the energy range of the other isomerization/fragmentation processes, although it takes place over a tight transition state in limonene. Based on the harmonic free energies and activation free energies, evaluated using thermo.py by Irikura,[51] we calculated equilibrium constants and rate constants as a function of temperature to gain further insights into the biradicals' role. As shown in Figure 8.5, the equilibrium fractional abundance of the biradical derived from β-pinene is on the order of 10^{-10} at temperatures where thermal dissociation does not yet convert the precursor into lighter fragments quantitatively. Statistical rates for ring opening in α-pinene and isoprene formation in limonene are also at least an order of magnitude higher than for biradical formation. The biradical energies are expected to be accurately reported by CBS-QB3. Consequently, biradicals are unlikely to be present in detectable amounts, irrespective of the experimental conditions. Furthermore, because of their high energies, they are not fragmentation or isomerization intermediates. However, because of the errors in the harmonic approximation and the uncertainties in the activation energies, we cannot exclude that biradical formation rates are higher and that they may still play a role in racemization in both pinenes.

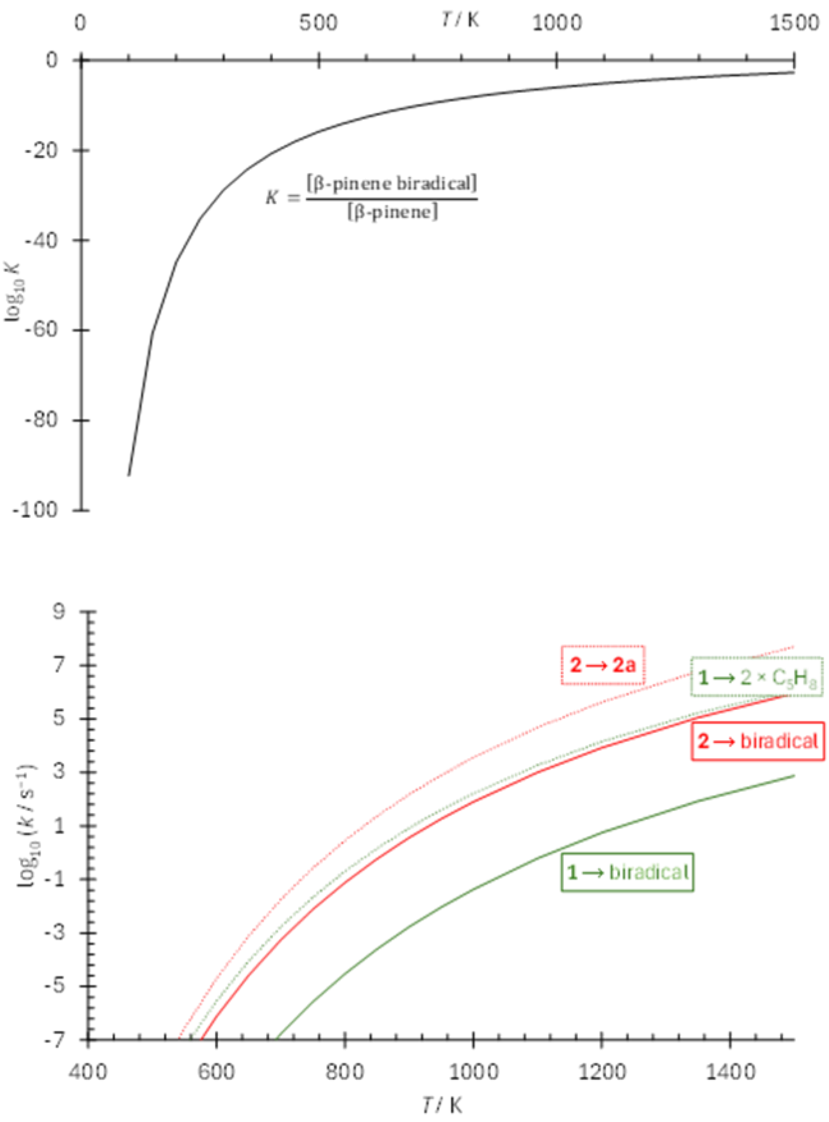

Figure 8.5: Equilibrium constant as a function of temperature for biradical formation from β-pinene and canonical harmonic RRKM rate constants for ring opening in α-pinene, isoprene formation from limonene (dashed lines) vs. biradical formation (continuous lines) in these species. Statistical calculations are based on the potential energy surface above.

Thus, the interconversion of the α-pinene/limonene/β-pinene system as well as the straightforward fragmentation of the limonene to isoprene takes place on the closed-shell singlet surface. Although the assumed biradical mechanisms are suitable to fit the reaction kinetics[12,17,19] and account for the racemization of the sample as well as deuterium scrambling,[16] our results suggest that biradicals may be responsible for racemization and hydrogen scrambling (as statistical rates may be off by more than an order of magnitude), but do not play a role in driving thermal decomposition chemistry (because of the high biradical energies). Furthermore, even if equilibrium biradical concentrations are reached, they will remain undetectable trace components in the reactive mixture at all temperatures. This insight underlines the importance of computational confirmation of the viability of assumed reaction intermediates.

At the same time, as mentioned earlier, the ring-opening transition states of α- as well as β-pinene are open-shell singlets, which brings the calculated surface more in line with the experimental observations. Open-shell singlet transition states appear to play a major role in driving monoterpene unimolecular thermal decomposition, but not their isomerization. These transition states, however, are not biradicals and exhibit substantial singlet–triplet gaps.

8.4 – Conclusion

The major flash pyrolysis products of limonene, α- and β-pinene were identified at a pyrolysis temperature of 950 °C based on their ms-TPES, recorded by imaging photoelectron photoion spectroscopy. A semi-quantitative analysis yielded a product matrix, which showed isoprene as the predominant product in limonene pyrolysis, strong aromatics as well as methyl radical signals in α-pinene thermal decomposition, and propargyl radicals and cyclopentadiene as well as isoprene as the most important β-pinene fragmentation products. Non-negative matrix factorization with two basis vectors could not reproduce the product matrix faithfully, confirming that the three samples fragment according to three mechanistic domains. NMF also indicated that these may be thought of as the limonene mechanism (retro-Diels–Alder reaction to isoprene), the α-pinene mechanism to aromatics, and about half of the β-pinene reactive flux proceeds via the limonene mechanism while the other half ultimately yields propargyl and cyclopentadiene as major products, likely over a myrcene intermediate. While NMF analysis yielded proof-of-principle mechanistic insights that were in line with the computational results, it was inherently limited by the low dimension of the data sets. Temperature-dependent product matrices of more monoterpene isomers would have yielded better-defined insights, but experimental developments, such as quantification approaches based on measurements at only one or a few photon energies, would be needed for more expansive data sets to be within reach.

We have explored the closed-shell singlet potential energy surface to identify the main monoterpene interconversion and fragmentation mechanisms using density functional theory and the CBS-QB3 method for single-point energies. This exploration was guided by the observed pyrolysis products, and only a small part of the phase space could be explored. Alternative, automatic reaction kinetics approaches[52] could account for a larger part of the mechanism, including the minor products, if coupled with a methods strategy that addresses closed- and open-shell singlet as well as triplet states consistently. Still, the isomerization reactions and the major limonene pathway, the formation of isoprene, are well-described by this approach. From α- and β-pinene, open-shell singlet ring-opening transition states lead to fragmentation at comparable energies, explaining the competition between interconversion and fragmentation, the latter of which dominates in α-pinene, and a combination is seen in β-pinene. Biradicals are very high in energy to be intermediates in thermal decomposition. While their formation is energetically allowed at

1.80–1.95 eV above limonene over moderate or even submerged transition states, statistical equilibrium constant and rate constant calculations suggest that they are at most fleeting species in the reactive mixture and not major fragmentation intermediates they were made out to be. Thus, we show that the flash pyrolysis of monoterpenes is driven by isomerization and fragmentation transition states, of which ring-opening transition states often have open-shell character and, contrary to the longstanding paradigm, biradical intermediates, while they may account for racemization, are unlikely to play a major role in thermal decomposition.

8.5 – Chapter 8 References

(1) Yu, J.; Griffin, R. J.; Cocker, D. R.; Flagan, R. C.; Seinfeld, J. H.; Blanchard, P. Observation of Gaseous and Particulate Products of Monoterpene Oxidation in Forest Atmospheres. *Geophys. Res. Lett.* **1999**, *26* (8), 1145–1148. https://doi.org/10.1029/1999GL900169.

(2) De Alvarenga, J. F. R.; Genaro, B.; Costa, B. L.; Purgatto, E.; Manach, C.; Fiamoncini, J. Monoterpenes: Current Knowledge on Food Source, Metabolism, and Health Effects. *Crit. Rev. Food Sci. Nutr.* **2023**, *63* (10), 1352–1389. https://doi.org/10.1080/10408398.2021.1963945.

(3) Vieira, C. G.; Dos Santos, E. N.; Gusevskaya, E. V. Synthesis of Fragrance Compounds from Acyclic Monoterpenes: Rhodium Catalyzed Hydroformylation and Tandem Hydroformylation/Acetalization of Linalool and β-Citronellene. *Appl. Catal. Gen.* **2013**, *466*, 208–215. https://doi.org/10.1016/j.apcata.2013.06.037.

(4) Koziol, A.; Stryjewska, A.; Librowski, T.; Salat, K.; Gawel, M.; Moniczewski, A.; Lochynski, S. An Overview of the Pharmacological Properties and Potential Applications of Natural Monoterpenes. *Mini-Rev. Med. Chem.* **2015**, *14* (14), 1156–1168. https://doi.org/10.2174/1389557514666141127145820.

(5) Harvey, B. G.; Wright, M. E.; Quintana, R. L. High-Density Renewable Fuels Based on the Selective Dimerization of Pinenes. *Energy Fuels* **2010**, *24* (1), 267–273. https://doi.org/10.1021/ef900799c.

(6) Kumar, M.; Tung Chong, C.; Karmakar, S. Comparative Assessment of Combustion Characteristics of Limonene, Jet A-1 and Blends in a Swirl-Stabilized Combustor under the Influence of Pre-Heated Swirling Air. *Fuel* **2022**, *316*, 123350. https://doi.org/10.1016/j.fuel.2022.123350.

(7) Turco, M.; Abatzoglou, J. T.; Herrera, S.; Zhuang, Y.; Jerez, S.; Lucas, D. D.; AghaKouchak, A.; Cvijanovic, I. Anthropogenic Climate Change Impacts Exacerbate Summer Forest Fires in California. *Proc. Natl. Acad. Sci.* **2023**, *120* (25), e2213815120. https://doi.org/10.1073/pnas.2213815120.

(8) Courty, L.; Chetehouna, K.; Lemée, L.; Mounaïm-Rousselle, C.; Halter, F.; Garo, J. P. Pinus Pinea Emissions and Combustion Characteristics of Limonene Potentially

Involved in Accelerating Forest Fires. *Int. J. Therm. Sci.* **2012**, *57*, 92–97. https://doi.org/10.1016/j.ijthermalsci.2012.02.012.

(9) Danon, B.; Van Der Gryp, P.; Schwarz, C. E.; Görgens, J. F. A Review of Dipentene (Dl-Limonene) Production from Waste Tire Pyrolysis. *J. Anal. Appl. Pyrolysis* **2015**, *112*, 1–13. https://doi.org/10.1016/j.jaap.2014.12.025.

(10) Farzad, S.; Mandegari, M.; Görgens, J. F. A Novel Approach for Valorization of Waste Tires into Chemical and Fuel (Limonene and Diesel) through Pyrolysis: Process Development and Techno Economic Analysis. *Fuel Process. Technol.* **2021**, *224*, 107006. https://doi.org/10.1016/j.fuproc.2021.107006.

(11) Pines, H.; Ryer, J. Studies in the Terpene Series. XXIII. Pyrolysis of (d-Limonene and of Related Hydrocarbons. Mechanisms of Pyrolysis. **1955**, *77*.

(12) Zheng, H.; Chen, J.; Li, C.; Chen, J.; Wang, Y.; Zhao, S.; Zeng, Y. Mechanism and Kinetics of the Pyrolysis of β-Pinene to Myrcene. *J. Anal. Appl. Pyrolysis* **2017**, *123*, 99–106. https://doi.org/10.1016/j.jaap.2016.12.020.

(13) Bierkandt, T.; Gaiser, N.; Bachmann, J.; Oßwald, P.; Köhler, M. Terpene Speciation: Analytical Insights into the Oxidation and Pyrolysis of Limonene and 1,8-Cineole via Molecular-Beam Mass Spectrometry. *Combust. Flame* **2025**, *272*, 113854. https://doi.org/10.1016/j.combustflame.2024.113854.

(14) Burwell, R. L. The Mechanism of the Pyrolyses of Pinenes. *J. Am. Chem. Soc.* **1951**, *73* (9), 4461–4462. https://doi.org/10.1021/ja01153a508.

(15) Crowley, K. J.; Traynor, S. G. Ground State Sigmatropic and Electrocyclic Rearrangements in Some Monoterpenes. *Tetrahedron* **1978**, *34* (18), 2783–2789. https://doi.org/10.1016/0040-4020(78)88420-8.

(16) Gajewski, J. J.; Kuchuk, I.; Hawkins, C.; Stine, R. The Kinetics, Stereochemistry, and Deuterium Isotope Effects in the a-Pinene Pyrolysis. Evidence for Incursion of Multiple Conformations of a Diradical. **2002**.

(17) Stolle, A.; Ondruschka, B.; Findeisen, M. Mechanistic and Kinetic Insights into the Thermally Induced Rearrangement of α-Pinene. *J. Org. Chem.* **2008**, *73* (21), 8228–8235. https://doi.org/10.1021/jo8012995.

(18) Kolicheski, M. B.; Cocco, L. C.; Mitchell, D. A.; Kaminski, M. Synthesis of Myrcene by Pyrolysis of β-Pinene: Analysis of Decomposition Reactions. *J. Anal. Appl. Pyrolysis* **2007**, *80* (1), 92–100. https://doi.org/10.1016/j.jaap.2007.01.005.

(19) Stolle, A.; Ondruschka, B. Comment to the Paper '"Synthesis of Myrcene by Pyrolysis of b-Pinene: Analysis of Decomposition Reactions"' by M.B. Kolicheski et al. [J. Anal. Appl. Pyrol. 80 (2007) 92–100]. *J Anal Appl Pyrolysis* **2008**.

(20) Coudour, B.; Chetehouna, K.; Lemée, L.; Bertin, P.; Garo, J.-P. Thermal Degradation of α-Pinene Using a Py–GC/MS. *J. Therm. Anal. Calorim.* **2019**, *137* (4), 1315–1328. https://doi.org/10.1007/s10973-019-08028-8.

(21) Bodi, A.; Hemberger, P.; Gerber, T.; Sztáray, B. A New Double Imaging Velocity Focusing Coincidence Experiment: *I* 2PEPICO. *Rev. Sci. Instrum.* **2012**, *83* (8), 083105. https://doi.org/10.1063/1.4742769.

(22) Sztáray, B.; Voronova, K.; Torma, K. G.; Covert, K. J.; Bodi, A.; Hemberger, P.; Gerber, T.; Osborn, D. L. CRF-PEPICO: Double Velocity Map Imaging Photoelectron Photoion Coincidence Spectroscopy for Reaction Kinetics Studies. *J. Chem. Phys.* **2017**, *147* (1), 013944. https://doi.org/10.1063/1.4984304.

(23) Bodi, A.; Hemberger, P.; Pérez-Ramírez, J. Photoionization Reveals Catalytic Mechanisms. *Nat. Catal.* **2022**, *5* (10), 850–851. https://doi.org/10.1038/s41929-022-00847-7.

(24) Hemberger, P.; Custodis, V. B. F.; Bodi, A.; Gerber, T.; Van Bokhoven, J. A. Understanding the Mechanism of Catalytic Fast Pyrolysis by Unveiling Reactive Intermediates in Heterogeneous Catalysis. *Nat. Commun.* **2017**, *8* (1), 15946. https://doi.org/10.1038/ncomms15946.

(25) Sztáray, B.; Baer, T. Suppression of Hot Electrons in Threshold Photoelectron Photoion Coincidence Spectroscopy Using Velocity Focusing Optics. *Rev. Sci. Instrum.* **2003**, *74* (8), 3763–3768. https://doi.org/10.1063/1.1593788.

(26) Hemberger, P.; Bodi, A.; Bierkandt, T.; Köhler, M.; Kaczmarek, D.; Kasper, T. Photoelectron Photoion Coincidence Spectroscopy Provides Mechanistic Insights in Fuel Synthesis and Conversion. *Energy Fuels* **2021**, *35* (20), 16265–16302. https://doi.org/10.1021/acs.energyfuels.1c01712.

(27) Acree, W. E.; Chickos, J., S. Phase Transition Enthalpy Measurements of Organic and Organometallic Compounds. In *NIST Chemistry WebBook, NIST Standard Reference Database Number 69,*; Linstrom, P. J., Mallard, W. G., Eds.; National Institute of Standards and Technology: Gaithersburg, MD, 20899.

(28) Guan, Q.; Urness, K. N.; Ormond, T. K.; David, D. E.; Barney Ellison, G.; Daily, J. W. The Properties of a Micro-Reactor for the Study of the Unimolecular Decomposition of Large Molecules. *Int. Rev. Phys. Chem.* **2014**, *33* (4), 447–487. https://doi.org/10.1080/0144235X.2014.967951.

(29) Grimm, S.; Baik, S.-J.; Hemberger, P.; Bodi, A.; Kempf, A. M.; Kasper, T.; Atakan, B. Gas-Phase Aluminium Acetylacetonate Decomposition: Revision of the Current Mechanism by VUV Synchrotron Radiation. *Phys. Chem. Chem. Phys.* **2021**, *23* (28), 15059–15075. https://doi.org/10.1039/D1CP00720C.

(30) Hemberger, P.; Wu, X.; Pan, Z.; Bodi, A. Continuous Pyrolysis Microreactors: Hot Sources with Little Cooling? New Insights Utilizing Cation Velocity Map Imaging and Threshold Photoelectron Spectroscopy. *J. Phys. Chem. A* **2022**, *126* (14), 2196–2210. https://doi.org/10.1021/acs.jpca.2c00766.

(31) Vasiliou, A. K.; Kim, J. H.; Ormond, T. K.; Piech, K. M.; Urness, K. N.; Scheer, A. M.; Robichaud, D. J.; Mukarakate, C.; Nimlos, M. R.; Daily, J. W.; Guan, Q.; Carstensen, H.-H.; Ellison, G. B. Biomass Pyrolysis: Thermal Decomposition Mechanisms of Furfural and Benzaldehyde. *J. Chem. Phys.* **2013**, *139* (10), 104310. https://doi.org/10.1063/1.4819788.

(32) Rogers, C. O.; Lockwood, K. S.; Nguyen, Q. L. D.; Labbe, N. J. Diol Isomer Revealed as a Source of Methyl Ketene from Propionic Acid Unimolecular Decomposition. *Int. J. Chem. Kinet.* **2021**, *53* (12), 1272–1284. https://doi.org/10.1002/kin.21532.

(33) Zaleski, D. P.; Sivaramakrishnan, R.; Weller, H. R.; Seifert, N. A.; Bross, D. H.; Ruscic, B.; Moore, K. B.; Elliott, S. N.; Copan, A. V.; Harding, L. B.; Klippenstein, S. J.; Field, R. W.; Prozument, K. Substitution Reactions in the Pyrolysis of Acetone Revealed through a Modeling, Experiment, Theory Paradigm. *J. Am. Chem. Soc.* **2021**, *143* (8), 3124–3142. https://doi.org/10.1021/jacs.0c11677.

(34) Lowe, B.; Cardona, A. L.; Salas, J.; Bodi, A.; Burgos Paci, M. A.; Mayer, P. M. Probing the Pyrolysis of Methyl Formate in the Dilute Gas Phase by Synchrotron Radiation and Theory. *J. Mass Spectrom.* **2022**, *57* (6), e4868. https://doi.org/10.1002/jms.4868.

(35) Lowe, B.; Cardona, A. L.; Bodi, A.; Mayer, P. M.; Burgos Paci, M. A. The Unimolecular Chemistry of Methyl Chloroformate Ions and Neutrals: A Story of Near-Threshold Decomposition. *J. Am. Soc. Mass Spectrom.* **2023**, *34* (12), 2831–2839. https://doi.org/10.1021/jasms.3c00334.

(36) Frisch, M. J.; Trucks, G. W.; Schlegel, H. B.; Scuseria, G. E.; Robb, M. A.; Cheeseman, J. R.; Scalmani, G.; Barone, V.; Petersson, G. A.; Nakatsuji, H.; Li, X.; Caricato, M.; Marenich, A. V.; Bloino, J.; Janesko, B. G.; Gomperts, R.; Mennucci, B.; Hratchian, H. P.; Ortiz, J. V.; Izmaylov, A. F.; Sonnenberg, J. L.; Williams; Ding, F.; Lipparini, F.; Egidi, F.; Goings, J.; Peng, B.; Petrone, A.; Henderson, T.; Ranasinghe, D.; Zakrzewski, V. G.; Gao, J.; Rega, N.; Zheng, G.; Liang, W.; Hada, M.; Ehara, M.; Toyota, K.; Fukuda, R.; Hasegawa, J.; Ishida, M.; Nakajima, T.; Honda, Y.; Kitao, O.; Nakai, H.; Vreven, T.; Throssell, K.; Montgomery Jr., J. A.; Peralta, J. E.; Ogliaro, F.; Bearpark, M. J.; Heyd, J. J.; Brothers, E. N.; Kudin, K. N.; Staroverov, V. N.; Keith, T. A.; Kobayashi, R.; Normand, J.; Raghavachari, K.; Rendell, A. P.; Burant, J. C.; Iyengar, S. S.; Tomasi, J.; Cossi, M.; Millam, J. M.; Klene, M.; Adamo, C.; Cammi, R.; Ochterski, J. W.; Martin, R. L.; Morokuma, K.; Farkas, O.; Foresman, J. B.; Fox, D. J. Gaussian 16 Rev. C.01, 2016.

(37) Peng, C.; Bernhard Schlegel, H. Combining Synchronous Transit and Quasi-Newton Methods to Find Transition States. *Isr. J. Chem.* **1993**, *33* (4), 449–454. https://doi.org/10.1002/ijch.199300051.

(38) Ochterski, J. W.; Petersson, G. A.; Montgomery, J. A. A Complete Basis Set Model Chemistry. V. Extensions to Six or More Heavy Atoms. *J. Chem. Phys.* **1996**, *104* (7), 2598–2619. https://doi.org/10.1063/1.470985.

(39) Montgomery, J. A.; Frisch, M. J.; Ochterski, J. W.; Petersson, G. A. A Complete Basis Set Model Chemistry. VI. Use of Density Functional Geometries and Frequencies. *J. Chem. Phys.* **1999**, *110* (6), 2822–2827. https://doi.org/10.1063/1.477924.

(40) Yamaguchi, K.; Fukui, H.; Fueno, T. Molecular Orbital (MO) Theory For Magnetically Interacting Organic Compounds. Ab-Initio MO Calculations of The Effective Exchange Integrals For Cyclophane-Type Carbene Dimers. *Chem. Lett.* **1986**, *15* (4), 625–628. https://doi.org/10.1246/cl.1986.625.

(41) Yamaguchi, K.; Takahara, Y.; Fueno, T.; Houk, K. N. Extended Hartree-Fock (EHF) Theory of Chemical Reactions: III. Projected Møller-Plesset (PMP) Perturbation Wavefunctions for Transition Structures of Organic Reactions. *Theor. Chim. Acta* **1988**, *73* (5–6), 337–364. https://doi.org/10.1007/BF00527740.

(42) Yamanaka, S.; Okumura, M.; Nakano, M.; Yamaguchi, K. EHF Theory of Chemical Reactions Part 4. UNO CASSCF, UNO CASPT2 and R(U)HF Coupled-Cluster (CC) Wavefunctions. *J. Mol. Struct.* **1994**, *310*, 205–218.

(43) David, G.; Trinquier, G.; Malrieu, J.-P. Consistent Spin Decontamination of Broken-Symmetry Calculations of Diradicals. *J. Chem. Phys.* **2020**, *153* (19), 194107. https://doi.org/10.1063/5.0029201.

(44) Buenger, E. W.; Bodi, A.; Burgos-Paci, M. A.; Mayer, P. M. Cyclopentene and Cyclopentadiene Formation in Isoprene Pyrolysis. *Phys. Chem. Chem. Phys.* **2024**, *26* (36), 23971–23978. https://doi.org/10.1039/D4CP02798A.

(45) Li, Y.; Yang, J.; Cheng, Z. Edited by JiuZhong Yang and Combustion Team. Photonionization Cross Section Database (Version 2.0)., 2017. http://flame.nsrl.ustc.edu.cn/database/.

(46) Pedregosa, F.; Varoquaux, G.; Gramfort, A.; Michel, V.; Thirion, B.; Grisel, O.; Blondel, M.; Prettenhofer, P.; Weiss, R.; Dubourg, V.; Vanderplas, J.; Passos, A.; Cournapeau, D. Scikit-Learn: Machine Learning in Python. *J. Mach. Learn. Res.* **2011**, *12*, 2825–2830. https://dl.acm.org/doi/10.5555/1953048.2078195.

(47) Lee, D. D.; Seung, H. S. Learning the Parts of Objects by Non-Negative Matrix Factorization. *Nature* **1999**, *401* (6755), 788–791. https://doi.org/10.1038/44565.

(48) Paatero, P.; Tapper, U. Positive Matrix Factorization: A Non-negative Factor Model with Optimal Utilization of Error Estimates of Data Values. *Environmetrics* **1994**, *5* (2), 111–126. https://doi.org/10.1002/env.3170050203.

(49) Puliyanda, A.; Sivaramakrishnan, K.; Li, Z.; De Klerk, A.; Prasad, V. Data Fusion by Joint Non-Negative Matrix Factorization for Hypothesizing Pseudo-Chemistry Using

Bayesian Networks. *React. Chem. Eng.* **2020**, *5* (9), 1719–1737. https://doi.org/10.1039/d0re00147c.

(50) Yin, D.; Yin, D.; Fu, Z.; Li, Q. The Regioselectivity of Diels–Alder Reaction of Myrcene with Carbonyl-Containing Dienophiles Catalysed by Lewis Acids. *J. Mol. Catal. Chem.* **1999**, *148* (1–2), 87–95. https://doi.org/10.1016/s1381-1169(99)00113-2.

(51) Irikura, K. K. THERMO.PY. *Natl. Inst. Stand. Technol.* **2020**.

(52) Zádor, J.; Martí, C.; Van De Vijver, R.; Johansen, S. L.; Yang, Y.; Michelsen, H. A.; Najm, H. N. Automated Reaction Kinetics of Gas-Phase Organic Species over Multiwell Potential Energy Surfaces. *J. Phys. Chem. A* **2023**, *127* (3), 565–588. https://doi.org/10.1021/acs.jpca.2c06558.

Chapter 9 – Conclusion

Each of the individual chapters of this thesis have dedicated conclusions related to the molecular system and conditions that were investigated. The goal of this conclusion section is to contextualize the collection of results into the broader picture of gas-phase terpene chemistry. It will be useful to separate the discussion into the different conditions, protonation and pyrolysis.

The terpene protonation studies represent the first look at the dissociation behaviour of these species, as previous studies focused particularly on their formation and oligomerization. These studies are useful at predicting what sort of products may be formed under the energetic excitation of protonated terpenes, a possible pathway in atmospheric chemistry. Due to the relatively large abundance of terpenes present in the atmosphere, if even a small fraction of them become protonated and subsequently dissociate under energetic excitation, that would still constitute a large quantity of protonated terpene fragmentation products present in the atmosphere.

When considering the unimolecular dissociation of protonated terpenes, with a few exceptions, the site of protonation played an instrumental role in the observed chemistry. These exceptions include isoprene and limonene; in each case there were multiple potential initial sites of protonation, but only one that was responsible for driving the dissociation chemistry that was observed. The incidence of multiple points of unsaturation within these molecules suggests that multiple sites of protonation are possible, however, when considering the dissociation chemistry just one of these sites contributed significantly, other sites that were accessible (within a 0.2 eV relative energy difference) did not contribute aside from rearrangement towards the reactive intermediate.

In all other cases of the terpene protonation studies, differing sites of protonation had a clear influence on the observed dissociations. In the study of pinene isomers, there was the presence of an additional, more stable site that was available by protonation in the cyclobutyl moiety of α-pinene, but not β-pinene. This additional stable structure helps to describe the subtle difference in fragmentation that has been observed between the two isomers. Since the protonated structure unique to α-pinene is more stable, it requires a greater energy input to overcome the initial barrier to access the calculated reaction pathway, leading to an energetic intermediate that can more readily access the higher energy pathway that yields the m/z 95 product ion. Although this example was subtle, the calculations showed that the site of protonation does impact the dissociation chemistry in these pinene isomers.

The site of protonation and its effect on the observed dissociation was more starkly evident in the case of myrcene. There were four protomer structures that were calculated from the six possible sites of protonation, with two sites that led to the same protomer, three of which with nearly equivalent relative energy values (within 0.01 eV of one another), and a fourth that was energetically non-competitive. These increased populations would thus in theory be double the population of the protomers that are populated through a single site. When calculating the pathway towards product ions from the starting protomers, it was evident that the most abundant product ion channels, m/z 95 and 81, had primarily resulted from the protomers that had this initially doubled population. The two lower abundance product ion channels, m/z 109 and m/z 93, resulted from competing pathways that arose out of the singly populated protomer. In all cases, the calculated reaction mechanisms related to the experimental observations due to the initial site of protonation of myrcene in the ion source.

The investigation of terpenoids was driven by the desire to observe the effect of the incorporation of oxygen into the terpene structure via hydroxylation. In the context of sites of protonation, this oxygen is significant as it represents a heteroatom that may readily accept a proton. There were some interesting observations when considering the terpenoids prenol, linalool and α-terpineol. Protonation on the oxygen was generally favourable when compared to protonation at an alkene position. Protonation on the hydroxyl ultimately lands up as a neutral water that is bound to a protonated terpene moiety as an ion-molecule complex. In the cases of prenol and linalool, this ion-molecule complex is not stable enough to survive the ion optics responsible for transmitting the protonated ion from the ion source to the first quadrupole for mass selection. Thus, all of the observed ion chemistry, particularly the relatively low abundance of water loss dissociation pathways, arise exclusively from protonation at alkene sites, since these protomers are stable enough to reach the collision cell for fragmentation. By contrast, in the case of α-terpineol, there is a relatively large dissociation barrier to remove the water that is formed from protonation at the hydroxyl group from the ion-molecule complex, allowing it to be stable enough to be mass selected. Thus, the dissociation experiment is dominated by the water loss channel.

The original goal of the protonated terpene work was to investigate their decomposition to help identify potential dissociation products that could be present in the troposphere. More broadly, this work has implications for analytical mass spectrometry.

In molecules that have multiple heteroatoms, or hydrocarbon sites that may accept protons like alkenes or alkynes, the site of protonation clearly has an impact on the observed fragmentation. These observations can have consequences in MS/MS experiments, as the dissociation product ions that are formed may be dependent upon the starting protonated structure that is formed in the ion source prior to mass selection. Considering this factor may contribute towards greater understanding of the fragmentation chemistry and enable complete annotation in cases where fragmentation products are not immediately obvious.

When considering the neutral pyrolysis experiments, some unique observations were able to be made due to the experimental design. For instance, the flash pyrolysis set up used at the Swiss Light Source enables very high temperature, short timescale experiments, a feature that has been lacking in the terpene thermal decomposition literature. Furthermore, the iPEPICO beamline allows for more precise identification of compounds that other methods like GC, IR spectroscopy and photoionization experiments are unable to. The key factor is that iPEPICO can differentiate structural isomers by their initial photoionization band, information that the aforementioned methods are unable to distinguish. In the studies on the pyrolysis of isoprene, the experimental TPES for m/z 68 obtained from the iPEPICO experiment showed an additional onset band at higher photon energy, which was able to be identified as cyclopentene. This observation represents a novel product in the pyrolysis of isoprene and allowed for the calculation of a new pathway that leads to cyclopentadiene that is comparable in energy to previously described reactions and features the observed cyclopentene as an intermediate. This information would not have been accessible without using iPEPICO to identify that key intermediate.

When considering the monoterpene pyrolysis experiments, previous reports in the literature were focused on either rigorous experimental work or theoretical work, with minimal combination and overlap of the two. This shortcoming presented an opportunity for this projects combinatorial approach to provide a deeper understanding of the reaction mechanisms involved in the pyrolysis of limonene, α-, and β-pinene. The pyrolysis experiments carried out at the iPEPICO beamline allowed for accurate identification of the products that were obtained. This identification was crucial for determining the theoretically calculated reaction mechanisms. For instance, the presence of substituted benzenes in the case of α-pinene allowed for the calculation of a pathway that relied on the sequential loss of methyl radicals, a process that was shown to be unique to this monoterpene. Furthermore, by using non-negative matrix factorization on the experimental data, it was possible to identify the decomposition pathways as unique to a specific monoterpene or correlated and shared with another one. This treatment showed that the decomposition products of α-pinene were largely unique to itself, while the limonene and β-pinene decomposition products were correlated with each other. Ultimately, the combination of experiment and theory were responsible for providing the insights that were gleaned from the pyrolysis of representative monoterpenes.

Chapter 10 – Appendix

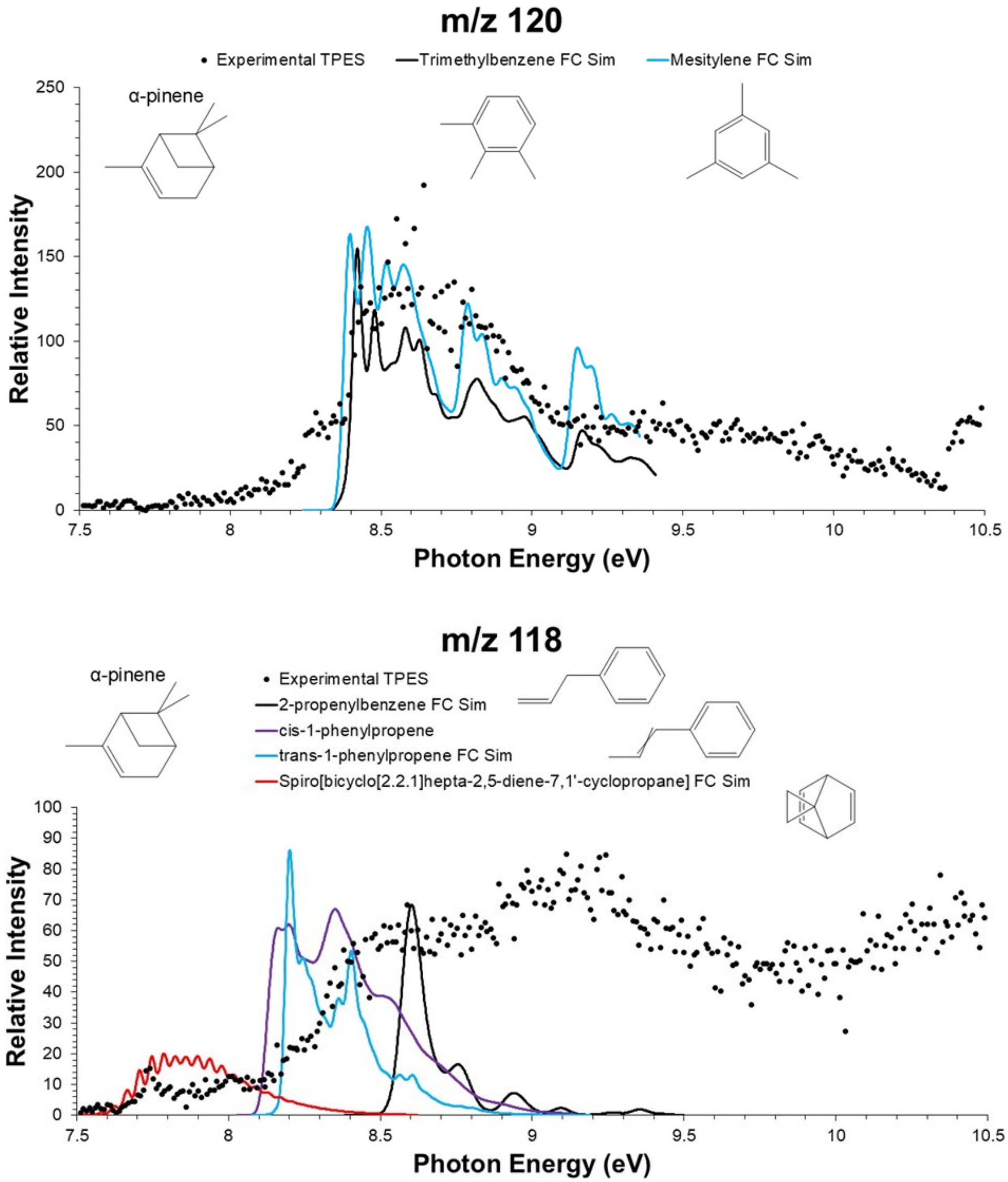

Figure A1: ms-TPES (black dots) and Franck-Condon simulations (solid lines) of m/z 120 and 118 obtained from α-pinene pyrolysis.

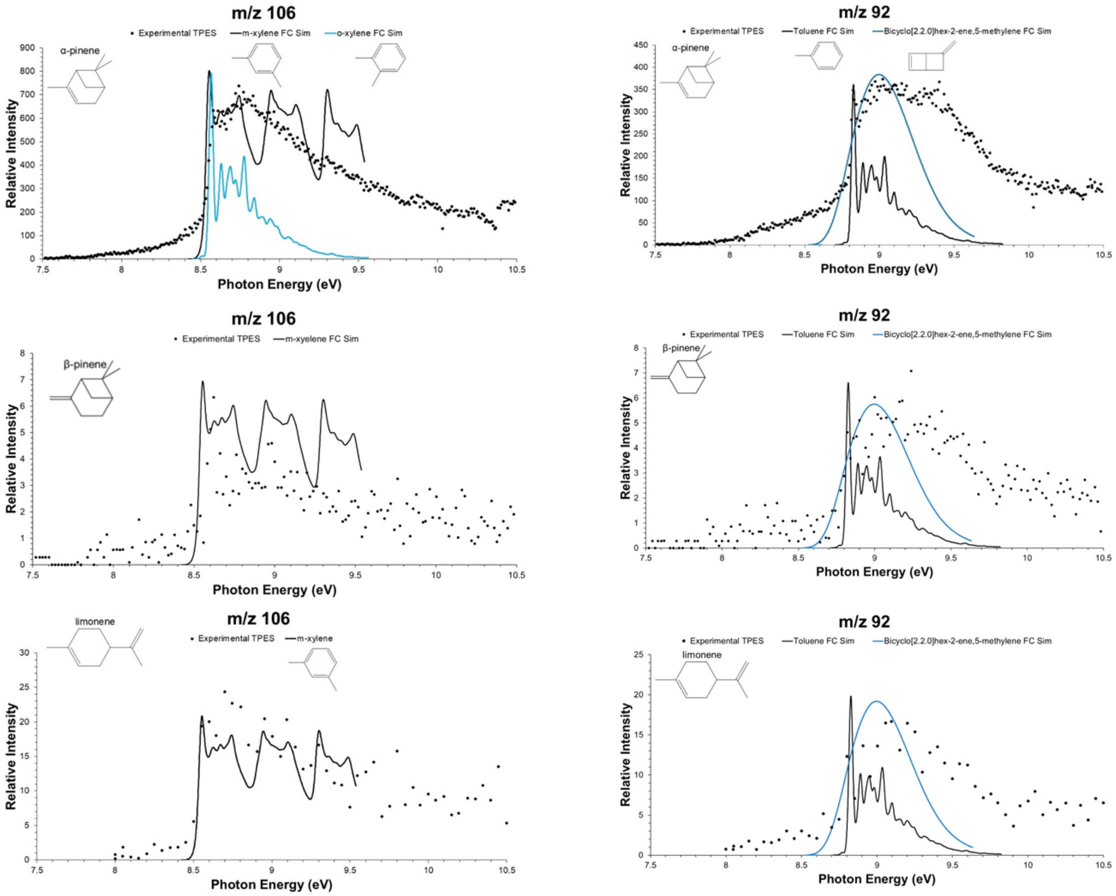

Figure A2: ms-TPES (black dots) and Franck-Condon simulations (solid lines) of m/z 106 and 92 obtained from α-pinene, β-pinene, and limonene pyrolysis.

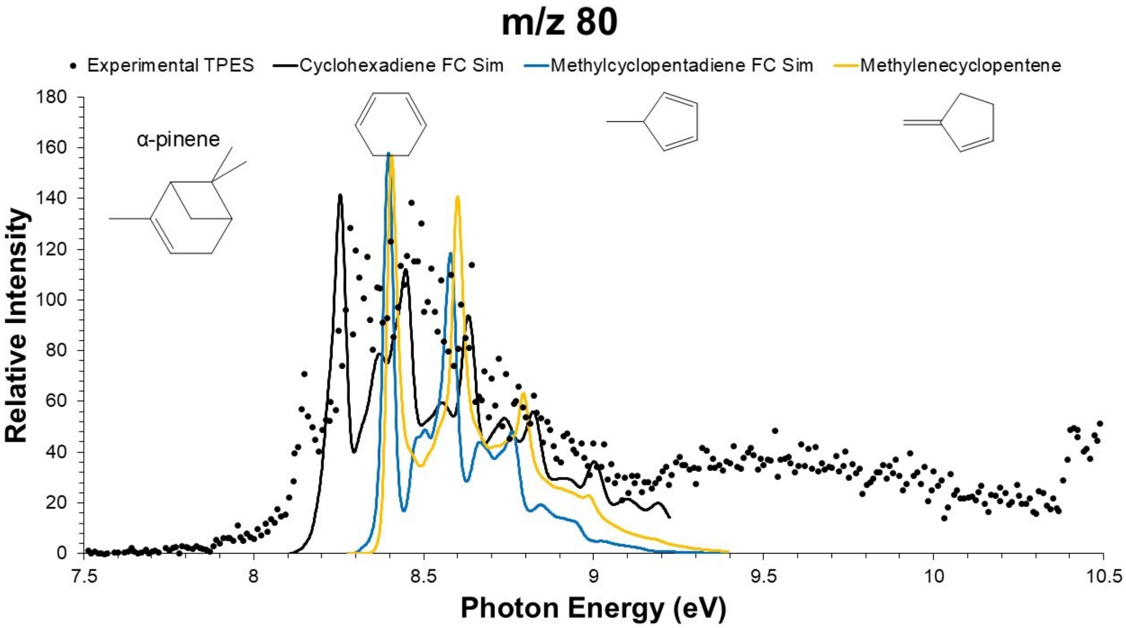

Figure A3: ms-TPES (black dots) and Franck-Condon simulations (solid lines) of m/z 106 and 92 obtained from α-pinene, β-pinene, and limonene pyrolysis.

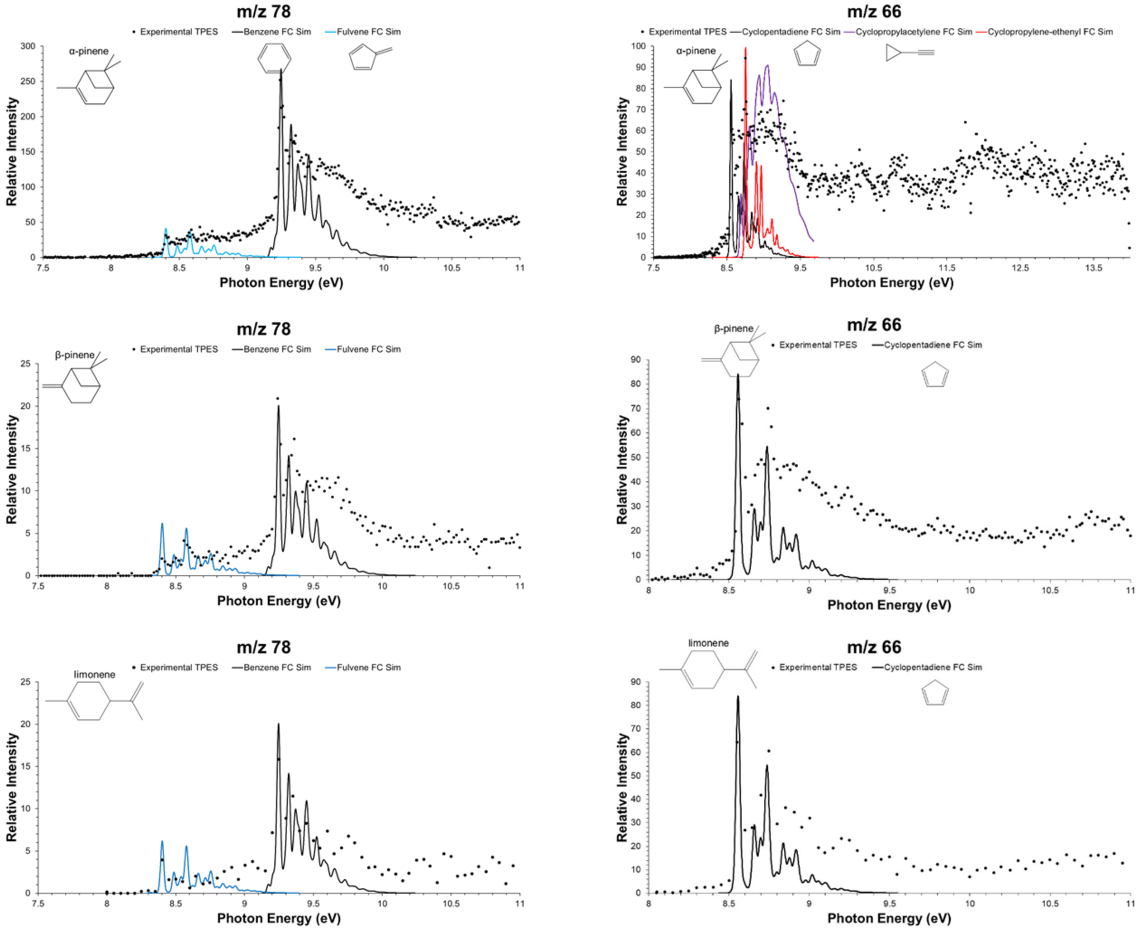

Figure A4: ms-TPES (black dots) and Franck-Condon simulations (solid lines) of m/z 78 and 66 obtained from α-pinene, β-pinene, and limonene pyrolysis.

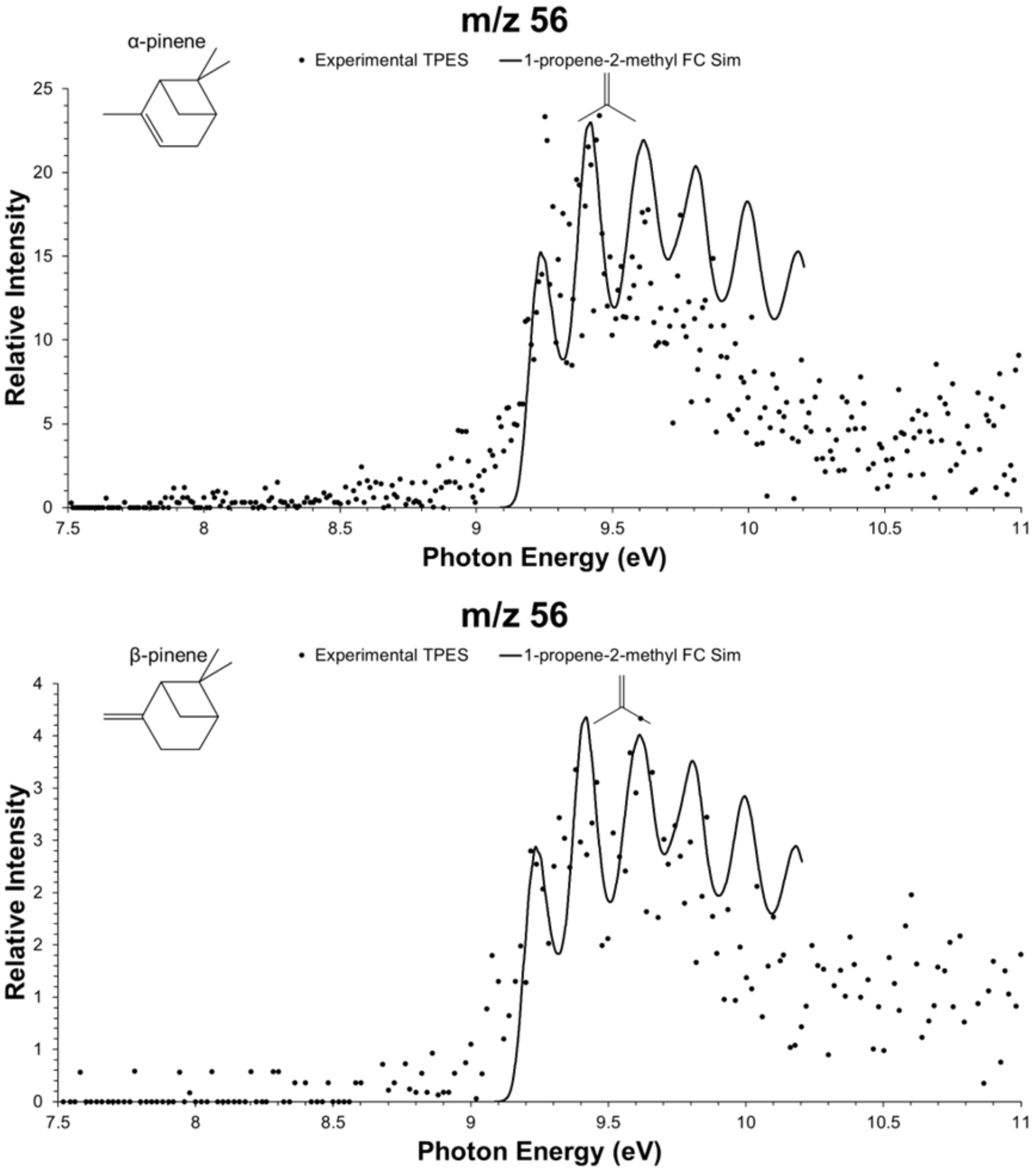

Figure A5: ms-TPES (black dots) and Franck-Condon simulations (solid lines) of m/z 56 obtained from α-pinene, and β-pinene pyrolysis.

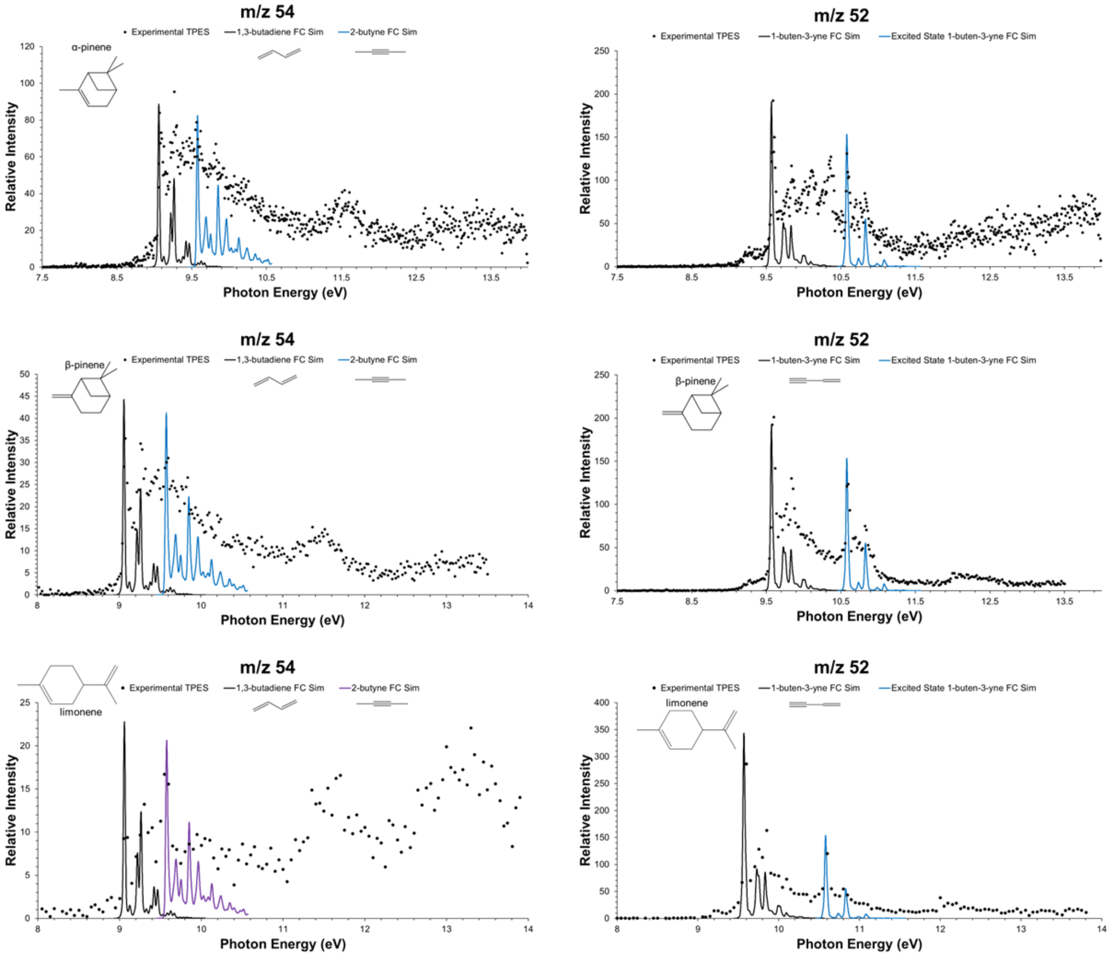

Figure A6: ms-TPES (black dots) and Franck-Condon simulations (solid lines) of m/z 54 and 52 obtained from α-pinene, β-pinene, and limonene pyrolysis.

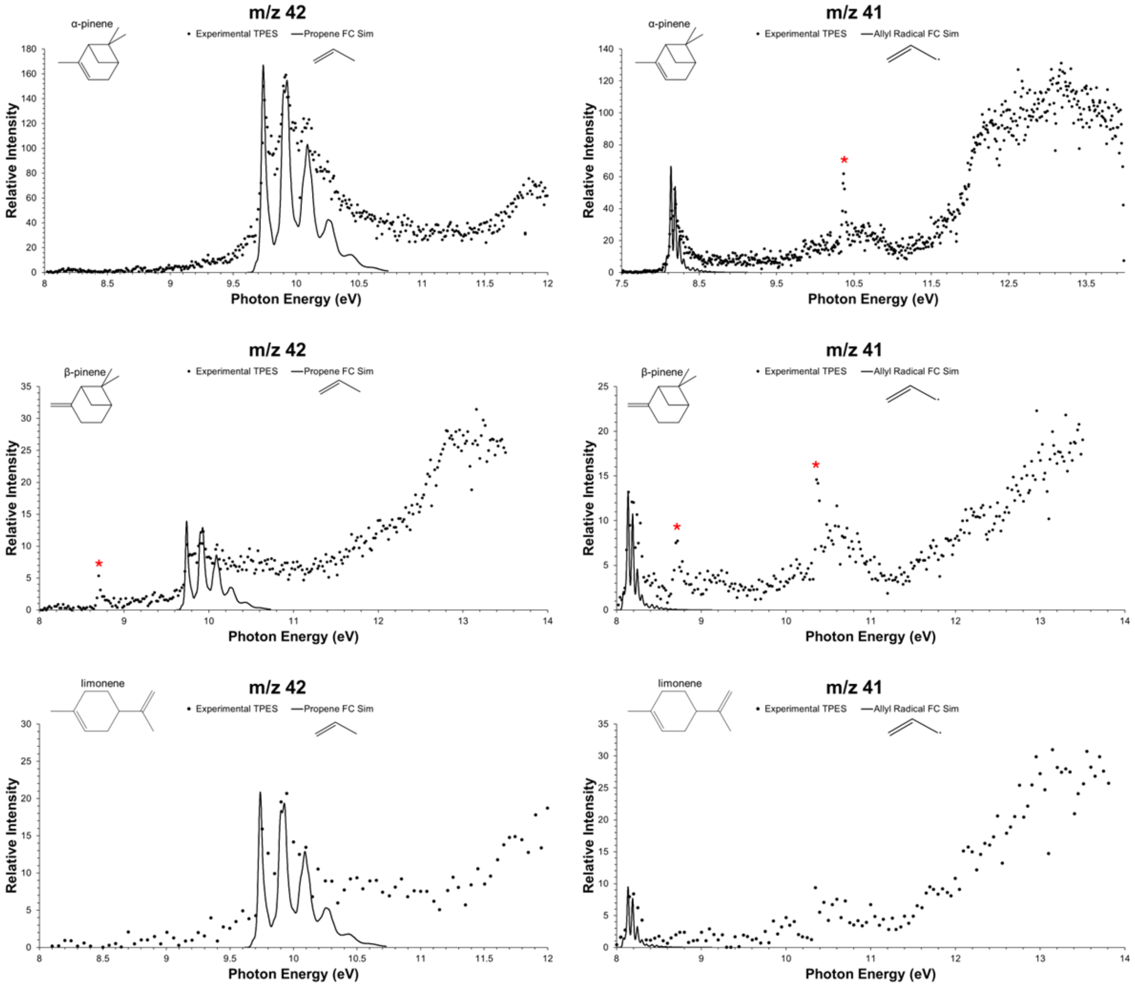

Figure A7: ms-TPES (black dots) and Franck-Condon simulations (solid lines) of m/z 42 and 41 obtained from α-pinene, β-pinene, and limonene pyrolysis.

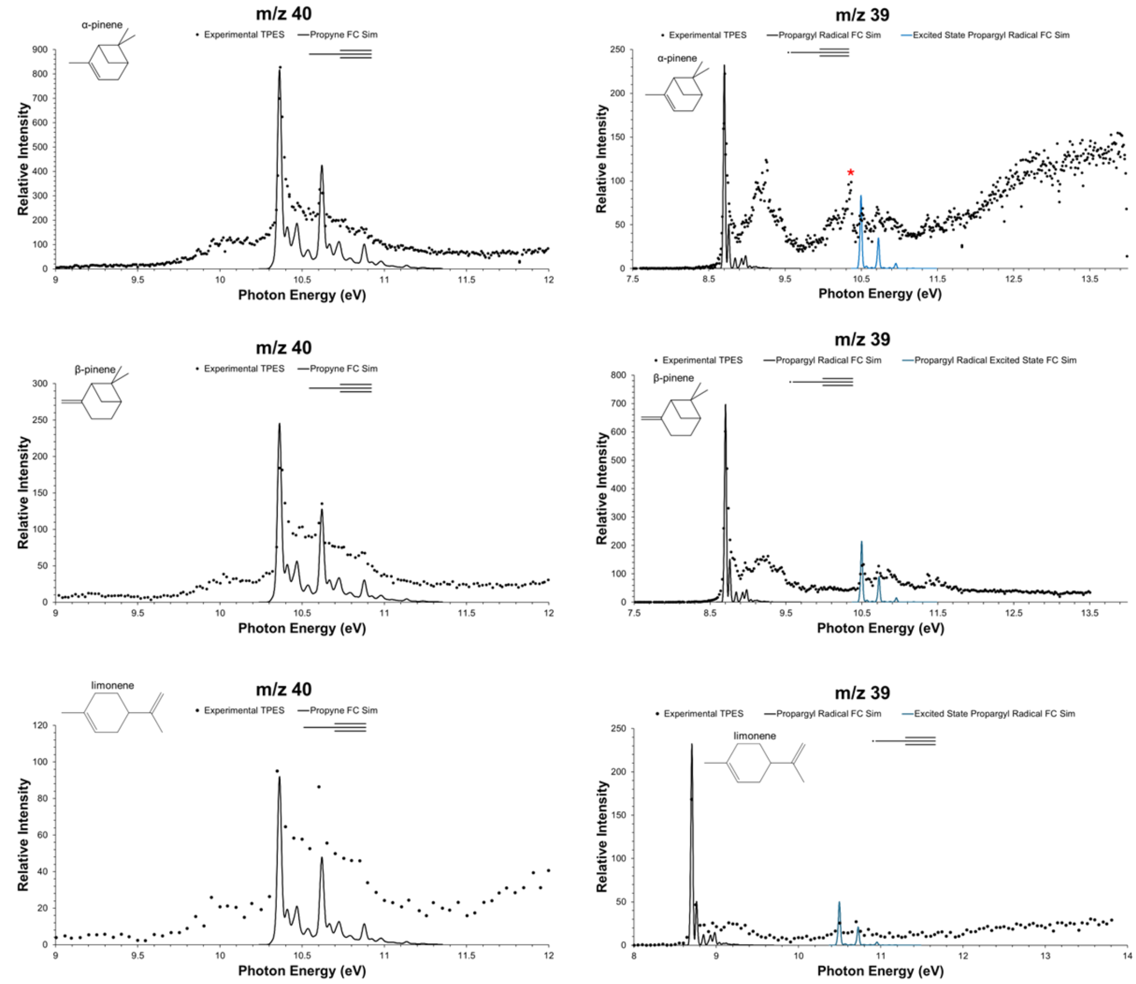

Figure A8: ms-TPES (black dots) and Franck-Condon simulations (solid lines) of m/z 40 and 39 obtained from α-pinene, β-pinene, and limonene pyrolysis.

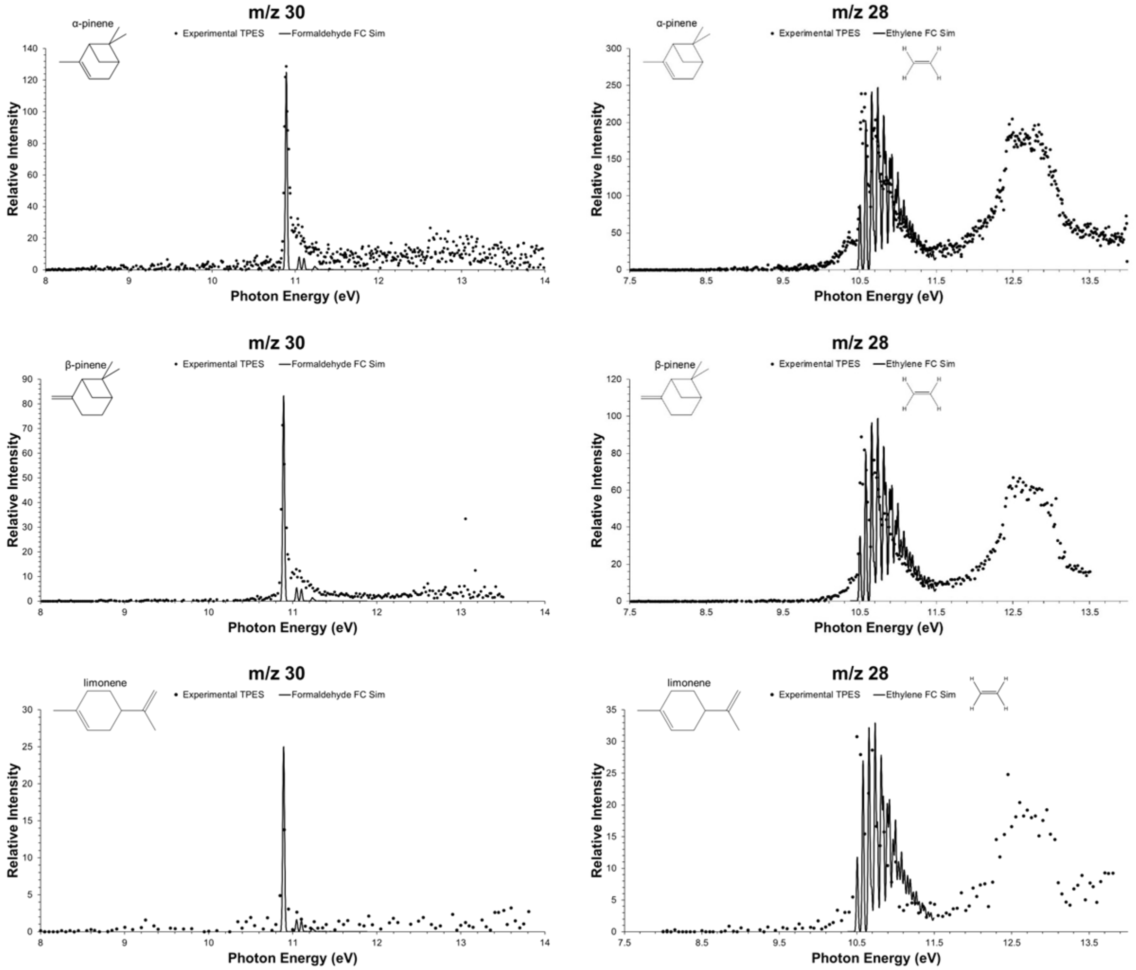

Figure A9: ms-TPES (black dots) and Franck-Condon simulations (solid lines) of m/z 30 and 28 obtained from α-pinene, β-pinene, and limonene pyrolysis.

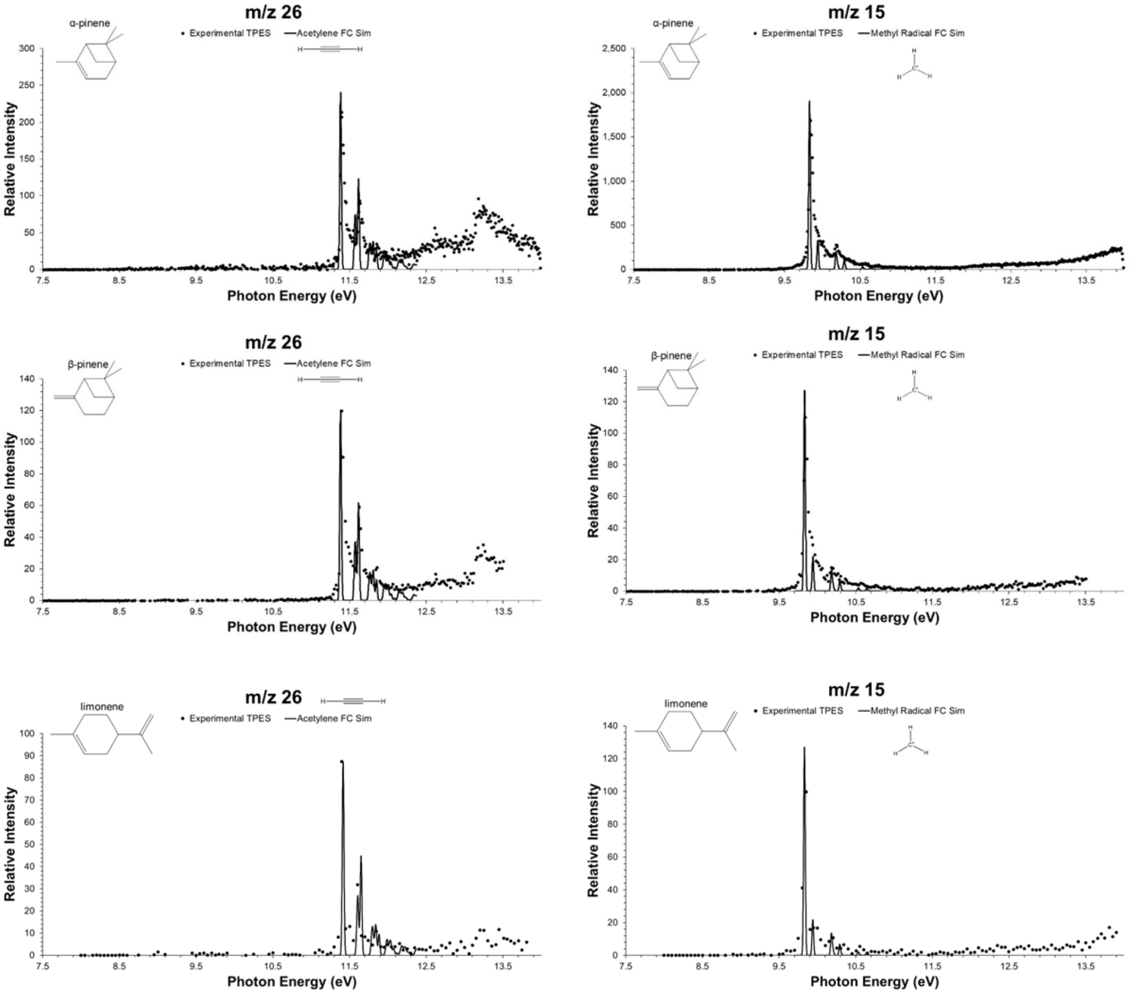

Figure A10: ms-TPES (black dots) and Franck-Condon simulations (solid lines) of m/z 26 and 15 obtained from α-pinene, β-pinene, and limonene pyrolysis.